Electron spectromicroscopy : from organic-inorganic drug nanocarriers to biological systems

Maeva Chaupard

To cite this version:

Maeva Chaupard. Electron spectromicroscopy : from organic-inorganic drug nanocarriers to biological systems. Material chemistry. Université Paris-Saclay, 2023. English. NNT : 2023UPASF051 . tel-04260509

HAL Id: tel-04260509
https://theses.hal.science/tel-04260509v1

Electron spectromicroscopy: from organic-inorganic drug nanocarriers to biological systems

Microscopie électronique analytique: des nanovecteurs thérapeutiques organiques-inorganiques aux systèmes biologiques

Thèse de doctorat de l'université Paris-Saclay

École doctorale n°571: Sciences Chimiques : Molécules, Matériaux, Instrumentation et Biosystèmes (2MIB)
Spécialité de doctorat: Chimie
Graduate School : Chimie. Référent : Faculté des sciences d'Orsay

Thèse préparée dans les unités de recherche **Laboratoire de Physique des Solides** (Université Paris-Saclay, CNRS) et **Institut des Sciences Moléculaires d'Orsay** (Université Paris-Saclay, CNRS), sous la direction de **Marta DE FRUTOS**, Chargée de recherche, et le co-encadrement de **Ruxandra GREF**, Directrice de recherche.

Thèse soutenue à Paris-Saclay, le 06 octobre 2023, par

Maeva CHAUPARD

Composition du jury

Membres du jury avec voix délibérative

Marie ERARD Professeure, Université Paris-Saclay, CNRS	Présidente
Aude DEMESSENCE Chargée de recherche (HDR), Université Lyon, CNRS	Rapporteuse & Examinatrice
Ovidiu ERSEN Professeur, Université de Strasbourg, CNRS	Rapporteur & Examinateur
Demie KEPAPTSOGLOU Directrice de recherche, University of York	Examinatrice
Gilles PATRIARCHE Directeur de recherche, Université Paris-Saclay, CNRS	Examinateur
Christian SERRE Directeur de recherche, Université PSL, CNRS	Examinateur

THESE DE DOCTORAT

NNT : 2023UPASF051

Acknowledgement

Tout d'abord, je tiens à remercier mes encadrantes, Marta de Frutos et Ruxandra Gref pour leur investissement dans ce projet et leur soutien tout au long de ces trois années. En particulier, je suis très reconnaissante à Marta de Frutos qui, au-delà des requis standards, s'est assurée aussi bien de la concrétisation de ces travaux que de mon bien-être professionnel.

Merci aux membres du jury, Marie Erard, Aude Demessence, Ovidiu Ersen, Demie Kepaptsoglou, Gilles Patriarche et Christian Serre, pour l'examen de mes travaux de thèse. C'est une grande fierté d'avoir pu bénéficier de votre expertise pluridisciplinaire, confronter mes idées et présenter les possibilités qu'ouvrent ce projet.

Je remercie également la totalité des membres de l'équipe STEM du Laboratoire de Physique des Solides (LPS) et de l'équipe Nanocage de l'Institut des Sciences Moléculaires d'Orsay (ISMO) pour leur accueil chaleureux et leur bienveillance. Nous avons passé de merveilleux moment au laboratoire et en dehors. Restaurant, barbecue, bar, tous les prétextes sont bons pour se réunir ! Une pensée spéciale à Odile Stéphan, Jean-Denis Blazit, Yves Auad, Xiaoyan Li, Michael Walls, Steffi Woo, Laura Bocher, Mathieu Kociak et Christian Colliex qui ont toujours répondu présent lorsque j'avais besoin d'eux. Une mention particulière aussi pour Marcel Tencé, partenaire de bureau et ingénieur de renom, sans qui de nombreux développements et résultats n'auraient jamais vu le jour.

Ce travail n'aurait bien-sûr pas abouti sans de précieuses collaborations au sein de l'Université Paris-Saclay mais également avec l'Institut Gustave Roussy et l'Université de Cádiz. Ainsi, je remercie Susana Trasobares, Miguel Lopez-Haro, Giorgia Urbinati, Jéril Degrouard, Claire Boulogne, Alexandre Dazzi, Ariane Deniset-Besseau et Jérémie Mathurin pour leur temps et leur gentillesse. Bien que toutes nos études ne soient pas présentées dans ce manuscrit, vous m'avez inculqué un savoir-faire de qualité qui se retrouve aujourd'hui dans ma méthode scientifique et ma rigueur d'analyse.

Enfin et surtout, un énorme merci à ma famille qui m'a accompagné dans les bons comme les mauvais moments. À mes parents, qui ont toujours fait preuve de patience et d'écoute. Vous avez été un soutien émotionnel incommensurable. À Victor Courtin, qui m'a épaulé au quotidien, dans les périodes les plus rudes, stressantes et pleines d'émotions; et ce malgré ses engagements en thèse. À mes beaux-parents, qui ont partagé mes péripéties et réussites.

université PARIS-SACLAY

ÉCOLE DOCTORALE
Sciences Chimiques : Molécules,
Matériaux, Instrumentation
et Biosystèmes (2MIB)

Titre: Microscopie électronique analytique: des nanovecteurs thérapeutiques organiques-inorganiques aux systèmes biologiques

Mots clés: STEM-EELS, STEM-EDS, nanomatériaux sensibles aux radiations, nanoparticules organiques-inorganiques, administration contrôlée de médicaments, systèmes biologiques

Résumé: En couplant la microscopie électronique à transmission à balayage (STEM) à la spectroscopie de perte d'énergie des électrons (EELS), il est possible d'analyser localement la structure chimique et les propriétés physico-chimiques des matériaux. Cependant, utilisé aux doses électroniques usuelles, le faisceau d'électron endommage irréversiblement les échantillons sensibles aux radiations, comme c'est le cas des composés organiques-inorganiques, organiques et en particulier, biologiques. Ce travail de thèse fournit de nouvelles méthodologies pour l'analyse sans dommage de tels systèmes, à une résolution supérieure à 10 nm. Ces approches ont été notamment appliquées à l'analyse nanométrique de vecteurs thérapeutiques métallo-organiques (MOFs), dans le but de mettre à jour leurs mécanismes de biodégradation dans les milieux physiologiques et de chargement en principe actif. Grâce à la large gamme spectrale couverte par l'EELS monochromaté, les données obtenues dans les domaines de l'infrarouge, de l'ultraviolet-visible et des rayons X mous ont été combinées pour caractériser la structure chimique de divers échantillons, qu'ils soient organiques-inorganiques (MOFs), organiques (médicaments) ou biologiques (macrobiomolécules). Néanmoins, dû aux faibles signaux spectraux, certains cas nécessitent des doses électroniques plus intenses qui se révèlent destructives pour le matériel. Une fois endommagés, les échantillons présentent des signatures modifiées, qu'il est toutefois possible de relier aux structures chimiques originelles. Pour cela, l'effet du faisceau a été étudié dans les trois gammes spectrales. Les mécanismes d'endommagement et les composés produits ont été identifié et reliés à des groupements chimiques spécifiques. À l'avenir, de telles méthodologies pourraient être appliquées à l'étude de systèmes biologiques complexes tels que les cellules.

Title: Electron spectromicroscopy: from organic-inorganic drug nanocarriers to biological systems

Keywords: STEM-EELS, STEM-EDS, radiation-sensitivity, organic-inorganic nanomaterials, drug delivery, biological systems

Abstract: Coupling Scanning Transmission Electron Microscopy (STEM) with Electron Energy Loss Spectroscopy (EELS) enables to study the chemical structure and the physico-chemical properties of nanomaterials. However, under usual electron doses, the electron beam irreversibly damages radiation-sensitive materials, such as organic-inorganic, organic and biological components. This thesis provides novel methodologies for the damage-free analysis of such systems at a spatial resolution better than 10 nm. These methodologies were applied to the individual characterisation of Metal-Organic Framework (MOF) drug nanocarriers, with the aim of providing a better understanding of their mechanisms of biodegradation in physiological media and their drug loading. Using the wide spectral range covered by monochromated EELS, observations obtained in the infrared, ultraviolet-visible and soft X-ray regions were correlated to decipher the complete chemical structure of various specimens, whether organic-inorganic (MOFs), organic (drugs) or biological (macrobiomolecules). In some cases, however, it is necessary to increase the electron dose, resulting in damage to the specimen. Nevertheless, it is possible to relate the damaged signatures to the original chemical structures by studying the beam effect. The three spectral ranges were used to monitor and understand the damage mechanisms. The species produced were identified and linked to specific chemical groups of the specimen. In the future, such methodologies could also be applied to the study of complex biological systems such as cells.

Résumé étendu en français

Au sein de la communauté scientifique, un effort important est consacré à la science du vivant. En effet, l'étude des mécanismes biologiques est essentielle pour faire avancer les progrès médicaux. C'est pourquoi, une multitude d'outils et techniques ont été développés pour l'analyse d'échantillons, allant de l'échelle macroscopique (organisme complet), à l'échelle microscopique (cellule et organelles).

La microscopie électronique analytique est l'une des techniques les plus prometteuses permettant l'analyse chimique avec une résolution spatiale sub-nanométrique. En particulier, la microscopie électronique à transmission à balayage (STEM) couplée à la spectroscopie de perte d'énergie des électrons (EELS) permet d'analyser la structure chimique et les propriétés physico-chimiques des échantillons. Bien que cette technique ait depuis longtemps fait ses preuves en science des matériaux, elle n'a été que très peu utilisée pour l'analyse de composés organiques-inorganiques, organiques et en particuliers, biologiques. En effet, utilisée aux doses électroniques usuelles, le faisceau d'électron endommage irréversiblement ces systèmes sensibles aux radiations.

Ce travail de thèse fournit de nouvelles méthodologies pour l'analyse sans dommages de tels composés, à une résolution supérieure à 10 nm. En utilisant des températures cryogéniques, des faibles doses électroniques et une détection directe des électrons, cette étude démontre la possibilité de collecter des signatures intactes de divers échantillons, qu'ils soient organiques-inorganiques (réseaux métallo-organiques, MOFs), organiques (médicaments) ou biologiques (macrobiomolécules). Grâce à la large gamme spectrale couverte par l'EELS monochromaté, les données obtenues dans les domaines de l'infrarouge, de l'ultraviolet-visible et des rayons X mous ont été combinées pour caractériser la structure chimique des échantillons.

En parallèle, cette étude a également apporté plusieurs éclaircissements sur le fonctionnement des nanovecteurs thérapeutiques métallo-organiques (MOFs) et leur interaction avec l'organisme. Une analyse nanométrique poussée a été menée afin de mieux comprendre leur biodégradation dans les milieux physiologiques et leur chargement en principe actif à l'échelle nanométrique.

Pour les signaux faibles, il a été nécessaire d'utiliser des doses élevées conduisant à l'endommagement des échantillons. Toutefois, il a tout de même été possible de relier les signatures spectrales endommagées aux structures originelles intactes. En étudiant in situ l'effet du faisceau dans les trois gammes spectrales, les mécanismes d'endommagement et les composés produits ont été identifiés et reliés à des groupements chimiques spécifiques. Il a notamment été constaté que l'irradiation induit une conversion chimique similaire pour les composés organiques et biologiques analysés produisant des gaz d'oxyde de carbone et des espèces insaturées. Cette étude de l'endommagement de la matière organique à des doses électroniques croissantes s'est avérée pertinente pour déceler l'hétérogénéité de l'altération chimique des MOFs par le milieu physiologique.

Bien que ce manuscrit présente des résultats prometteurs pour l'utilisation du STEM-EELS en science du vivant, les limites de la technique quant à la détection de faibles concentrations de composés sensibles (i.e. MOFs chargés en principe actif) ont été explorées. Dans ce cas, les résultats montrent qu'il s'avère nécessaire de coupler différentes techniques de microscopie électronique analytique (EELS et EDS, Energy Dispersive X-ray Spectroscopy) afin de fournir une analyse complète des nanostructures complexes.

Contents

List of abbreviations

ABSF	Average background subtraction filter
ADF	Annular dark-field
BF	Bright-field
BSA	Bovine serum albumin
cFEG	Cold field-emission gun
Cryo-TEM	Cryogenic transmission electron microscopy
Cs	Spherical abberation
DED	Direct electron detection
DLS	Dynamic light scattering
DNA	Deoxyribonucleic acid
EDS	Energy dispersive X-ray spectroscopy
EELS	Electron Energy Loss Spectroscopy
EM	Electron microscopy
FTIR	Fourier transform infrared spectroscopy
GMP	Gemcitabine monophosphate
HAADF	High-angle annular dark-field
iDPC	Integrated differential phase contrast
IR	Infrared
MIL	Materials of Institute Lavoisier
MOF	Metal-organic framework
NLLS	Non-Linear Least Squares
PBS	Phosphate-buffered saline
PCA	Principal component analysis
SNR	Signal-to-noise ratio
STEM	Scanning transmission electron microscopy
TEM	Transmission electron microscopy
TGA	Thermogravimetric analysis
UiO	Universitetet i Oslo
UV-vis	Ultraviolet-visible
XR	X-ray
ZIF	Zeolitic imidazolate framework
ZLP	Zero-loss peak

List of Figures

List of Tables

Chapter 1 .

Introduction

1.1 . Nanomaterials for drug delivery

Over the years, humanity has continued to improve health and life expectancy. As the world's second most deadly disease, cancer represents the most urgent need for more effective and personalised therapies. In 2020, the World Health Organization registered more than 19 million people affected by cancer (all types). Lung, colorectal, liver, stomach and breast cancers are the most deadly, accounting for nearly 5 million deaths. This number is expected to almost double to 9 million by 2040.[1]

In order to develop innovative therapeutic strategies, the biomedical field has become increasingly interested in nanotechnologies. Nowadays, nanomaterials are notably used for drug delivery, to load and locally release a drug of interest in specific tissues, such as tumours. This allows to overcome the main limitations of conventional systemic therapies (*e.g.* chemotherapy), which are *i)* a poor absorption of the drug by the tissues due to unfavorable physico-chemical properties, *ii)* a low bioavailability due to the rapid clearance of the drug (enzymatic degradation and natural excretion), and *iii)* a non-specific action resulting in severe side effects.[2–4] In drug delivery, the nanocarrier acts as a protective matrix that transports a large amount of the drug to the diseased tissue.

In order to be injected into the patient, drug nanocarriers must be nano-sized and non-toxic. First, their size should be suitable for circulation in the bloodstream, typically less than 200 nm.[5, 6] Their colloidal stability is also crucial to avoid aggregation and vascular occlusion.[5–7] Secondly, the use of biocompatible nanomaterials is obviously the best choice for biomedical applications. Note that, biocompatibility also includes the non-toxicity of the by-products generated by interaction with the organism. To avoid undesired toxic effects, more and more studies focus on biocompatible and biodegradable nanomaterials. Yet, extensive *in vitro* and *in vivo* studies are required to determine the cellular fate of nanocarriers.

Once administrated in the bloodstream, the loaded nanomaterials are designed to target the diseased organ for local drug release. In cancer therapy, specific targeting is based on a passive and/or active approach. Passive targeting is based on the so-called "enhanced permeability and retention effect".[8, 9] Taking advantage of the leaky tumour blood vessels, the nanoparticles spontaneously accumulate nearby cancer cells over time. The active approach further enhances cancer targeting and cell internalisation. It is based on the molecular recognition between the overexpressed tumour receptors (growth factors, antigens or proteins) and active biomolecules anchored to the surface of the nanocarrier.[5, 7, 10] Once the nanomaterials are on site, the release can be achieved by gate opening, cleavable linkers or dissolution, depending on the nature of the nanocarriers. In advanced approaches, different stimuli can induce the drug release in response to internal triggers (pH, temperature, enzymatic activity, oxidative stress, reducing agent) or external triggers (magnetic field, light).[7, 11]

1.1.1 . Metal Organic Frameworks

Since the first development of drug nanocarriers, the scientific community has designed a series of nanomaterials with different properties to continuously improve the therapeutic efficacy (drug payload, release efficiency, targeting).[4] Nowadays, several nanocarriers are described in the literature, either organic, inorganic or hybrid organic-inorganic.[5, 7] In the last fifteen years, Metal Organic Frameworks nanoparticles (MOFs) have shown interesting capabilities for transporting large amounts of drug in the living body.[12, 13]

MOFs are organic-inorganic nanomaterials, composed of metal nodes coordinated with organic linkers. They have a versatile composition that makes their properties tunable and a highly porous structure that can be two or three dimensional. They have been widely studied in the literature for gas storage and separation, catalysis, chemical sensing or electrical conductivity.[14] When applied to drug delivery, their building blocks can be carefully chosen to ensure biocompatibility and biodegradability, while their inherent porosity ensures high drug payloads.[6, 15] Interestingly, their pore size can also be tuned to match the entrapped molecule and increase the drug payloads, by adjusting the length of the organic linkers.[16, 17] In addition, impressive breakthroughs have been made by designing MOFs as composite nanomaterials, either by anchoring engineered polymer coatings[18] or by coupling with responsive inorganic nanoparticles.[19]

Among the wide variety of MOFs, MIL-100 are one of the most studied for biomedical applications. In particular, MIL-100(Al) and MIL-100(Fe) have been shown to be biocompatible by several *in vitro* and *in vivo* assays (see Table 1.1). MIL-100(Al) were found to be non-toxic to human alveolar, hepatic and cervical cancer cells.[20, 21] Various human cells (healthy and cancerous) also showed no cytotoxicity after incubation of MIL-100(Fe) from 24h to 72h.[22–28] Some exceptions were obtained for human liver cells due to the inherent biological activity of iron, which generates an oxidative-stress.[20, 29] In addition, *in vivo* studies have been carried out on Wistar female rats [23, 30–32] and Danio Rerio zebrafish embryos [29] by intravenous administration of high doses of MIL-100(Fe), up to 220 mg/kg. All report no toxicity over 24h and up to 3 months. A rapid accumulation of MOFs in the liver and spleen of the mice was typically observed due to the immune recognition and macrophage capture (Kupffer cells and splenic macrophages).

1.1.2 . A strong therapeutic asset

Both MIL-100(Al) and MIL-100(Fe) have been studied to incorporate a wide range of drugs. Table 1.2 depicts a non-exhaustive list of the encapsulated anti-infective and anticancer drugs in these nanoparticles. This highlights the therapeutic potential of MOFs. Moreover, these nanoparticles have also been used for the co-encapsulation of synergistic drugs, such as azelaic acid and nicotinamide,[40] amoxicillin and potassium clavulanate,[24] and azidothymidine triphosphate and lamivudine triphosphate [41]. This synergic activity is particularly interesting for improving the therapeutic efficacy.

Note that, contrary to MIL-100(Al), MIL-100(Fe) nanoparticles have been more extensively studied due to their endogeneous metal. The trivalent iron of MIL-100(Fe) provides advantageous synergistic properties with the drug such as antibacterial [24] and anticancer activities [33] related to the catalytic production of reactive oxygen species (Haber-Weiss and Fenton reactions [34, 35]), and theranostic properties making the nanoparticles a potential candidate for magnetic resonance imaging contrast agents.[23]

For cancer therapies, MIL-100(Al) and MIL-100(Fe) have been shown to improve pharmacokinetics of the drugs and hence, the treatment efficacy. Gemcitabine-monophosphate showed 3 times higher toxicity when delivered by MIL-100(Fe) in human pancreatic cancer cells (after 5h) [42] and in xenograft mice (after 29 days).[43] Similarly, encapsulated doxorubicin showed a 2-fold reduction in the tumour volume in female BALB/c nude mice.[37] Bi *et al.*[39] also evidenced that encapsulation of nitidine chloride not only enhanced its anticancer activity against liver cancer cells, but also reduced the drug toxicity to healthy liver cells.

1.1.3 . Drug uptake and release: a set of interactions

The high drug payload capacity of MOFs results not only from their porosity but also from their amphiphilic character (hydrophilic open metal sites and more hydrophobic organic linkers). Drugs can be physically incorporated into the pores and can also interact with the open metal sites of MOFs or the functional groups of their linkers. When designing the MOFs, these host-guest interactions need to be balanced. On the one hand, the drug uptake should be maximised to improve tumour reduction. On the other hand, the drug release should be achieved in a controlled manner over time, once the target tissue is reached. Any premature leakage or burst release reduces the efficacy of the nanoformulation. Once in contact with the biological media, MOFs undergo multiple interactions with the surrounding ions and molecules. This destabilises and degrades the drug-loaded MOFs and can lead to premature drug release. Indeed, previous work has shown that pH variations weaken the host-guest interactions of loaded-MOFs, resulting in the uncontrolled drug release. In a mimicking physiological medium (phosphate-buffered

Table 1.1: Non-exhaustive list of the cytotoxicity assays of MIL-100(Al) and MIL-100(Fe) on human healthy and cancerous cell lines.

MOFs	Cell line	Assay	Concentration	Incubation time	Toxicity	Cell viability	Ref.
MIL-100(Al)	Human alveolar adenocarcinoma (A549 and Calu-3)	TO-PRO®3	100 μg/mL	24h	None	> 85%	[20]
	Hepatic carcinoma (HepG2)	TO-PRO®3	100 μg/mL	24h	None	> 95%	[20]
	Hepatic carcinoma (Hep3b)	TO-PRO®3	100 μg/mL	24h	None	$\backsim$ 80%	[20]
	Carcinoma (HeLa)	MTT	100 μg/mL	24h	None	> 90%	[21]
MIL-100(Fe)	Microvascular (HMEC)	FACS-based	200 μg/mL	72h	None	> 70%	[36]
	Cervical carcinoma (HeLa)	MTT	1.1 mg/mL	24h	None	IC_{50}	[28]
	Breast carcinoma (MCF-7)	MTT	100 μg/mL	72h	None	> 90%	[27]
		XTT	200 μM	24h	None	> 70%	[29]
		MTT	200 μg/mL	24h	None	90 %	[37]
	Normal hepatic (HL-7702)	MTT and LDH	160 μg/mL	48h	Moderate	80 %	[38]
	Normal hepatic (LO2)	MTT	100 μg/mL	24h	None	< 90%	[39]
	Hepatic carcinoma (HepG2)	XTT	200 μM	24h	Moderate	$\backsim$ 53%	[29]
		MTT and LDH	160 μg/mL	48h	None	90 %	[38]
		TO-PRO®3	100 μg/mL	24h	None	> 95%	[20]
	Hepatic carcinoma (Hep3b)	TO-PRO®3	100 μg/mL	24h	Moderate	$\backsim$ 60 %	[20]
	Leukaemia (CCRF-CEM)	MTT	10 μM	48h	None	$\backsim$ 90%	[23]
		MTT	50 μg/mL	48h	None	> 80%	[26]
	Multiple myeloma (RPMI-8226)	MTT	10 μM	48h	None	> 90%	[23]
		MTT	50 μg/mL	48h	None	> 80%	[26]
	Pancreatic carcinoma (MiaPaCa-2 and PANC1)	MTT	300 μg/mL	72h	None	> 80%	[25]
	Alveolar adenocarcinoma (A549 and Calu-3)	MTT	300 μg/mL	72h	None	> 80%	[25]
		TO-PRO®3	100 μg/mL	24h	None	> 85%	[20]

FACS: Fluorescence Activated Cell Sorting; LDH: lactate dehydrogenase; MTT: 3-(4,5-dimethylthiazol2-yl)-2,5-diphenyltetrazolium bromide; TO-PRO®3: monomeric cyanine strain used as a dead cell indicator; XTT: 2,3-bis-(2-methoxy-4-nitro-5-sulfophenyl)-2H-tetrazolium-5-carboxanilide.

Table 1.2: Examples of the variety of drugs incorporated into MIL-100(Al) and MIL-100(Fe) by soaking after single or succesive impregnations.

MOF	Therapy	Drug	Loading	Ref.
MIL-100(Al)	Arrhythmia	Adenosine-TP	20 wt%	[44, 45]
	Cancer	Doxorubicin	27 wt% (62 wt% in gels)	[21, 46]
MIL-100(Fe)	Infection	Azidothymidine-TP	21-24 wt%	[23, 47–50]
		Co-encapsulation of azidothymidine-TP and lamivudine TP	9 wt%	[41]
		Cidofovir	16 wt%	[23]
		Co-encapsulation of amoxicillin and potassium clavulanate	35 wt%	[24]
		Nitric oxide	n.a.	[51]
		Tetracycline hydrochloride and doxycycline monohydrate	n.a.	[52]
		Isoniazid	n.a.	[53]
	Cancer	Topotecan	12 wt%	[25]
		Doxorubicin	9-33 wt%	[23, 37, 46, 54, 55]
		Gemcitabine MP	10-31 wt%	[33, 42, 56]
		Busulfan	25-32 wt%	[23, 26, 32]
		Organometallic RAPTA-C	42 wt%	[57]
		Docetaxel	57 wt%	[27]
		Nitidine chloride	33 wt%	[39]
	Inflammation	Prednisolone MP	30 wt%	[58]
		Ibuprofen	33 wt%	[12, 23, 59, 60]
		Aspirin	25 wt%	[59, 61]
	Skin disorders	Co-encapsulation of azelaic acid and nicotinamide	77 wt%	[40]

MP: monophosphorylated, TP: triphosphorylated, n.a.: not available.

saline, PBS), acidic pH induced a faster release of encapsulated docetaxel (pH 5.5: 16% vs. pH: 7.4, 5%) [27] and doxorubicin (pH 5.5: 66% vs. pH 6.8: 37% vs. pH 7.4: 30%).[37] In contrast, encapsulated isoniazid was released more rapidly at neutral pH (pH 5.8: 50% vs. pH 7.4: 72%).[53] These different behaviours were attributed to the protonation (pH 5.5) [27,37] or competitive complexation of surrounding anions with the metal clusters (pH 7.4).[53] Consistent with this, other studies have also correlated the release of phosphorylated drugs with the competitive complexation of phosphate anions present in PBS at neutral pH.[33,42,48]

In addition to destabilising the drug-loaded MOFs, the interactions with the biological media induce the biodegradation of the framework. This easily compromises the integrity of the MOFs, leading to their dissolution and hence, drug release. In a mimicked physiological medium (PBS), biodegradation induced a loss of linker and crystallinity of MOFs.[56, 58, 62, 63] This was mainly attributed to competitive complexation with phosphate anions present in PBS, which replace the organic content of the whole structure. Christodoulou *et al.*[63] have recently shown that a neutral pH also accelerates the degradation of MIL-100(Fe). In more complex biological media, such as serum, blood and simulated gastric and intestinal fluid, the presence of different ions and proteins multiplies the interactions with the framework: internal diffusion of ions, surface adsorption of proteins and possible enzymatic degradation.[58,64,65] To date, no clear mechanisms has however been revealed.

1.2 . The need of an individual characterisation

The therapeutic efficacy of MOFs drug nanocarriers depends mainly on the drug uptake in the framework and the drug release in the tissues. While the drug uptake can be tuned by improving the host-guest interactions in the *ex situ* environment (laboratory), the drug release mainly depends on the interactions with the biological medium occurring *in vivo*. Since the organism contains thousands of biomolecules, multiple interactions are ultimately involved in the release mechanisms. However, understanding these processes is essential to ensure a sustained delivery and thus improve the therapeutic efficacy. Besides, the elucidation of the biodegradation processes is also a key step in assessing the cellular fate of MOFs and their clearance from the organism.

To date, these complex processes occuring in biological media have mainly been studied using *bulk* techniques. These *bulk* techniques are based on an average measurement of large populations, which is irrelevant for studying the nanoscale behaviour of MOFs, their stability and biodegradation. The heterogeneity of the specimen inevitably leads to variations in physicochemical properties. For example, deviations in size or crystallinity can induce different interactions with the biological media and the cells. Therefore, failure to assess the heterogeneity of the MOFs features could lead to a misunderstanding of their nanoscale behaviour and mechanisms of action.

Unravelling the physico-chemical properties of MOFs and their interactions with the biological material requires the use of dedicated techniques for a nanoscale analysis, on an individual basis. During this thesis, a review article was written outlining the urgent need for nanoscale investigation of drug nanocarriers. More than 200 research articles were reviewed to describe the limits of *bulk* techniques and the existing spectromicroscopies that can be used for individual characterisation. In particular, this article points out the high potential of electron spectromicroscopy, which has been used in this work. Finally, it highlights the capabilities of the described spectromicroscopies for *in vitro* studies. This work has been published in the journal Particle & Particle Systems Characterization. It can be found at the end of Chapter 1 (page 7).

Article published in:
Chaupard, M.; de Frutos, M.; Gref, R. Deciphering the structure and chemical composition of drug nanocarriers: from bulk approaches to individual nanoparticle characterization. *Particle & Particle Systems Characterization*, **2021**, 38, 9, 2100022. doi: 10.1002/ppsc.202100022.

The contribution to this work was made as follows: Dr Marta de Frutos wrote the section *2.Electron microscopy approaches*, while I wrote the sections *3.Near-field approaches* and *4.Single particle analysis in suspensions*. We both wrote the section *5.Other approaches*. Dr Ruxandra Gref was in charge of the conclusion and we all contributed to the introduction.

1.3 . Electron spectromicroscopy for organic (- inorganic) nanostructures

Invented in the 1930s, electron microscopy (EM) allows the direct observation and analysis of nanostructures down to the atomic scale.[66] It is therefore a technique of choice for characterising complex nanomaterials such as MOFs. Its powerful capabilities were recognised in 1986 by the Nobel Prize in Physics. Over the years, different types of electron microscopy have been developed. For example, Transmission Electron Microscopy (TEM) and Scanning Transmission Electron Microscopy (STEM) are based on the transmission of a parallel and focused beam, respectively. In both techniques, electrons pass through the specimen and interact with it, providing an image of its structure. Hence, the morphology and crystalinity of the nanomaterial can be analysed locally. STEM is also capable of high-resolution quantitative chemical analysis and can therefore be used to study the chemical composition of nanostructures. By combining imaging and spectroscopy, this technique is described as an atomic spectromicroscopy. It is now an essential tool in Materials Science and is widely employed to study the physico-chemical properties of numerous nanomaterials.

Since the introduction of EM, there has been a growing interest in the study of living matter. By overcoming the diffraction limit, this technique has made it possible to analyse biological structures at the molecular level. However, because of the high-energy electron beam, organic and biological materials are easily damaged during analysis. Interactions between electrons and matter can lead to thermal degradation, displacement of atoms or radiolysis of chemical bonds. This results in a loss of information due to structural collapse or changes in the composition of the material. As the structure-function of various biological systems remains to be elucidated, many efforts have been made to develop methodologies suitable for non-destructive analysis. Reducing electron doses and using cryogenic temperatures have been shown to be effective strategies for limiting the radiation damage.[67–69] On the one hand, reducing the electron dose reduces the probability of destructive interactions. On the other hand, cooling the sample to the temperature of liquid nitrogen or helium slows down the diffusion of free radicals generated by radiolysis and their cascade reactions. Taking advantage of these two features, cryogenic TEM (cryo-TEM) has been widely used to study organic and biological materials.[70–74] By introducing new methods of specimen preparation (vitrification), it has also opened the way to the study of materials in the hydrated state (in a film of vitreous ice).[74] This revolution has enabled to study, at high resolution, the structural properties of materials close to their native state. It was notably awarded by the Nobel Prize in Chemistry in 2017.

Conversely, STEM has not attracted as much interest in biology and has tended to be used to study inorganic materials at atomic or even sub-atomic resolution. But today, STEM microscopes are increasingly being developed to study radiation-sensitive nanomaterials, whether biological, organic or organic-inorganic. Thanks to the recent introduction of direct electron detectors (DED), acquisitions are more sensitive to small signals acquired at low electron doses, and therefore more effective for damage-free studies.[75] For example, DED has enabled phase-contrast STEM and STEM ptychography to image the structure of undamaged MOFs [76] and biological specimens in three dimensions.[77, 78]

As complex nanostructures cannot be fully resolved by imaging alone, chemical analysis is required. As mentioned above, STEM enables spectromicroscopic approaches to simultaneously image and chemically analyse the specimen. This can be achieved using two techniques, Energy Dispersive X-ray Spectroscopy (EDS) and Electron Energy Loss Spectroscopy (EELS). These are used to assess the elemental and chemical composition. EDS collects the characteristic X-rays emitted by the sample, while EELS measures the energy lost by the incident beam after interaction with the material. EDS and EELS have already been used to map the elemental composition of organic and organic-inorganic materials and to localise sub-cellular compartments (see review article at the end of Chapter 1 and [79]). Furthermore, the power of EELS lies in its ability to distinguish between different organic components by characterising their chemical structures. With the recent development of monochromated electron sources,[80] EELS is now able to probe the chemical composition of nanomaterials in three energy ranges with high spectral resolution (> 5 meV): the infrared (IR, < 2 eV), the ultraviolet-visible (UV-vis, 2 - 50 eV) and the soft X-ray (XR, 50 eV - 5 keV) regions. In the UV-vis, the signatures have a relatively high cross-section, which produces an intense signal. Thus, this range is more favourable for damage-free analysis as the signals remain detectable even at low electron doses. Previous studies have revealed the UV signature of undamaged molecules, polymers and biological components.[81–86] Others have also mapped the distribution of copolymers with a spatial resolution of > 8 nm.[87,88] With a better spectral resolution (0.9 eV), Ricarte *et al.*[89] have also demonstrated the possibility of quantitative drug analysis. However, the UV-vis energy range does not provide direct information on chemical bonding and would require theoretical calculations to be understood. More recently, other works have exploited the highly delocalised character of vibrational excitations (> 100 nm) in an aloof geometry to collect a signal without penetrating into the specimen, thereby reducing its damage. Such a mode has notably been used to collect the IR spectra characteristic of the chemical structure of MOFs and organic molecules.[90–94] Unfortunately, because they are based on long-range interactions, these results showed poor spatial resolution. Over the last few years, there has been more interest in the soft XR region, which is based on localised interactions. Previous studies have characterised MOFs and polymers with a spatial resolution < 25 nm.[95–98] Nowadays, higher spatial resolution could be achieved by using DED and advanced denoising processing algorithms for more efficient sensitivity to small signals collected at low electron doses. This could be used to study the composition of various radiation-sensitive specimens. However, it should be noted that achieving angström resolution remains difficult, as spatial resolution is mainly determined by the specimen thickness, crystallinity and radiation sensitivity.

1.4 . Setting up tools for the study of radiation-sensitive materials

As mentioned above, recent developments (low-dose, cryogenic temperature, DED, monochromator) have opened up new possibilities for nanoscale chemical analysis by analytical STEM of radiation-sensitive nanomaterials, whether organic-inorganic, organic or biological. However, the experiments still require appropriate methodologies to elucidate the complex undamaged structures with high spatial resolution. Firstly, the damage-free experimental conditions need to be defined. Secondly, the damage caused by the radiation and the species produced must be understood in order to characterise specific spectral signatures. Thirdly, the spatial resolution and the experimental conditions must be optimised according to the sensitivity of the specimen, but also according to the goal of the study.

This thesis has provided a unique opportunity to address these issues, as all of the above developments have recently been brought together in a single instrument at the Laboratoire de Physique des Solides, Orsay, France. In particular, this work has been carried out mainly on a monochromated STEM-EELS microscope equipped with a cryoholder and a DED for collecting low-dose signals. The conception of robust working methodologies was achieved in the context of studying organic-inorganic drug nanocarriers. In particular, individual MOFs, their biodegradation and interactions with drugs have been studied. Thanks to the methodologies developed in this work, it was possible to extend the study to the analysis of biomolecules. The manuscipt is divided into seven chapters as follows:

Chapter 2 provides a detailed description of the experimental methods used in this thesis work. The first part presents the different nanomaterials used and their preparation as specimens. The second part focuses on electron microscopy, with an overview of the different techniques and their operation, a discussion of the beam damage effects and additional details on the data acquisition and processing procedures.

Chapter 3 focuses on the analysis of the MOFs alone by STEM-EELS spectromicroscopy. This chapter lays the foundation for the thesis work by developing an innovative acquisition strategy to analyse the chemical structure of organic and organic-inorganic nanosystems without beam damage. The multimodality of EELS was used to ensure a robust methodology that is of general interest for the study of other radiation-sensitive specimens. The behaviour of MOFs under the electron beam was also characterised. This beam-effect study is shown to be useful for relating damaged chemical fingerprints obtained at high electron doses to the original chemical structure of the specimen.

Chapter 4 presents the study of the biodegradation of MOFs in a medium mimicking the physiological environment. To elucidate such complex mechanisms, it uses a correlative strategy that combines information obtained from four different electron microscopy techniques, namely TEM, integrated Differential Phase Contrast (iDPC)-STEM, STEM-EDS and STEM-EELS. It is also shown that a complete understanding of complex structures and mechanisms requires the use of both low and high electron doses, despite the radiation-sensitivity of the specimens. This points out that the experimental conditions should be optimised according to the goal of the study, and not only the specimen preservation.

Chapter 5 introduces the study of the MOFs drug loading by electron spectromicroscopy and explores the capabilities of the technique for the chemical analysis of organic molecules and biological specimens. While the study of low concentration radiation-sensitive nanomaterials is revealed limited, major interests for biological matter are outlined. Then, by comparing the beam-effect study obtained on five different (bio)molecules, it demonstrates common radiolysis mechanisms for organic matter.

Deciphering the Structure and Chemical Composition of Drug Nanocarriers: From Bulk Approaches to Individual Nanoparticle Characterization

Maeva Chaupard, Marta de Frutos, Ruxandra Gref

To cite this version:

Maeva Chaupard, Marta de Frutos, Ruxandra Gref. Deciphering the Structure and Chemical Composition of Drug Nanocarriers: From Bulk Approaches to Individual Nanoparticle Characterization. Particle & Particle Systems Characterization, 2021, 38 (9), pp.2100022. 10.1002/ppsc.202100022 . hal-03365457

Deciphering the Structure and Chemical Composition of Drug Nanocarriers: From Bulk Approaches to Individual Nanoparticle Characterization

Maeva Chaupard [1,2], *Marta de Frutos* [1*], *Ruxandra Gref* [2*]

[1] Laboratoire de Physique des Solides, CNRS, UMR 8502, Université Paris-Saclay, F-91405 Orsay, France
[2] Institut des Sciences Moléculaires d'Orsay, CNRS, UMR 8214, Université Paris-Saclay, F-91405 Orsay, France

KEYWORDS: drug nanocarrier; single particle characterization; nanomedicine; spectromicroscopy; cell interaction.

ABSTRACT: Drug nanocarriers (NCs) with sizes usually below 200 nm are gaining increasing interest in the treatment of severe diseases such as cancer and infections. Characterization methods to investigate the morphology and physicochemical properties of multifunctional NCs are key in their optimization and in the study of their *in vitro* and *in vivo* fate. Whereas a variety of methods has been developed to characterize "bulk" NCs in suspension, the scope of this review is to describe the different approaches for the NC characterization on an individual basis, for which fewer techniques are available. We put the accent on methods devoid of labelling which could lead to artefacts. For each characterization method, the principles and approaches to analyze the data are presented in an accessible manner. Aspects related to sample preparation to avoid artefacts are indicated, and emphasis is put on examples of applications. NC characterization on an individual basis allows gaining invaluable information in terms of quality control, on: i) NC localization and fate in biological samples; ii) NC morphology and crystallinity; iii) distribution of the NC components (drugs, shells), and iv) quantification of NCs' chemical composition. The individual characterization approaches are expected to gain increasing interest in the near future.

SHORT BIOGRAPHIES OF THE AUTHORS

Dr. Ruxandra Gref is research director at CNRS, responsible of the “NanoBio” team in the Institute of Molecular Sciences, Paris-Saclay University, France. Her interdisciplinary research is focused on the design, synthesis, characterization and biological evaluation of “cage” nanomedicines with application in the treatment of cancer and resistant infections. She was among the pioneers to develop “stealth” nanoparticles to escape the recognition by the immune system, and hybrid metal-organic frameworks nanoparticles for drug delivery. Dr. Gref is interested in multifunctional “all in one” nanocarriers, where both incorporated drugs and their vehicle play synergic roles in fighting the disease.

Dr. Marta de Frutos is a researcher at CNRS, working in the Laboratoire de Physique des Solides, Paris-Saclay University, France. Her interdisciplinary research focuses on the development and use of analytical approaches based on scanning transmission electron microscopy (STEM) for the structural and chemical characterization at the sub-nanometer scale of biomaterials, nanomaterials, biological and medical systems. She has an extensive experience in Electron Energy-Loss Spectroscopy (EELS) on sensitive specimens. Her current interest includes the investigation of the physico-chemical properties of synthetic and natural hybrid organic-inorganic materials to elucidate their formation mechanisms.

Maeva Chaupard obtained a chemistry master’s degree from Sorbonne University (Pierre and Marie Curie) in 2020. She is currently a Ph.D. student working under the supervision of Dr. Marta De Frutos and Dr. Ruxandra Gref at Paris-Saclay University, France. Her main interests include the synthesis and characterization of drug-loaded nanoparticles with applications in the field of nanomedicine. She is focusing her research on the in-depth characterization of biocompatible hybrid metal-organic frameworks nanoparticles. In particular, she uses advanced STEM-EELS and AFM-IR spectromicroscopies to unravel the structural and chemical properties of the nanoparticles, as well as their intracellular fate.

1. INTRODUCTION

Progress in nanomedicine has led over the last five decades to the discovery of drug nanocarriers able to efficiently incorporate, protect towards degradation and ferry the active molecules from the administration site to their target (diseased organs, tissues and cells). Drug nanocarriers improved the payload's pharmacokinetics and contributed to achieve the desired pharmacological response at the target. They are now widely exploited for therapeutic purposes, including the treatment of severe diseases such as cancer and infections.[1] A plethora of natural and synthetic materials have been engineered at a nanoscopic level and explored for drug delivery (**Figure 1**). Liposomes, the first nanotechnology-based drug delivery system, were discovered early in the 1960s.[2] The first Food and Drug Administration (FDA)-approved nanotechnology was the liposomal Doxil formulation designed for the treatment of Kaposi’s sarcoma and since then, more than twenty liposomal and lipid-based formulations have been approved by regular authorities.[3] Many other types of drug nanocarriers have been developed, including polymeric, hybrid or metal nanoparticles (NPs), nanogels, dendrimers, quantum dots, carbon nanotubes (CNTs) and micelles (**Figure 1**). Several nanotechnologies containing an active molecule or a drug combination, such as Onpattro and Vyxeos, were FDA-approved in recent years, demonstrating the potential of nanomedicine and the growing interest in this field.[4][5] Moreover, the FDA-approved NP-based vaccines represent a giant step in the fight against the COVID-19 pandemic.[6]

Nowadays, a large variety of materials is used to prepare drug nanocarriers: ***i)*** organic compounds (lipids, synthetic or natural polymers, biomolecules); ***ii)*** inorganic materials (silica, carbon networks, metals, or metal oxides) and ***iii)*** hybrid organic-inorganic networks combining the properties of both their organic and inorganic counterparts. Generally, drug nanocarriers have a core-shell structure: ***i)*** the cores incorporate the drugs and release them in a controlled manner and ***ii)*** the shells govern the interactions with the living media (control protein adsorption, avoid recognition by the immune system, allow targeting diseased tissues and organs, confer bio-adhesion properties). Organic compounds remain the most employed materials for drug incorporation and for engineering multifunctional shells. Additionally, the presence of metals in drug nanocarriers’ composition offers new functionalities, such as antibacterial or antifungal properties,[7] radioenhancement[8] or imaging abilities for personalized therapies.[9] More recently, nanoscale hybrid metal-organic frameworks (MOFs) emerged as versatile materials for drug delivery and theragnostic in reason of their intrinsic properties as contrast agents for imaging.[10]

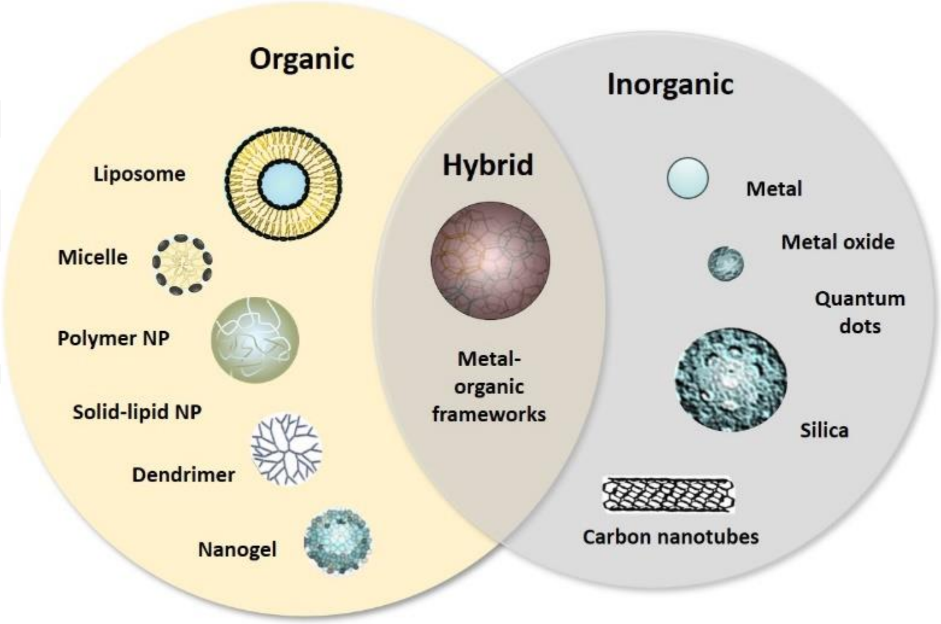

Figure 1. Schematic representation of the main drug nanocarriers classified according to their composition: organic, inorganic or hybrid organic-inorganic.

The architectures of the core-shell drug nanocarriers (NCs) are complex as they combine several functionalities among: drug co-incorporation, imaging properties for theragnostic, targeting abilities, stimuli-responsiveness, on demand drug release and triggered degradation.[11] The fast growing field of nanomedicine is in need for reliable, cutting-edge methods devoid of artefacts to investigate the morphology and physicochemical properties of the complex core-shell drug nanocarriers.

It is well recognized that the physicochemical properties of NCs play a major role in their interactions with the biological milieu. Several parameters (size, shape, surface charge and chemistry, roughness, porosity, elasticity, and many others) influence the NC' biological identity, their *in vivo* interaction with biological barriers and ultimately the therapeutic index of the drug cargo. Once administered *in vivo*, a protein corona forms rapidly at the surface of the NCs.[12] The NCs can get engulfed inside cells through different endocytic processes including phagocytosis, pinocytosis, and/or macropinocytosis.[13]–[15] The cell entry mechanisms and more globally, the NCs' distribution in tissues and organs are investigated in most of the cases by labelling the NCs with fluorescent molecules. However, it is well documented that the label molecules can sometimes profoundly alter the NC's physicochemical properties, or they can leak out or be transferred from the NCs to biological tissues, leading to artefacts.[16]–[18] It is therefore important to develop and use reliable methods to detect the NCs in their biological environment without the need of labelling.

In a nutshell, characterization methods are key in the design of core-shell drug NCs and in the study of their *in vitro* and *in vivo* fate. However, despite the huge progresses in the synthesis of novel materials and in the development of preparation methods for NCs, several aspects related to NC characterization are still not tackled. For instance, the homogeneity of the NC formulations should be assessed in terms of both size and composition. Whereas well-established methods are routinely used to determine the NC's size distribution and polydispersity, the techniques to assess the chemical composition of individual NCs are still in their infancy. However, it is important but very challenging to chemically map the locations of the incorporated drugs and of the targeting ligands. For example, drug location (in the NC' top layers or/and embedded in the cores) determines the drug release mechanism (diffusion/desorption/degradation related). Other crucial parameters govern the NC fate in biological media, such as the homogeneity of the coatings and the successful grafting of targeting ligands onto each NC's surface. Mapping the chemical composition and the structure (morphology, crystallinity) of individual NCs is a hard task given their small size (generally less than 200 nm) and complex core-shell composition, but a crucial one to ensure the successful transfer of scientific knowledge in nanomedicine to industrial real-world applications.

In terms of quality control, an in-depth characterization of *individual* NCs is key in optimizing their formulation and uses. The aim of this review is to give a comprehensive overview of the methods available to investigate NCs structures and compositions, with special emphasis on those allowing to characterize individual NCs and to detect them in biological media without labelling. Therefore, the methods to study the NC fate *in vitro* and *in vivo* using fluorescent dyes such as confocal or super-resolution microscopies are not reviewed here.

The current techniques that enable the measurement of the most fundamental NC properties such as size distribution, shape and surface properties (charge and chemical composition) are presented in the first part of **Table 1**, highlighting their advantages and main limits. These techniques are qualified as "bulk" as they give average information on a large population of NCs. Important properties are obtained such as size distribution, polydispersity, chemical composition, surface charge, crystallinity and porosity. In the second part of Table 1 are presented the methods adapted for individual NC characterization. The review focusses on these last methods, with special emphasis on examples of applications, principles of the methods, different approaches to analyze the data for a same technique, as well as aspects related to sample preparation to avoid artefacts.

Table 1. Main “Bulk” and individual methods used for NC characterization.

Method	Principle/advantages	Information	Limits/inconveniences
“Bulk” methods			
Dynamic Light Scattering (DLS)	Measurement *in situ* of the fluctuations of the scattered light by NC in Brownian motion	Rapid evaluation of size distribution	Highly biased towards larger particles in suspension; cannot distinguish particle types and provides no information on shape; measurements can be concentration-dependent; no chemical information
Zeta potential	Measurement *in situ* of the potential difference between the dispersion medium and the stationary layer of fluid attached to the NC	Rapid, typically combined with DLS	Requires low NC concentrations and low ionic strength
High Performance Liquid Chromatography (HPLC)	Chromatographic separation of drug(s) and their possible metabolites	Gives reliable information of NC composition (drug loading and release) and drug integrity	Trained users; needs to set up analysis methods
Spectroscopies: Fourier Transform Infrared spectroscopy (FTIR); Ultraviolet-visible Spectrophotometry (UV-vis); Mössbauer; Solid and liquid Nuclear Magnetic Resonance (NMR)	Relatively user-friendly methods routinely used to characterize NCs and drug release	Give information on NC chemical composition and interactions drug-matrix; oxidation state, symmetry, surface spins, magnetic ordering and anisotropy	In some cases, need the use of large samples and/or sample dehydration
Thermogravimetric Analysis (TGA)	Provides information about mass loss during heating	Composition (drug loading, amount of coating material)	Reduced sensitivity in the case of low drug loadings; not reliable for complex NC
Elemental analysis; Inductively Coupled Plasma-Mass Spectroscopy (ICP-MS)	Gives information of chemical composition of the NCs	Composition (drug loading, amount of coating material)	Difficult to interpret for complex NC
Porosimetry	A dried sample is allowed to adsorb an inert gas (typically nitrogen) at liquid nitrogen temperature.	The (Brunauer, Emmett and Teller) BET theory is generally applied to interpret the adsorption data into information on the surface area and porosity	Needs extensive sample dehydration, delicate for fragile samples
Ellipsometry	Measures the change of polarization upon reflection or transmission	In the case of NPs deposited on a surface, measures film thickness, color and refractive index	Complex sample preparation, needs adhesion of NPs onto a substrate
Analytical centrifugation	Separates population with similar sizes based on their sedimentation properties	High-sensitivity; compatible with multimodal population; distinguish between different populations	High-cost equipment; highly trained users
Field flow fractionation (FFF)	Separates populations of NCs which are eluted in a narrow channel on which a field (thermal, electric, magnetic, hydraulic, gravitational) is perpendicularly applied	Highly tunable (different accumulation forces can be used); provides monodisperse sample fractions	Sample recovery and choice of experimental parameters can be challenging; highly trained users; needs diluted NC suspensions
X-Ray Diffraction (XRD) and Small Angle X-rays Scattering (SAXS)	Give information on NC and drug crystallinities	Crystal structure, composition, crystalline grain size	Poor information if the sample is not well crystallized; need in some cases large amounts of samples; in most cases, need dried sample
X-ray Photoelectron Spectroscopy (XPS); Secondary Ion Mass Spectroscopy (SIMS), Matrix Assisted Laser Desorption	Identify the elements in the NCs (elemental composition) as well as their chemical state	Give information on the composition of the top layers of the NCs	Need sample dehydration; highly trained users

Ionisation (MALDI)			
“Individual” methods for NC characterization			
Scanning Tunnelling Microscopy/Spectroscopy (STM/STS)	Probes the tunnelling current with a conductive tip scanning the sample surface	Topography (size, shape), local electronic states.	Conductive surface requires: (semi-) conductive samples or conductive substrate for thin samples; only surface analysis
Atomic Force Microscopy (AFM)	Measures the tip-sample interaction forces while scanning the surface	Topography (size, shape), mapping of the nanomechanical properties. With a specific functionalization or coating, the tip can probe other interactions (electrostatic, magnetic, thermal). Imaging can be used in combination with spectroscopic methods	The contact mode can induce sample damaging through shear forces. The tapping mode is used as an alternative; only surface analysis except when combined with certain spectroscopic methods
Scattering type Scanning Near-field Optical Microscopy (s-SNOM)	The tip scans the sample surface and detects its optical-near-field response upon light illumination	Topography and optical properties of the sample: scattering (Tip-enhanced Raman Spectroscopy) and absorption (Nano-FTIR Spectroscopy)	Requires sample drying to prevent from water absorption, not well appropriated for poorly scattering samples, reproducibility depending on the scanning mode and the tip nature and geometry.
Photothermal-induced Resonances (PTIR or AFM-IR)	The AFM cantilever measures the fast-thermal expansion of the sample induced by pulse laser light absorption	Topography and IR absorption of the sample	Requires sample drying to prevent from water absorption
Scanning Electron Microscopy (SEM) and 3D-Scanning Electron Microscopy (3D-SEM)	Classically, images formed by detection of the back-scattered or secondary electrons generated by scanning specimen surface with a focused electron beam	Analysis of the morphology of the specimen surface. 3D analysis of large volumes with a dedicated equipment (ultramicrotome or FIB slicing). Elemental composition when combined with EDX	Limited spatial resolution and only surface analysis on classical SEM
TEM, STEM, High-resolution (HR)	Images formed by the detection of the electrons transmitted through the specimen	Size, size distribution, morphology and structure (down to atomic scale for HR), detection and localization of NPs in cells, study of the formation mechanisms. Imaging can be combined to spectroscopic measurements	High-cost equipment; highly trained users; requires thin and dried samples which might induce other artefacts during preparation protocols; beam damage on sensitive specimens
Cryo-transmission electron microscopy (Cryo-TEM)	Same principle than TEM but observation of vitrified specimens at low doses	Analysis of sensitive particles in their native (hydrated) environment. Study of growth mechanisms, dispersion and aggregation	No information on chemical composition; preparation protocols might induce artefacts
Electron Energy Loss Spectroscopy (EELS) and Energy Dispersive X-ray spectroscopy (EDX)	Spectral analysis of the signals resulting from the interaction of the electronic beam in TEM or STEM with the specimen (X-rays for EDX and inelastically scattered electrons for EELS)	Identification of the atoms composing the specimen (qualitatively and quantitatively) and their chemical state (EELS only)	Requires relatively high electron doses that makes them not compatible with very sensitive specimens
Electron tomography (ET) and single particle analysis (SPA)	Acquisition of series of tilted 2D images in TEM or STEM for ET or of collections of individual images from particles with random orientations for SPA	3D visualisation of inorganic, hybrid and organic particles. Compatible with cryo-conditions and HR	Same limitations as 2D approaches in terms of specimen preparation and damage magnified by the higher electron doses required to record an image series
Nanoparticle tracking analysis (NTA)	Analyses the Brownian motion of NPs by tracking the scattered light	Concentration and size distribution. NTA is suitable for highly polydisperse samples and can detect fluorescent particles	Requires sample dilution and highly scattering objects; detects only NPs larger than 30 nm and which do not sediment; provides no chemical nor structural information

Single Particle Extinction and Scattering (SPES)	Measures the polarizability and optical thickness of nanoparticles passing through a flow cell	Refractive index, size and size distribution. SPES can detect single NPs suspended in a complex media.	High-cost equipment; highly trained users
Tunable Resistive Pulse Sensing (TRPS)	A set of voltage and pressure drives NPs suspended in an electrolyte through a nanopore in an elastomeric membrane	Individual particle size and charge, particle concentration	Requires sample dilution and highly conductive solutions; not appropriate for highly polydispersed samples; measures particles of > 40 nm; possible nanopore blockage; requires careful calibration
Nano-Secondary Ion Mass Spectrometry (nanoSIMS)	Analyses the secondary ions generated by the sputtering of the sample surface by a focused primary ion beam	Analysis of elemental compositions. Detection of trace elements down to parts-per-billion	Usually information on the top layers; adapted mostly for metal NPs, need isotopic labelling for organic materials
X-ray spectromicroscopy	Chemical images obtained by collecting i) the transmitted X-rays and/or ii) the emitted characteristic fluorescent X-ray or electrons	Morphology and chemical composition of NCs. Mostly employed to determine the distribution and chemical changes of NCs inside cells	Highly trained users, limited number of synchrotron sources, requires thin samples (few microns) to image in the soft X-rays regime, beam damage of radiation sensitive materials, weak spatial resolution from tens to hundreds of nanometers

2. ELECTRON MICROSCOPY APPROACHES

Microscopies are the pillars of the characterization tools to observe drug NCs and to investigate their interaction with biological systems. Among them, electron microscopy (EM) is the most employed method. A large panel of imaging and analytical modes is accessible based on the detection of the different signals generated by the interaction of the primary electron beam with the analyzed specimen. Images can be collected simultaneously to spectroscopic data in a multimodal manner providing both structural and chemical analysis. Analytical EM is a method of choice for the investigation of drug NCs, whatever their composition, giving access to valuable information on their morphology, structure and chemical composition. However, certain EM approaches are more suitable for the analysis of organic nanomaterials while others better meet the needs of inorganic ones.

The NC visualization in biological environment imposes constraints in terms of specimen preparation and imaging conditions. Thus, the main limitation of EM comes from its restriction to fixed cells and its impossibility to analyze live cells and follow processes in real time. Correlative light and electron microscopy approaches have proven to be a good way to circumvent this drawback by combining EM ultrastructural information with dynamic fluorescence microscopy analysis. Numerous studies on NCs are found in the literature coupling cryo-transmission electron microscopy with confocal microscopy (for instance [19]–[24]). It is also important to keep in mind that EM images provide information only on a small fraction of the sample. Consequently, a single EM image is not representative of the sample and care should be taken to acquire a collection of images large enough to get a good description of the whole specimen.

The aim of this review is not to give an exhaustive overview of the numerous publications concerning NC studies based on EM but rather to illustrate the possibilities offered by these approaches in the investigations of these systems. Extensive EM data can be found in reviews concerning the characterization of inorganic or organic NCs [25]–[28], and their interaction with cells.[29][30] However, to the best of our knowledge, no publication resumes all EM approaches for NCs, including 2D and 3D imaging, analytical modes and cryo-EM.

2.1. Electron microscopy approaches for individual NC analysis

2.1.1. 2D imaging by SEM, TEM and STEM

Schematic representations of a scanning electron microscope (SEM), a transmission electron microscope (TEM) and a scanning transmission electron microscope (STEM) are given in (**Figure 2**). In SEM (**Figure 2A**), a focused electron beam is used to scan the specimen and the image is obtained point by point. These microscopes are usually operated at rather low voltages (typically from 500 V to 30 kV) and most commonly, the secondary electrons generated by the primary beam and emitted close to the specimen surface are collected to obtain an image related to the surface topography. Another imaging possibility relies on back-scattered electrons that are mainly sensitive to the atomic number variations providing an image contrast related to the chemical composition. Other signals can also be measured including the emission of visible photons (cathodoluminescence), of X-rays (energy dispersive X-ray spectroscopy), the specimen conduction... SEM advantages are mainly the simplicity of the specimen preparation and the quick characterization of the size distribution and shape of a large variety of nanoparticles (NPs). As an example, the facetted structures of oligonucleotide-functionalized UiO (standing for Universitetet i Oslo)-66 MOF NPs was revealed (**Figure 3A)**.[31] The mean diameter of mesoporous silica NPs (MSNs) was found equal to 200–300 nm in agreement with the hydrodynamic diameter of 293 nm estimated by DLS[32] and uniform and interconnected pore channels (of 15 nm in average diameter) were observed at their surfaces (**Figure 3B)**. The hollow flower-like morphology of silver nanostructures was observed by SEM in Eid and Azzazy[33] **(Figure 3C**). Some other examples can be found in Klang *et al*. and Ž. Knežević *et al.*[26][34].

In SEM, the internal structure of the specimen is not accessible because the detected signal comes from the interaction of the probe with a small volume close to the surface. In contrast, in transmission microscopes, the beam goes through the sample providing information on its inner structure. This constitutes an essential advantage because it is well known that the internal structure of NCs (for instance a hollow shell or a core-shell structure) may have a strong influence on their properties and their potential applications. Another SEM limitation comes from its relatively low spatial resolution. In most studies, SEM has been used for micro-sized particles larger than the ones under the scope of the present review. SEM spatial resolution can approach one nanometer for the most efficient microscopes equipped with a field emission gun (FEG) as the electron source but the atomic structure is never accessible by this approach. Higher resolution analysis is provided by transmission microscopes, both in their conventional (CTEM) and scanning (STEM) modes (**Figure 2B and C** respectively). These microscopes are among the most effective tools for the structural and chemical characterization of nanomaterials from the micro-scale down to the atomic level. Accelerating voltages of 80–300 kV are typically used to ensure the transmission of the electrons through the specimen and the high resolution imaging (resolution increases with electron energy).

In CTEM (or simply TEM), the complete area of interest is illuminated with a nearly parallel beam and the transmitted electrons are collected simultaneously on a CCD camera to form the image of the specimen (**Figure 2B**). Part of the electrons are transmitted without any modification of their energy and trajectory, while the rest are elastically or inelastically scattered. The image contrast results from different local parameters such as the thickness, the atomic arrangement and the elemental composition that determine the interaction with electrons, resulting in a modification of the amplitude (influence of atomic mass, thickness, diffraction) and/or the phase of the electron wave. Organic NCs without staining have an inherent low contrast because they contain mainly light atoms (C, N, O) and they behave as phase objects because the primary electrons are not absorbed. High-resolution TEM (HRTEM) relies on the phase-contrast imaging and allows the observation of the atomic arrays in the crystalline structures of thin specimens (~100 nm). TEM gives access to the NC size, morphology and structure (**Figure 3D, E and F**) giving relevant information to analyze the influence of the different parameters during their synthesis. For instance, He and coworkers reported a drastic change of the size, morphology and mesostructure of MSNs when changing the nature of the surfactant used for their synthesis.[35] In another study, the analysis of the spherical shape and porous structure of MSNs shows that they remained unchanged after the covalent grafting of a poly(acrylic acid) (PAA) shell and platinum coating (**Figure 3D**).[36] Silver NPs were analyzed by HRTEM revealing several morphologies associated with specific crystallographic structures (**Figure 3F**) that may have an influence on their properties.[37]

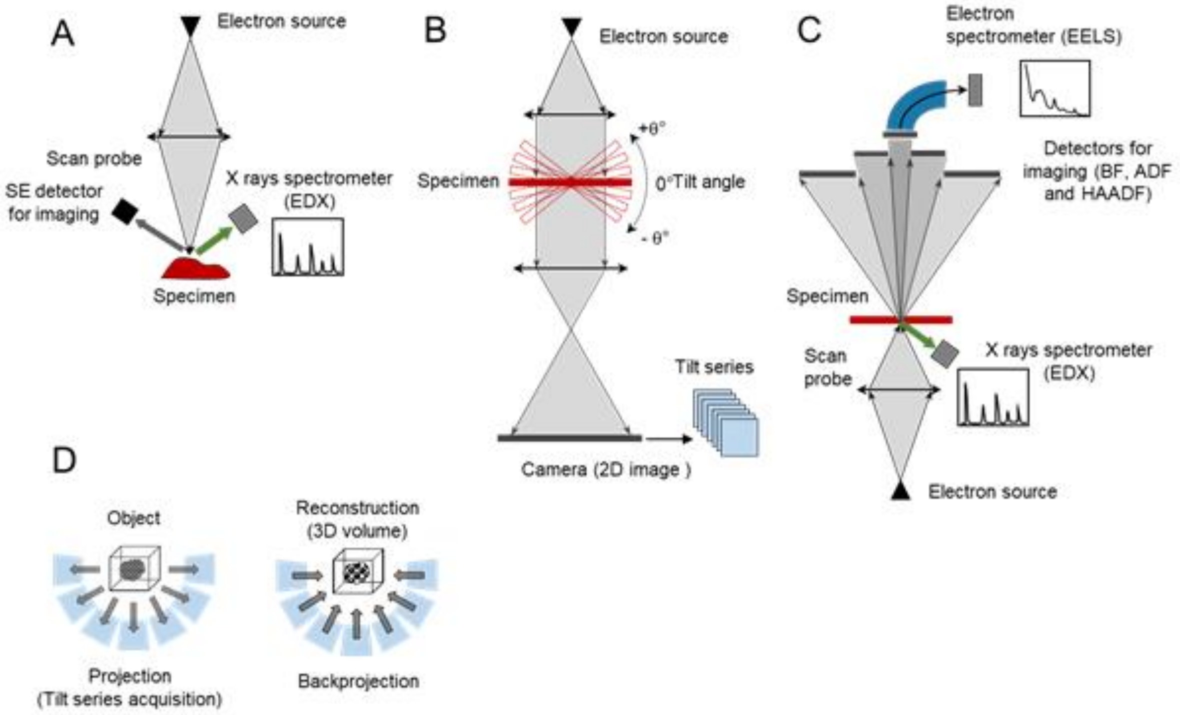

Figure 2. Schematic representations of: (A) a SEM setup including an EDX spectrometer; (B) a conventional TEM setup with the possibility to tilt the specimen for electron tomography measurements; (C) a STEM setup equipped with EELS and EDX; (D) the acquisition of a tilt series and the tomographic reconstruction.

In STEM (**Figure 2C**), the incident electrons also cross the sample but the beam is focused and scanned in a raster as in SEM. The STEM spatial resolution is determined by the beam size. On last generation STEM, the spatial resolution can reach values better than 1 Å.[42] Different images are formed by collecting the electrons scattered by the specimen at different angles. The bright-field (BF) detector is an on-axis solid disc collecting the direct beam whereas Dark-field (DF) detectors are ring shaped (annular) with given inner and outer collection angles. Electrons scattered incoherently at high angle by nucleus are detected by the high-angle annular dark-field (HAADF) detector that produces an image highly sensitive to the atomic number variations (Z-contrast images). The Z-contrast is useful to distinguish between materials with large differences in atomic number. A clear illustration of the sensitivity of HAADF-STEM imaging compared with TEM for heavy elements can be found for instance in Félix *et al.*, Morones *et al*. and Niu *et al*.[32][37][43] Light elements such as C or O are only weakly visible in the HAADF image, but are clearly seen in annular dark-field (ADF) images acquired with an annular detector with smaller collection angles. ADF is a good compromise to detect both light and heavy elements. As an example, silver NPs (bright signals) could be detected inside the cages of porous iron-based MIL-100(Fe) (MIL standing for Material of Institute Lavoisier) MOFs (**Figure 3H and I**).[40]

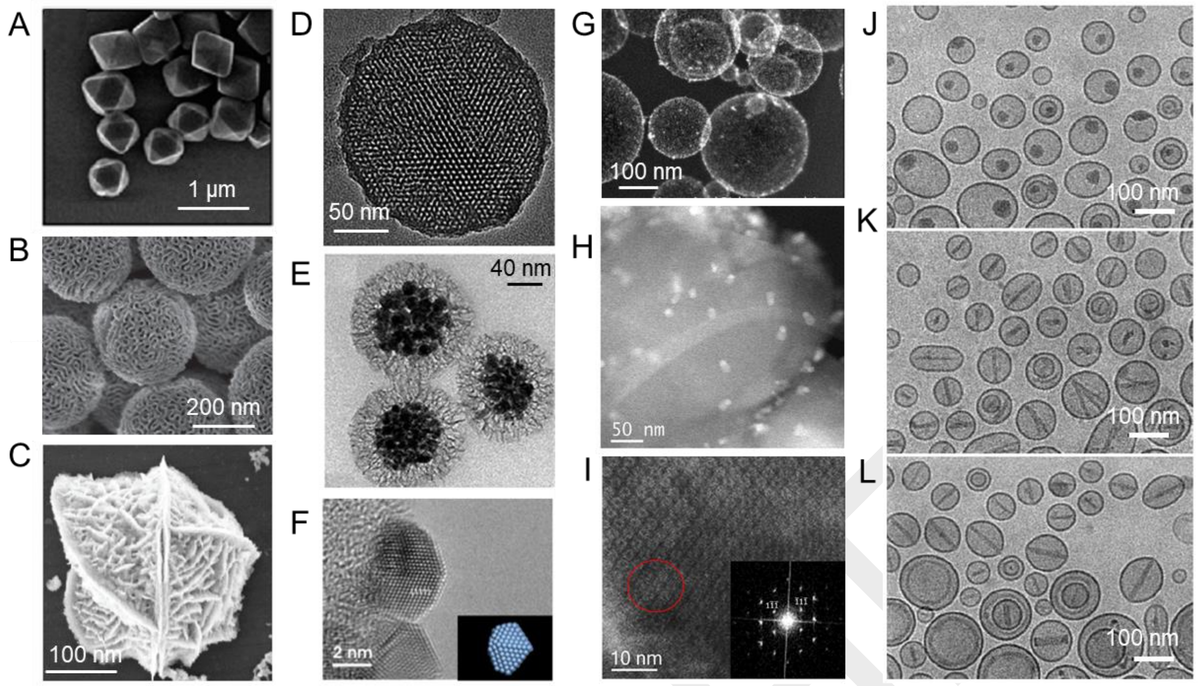

Figure 3. SEM, TEM, STEM imaging: (A) Oligonucleotide- Functionalized UiO-66 MOF NPs by SEM,[31] (B) Large-pore MSNs observed by SEM[32] and (C) hollow flower-like silver nanostructures by SEM.[33] (D) HRTEM of MSNs co-loaded with cisplatin and doxorubicin;[36] (E) mesoporous silica coated iron oxide photothermal nanoprobe;[38] (F) HRTEM of a silver NP and its respective crystallographic model given as insert;[37] (G) Cryo HAADF-STEM image of metal-shell nanocapsules;[39] (H) ADF-STEM showing silver NPs associated to MIL-100(Fe) MOFs and (I) HR ADF-STEM image of the MOF structure allowing the visualization of the porous system along with contrast variations related to the presence of Ag within the pores (indicated by red circle). The lattice periodicity is clearly visible as spots in the Fourier transform of the HR image (inset in I).[40] (J-L) Liposomes loaded with an iodinated amino-benzyl derivative of daunorubicin (J), the non-iodinated compound (K) and with doxorubicin (L).[41] (A) Adapted with permission.[31] Copyright 2017, American Chemical Society. (B) Adapted with permission.[32] Copyright 2014, Wiley-VCH. (C) Adapted with permission.[33] Copyright 2012, Dove Medical Press. (D) Adapted with permission.[36] Copyright 2016, Royal Society of Chemistry. (E) Adapted with permission.[38] Copyright 2017, Royal Society of Chemistry. (F) Adapted with permission.[37] Copyright 2005, Institute of Physics. (G) Adapted with permission.[39] Copyright 2020, Elsevier. (H-I) Adapted under the terms and conditions of the Creative Commons Attribution License.[40] Copyright 2019, Frontiers. (J-L) Reproduced with permission.[41] Copyright 2009, Springer Nature.

EM approaches impose several major constraints related to the specimen characteristics and the preparation has to be adapted consequently. A first limitation comes from the high vacuum needed in an electron microscope, requiring a complete drying of the specimen and, for NP suspensions, the complete removal of the suspension medium. Typically, NC suspensions are drop-casted and dried onto a TEM grid (a thin carbon film deposited on a copper grid). Another limitation comes from the specimen thickness which should be generally below 500 nm to allow the transmission of the electron beam through the specimen, so larger particles cannot be observed unless they are sectioned by focused ion beam (FIB) or ultramicrotomy. Large NCs can be directly imaged in SEM if they are electrically conductive, otherwise they have to be metallized prior observations by depositing a gold or a carbon film but metallization can hide surface fine features.

EM observations at room temperature are well adapted for inorganic particles and for hybrid ones resistant to beam damage and solvent removal (as metallic, silica,…) but not for very sensitive particles as the organic ones. In all cases, drying makes impossible the analysis of the NC in their suspension medium. Environmental SEM and TEM or the use of liquid cells can help bypassing theses inconveniences, but working under partial pressure or with a liquid imposes strong limitations in terms of equipment, resolution and accessible information.[26]

2.1.2. *Cryo- approaches*

Introduced in the 1980's, cryo-EM methods are a good alternative to image sensitive objects in conditions close to their native state[44][45] and constitutes a clear breakthrough for the 2D and 3D high resolution imaging of organic systems. The cryo-EM principle can be found in numerous reviews (see for instance [46]–[49]). Briefly, cryogenic preparations are obtained by freezing water at a very high cooling rate, leading to an amorphous (vitreous) state devoid of crystalline ice. As a result, the NPs can be immobilized in their native state, without alteration of their conformation and geometry.

Advantageously, the method requires only a droplet of the NP suspension which is deposited on a carbon-coated holey grid and the excess of liquid is quickly removed leaving a thin film on the grid. Then, the specimen is rapidly frozen leading to a vitreous thin film containing the NPs. However, the main drawback of this method is related to the film thickness that imposes a limit to the size of the NPs which can be observed. Indeed, particles larger than the film thickness are not incorporated or may be found near the grid bars where observations are not possible. Moreover, images are usually acquired in the holes of the grid and since the vitreous film is thinner in the hole center, smaller particles are found in these regions as compared with the edges. Cryogenic methods are also time-consuming and costly but they are essential for the characterization of specimens sensitive to drying or to electron beam damage as organic and certain hybrid NPs, and to study particle aggregation and dispersion.[23] They can be applied to all EM microscopes (**Figures 3G-L)** but they need dedicated equipment in order to avoid specimen devitrification: a cryo-holder and a sensitive detection (ideally a direct detection camera) to achieve imaging at very low electron doses.

Numerous examples illustrate the usefulness of cryo-TEM. For instance, the stability of phospholipid liposomes that is limited by hydrolysis has been studied as a function of storage time, temperature and pH by heating above the phospholipids phase transition.[50] The three-component lipid NPs synthesis could be optimized based on an accurate determination of their composition and phase behavior.[51] In addition, it could be revealed that the incorporated anticancer drugs (doxorubicin and a daunorubicin derivative) precipitated inside liposomes (**Figures 3J-L**).[41] Other examples of cryo-TEM studies are reviewed by Kuntsche *et al*.[27]

2.1.3. 3D imaging by single particle analysis and tomography

EM imaging provides two-dimensional (2D) images that are the projection of three-dimensional (3D) objects. Electron tomography (ET) and single particle analysis (SPA) are powerful techniques developed to achieve realistic 3D particle visualizations. 3D imaging by ET relies on the acquisition of a set of 2D images from the specimen by varying its orientation (tilting angles typically from -60° to +60°) relative to the incident electron beam (**Figure 2B**). The actual 3D images are obtained using mathematical algorithms to combine the information of the different projections from the tilt series (**Figure 2D**).[48][52] In SPA, the 3D reconstructions are built up from individual images of identical particles with random orientations by processing the data using iterative algorithms.[53]–[55]

ET and SPA can be applied to resin embedded or frozen-hydrated specimens. In cryo-conditions, due the radiation sensitivity, image series should be acquired with minimum electron doses in order to preserve high-resolution features.[53][56] A collection of reconstructions obtained by cryo-TEM imaging from NPs can be found in [57]. Some representative NC examples are given here: i) SPA investigation of RNA-NPs loaded with paclitaxel for targeted cancer therapy (**Figure 4A**);[58] Cryo-ET study of: ii) the 3D architecture of phytantriol cubosomes stabilized with Tween 80 (**Figure 4B**);[59] iii) liposomes containing doxorubicin[60] (**Figure 4C**) and iv) superparamagnetic iron oxide NPs (SPIONs) within liposome membranes (**Figure 4D**).[61] Similarly, the engulfment of silica NPs in liposomes was analyzed by Cryo-ET for unveiling the dynamics of the process.[62]

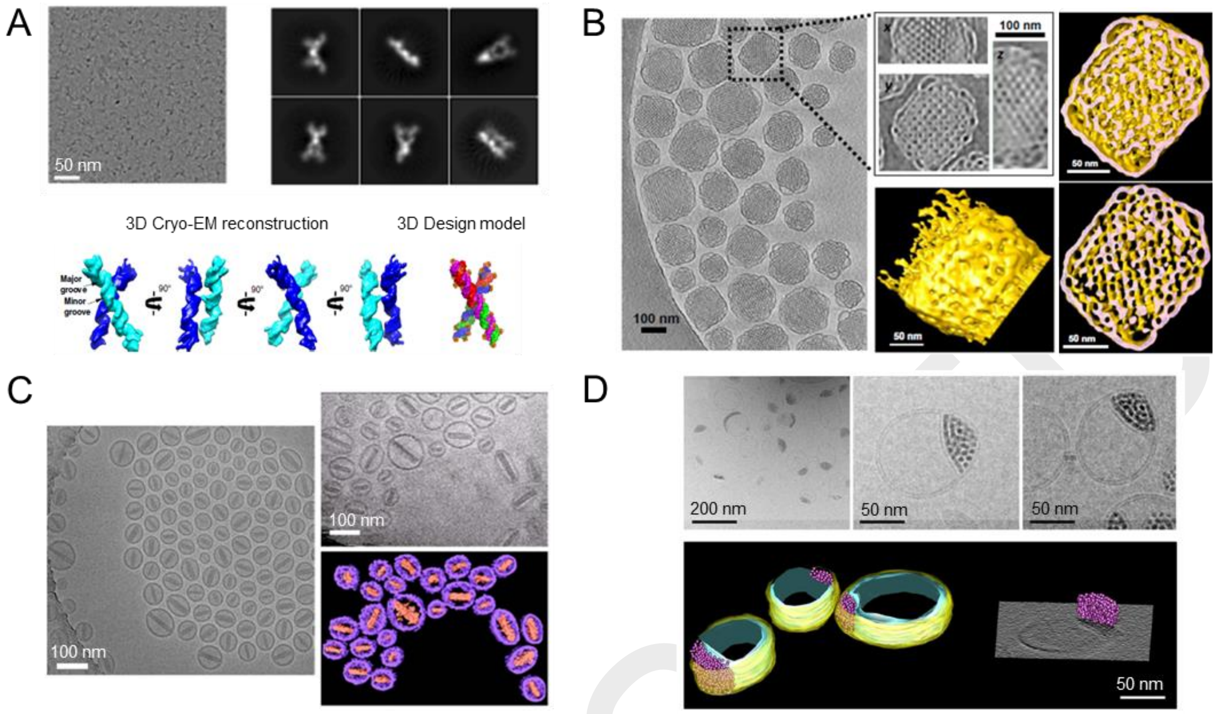

Figure 4. (A) 3D reconstructed maps from SPA of the structure of RNA four-way junction NPs loading 24 paclitaxel molecules. A typical cryo-EM micrograph from an area showing a large number of NPs and the 2D class averages are presented.[58] 3D reconstructions from cryo-ET imaging of (B) Phytantriol cubosomes stabilized with Tween 80. Cross sections of the reconstructed particle are shown at different positions showing the water channels;[59] (C) liposomes containing doxorubicin;[60] (D) Liposomes with inclusion of SPION clusters.[61] Typical cryo-TEM images and subsequent tomographic reconstructions are shown for each system. (A) Adapted under the terms and conditions of the Creative Commons Attribution 4.0 International License.[58] Copyright 2020, Springer Nature. (B) Adapted with permission.[59] Copyright 2016, Elsevier B.V. (C) Reproduced with permission.[60] Copyright 2008, Future Medicine Ltd. (D) Reproduced with permission.[61] Copyright 2014, American Chemical Society.

In life sciences, most of the 3D studies rely on BF-TEM imaging but in material sciences, HAADF-STEM images whose resolution can reach atomic scale are frequently preferred for tomographic reconstructions.[63] For amorphous or partially crystalline materials with small crystalline domains, TEM tomography provides reliable 3D structural information. But for highly crystalline materials, HAADF-STEM tomography is better suited due to its contrast proportional to the specimen thickness and density, with a negligible influence from the diffraction contrast. Moreover, due to its Z-contrast, HAADF-STEM tomography enables a very high sensitivity to detect small metallic particles in an organic environment.[64]

2.1.4. *Analytical EM approaches (EDX, EELS, EFTEM)*

Despite the chemical information provided by Z-contrast HAADF-STEM, EM imaging is often not sufficient to understand the morphology and the organization of heterogeneous particles made of several constituents of different chemical natures assembled together. Analytical EM approaches are ideal tools to investigate these complex systems. However, the corresponding signals may be orders of magnitude weaker than imaging signals involving scattered electrons. As a consequence, analytical methods require quite high electron doses that are not compatible with vitrified specimens imaged in cryo-conditions.

The most common EM analytical techniques used for chemical mapping are based on the detection of the X-rays emitted (energy-dispersive X-ray spectroscopy, EDXS or EDX or EDS) or on the analysis of the energy lost by the incident electrons when interacting with the sample (Electron Energy Loss Spectroscopy, EELS). When an electron ionizes an atom, a cascade of electronic transitions occurs and the hole left in the inner shell results in the emission of either a characteristic X-ray or an Auger electron. By collecting and analyzing the emitted X-rays, the elemental composition can be deduced for the current position of the electron beam on the specimen. EDX setups are compatible with SEM, TEM and STEM, allowing different spatial resolution and sensitivity of the resulting spectroscopic data. EDX can provide qualitative, semi-quantitative or quantitative information[64] on the elements present in the specimen. Concerning NCs, this approach is mainly applied to detect metallic compounds. For instance, EDX signal of platinum was analyzed to check the incorporation of Cisplatin in single-walled CNTs[65] and in poly(acrylic acid)-modified MSNs (**Figure 5A**).[36] In another study, the gold coating of iron oxide NPs (30 nm diameter) was monitored by EDX.[66]

In a STEM, the kinetic energy of the transmitted electrons can be analyzed by an EELS spectrometer (**Figure 2C**). The fraction of electrons transmitted without losing energy is found in the “zero loss peak” of the EEL spectrum (not visible in **Figure 5B**). The low energy range (few tens of eV) is associated to the valence electron excitations (“low loss excitations”) and the features found in the high energy range (from 100 to 1000 eV approximately) are related to the atomic ionization edges (“core loss edges”) (**Figure 5B**). These last features appear as small signals (compared to the zero-loss peak) superimposed on an intense decreasing background. EELS provide information on the elements composing the specimen but also on their chemical state by analyzing the edge fine structures. Quantitative information on the relative chemical concentrations can also be accessible from the EELS signal.[67]

The probe rastering makes SEM and STEM particularly well appropriated for spectromicroscopy approaches based on the acquisition of a spectrum at each beam position over the area of interest (the so called “spectrum-imaging mode”), providing information about the spatial distributions of the chemical composition (chemical maps) (**Figure 5C-E**). The spatial distributions of the elements composing silver and gold NPs were mapped by EDX in Ristig *et al*.[68] (**Figure 5C**). The synthesis of small magnetic iron NPs (size < 10nm) was monitored by EELS to characterize the distributions of iron and gadolinium (**Figure 5D**).[69] In Mahugo *et al*.[40], silver was loaded in MIL-100(Fe) nanoMOFs and a very peculiar contrast was observed for certain silver NPs together with a difference in their crystallization. EELS elemental maps reveal that this difference comes from the presence of residual chloride from MOF synthesis which associates with a fraction of silver NPs, while the rest is pure silver NPs **(Figure 5E).**

EELS maps can also be obtained in TEM by forming a filtered image with electrons of given energies (corresponding to the core-loss atomic edge) but energy filter TEM (EFTEM) is delicate and limited to some elements with edges clearly visible. For example, the distributions of three drugs (heparin, protamine and ferumoxytol) were detected in NCs based on their respective signals of sulfur, nitrogen, and iron (**Figure 5F**).[70] In Weiss *et al*.[71], gelatin coating was (hardly) detected on the surface of poly (lactic-co-glycolic acid) (PLGA) NPs by its weak nitrogen signal. EFTEM does not allow to analyze the chemical state of the sample. Alternatively, low-loss EFTEM has be used to image organic coatings on gold NPs at ambient temperature with sufficient contrast without the need for staining.[72]

Analytical EM approaches are well adapted for the elemental mapping but could be not very informative on the nature of the organic components and some studies combine EDX to Fourier Transform Infrared (FTIR) spectroscopy to compensate for this lack of information. In Li *et al*.[36], MSNs were covalently grafted with a PAA shell which was further cross-linked by a platinum(II) complex which reacted with the PAA carboxyl groups giving Pt@PAA-MSN. The successful NP coating with a PAA shell was confirmed by FTIR while the reaction with the Pt(II) complex was followed by FTIR and EDX.

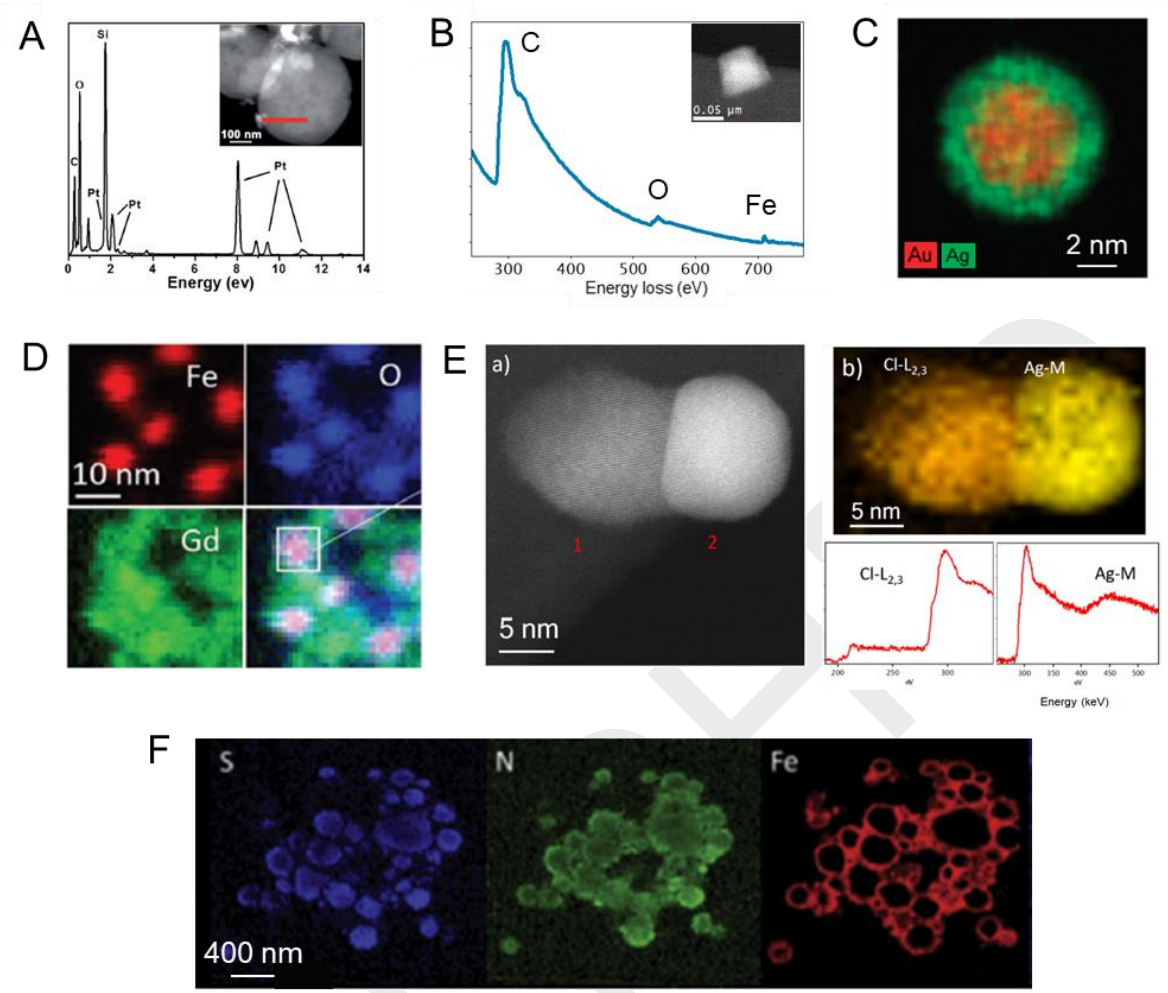

Figure 5. (A) EDX spectrum of cisplatin+doxorubicin dual-loaded MSNs with inset TEM image[36] and (B) EELS spectrum from a MIL-100(Fe) showing peaks for the ionization edges of C, O, and Fe (unpublished results). The strong peak corresponding to C can be due to the carbon film from the TEM grid and nothing can be said about the presence of carbon inside the NPs. The respective STEM image is given in inset ; (C) EDX maps from a bimetallic silver–gold NP coated with PVP for colloidal stabilization (Diameter ~6 nm);[68] (D) EELS elemental maps from FeGd-HN$_3$ NPs used as contrast agents for MRI. Iron (red), oxygen (blue), and gadolinium (green) maps were generated by integrating 10–20 eV windows above the respective core edges. The fourth image corresponds to the overlay of the three maps, showing all three colors.[24] (E) STEM-ADF image showing one silver particle incorporated in MIL-100(Fe) with two different regions and the associated EELS elemental maps. The different structures observed on certain silver NPs is associated with the presence of chloride (Cl in orange and Ag in yellow). The spectra are shown below for each edge;[40] (F) EFTEM maps of heparin, protamine and ferumoxytol distributions in nanocomplexes formed by mixing the three drugs. Heparin, protamine and ferumoxytol are revealed by the presence of S (blue), N (green) and Fe (red) respectively.[70] (A) Adapted with permission.[36] Copyright 2016, Royal Society of Chemistry. (C) Adapted under the terms and conditions of the Creative Commons Attribution-NonCommercial 3.0 Unported Licence.[68] Copyright 2015, Royal Society of Chemistry. (D) Adapted with permission.[24] Copyright 2018, Wiley-VCH. (E) Adapted under the terms and conditions of the Creative Commons Attribution License.[40] Copyright 2019, Frontiers. (F) Adapted with permission.[70] Copyright 2017, Elsevier.

2.1.5. Combining EM approaches for the monitoring of the NC design.

The great diversity of complementary EM approaches can be combined allowing a direct view of the NCs' sizes and shapes, crystallographic structures, chemical compositions and 3D structures. The study Wang *et al*.[31] illustrates well this complementarity. The authors investigated a strategy for functionalizing a series of different nanoMOFs with oligonucleotides (four metal nodes, Zr, Fe, Cr and Al, combined to four different organic linkers). The unsaturated metal sites on the MOF surface were chemically associated to terminal phosphate modified oligonucleotides. The nanoMOF sizes (~ 200 nm) were first determined by SEM (**Figure 3A**). Then TEM was used to verify that the particle shapes were preserved after DNA-nanoMOF functionalization. Finally, gold NPs (~ 20 nm) were functionalized with a DNA sequence complementary to those associated onto the nanoMOFs surfaces in order to synthetize hybrid nanoclusters termed core-satellite. The loading of metal NPs on the nanoMOF could be controlled by modifying the stoichiometry of the DNA-mediated hybridization reaction (**Figure 6A**). The approach could be extended to other satellite structures (gold nanostars, cubes, octahedra, and triangular prisms, silver and Fe_3O_4 spheres). TEM and HAADF-STEM imaging coupled with EDX mapping were crucial to determine the complex morphologies of the resulting core-satellite architectures (**Figure 6B and C**).

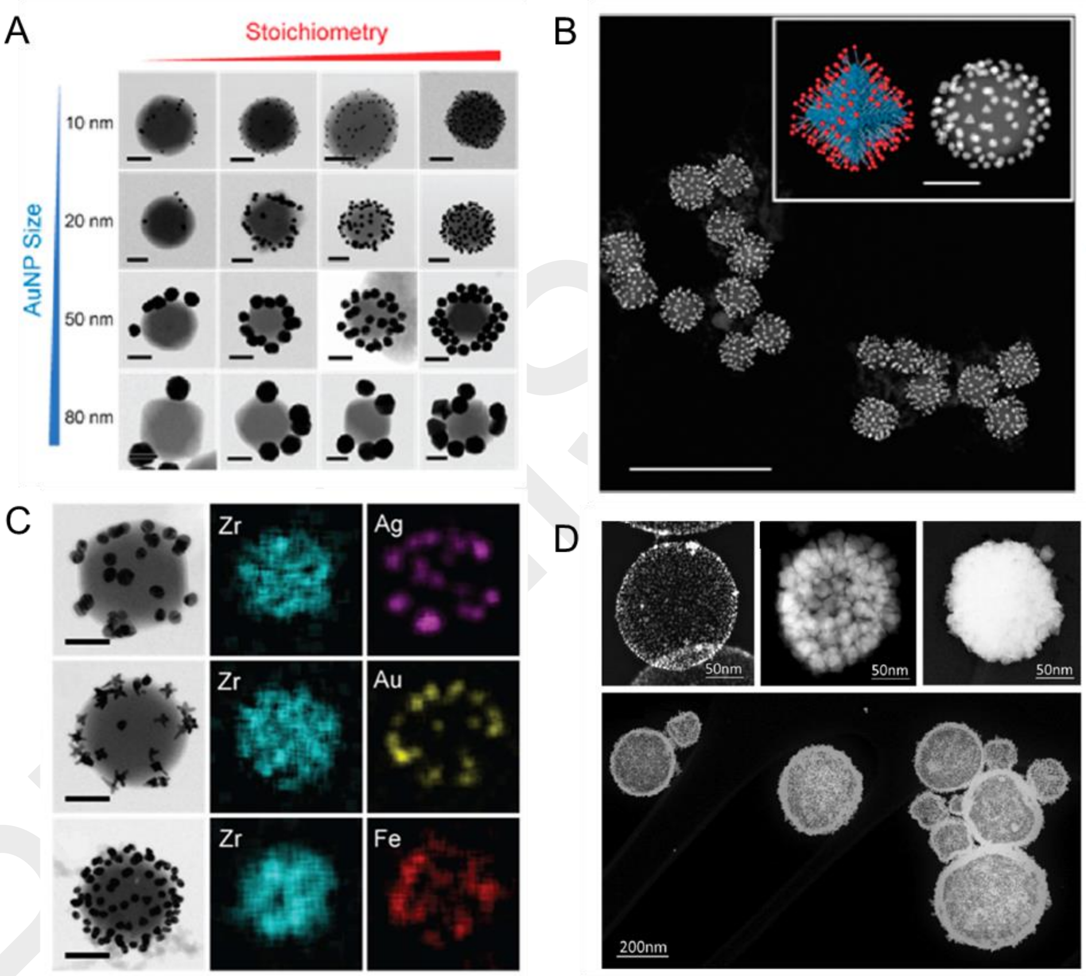

Figure 6. (A) TEM images of nanocluster assemblies demonstrating how the DNA ligands on MOF NPs and gold NPs provide control over the structural makeup of the assemblies (scale bars = 100 nm); (B) HAADF image of nanoclusters formed from complementary 225 nm DNA-UiO-66 MOF NPs and 20 nm DNA-Au NPs. Inset: schematic illustration of a MOF - gold NP cluster and a single nanocluster (scale bar = 1µm for main figure and 100 nm for inset); (C) EDX elemental mapping showing (from top to bottom): DNA-modified silver NPs assembled around a DNA-UiO-66 MOF NP; DNA-modified gold nanostars assembled around a DNA-UiO-66 MOF NP and DNA-modified iron oxide NPs assembled around a DNA-UiO-66 MOF NP (scale bars =100 nm). Images (A-C) from Wang *et al.*[31]. (D) Cryo HAADF-STEM images on a nanoPickering emulsion drop with a gold film with increasing thickness on its surface (top images). The bottom image shows a wider field of the sample.[39] (A-C) Reproduced with permission.[31] Copyright 2017, American Chemical Society. (D) Reproduced with permission.[39] Copyright 2020, Elsevier.

Another interesting example is provided by Hitchcock and coworkers who aimed to prepare NCs with oily cores containing paclitaxel and metallic shells to avoid drug leakage. First, the oily droplets were stabilized with Pt NPs (Pickering emulsion) and then a gold shell was synthesized onto them. TEM and HRTEM were employed to control the size and crystallinity of the Pt NPs and to optimize the gold coating. Cryo-TEM and cryo-HAADF-STEM provided crucial information at different stages of the synthesis and in particular, the very small Pt particles (~ 5 nm) could be visualized at the surface of the emulsion droplets (**Figure 6D**). In addition, SEM was used to image the metal-shell microcapsules at the end of the process.[39]

2.2. Exploring NC interactions with cells by EM approaches

The combination of imaging and spectroscopic approaches provides an ideal tool to investigate the mechanisms of cellular uptake and the action of individual NCs on cells. EM imaging is well established and widely used in biology to investigate the cellular ultrastructure (organelles and membrane structures) with an appropriate contrast and high resolution. However, studies on NCs can be hampered if they are modified or destabilized by the specimen preparation (dissolution or displacement of some constituents) or if NCs are not visible due to a lack of contrast compared to the cellular framework.

2.2.1. Cell preparation and 2D imaging by TEM and STEM

Three major limitations have to be circumvented to image NCs in cellular specimens: (i) whereas biological samples contain more than 2/3 of water, EM observations have to be done under vacuum; (ii) cells are much larger than the maximum thickness accessible by (S)TEM so they have to be sliced; (iii) visualize cell features often needs contrasting agents as the intrinsic contrast of the organic biological samples is low. Many well-established preparation protocols have been developed to meet these constraints for a variety of biological specimens[49] giving reproducible and reliable data with a nanometric resolution. However, when dealing with NC cellular uptake, the effect of each preparation step has to be carefully evaluated and adapted accordingly in order to preserve the NC integrity and their cellular localization.[29][30][73]

The different steps of standard protocols (non-cryogenic) correspond to: (i) the cell fixation in order to preserve the cellular ultrastructure; (ii) the embedding into a resin that forms a 3D polymeric network able to stiffen the soft biological sample, enabling to cut the specimen into ultrathin sections (typically 50–150 nm) and (iii) the highlight by staining of the low contrast features (cellular structures but also NCs in certain cases). Many NCs are resistant to these protocols and are quite easily detected in the cellular context by their high contrast compared to the biological framework. The only limitation for robust particles is that the sectioning thickness has to be adjusted to their sizes. Good examples are inorganic NCs and certain hybrid NCs because of their chemical stability and high electron density (atomic number) compared to organic compounds. Despite their high sensitivity to beam damage, MOFs present also a good contrast due to their content of metallic ions. For instance, metallic magnetic NPs were well observed in cancer cells by TEM, revealing that their localization was modulated by incubation conditions.[74] In another study, UiO nanoMOFs internalized by endocytosis in H460 cancer cells remained structurally intact inside endosomes **(Figure 7A)**.[20] Iron-based MIL-100(Fe) nanoMOFs co-incorporating two antibiotics were localized by TEM in *Staphylococcus aureus* infected macrophages.[75] Noticeably, some NCs colocalized with the intracellular pathogens and they degraded within a few hours **(Figure 7B)**. In Balfourier *et al*.[64], the long-term fate of gold NPs was analyzed in fibroblasts and, against generally admitted ideas, it was shown that they were bio-dissolved forming diffuse electron-dense areas visible in TEM and STEM **(Figure 7C)**.

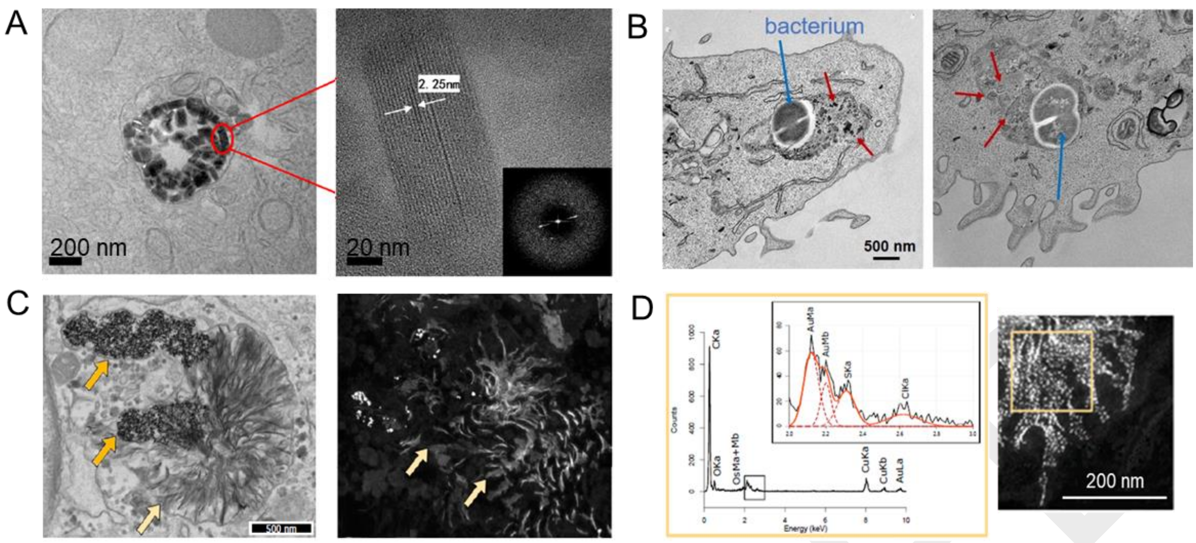

Figure 7. (A) TEM observations of UiO nanoMOFs in the endosomes of H460 cells. The zoomed-in view (right) of the nanoMOF marked by red circle (left) shows their structural integrity.[20] (B) TEM observations showing the internalization of drug loaded MIL-100(Fe) nanoMOFs in infected macrophages after 1h incubation (left) and after 6h (right). MOFs are indicated by red arrows and bacteria by blue ones;[75] (C) TEM (left) and STEM (right) images of human fibroblasts after 2-week exposure to 4 nm gold NPs.[64] They show the existence in lysosomes of dense and diffuse electron-dense areas resulting from the particle degradation; (D) After 2 week exposure, the composition of the diffuse area (marked by the yellow square on the right image) reveals a specific signal of sulphur associated to gold in the degraded particles (Inset). (A) Adapted with permission.[20] Copyright 2014, American Chemical Society. (B) Adapted with permission.[75] Copyright 2019, Wiley-VCH. (C-D) Adapted with permission.[64] Copyright 2020, National Academy of Sciences.

The main challenges arise for the intracellular observation of certain organic and hybrid NCs that may be destabilized by specimen preparation or whose identification in the cellular context is not straightforward due to their weak inherent contrast.[29][30] The contrast of biological specimens is usually enhanced by staining with heavy ions (uranyl acetate and lead citrate). Depending on their functional groups, some polymeric NPs are stained efficiently while some others are unaffected. A strategy to enhance NC contrast consists of incorporating metal particles in the NCs but this can profoundly affect the physicochemical properties of the NCs and their interaction with cells. Other artefacts might arise from the embedding process (dehydration, chemical reactions, temperature increase for resin polymerization, pH changes). Cryogenic approaches such as high-pressure freezing constitute a good alternative by replacing the chemical fixation by a physical fixation associated with a temperature decrease.[49][76] To date, only a few studies dealt with NC observations in the cellular context in cryo-conditions.[21] Alternatively, in the Tokuyasu method, specimen is treated with a sucrose-solution used as cryo-protectant, sectioned in cryo-conditions and observed at room temperature. This method has been used to study the uptake in human mesenchymal stem cells and the intracellular degradation of NCs made of poly(L-lactic acid) particles (~120 nm) decorated with 25nm-magnetite NPs.[77] NCs were clearly identified by the dark contrast of the magnetite NPs surrounding bright round-shaped areas. An interpretation of these bright areas was given in a study concerning PLGA rifampicin NPs in macrophages.[19] By comparing conventional epoxy resin embedding to Tokuyasu protocol, it was shown that the solvents used for dehydration completely dissolved the PLGA NCs producing holes in the sections resulting in bright areas at NC initial positions.

2.2.2. *Analytical EM approaches (EDX, EELS, EFTEM)*

Analytical EM approaches (EDX and EELS) represent a good way to avoid ambiguities related to particle identification in the cellular context, provided that at least one element composing the NCs is not present in the cell. For instance, TEM coupled to EDX analysis was used to identify ultrafine SPIONs in MCL5 cancer cells[78] and SiO_2 NPs in human B lymphoblastoid cells (TK6) in different environments containing serum.[23] It was also helpful to localize silver NPs on gram-negative bacteria where a sulphur signal was found associated with silver.[37] Analytical EM also offers the possibility to follow the NP degradation in cells. An interesting example concerns the degradation of gold NPs in human fibroblasts.[64] After two weeks degradation, EDX analysis reveals a specific signal of sulphur associated with gold allowing the authors to propose possible degradation mechanisms (**Figure 7D**).

EELS has been more rarely used than EDX to analyze NCs in cells and very few examples are found in the literature. Allard-Vannier and coworkers investigated how folic acid-capped polyethylene glycol (PEG)ylated magnetic NPs enter in cancer cells and NPs were localized by EELS.[79] Compared to EDX, EELS offers the advantage of a better sensitivity for light elements and the possibility to provide information concerning their chemical bonds allowing to distinguish between different compounds.[80] Despite these advantages, to the best of our knowledge, the possibility to analyze chemical bonds has not been exploited so far for the study of NCs in cells.

2.2.3. Imaging large volumes by 3D-SEM

As previously stated, most EM approaches provide information only on a reduced volume. This constitutes a major limitation when dealing with NCs in cells and moreover, in tissues. The probability of finding a particle is very low if the incorporated quantity is small and the provided information may be not representative of their localization in the complete specimen. The specimen thickness has also to be adjusted to the NC sizes in order to observe them. In recent years, a revolutionary technique has emerged based on the use of SEM to determine the 3D structure of thick biological samples. As SEM by itself can only characterize the specimen surface, it was coupled with a system able to remove successively thin sections from the specimen surface and a new SEM image is recorded from the new top surface. Images stacking allowed to reconstitute the full volume of the object. Standard TEM protocols can be used for specimen preparation but, as SEM provides little contrast for imaging cellular thin sections, higher concentrations of staining agents are used in order to achieve a good contrast.

Two approaches have been used to slice the specimen inside the SEM chamber. In serial block-face SEM (SBF-SEM), an automated ultramicrotome is used to obtain thin sections of about 20 nm. In Cabezón *et al*.[81], SBF-SEM was applied to study the trafficking across the blood-brain barrier of gold NPs coated with specific antibodies. Au-NPs were identified inside endocytic vesicles in the brain capillary endothelial cells (**Figure 8A**). Alternatively, SEM can be combined with a FIB used as a nano-scalpel able to cut thinner sections (< 20 nm), avoiding the artefacts associated with the mechanical sectioning. The ultrastructure of spheroids and their uptake of magnetic NCs was investigated by FIB–SEM in Mollo *et al*.[82] (a video of the reconstructed volume is given in SI). In Félix *et al*.[43], small gold NPs attached to Fe_3O_4 cores were designed for hyperthermia applications and their distribution was analyzed by FIB-SEM in microglial BV2 cells. Imaging was combined to an EDX analysis in order to unambiguously identify NPs by their chemical composition (**Figure 8B**).

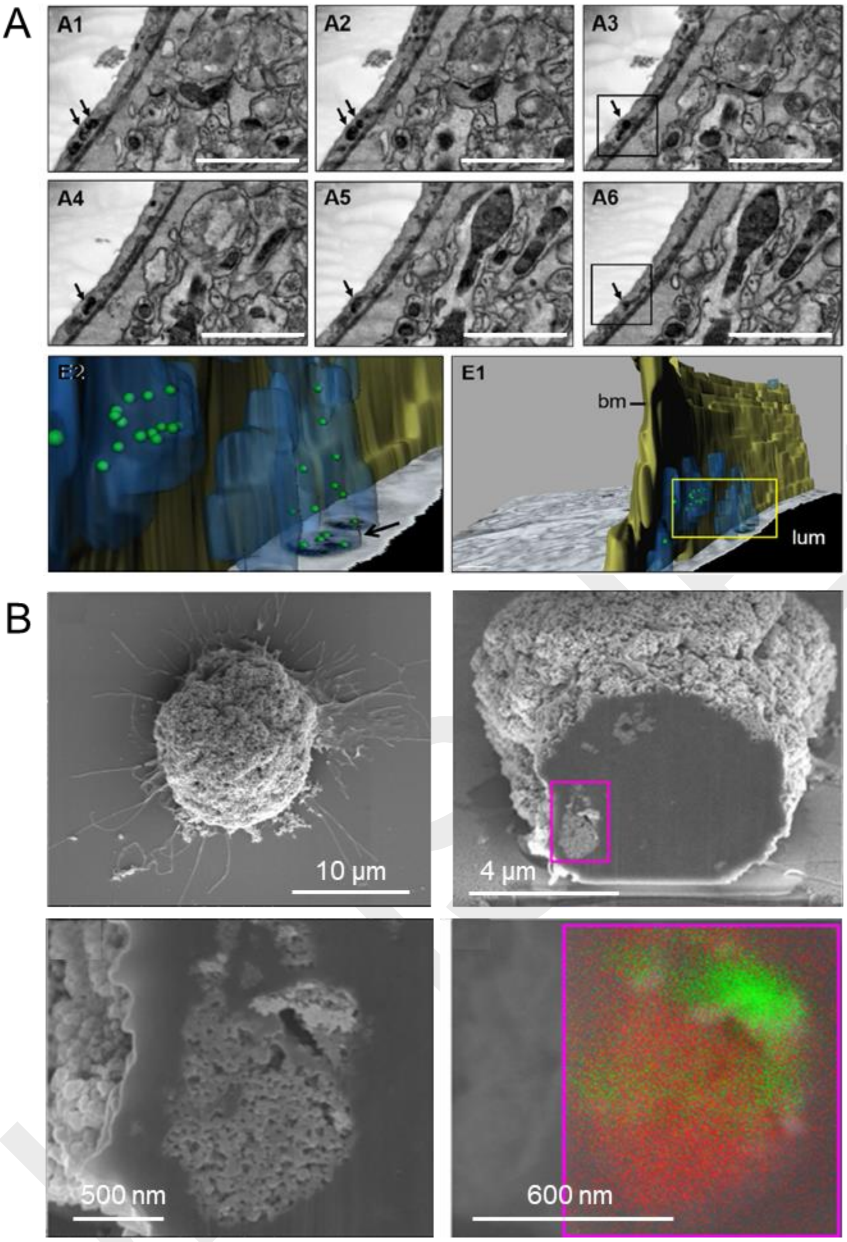

Figure 8. 3D SEM imaging: (A) the trafficking through the blood–brain barrier of gold NPs (20 nm) coated with specific antibodies (8D3) were studied by SFB-SEM. A1-A6 correspond to selected serial images from an image stack. The arrows indicate vesicles containing gold NPs. Bottom views correspond to the 3D reconstruction of the image stack. Gold NPs are represented as green spheres and the endothelial vesicles in blue (bm basal membrane, lum lumen of the capillary).[81] Scale bar = 2 µm; (B) Au@PEI-Fe_3O_4 NPs (gold NP size ~ 4 nm and Fe_3O_4 NP core size ~ 50 nm) in microglial BV2 cells. The specimen sectioning was obtained by FIB and NPs were found agglomerated on the cell membrane surface. EDX maps allow the identification of NPs in the cellular context by their signals associated with Fe (red) and Au (green).[43] (A) Adapted with permission.[81] Copyright 2017, Springer Nature. (B) Adapted under the terms and conditions of the Creative Commons Attribution 4.0 International License.[43] Copyright 2019, Springer Nature.

3. NEAR-FIELD APPROACHES

Scanning Tunnelling Microscopy (STM) and Atomic Force Microscopy (AFM) are non-destructive scanning probe microscopies, widely employed to determine the specimens' size and surface properties (conductivity, rugosity, viscoelascity…). They consist in scanning a nanosized probe composed of a cantilever ended by a sharp tip over the sample surface. The tip acts as a near-field detector, measuring the local interactions at the sample surface. The cantilever motion generates 3D images related to the sample topography. Its x,y,z movements are enabled by applying a voltage on a piezoelectric scanner which supports the cantilever. Both the piezoelectric crystal high sensitivity (angstrom scale) and the probe nanosize (~ 20 nm) contribute to reach a high spatial lateral resolution, down to the sub-nanometer scale under certain conditions. Inversely, the vertical resolution depends only on the z-piezo scanner and can reach values as low as 0.01 nm for scanning tunnelling microscopes.

Although STM and AFM are only surface techniques, they can provide information on buried materials. For instance, the presence of drug inside NPs or NPs inside cells, changes the physicochemical properties of the sample surface and hence, the tip-surface interaction. Thus, their location and distribution can also be mapped with a high resolution.

3.1. Scanning Tunnelling Microscopy and Atomic Force Microscopy

3.1.1. Principle of the techniques

STM can image the topography of (semi)conductive samples. The conductive probe measures the tunnelling current between the tip and the sample when applying a voltage (**Figure 9A**). The tunnelling current decays exponentially with the distance between the tip and the sample surface. Two modes can be employed to analyze the sample: the constant height and the constant current modes. In the constant height mode, the z-position of the tip is kept constant while in the constant current mode, the tip-sample distance is kept constant, generating topographic images.[83] In the last decade, STM has been applied to investigate the helical wrapping of self-assembled doxorubicin[84][85] and DNA[86] on single-walled CNTs. The physical adsorption of doxorubicin was related to the π-stacking between aromatic molecules and CNT benzene rings. As shown in **Figure 9C,** different conformations of the adsorbed doxorubicin have been revealed such as monomeric or dimeric molecules adsorbed in single-stranded or double-stranded structures. The resulting closely packed helical structures could be the reason of the high loading efficiency of CNTs for doxorubicin (up to 80-160%).

The need for conductive surfaces to allow the tunnelling current represents the main drawback of this technique. Conductive substrates are employed to analyze thin layers of organic and biological materials. In the previous examples, both CNTs and magnetoelectric NPs (upon application of a direct current magnetic field) behave as semi-conductive materials. For thicker specimens, metal coating or tagging is used to make them conductive. For instance, the structure of poly(amidoamine) dendrimers has been imaged using platinum and copper metal ion tagging allowing a spatial resolution down to 0.2 nm.[87]–[90]

In contrast to STM, AFM is suitable to characterize both conductive and insulating materials. The tip probes the local tip-surface interactions to map the sample topography and its mechanical properties. A visible laser beam is reflected from the backside of the cantilever onto a four-quadrant photodetector to record the tip position (**Figure 9B**). The tip apex interacts with the sample surface (through repulsive or attractive forces) inducing the cantilever deflection during the scanning. The measurement of the deflection (or of the amplitude of oscillations) provides topographic images.[91] Since 1994, AFM has been applied to determine the size and shape of NCs, such as biodegradable polymeric nanospheres of 90-150 nm,[92] and is now widely employed in the field of nanomedicine.[93]

The major advantage of AFM is its high-resolution imaging without complex sample preparation. At the opposite of EM, not only experiments can be carried out in vacuum but also in air or in liquid conditions. Nevertheless, the air conditions require sample drying since humidity induces an additional interaction between the tip and the water molecules, introducing distortions in the measurement. This drying step may alter the native morphology of hydrated NCs such as liposomes whose shape changes from spherical to ellipsoidal with an overestimated size due to osmotic stress.

AFM imaging is mainly performed according to three modes: the contact mode (static mode), the non-contact and the tapping modes (dynamic modes). In the contact mode, the static tip touches the sample surface resulting in repulsive interactions. In the non-contact mode, the probe is slightly oscillating (~10 nm) at the vicinity of the sample surface without contact. In the tapping mode, also known as intermittent-contact mode, larger oscillation amplitudes (~200 nm) are applied. At each cantilever oscillation, the tip touches the sample and moves (far) away.[91]Strong lateral forces and tip penetration occur in contact mode and may damage both the tip and the sample, distort soft material or sweep weakly bounded particles. Dynamic modes induce lower interaction forces and are more appropriate to preserve the sample integrity of sensitive materials such as polymeric NCs[94] and biological materials.[95]

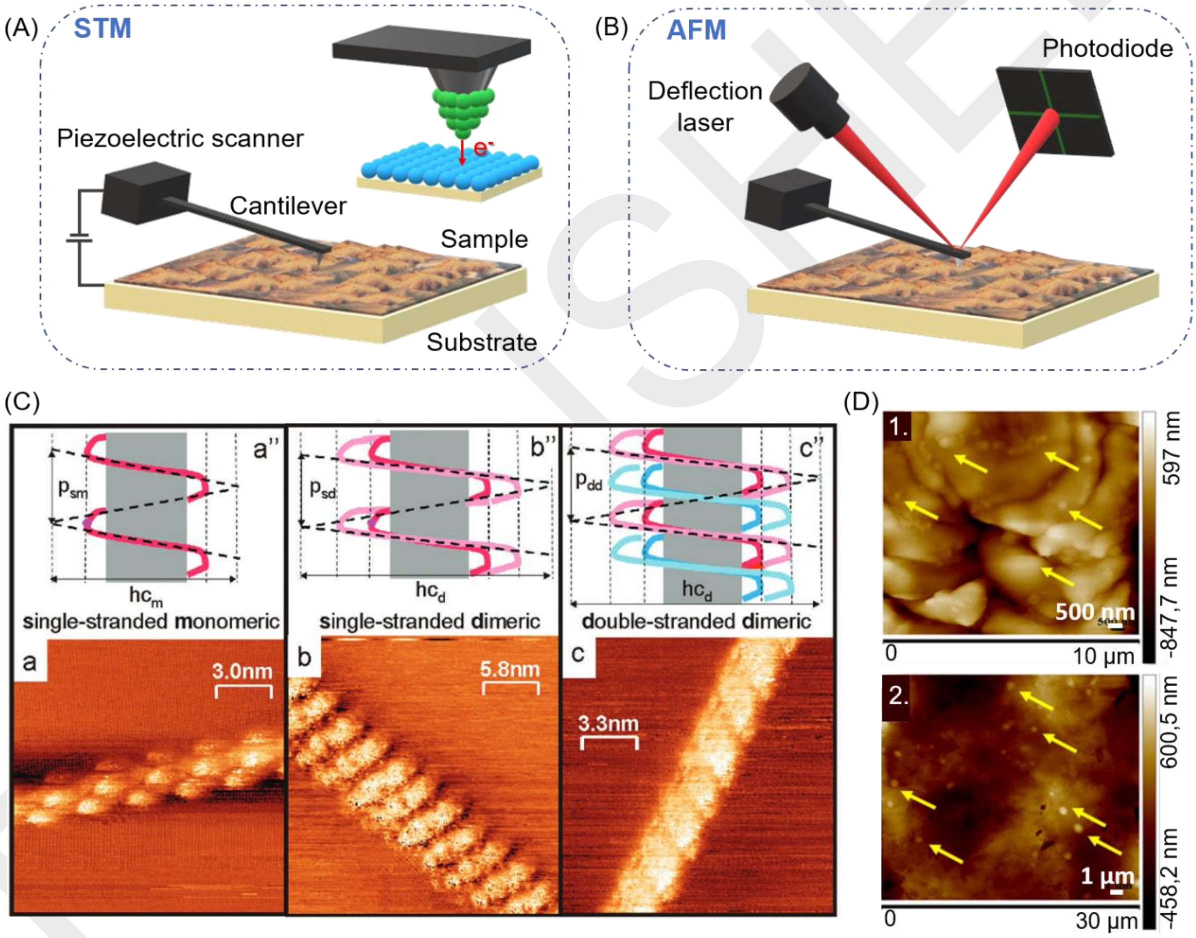

Figure 9. Schematic illustration of a (A) STM and an (B) AFM setup. Both are based on the scanning of the sample surface to measure the tip-sample interactions. The probe consists of a cantilever ended by a sharp tip. A piezoelectric scanner allows three-dimensional movements of the cantilever. STM probes the tunnelling current (red arrow) between the conductive tip and the (semi-)conductive sample. The feedback system monitors the cantilever z-position according to the applied voltage. AFM measures the tip-sample force interaction. The feedback system adjusts the cantilever position with respect to the four-quadrant photodiode. (C) Schematic representations (top row) and STM images (bottom row) of the helical structures of doxorubicin self-assembled onto carbon nanotubes.[85] (D) AFM images of rat blood (1) and liver tissue sections (2) after intravenous administration of cyclosporine-loaded PLGA nanoparticles (indicated by yellow arrows).[98] (C) Adapted with permission.[85] Copyright 2017, Wiley-VCH. (D) Adapted under the terms and conditions of the Creative Commons Attribution License.[98] Copyright 2013, Public Library of Science.

Besides, the tapping mode allows to study the nanomechanical properties of the sample. When the tip approaches the surface (down position), the resulting interactions causes the cantilever damping and the reduction of the oscillation resonant frequency. As the oscillation damping depends on the energy dissipation, it can be related to the sample viscoelasticity and adhesiveness.[96] The tapping mode has been used to provide information on one hand on the morphology, the structure and the surface properties of drug NCs and, on the other hand, on the NC location within biological systems. As an example, AFM revealed a disk-like shape of prednisolone-loaded solid lipid NPs of approximately 200 nm and by measuring the tip frequency changes, it suggested a soft shell surrounding the NPs.[97] Another work located cyclosporine-loaded PLGA NPs of ~280 nm in blood and liver after intravenous and *peroral* administration (**Figure 9D**) by the detection of the local increase of the tissue stiffness induced by the NPs.[98]

3.1.2. AFM tip modifications

A variety of AFM technological developments were made, such as multiparametric, molecular recognition, multifrequency and high-speed imaging.[99] In particular, AFM tip has been modified to measure additional physicochemical properties of the sample surface. Electrostatic, magnetic, thermal interactions and chemical forces can be measured at the sample surface by coating or functionalizing the tip surface. For instance, a metal coated-tip is used to map the local variations of the electrostatic forces (Electrostatic force microscopy) or the work function (Kelvin probe force microscopy). In contrast, the magnetic field is measured (Magnetic force microscopy) by a magnetic tip. Electrostatic force microscopy was applied to study the biosynthesis of bacterial cellulose-graphene oxide NPs which were further used to incorporate ibuprofen as a model drug.[100] Kelvin probe force microscopy was employed to map the surface potential of gold nanorods during the removal of their surfactant.[101] The electric properties of paclitaxel-loaded magnetoelectric NPs have been analysed by magnetic force microscopy.[102] This approach has also enabled to monitor the cellular uptake of magnetic NPs in niosomes,[103][104] in human leukemia cells[105] and in human breast carcinoma epithelial cells.[106][107]. In another strategy, the AFM tip was functionalized with NPs in order to investigate their interaction with lung epithelia cells in biological media.[108] More recently, an AFM tip (diameter 20 nm) coated with serum proteins was used to mimic a NP in contact with blood and directly examine its interactions with cells.[109] These are only few examples that highlight the growing interest of these approaches in the scientific community.

3.2. Optical near-field spectromicroscopies

When coupled with optical spectroscopy, AFM reveals to be a multifunctional approach to perform simultaneous imaging and chemical analysis. The so-called optical near-field spectromicroscopy is fully appropriate to determine both the structure and composition of NCs. Besides, this technique enables to determine the optical response of buried materials, such as drug inside NPs or NPs inside cells, since their presence affects the signal detected in the top layers of the sample.

Conventional optical approaches are constrained due to the Abbe diffraction limit (~wavelength/2) to low spatial resolutions of few hundreds of nanometers, not enough to resolve individual NPs. Optical near field spectromicroscopies coupling optical microscopy with scanning probe microscopies allow to drastically improve the spatial lateral resolution down to tens of nanometers.

In the following sections, two techniques will be detailed: (i) scattering-type Scanning Near-Field Optical Microscopy that probes the optical response of the sample, and (ii) Photothermal Induced Resonance that measures the sample photothermal expansion. Both are based on an AFM setup where a sharp tip scans the sample surface while being locally illuminated with a focused laser beam. Spectroscopic images are obtained simultaneously with topographic and nanomechanical information. Hence, the optical properties of the sample (absorption and scattering) are locally determined and mapped.

3.2.1. Scattering-type Scanning Near-Field Optical Microscopy

In the scattering-type Scanning Near-Field Optical Microscopy (s-SNOM), an AFM is coupled with an optical microscope (**Figure 10A**) to measure simultaneously the topography and the optical near-field response of the sample. Here, the tip operates both as a source and as a near-field detector: under illumination, it generates an evanescent wave (apex radius smaller than the wavelength) which locally interacts with the sample. This leads to a resolution independent of the laser wavelength and only defined by the tip apex radius (~10nm).[110] When the sample interacts with the incident light, it produces scattered fields that depend on its optical properties (reflective index and absorption). The local measurement of the optical response provides the amplitude and the phase contrast of the scattering signal.[111][112]

Because the image contrast depends on the scattered light, s-SNOM is not well appropriated for poorly scattering samples such as polymer NCs and biomaterials. The s-SNOM sensitivity can be improved by using metal-coated tips and more particularly a plasmonic metal coating (gold or silver). In plasmon-enhanced spectroscopy, the electrical near-field confinement of the light in the vicinity of the tip apex is enhanced, thus improving the signal sensitivity.[111]

Nuño *et al.*[113] have used the plasmonic properties of gold to discriminate 50 nm sized gold, silica and silica-capped gold NPs. Thanks to gold scattering response, gold NPs appear brighter in near-field amplitude images (**Figure 10B**) and gold core also improves the scattering contrast of the silica coating layer (higher amplitude, red line in **Figure 10C**) as compared to bare silica NPs (blue line in **Figure 10C**).

Tip-Enhanced Raman Scattering

s-SNOM can be coupled with Raman spectroscopy by collecting the light inelastically scattered by the sample. This technique, known as Tip-Enhanced Raman Scattering (TERS), usually employs a plasmonic metal-coated tip (gold or silver) to improve the weak Raman signal. More details on TERS can be found in Kurouski *et al*.[114] Beyond a simple differentiation by dielectric mapping, TERS allows a nanoscale Raman spectroscopic imaging. NCs components can be readily identified by their specific molecular vibrational modes. Ashtikar *et al*.[115] used deuterated phospholipids to track liposomal systems of around 80 nm in human skin upon topical applications. The liposomal systems were detected in the topographic images, where a high density of flattened vesicular structures (50–300 nm diameter) were observed in the deep layers of the *stratum corneum*. The detection of the vibrational signature (characteristic C-D band at 2170 cm^{-1}) of the deuterated lipids enabled to ascertain that the liposomal formulations were intact inside the skin. Interestingly, TERS has also shown the presence of free deuterated-phospholipids.

Nano-FTIR spectroscopy

In the Fourier transform infrared nanospectroscopy (Nano-FTIR spectroscopy), s-SNOM is coupled with IR spectroscopy to map the vibrational modes of the specimen. An IR laser is used to illuminate the sample at its vibrational resonance and the scattered light is analyzed by a Michelson interferometer. This signal (related to the sample reflection and absorption properties) allows the NC analysis of by their specific IR absorption. The use of monochromatic lasers requires repeated scans at different wavelength involving time-consuming acquisitions, sample drift, tip wearing and finally measurement distortion.[116] Alternatively, broadband IR sources are generally employed to record the information over the complete IR spectral range. Notably, synchrotron sources provide a high-power density in a wide spectral range, from 500 to 5000 cm^{-1}, particularly interesting since it includes the biological window (approximately from 530 to 1430 cm^{-1}). With this approach, the interactions between antimicrobial NPs and *Escherichia coli* bacteria were investigated by Capeletti *et al.*[117] Carbohydrate-coated silica NPs of around 100 nm were designed to target the membrane of gram-negative bacteria. **Figure 10D** shows that, in agreement with topographic data, the characteristic bands of NP silica and amide from membrane proteins are detected together only at the NP-bacteria interface (purple areas in **Figure 10D**). These results also reveal shifts of the amide bands related to a hydrogen bonding between the NPs and the bacteria membrane.

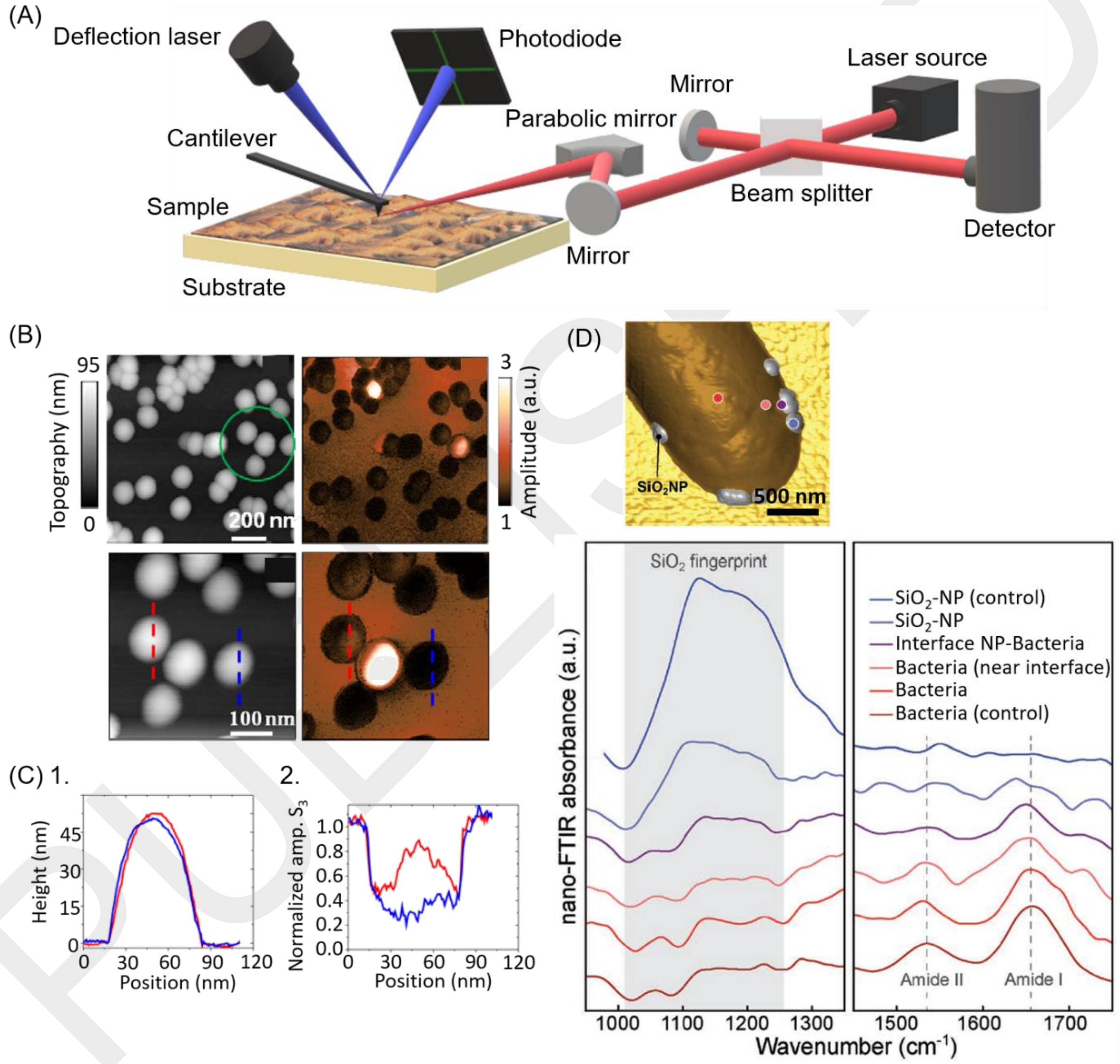

Figure 10. (A) Schematic illustration of an s-SNOM setup. While a sharp tip is scanned over the sample, a focused light source (visible or IR, monochromatic or broadband) locally illuminates the surface. The detector collects the sample optical response. (B) Topographic and s-SNOM amplitude images of gold, silica and silica-capped gold NPs. Gold NPs appear as brightest in near-field amplitude images due to their larger scattering response. The selected region of interest is indicated in green.[113] (C) Topographic (1.) and amplitude signal (2.) line profiles of the two silica and silica-capped gold NPs shown respectively in red and blue dashed lines in (B). The gold core improves the scattering contrast of the silica coating layer.[113] (D) Topographic image of a bacterium incubated with gluconamide-functionalized silica NPs (SiO$_2$-NP) and nano-FTIR spectra of corresponding regions. The redshift of amide I and blueshift of amide II spectral bands indicate the NP-bacterium interaction.[117] (B-C) Reproduced with permission.[113] Copyright 2011, Optical Society of America. (D) Adapted with permission.[117] Copyright 2019, Wiley-VCH.

In a nutshell, s-SNOM is a powerful technique to characterize NPs from their optical response. Although it is not well appropriated for poorly scattering samples, plasmon-enhanced spectroscopy can be used to improve its sensitivity. However, to minimize artefacts due to water IR absorption, the sample is typically dried which might also distort its native structure. It has also to be mentioned that s-SNOM is poorly reproducible. As the near-field signal depends on the tip-sample interaction, the acquisition conditions such as the scanning mode and the tip nature and geometry, can affect the measurement. The acquired spectra can be quite different from the one obtained by conventional far-field techniques.

3.2.2. Photothermal-induced Resonances

Photothermal Induced Resonances (PTIR) (also named Atomic Force Microscopy-based Infrared, AFM-IR) combines an AFM with IR spectroscopy to map the molecular IR absorption at a nanoscale resolution.[118] A pulse tunable IR laser locally illuminates the sample to excite molecules at their specific absorption wavelength (**Figure 11A**). The non-radiative relaxation of molecules generates a local heating and a fast thermal expansion that is detected by the AFM cantilever whose oscillations decay into a ring-down signal. Of main interest, when processed by Fourier Transform the obtained local spectroscopic data are similar to conventional FTIR.[119] Therefore, PTIR can be applied to (i) map the chemical information during the scanning of the sample surface at a fixed wavelength or (ii) acquire IR spectra at a specific location with the precision of AFM, by measuring the amplitude of the cantilever oscillations as a function of the wavelength.[114][120]

Drug and shell location in NCs

Mathurin *et al.*[121] have compared the effects of contact and tapping modes on PLGA NPs of 100-200 nm loaded with an antibiotic, pipemidic acid (PIP). As shown in **Figure 11B**, the contact mode destroys the particles. Conversely, the tapping mode allows observing the specific core-shell structure of the PLGA NPs, where the poly(vinyl alcohol) (PVA) surfactant is clearly visible surrounding the PLGA core. Besides, the 10 nm-resolution achieved in tapping mode enabled observing the drug distribution within the NCs. For PIP-loaded PLGA NCs, chemical maps reveal the drug location in the corona (**Figure 11 C-D**) which is due to a higher affinity of PIP for the PVA shell than for the PLGA core. These results are in good agreement with the drug release behavior: the drug location near the surface leads to an undesired fast “burst” release. Note that, despite the low amount of loaded drug (< 1 wt%) it was well detected in the NCs. This pioneering study demonstrated that PTIR is a powerful tool to study drug location in single NPs, opening news avenues for their characterization in the nanomedicine field.

More recently, Wieland *et al.*[122] investigated cytarabine-loaded liposomes of 80 nm by tapping PTIR. In contrast to PIP-loaded PLGA NPs, the chemical maps of cytarabine-loaded liposomes (**Figure 12E)** showed that the drug was located in the liposome core. Since the drug location affects the local nanomechanical properties of the liposome, it was also visible on frequency maps: **Figure 12F** shows that the liposome central region is harder than its periphery, in agreement with the drug distribution. In addition to the 10 nm spatial resolution achieved, the high sensitivity of PTIR has allowed to detect very small amounts of cytarabine within liposomes (7.10^{-21} mol). However, despite that the tapping PTIR mode is non-destructive, the drying step required during the sample preparation had influenced the native morphology the liposomes. Due to the osmotic pressure, their shape changed from spherical to ellipsoidal and an increase in size from 80 nm to 100-200 nm were also observed. Note that the drying step could not only alter the liposome structure but also influence the drug distribution within the NCs: the dehydration can induce the drug crystallization. Khanal *et al.*[123] applied PTIR to discriminate liposomes of 97-130 nm containing ciprofloxacin in dissolved or in crystalline form. To maintain the liposome stability upon the drying process, they have included a sucrose solution in the formulation. While the liquid drug generated an IR signal related to ionized carboxyl groups, it was absent or weaker for the crystalline form. The results were compared to nanomechanical imaging where a uniform distribution was obtained for the liquid drug whereas the crystalline form was centered within the liposome.

Several other studies have applied plasmon-enhanced PTIR with a polarized IR beam to determine the geometry and molecular orientation of drugs immobilized onto gold and silver NPs, such as a selective Y5 receptor antagonist,[124] α-methyl-DL-tryptophan,[125] erlotinib[126][127] and nocodazole.[128] This highlights the significant interest of PTIR for analysing the drug interactions with NCs.

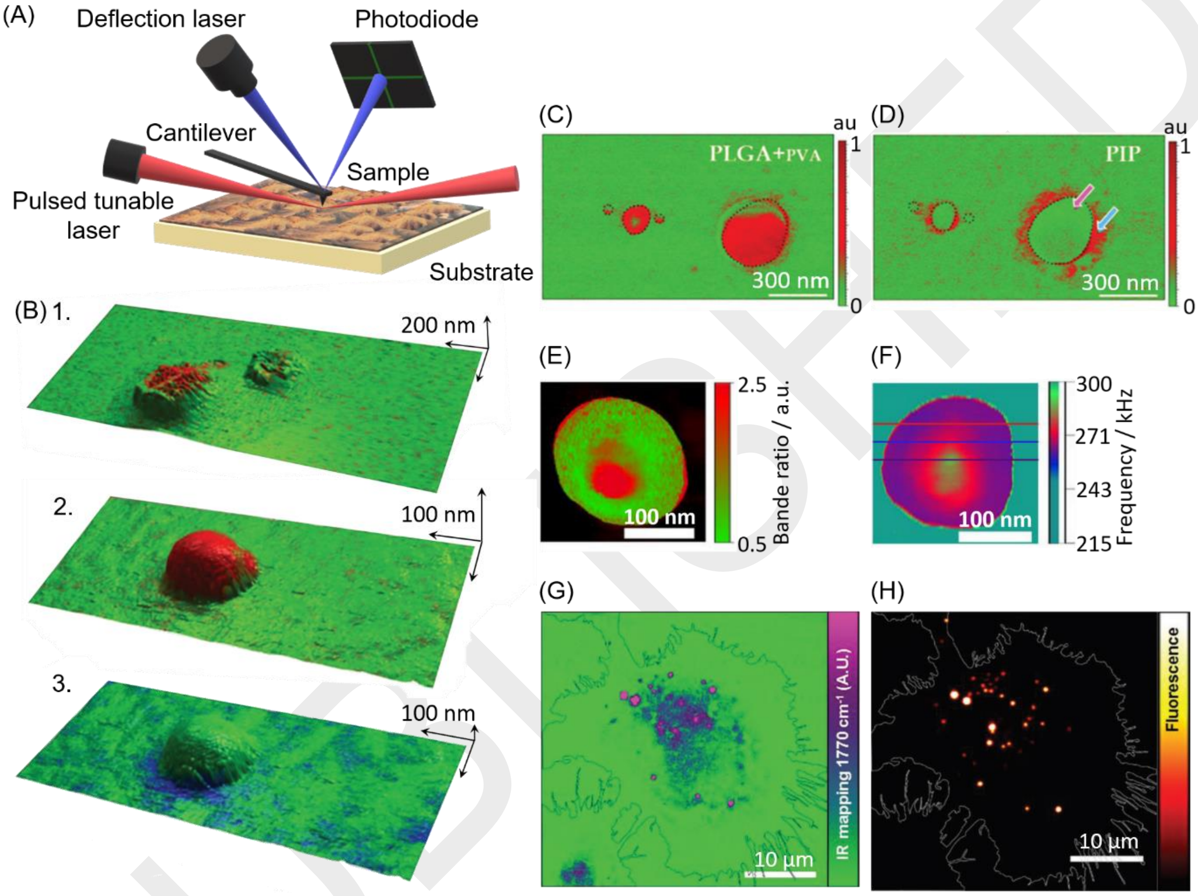

Figure 11. (A) Schematic illustration of a PTIR setup. An IR laser illuminates the sample and induces a fast thermal expansion. The sample IR absorption is then deduced from the AFM cantilever deflection. (B) Overlay of topographic and chemical maps for PLA NPs in contact (1.) and tapping (2.-3.) modes. Red and blue color represent the PLA C=O stretching vibration at 1760 cm^{-1} and the PVA C-H bending vibration at 1415 cm^{-1}. The comparison highlights the damages induced in contact mode. (C-D) Chemical maps in tapping mode of PIP-loaded PLGA NPs at (C) 1425 cm^{-1} (PLGA C-H vibration band) and (D) 1640 cm^{-1} (PIP C=O stretching vibration band). The co-location of PIP and PVA is clearly visible in the NP shell (cyan arrow), around the PLGA core (pink arrow).[121] (E) Chemical map of cytarabine-loaded liposomes, performed in contact mode, at 1528 cm^{-1} (pyrimidines C=N and C=C vibrations) and 1734 cm^{-1} (lipids C=O stretch vibration). The image ratio shows red and green colors corresponding to the cytarabine rich and lipid rich regions, respectively. (F) Frequency map of cytarabine-loaded liposomes showing a stiffer region in the center related to the encapsulated drug.[122] (G) Chemical map and (H) fluorescence images of internalized Rho-PLA NPs in a THP-1 macrophage acquired with a PTIR laser at 1770 cm^{-1} (PLGA ester groups) and a confocal microscope, respectively.[129] (B-D) Adapted with permission.[121] Copyright 2018, Royal Society of Chemistry. (E-F) Adapted with permission.[122] Copyright 2019, Springer Nature. (G-H) Adapted with permission.[129] Copyright 2018, Wiley-VCH.

Detecting NCs in cells and tissues

An interesting application of PTIR lies in mapping organic NPs embedded within cells. Pioneering studies by Pancani *et al.*[129] allowed tracking biodegradable poly(lactic acid) (PLA) NPs of 170 nm inside cells without the need of labelling them with fluorescent dyes. The intense ν(C=O) stretching vibration band of PLA NPs was used as a fingerprint to detect unambiguously PLA NPs while embedded inside the cell (**Figure 11G**). Close-up images revealed individual NPs with a spatial resolution of approximately 10 nm. A correlative study with confocal microscopy has highlighted the successful detection by both techniques of all NPs whatever their location inside the cells (**Figure 11G** and **Figure 11H)**. More recently, Kemel *et al.*[130] investigated the penetration of Janus NPs (~150-300 nm) in human skin with a sub-100 nm spatial resolution. In this regard, they performed *in vitro* chemical mapping of human skin slices after cutaneous application of Janus NPs (JNP) and vertical sectioning of the skin. Because of the spectral similarities between JNP and biomaterials, the characteristic IR signals of JNP could not be employed as spectral markers to track them. Thus, the study only compared the evolution of the signals from the chemical maps. After 24 h application, the increase of the signal enables to monitor their penetration. Among the constant protein signal, the JNP signal reveals a gradient from the surface into the deepest layers of the *stratum corneum*.

However, despite the capacity of AFM-IR to characterize NCs interactions with drugs and biomaterials, it is constrained by several limitations. First, it is difficult to estimate the sample depth from which the signal is recorded. Hence, it is not possible to distinguish materials buried at different penetration depth (for example, NPs inside cells). Secondly, to prevent from water IR absorption, samples are typically dried with air or nitrogen. This significantly limits *in situ* experiments that are needed to analyze hydrated NPs and determine biological processes.

4. SINGLE PARTICLE ANALYSIS IN SUSPENSION

Dynamic Light Scattering (DLS) is the most common method to determine the NPs' size distribution in their native environment in solution. As shown in **Figure 12A-i**, it consists of a polarized laser that illuminates the sample and a photodiode that collects the light scattered by NPs. NP Brownian motion leads to a time-dependent intensity of the scattered light and its characteristic time can be extracted from the signal autocorrelation function. The diffusion coefficient is then determined from the Stokes-Einstein equation that is related to the NP hydrodynamic radius.[131] Nevertheless, only an averaged size can be measured. Three techniques able to provide the size and size distribution of individual particles in suspension are discussed here: Nanoparticle Tracking Analysis, Single Particle Extinction and Scattering, and Tunable Resistive Pulse Sensing.

4.1. Nanoparticle Tracking Analysis

Nanoparticle tracking analysis (NTA) determines both the concentration and the size distribution of NPs in suspension by analyzing the Brownian motion of the individual NPs. The sample is illuminated with a laser at a low incidence angle and the scattered light emitted by each NP is collected with an optical microscope fitted with a camera (**Figure 12B-ii**). Each NP appear as a bright spot and its trajectory allows determining its diffusion coefficient and then, its hydrodynamic radius. From these data, the size distribution of the sample can be unambiguously determined for NPs large enough to scatter light, generally larger than 50 nm.This size limitation can be lowered down to 15 nm for high refractive index NPs, such as gold particles.[132] The NP concentration can be determined, in a range typically from 10^6 to 10^9 particles per mL. In addition, with an appropriate experimental design, NTA may advantageously be used to characterize the size and concentration of NPs intrinsically fluorescent or after labelling.

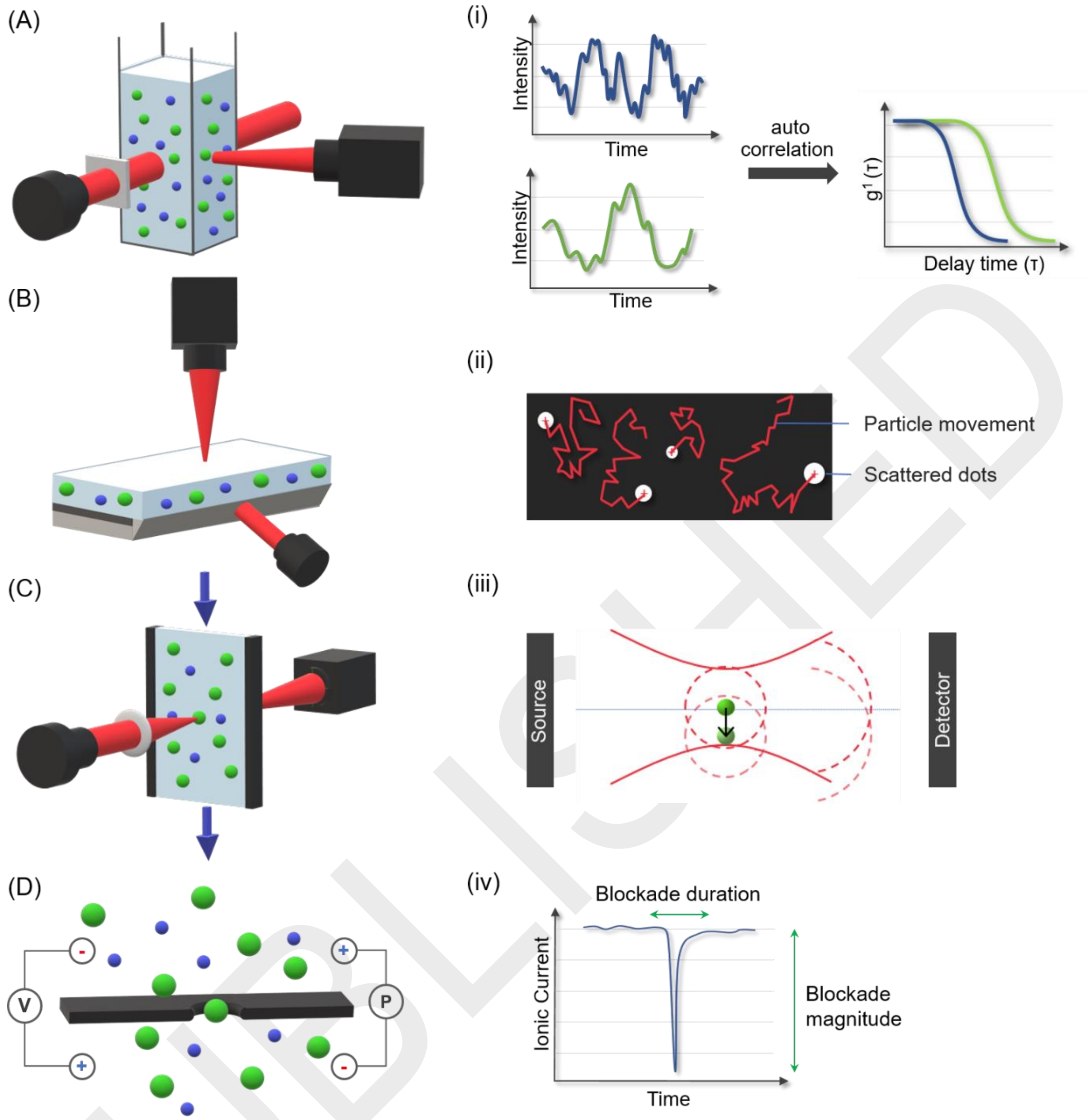

Figure 12. Schematic illustration of Dynamic Light Scattering (A), Nanoparticle Tracking Analysis (B), Single Particle Extinction and Scattering (C), Tunable Resistive Pulse Sensing (D) techniques and their corresponding signals (i-iv). (A) DLS provides the average mean diameter and size distribution of NPs. A polarized laser beam illuminates the sample and a photodiode collects the scattered light. (i) The intensity fluctuations are related to the Brownian motion allowing the determination of NPs hydrodynamic radius. (B) NTA measures the size of individual NPs by tracking their Brownian motion. The sample is illuminated by a laser beam through a prism-edge optical substrate and an optical microscope allows the visualization of the trajectories of individual NPs which appear as spots when scattering light. (ii) The NP hydrodynamic diameter is determined from their diffusion coefficient. (C) SPES determines the polarizability and the optical thickness of single NPs. A laser beam is focused into a flow cell where particles in suspension are driven with a laminar flow and a constant speed. Each particle passes through the focal plane producing a scattered field. (iii) The transmitted and scattered fields are collected by a quadrant detector. They generate time-dependent interferences whose intensity fluctuations are related to the extinction cross section and size of individual particles. (D) TRPS determines single NP size and surface charge. The NPs are suspended in an electrolyte and forced to pass one by one through a membrane which has a single well calibrated nanopore. A voltage is applied across the membrane, and the passage of individual NPs through the nanopore generates current blockage events resulting in a signal (iv) whose intensity and duration are characteristic of the NP size and charge. The blockage frequency is related to the sample concentration.

Filipe *et al.*[133] have compared the ability of DLS and NTA to determine the size distribution of several monodisperse or polydisperse NP samples. As expected, DLS measurements were strongly affected by the presence of large particles because the scattering intensity is proportional to the sixth power of the NP size. In contrast, NTA provided a better size accuracy for polydisperse samples such as poly (lactic-co-glycolic acid) (PLGA) NPs since it detects individual NPs (**Figure 13A**). However, NTA was limited by its inability to detect particles smaller than 30 nm, such as insulin monomers, as shown in **Figure 13B.** In this case, DLS was a more adapted method. Therefore, by opposition to DLS, the NTA data are not an intensity weighted mean but a high-resolution particle size distribution analysis offering a single NP characterization. Nevertheless, both require stable NPs in solution during measurements and the analysis in complex media (for example in the presence of proteins and aggregates) can be difficult due to the scattering background arising from other materials in the suspension.

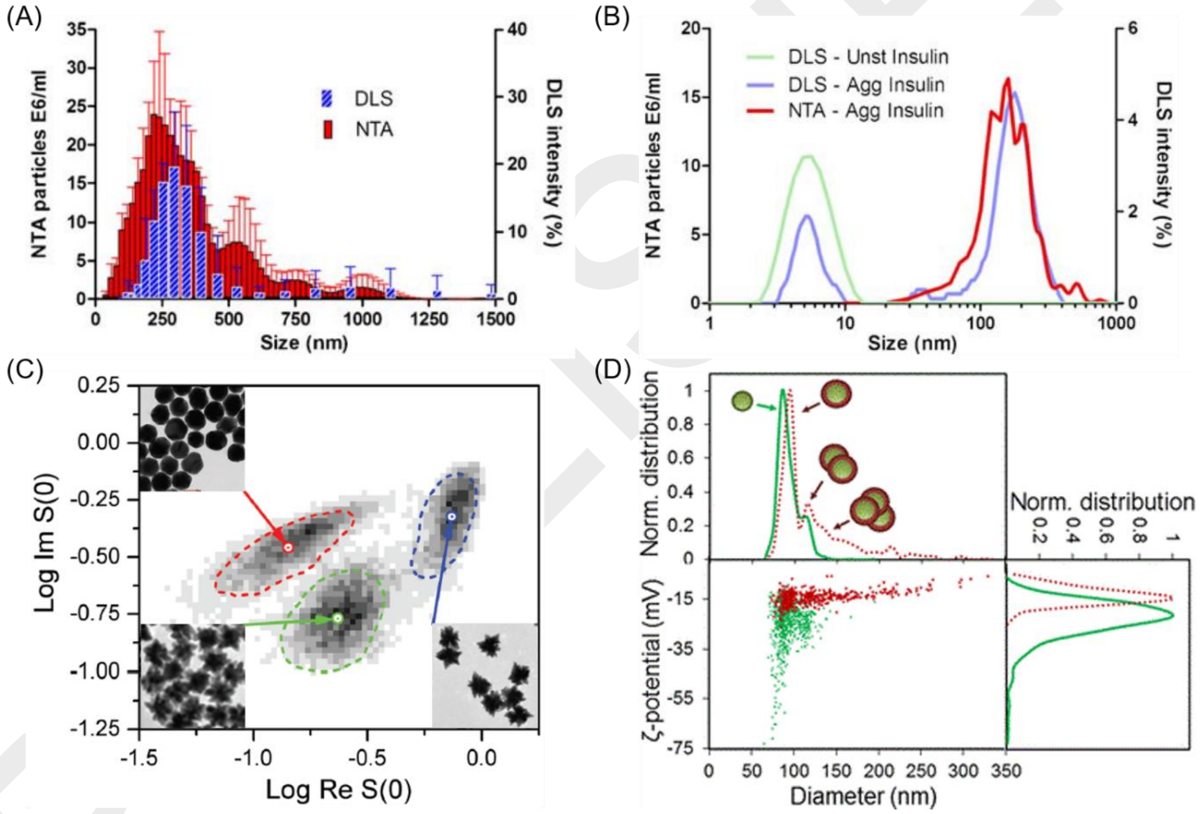

Figure 13. Size distribution of (A) PLGA NPs and (B) insulin aggregates measured with DLS (blue) and NTA (red). Unst stands for unstressed insulin, present as monomers (green).[133] (C) Histogram of the real (Re S(0)) and imaginary (Im S(0)) parts of the scattered field of mixed spherical (80nm, red) and branched gold NPs (60 nm, green and 124 nm, blue) measured with SPES. The different populations are quantitatively identified from their different optical response. The corresponding TEM images are shown in the insets. The grey tones indicate the number of particles.[136] (D) Size and ζ-potential distributions of silica NPs uncoated (green) or coated with a protein layer (red) measured by TRPS. Norm. stands for normalized distributions, calculated from the measurements of ζ-potential and sizes of individual NPs.[138] (A-B) Adapted under the terms and conditions of the Creative Commons Attribution Noncommercial License.[133] Copyright 2010, Springer Nature. (C) Adapted under the terms and conditions of the Creative Commons Attribution 3.0 Unported Licence.[136] Copyright 2017, Royal Society of Chemistry. (D) Adapted under the terms and conditions of the Creative Commons Attribution 3.0 Unported Licence.[138] Copyright 2016, American Chemical Society.

4.2.Single Particle Extinction and Scattering

Although not widely used in drug NC investigations, Single Particle Extinction and Scattering (SPES) is an interesting approach to analyze polydisperse samples and suspensions in complex media by measuring the polarizability and the optical thickness of each particle. Particles in suspension pass through a flow cell with a laminar flow and a constant speed, under a laser beam illumination (**Figure 12C-iii**). The transmitted and scattered fields are both collected by a photodiode and superimposed to produce interference patterns. As the scattered field amplitude changes with the flowing particle position, the interference patterns are time-dependent. This enables to measure the extinction cross section and optical thickness of single NPs. Then, the particle diameter and refractive index are deduced with the following formula $\rho = d\,(m-1)$, where ρ is the optical thickness, d is the particle diameter and m is the refractive index relative to the surrounding medium.[134]

The major advantage of SPES is its ability to assign a refractive index and size to each NP, allowing to distinguish NCs with different composition within the analyzed sample. The evolution of the size distribution of PLGA and model polystyrene (PS) NPs has been studied in complex biological media and the results were compared with DLS.[134][135] While DLS is limited by the scattering background raising from biological materials, SPES enables to distinguish the NPs from the other components in the suspension. This enables to monitor the degradation of PLGA NPs in phosphate buffered saline[134] and the protein corona formation around PS NPs incubated in murine serum, filtered and unfiltered murine blood.[135] In addition to size determination, Potenza *et al.*[136] have demonstrated the possibility to distinguish plasmonic metal NPs with different shapes. The NP morphology (shape and size) affects its plasmonic properties and, consequently, its optical properties. For a sample composed of mixed spherical and branched NPs, in a comparable size range, the plotting of the real (reflective index, Re S(0)) and imaginary part (absorption, Im S(0)) of the scattering field reveals optical responses of each fraction (**Figure 13C**) and so, the size dispersion of the sample, from which the different populations can be identified.

4.3.Tunable Resistive Pulse Sensing

Tunable Resistive Pulse Sensing (TRPS) is a versatile technique to measure the size, shape and surface charge of individual NPs and their concentration. The NPs are suspended in an electrolyte and placed in a cell separated in two parts by an elastomeric single-nanopore membrane. The NPs are driven to pass one by one through the nanopore by applying a difference of voltage and pressure. This results in an ionic current, whose fluctuations are measured. Current blockade events (resistive pulses) are recorded at each particle crossing. The particle size, surface charge and concentration are determined from the magnitude, duration and frequency of the blockade signal, respectively (**Figure 12D-iv**). However, TRPS is mainly limited by the nanopore size range and the sample concentration. The nanopore size is tunable by membrane stretching or relaxation. Although it provides several dynamic size ranges from 40 nm to tens of micrometers to fit with the sample, TRPS is not appropriate for highly polydisperse NPs and excludes the detection of small ones (< 40nm). Besides, very low concentrations are necessary for the NPs to pass individually through the nanopore and high ionic strength are required. These conditions might lead to artefacts and a misrepresentation of the sample in its native environment.[137]

Sikora *et al.*[138] have compared TRPS with DLS, Differential Centrifugal Sedimentation (DCS) and Electrophoretic Light Scattering (ELS) for the study of the protein shell formation around silica NPs. They monitored the size and surface charge evolution of plain and aminated silica NPs incubated in tris(hydroxymethyl)aminomethane buffer and serum solution. While DLS overestimates the NP size distribution due to the presence of aggregates in serum, DCS requires density information on the protein coating to determine its thickness. In contrast, TRPS successfully revealed the formation of a 5 nm sized-protein shell

(**Figure 13D**). This coating was corroborated by the increase of the NP surface charge. The TRPS results were similar to the ELS ones.

5. OTHER APPROACHES

5.1. Nanoscale Secondary Ion Mass Spectrometry

Secondary Ion Mass Spectrometry (SIMS) is a highly sensitive analytical approach (detection limit of the order of parts-per-billion) based on the analysis of the secondary ions generated by the sputtering of the sample surface by a focused primary ion beam.[139] Ion impact energy is about few keV and can be adjusted depending on the depth of interest and spatial resolution reaches values down to 50 nm. For each position of the beam, the secondary ions are then analyzed by a mass spectrometer allowing the identification and the mapping of the different elements constituting the specimen. It is particularly interesting to mention that isotopes can also be identified offering the possibility of an isotope labelling. In addition, the specimen surface can be imaged by detecting the emitted secondary electrons like in a SEM. Nanoscale SIMS (nanoSIMS) is a method of choice to analyze trace elements, but this approach is not able to detect changes in speciation and obtaining quantitative information is an arduous task because the yields of secondary ions are different for each investigated element and are influenced by their environment. As for the electron microscopies depicted here, SIMS is operated under high vacuum and requires sample dehydration and embedding (see paragraphs 2.1.1 and 2.1.2).

Proetto *et al.*[140] took advantage of the capabilities of nanoSIMS to discriminate between different isotopes to investigate the cellular uptake of drug-loaded polymeric NPs. The two labels (^{195}Pt from the anticancer drug oxaliplatin and ^{15}N from the polymer) were detectable by NanoSIMS and were used to determine the NPs location after their incubation with cancer HeLa cells. Surface morphological features of HeLa cells were observed *via* a secondary electron image that was overlaid with enriched ^{195}Pt and ^{15}N maps obtained from NanoSIMS. The 3D localization of NPs was determined by eroding the cell with the NanoSIMS beam and acquiring maps of ions coming from different depths within the cell. The co-localization of ^{195}Pt and ^{15}N signals provided a clear evidence that the internalized NCs were intact (**Figure 14A**). However, after 24h incubation with the cells, the slight decrease of the ^{15}N as compared to the ^{195}Pt suggested that the drug was released out of the NCs (**Figure 14B**).

Polymeric NCs loaded with ^{13}C-labelled resveratrol and tiny magnetite NPs were studied by nanoSIMS to determine their interaction with cells.[141] Tracking of both labels (^{13}C from the drug and Fe from magnetite) enabled assessing the fate of the NCs, which were targeted efficiently to macrophages and astrocytes to exert a protective effect after neuronal injury.

In another study, multifunctional NPs were made of 60 nm Raman-active gold cores covered by a monolayer of Raman-active dye and surrounded by a 30 nm thick silica shell.[142] Their location in human macrophages was analyzed both by SEM and NanoSIMS. Fewer NPs were detected by NanoSIMS due to its lower spatial resolution as compared to SEM. Moreover, this study underlines the low depth of penetration of NanoSIMS: NPs deeper than 1-2 nm from the surface were not detected because ion generation and sputtering only occurred in a very reduced volume.

More recently, SIMS has been coupled with time-of-flight secondary ion mass spectrometry (ToF-SIMS) for the detection of coatings on NPs[143] and the biomolecular imaging of NP-cell interactions[144] representing a valuable tool in nanotoxicology.

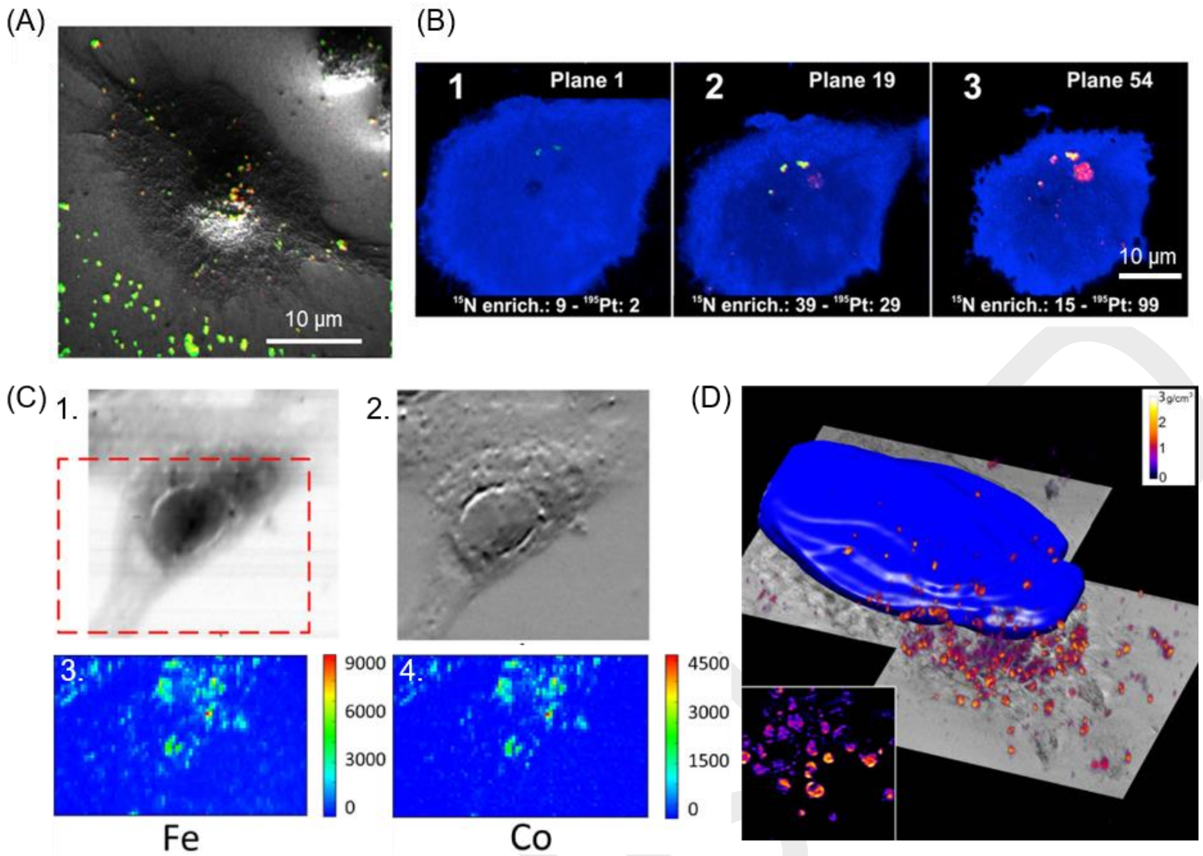

Figure 14: NanoSIMS maps from Hela cells incubated with polymeric NPs labelled with ^{15}N and loaded with oxaliplatin from [140] . Red and green colors represent ^{195}Pt and ^{15}N signals while yellow color corresponds to the colocalization of those two signals: (A) ^{15}N and ^{195}Pt maps overlaid on the secondary electron image of the cell; (B) Successive maps from an HeLa cell incubated 24h with NPs obtained by removing layers of organic matter from the cell surface and subsequent imaging. The cell surface is represented by the ^{12}C^{14}N− ion map (in blue). (C) Absorption (1) and phase (2) contrast images of $CoFe_2O_4$ NPs internalized within a human glioblastoma-astrocytoma cell. The corresponding XRF maps of Fe (3) and Co (4) acquired in the region of interest indicated in red in (C1) (40 x 40 µm² size).[159] (D) 3D representation of SPION densities within human adenocarcinoma cells (color grading = 0-3 g/cm^3 from purple to white). Blue area represents the nucleus.[176] (A-B) Adapted with permission.[140] Copyright 2016, American Chemical Society. (C) Adapted with permission.[159] Copyright 2013, Wiley Ltd. (D) Adapted under the terms and conditions of the Creative Commons Attribution 4.0 International License.[176] Copyright 2016, Springert Nature.

5.2. Synchrotron based-X-ray spectromicroscopies

Synchrotron based-X-ray spectromicroscopies constitute highly sensitive and rather non-destructive approaches allowing to image and to map quantitatively the chemical composition (including trace elements) at a sub-micron resolution. The description of the principles and analytical capabilities of this huge panel of approaches goes beyond the scope of the present review which will focus on a few examples to illustrate the interest and limitations of these techniques.

X-ray spectroscopic information can be obtained from two techniques: X-ray fluorescence spectroscopy (XRF) and X-ray absorption spectroscopy (XAS). In XRF, the specimen composition is determined by analyzing the secondary X-rays emitted by the specimen (fluorescence) when irradiated with a fixed X-ray incident energy. The X-rays energy should be higher than the binding energy of the electrons in their atomic orbitals and all the elements with electronic edges below the incident energy will fluoresce. When using hard X-rays (above 5 keV), this approach enables the simultaneous, qualitative and quantitative detection of multi-elements by their Kα specific fluorescence. In XAS, the incident X-ray energy is tuned and the absorption coefficient of a fixed edge is determined as a function of incident energy. By using soft X-rays (from 50 to 3000 eV approximately), this approach gives access to the full speciation of the specimen by examining the fine structures of the absorption edges (the so-called X-ray absorption near edge structures, XANES, also called near edge X-ray absorption fine structure, NEXAFS) that are related to the density of the empty/partially filled electronic states. The data obtained from XANES measurements are very similar to EELS spectra and can be directly compared. XRF and XAS can be combined to access to the elemental composition and chemical speciation.

The X-ray energies define the current capabilities and impose the specific instrumental constraints of each approach. The first limitation comes from the attenuation length that determines the provided information and the specimen preparation. Soft X-ray penetrations are in the micron range whereas hard X-rays are able to penetrate deeper and even to pass through macroscopic specimens. This deep penetration has been exploited to image large specimens without the need of sectioning, as whole cells or complete small animals, including live ones.[145] Concerning spectroscopic analysis, hard X-rays are restricted to elemental characterization due to their low spectral resolution. Soft X-rays offer the advantage of a very high spectral resolution compatible with compound identification and are particularly well adapted to organic and biological specimens because of their energy that gives access to the K and L-edges of the light elements composing these systems. The primary energy is usually adjusted in the spectral region bounded by the carbon and oxygen K-edges (284–540 eV), the so-called “water window”, in order to enhance the contrast of organic compounds so that biological specimens and their interaction with NCs can be studied without staining nor labelling. Besides, X-ray spectromicroscopies are not constrained to the analysis of fixed or dried samples in vacuum, since experiments can also be carried out on wet samples under atmospheric pressure (helium) which is an advantage for biological systems. X-ray approaches are rather non-destructive but for sensitive samples, low-dose imaging and cryogenic conditions are in many cases recommended (see paragraph 2.1.2).

5.2.1. 2D imaging

Like electron microscopes, X-ray imaging relies on different setups based on full-field (Transmission X-ray Microscopy, TXM) or scanned (Scanning Transmission X-ray Microscopy, STXM) modes. STXM is well adapted to image the NC distributions within cells due to its high spatial resolution (down to 20 nm approximately). Specimen images are obtained from the detection of the transmitted X-rays, or of the X-ray fluorescence or photoelectrons secondary emitted when the specimen is illuminated by the primary X-ray beam.[145]–[148] As in electron microscopy (see paragraph 2.1.1.), the transmitted X-rays produce 2D images with an amplitude and phase contrast. Because biological systems are mainly composed of the same light elements, the amplitude contrast is usually very weak and the phase contrast is then more appropriated to image the intracellular structure. However, an enhanced amplitude contrast can be obtained by adjusting the primary X-ray energy according to the absorption edges of the atoms composing the specimen. In Graf *et al.*[149], soft-STXM was employed to investigate at a 40 nm resolution the penetration of core-shell (silica-gold and gold-silica) NPs (sizes ~ 100-300 nm) into human skin after ultramicrotome sectioning. The photon energy was finely adjusted in order to get an optimized contrast for the NPs compared to skin. Compared to TEM that is limited to ultrathin section, STXM has the advantage to be usable on thicker sections (500 nm) compatible with the largest studied NPs (300 nm). However, the smallest ones (94 nm total diameter with 49 nm gold core) were at the STXM resolution limit and they were only detectable by carrying out and comparing measurements at different photon energies (below the C 1s and at the O 1s edges). More recently, Graf *et al.*[150] have combined cryo-SEM, EDX and soft-STXM to assess the penetration of gold nanospheres (80 nm) and nanorods (250 nm) on 3-5 µm sections of human skin prepared by plunge freezing and freeze drying. The results demonstrated that the uptake was less efficient on intact than on damaged (mechanical pricking) human skin.

An X-ray microscope can be coupled to a spectroscopic analysis, XRF or XAS, to acquire elemental maps and efficiently localize NCs in biological systems. X-ray fluorescence microscopy (XFM) couples X-ray fluorescence microscopy to XRF enabling to map the elemental distributions by collecting their specific fluorescence. NCs composed of exogenous elements can be identified without any ambiguity in cells. Besides, the fluorescence emission of cell endogenous elements (notably zinc and phosphate) can also be mapped to locate the cell borders and to detect the nucleus region. Paunesku and coworkers used hard X-rays (10 keV) to characterize the distribution of TiO_2-DNA oligonucleotide within different cell lines by mapping the titanium Kα fluorescence. The nanoconjugate sizes were about tens of nanometers well below the spatial resolution imposed by the X-ray spot size (0.3 µm × 0.2 µm at best).[151] In Liu *et al.*[152], the distribution of 100 nm transferrin-conjugated gold NPs was analyzed with a 2 × 2 μm^2 X-ray beam within multicellular tumour spheroids at different incubation times. In good agreement with confocal microscopy analysis, XFM showed that the penetration increased over the incubation time. Because of their poor transport in the dense extracellular matrix, the NP penetration was limited to 50 µm even after 48h. More recently, Luan *et al.*[153] have investigated the distribution of polymer-modified gold NPs of tens of nanometers into entire zebrafish larvae (15.8 keV X-rays focused to a spot of ~ 2 µm). After an injection in the trunk region of the larva, gold NPs were detected in the head region. Another study, based on soft-XRF, reports the tracking of iron oxide NPs-loaded PLGA NPs of 200 nm within mesothelial cells.[154] An X-ray energy of 1.1 keV was chosen for the mapping of C, O, Na, Fe atoms and the specimen was raster-scanned across the X-ray spot (diameter ~ 600 nm) on fields ~ 40×40 µm to map the NP distributions over the complete cells.

The coupling of STXM with XRF or XAS is more appropriated for spectroscopic analysis at high spatial resolution. Two acquisition modes are then possible: chemical spectra can be obtained at a fixed specimen position over a wide energy range and chemical maps can be acquired by scanning the specimen across the beam position at a fixed energy. The latter mode is rather time consuming because it requires several scans at different energies to cover the full energy range of the absorption edge. Soft-STXM was combined with XRF in several studies analyzing the internalization and toxicity of single-walled CNTs (from 5 nm to 1000 nm in length). They demonstrated that CNTs accumulate into intracellular vesicles of the cervical epithelial cells[155] and induce morphological changes of mesothelial cells[156] and human choriocarcinoma.[157] Another study, coupling soft-STXM with XRF, determined the distribution of cobalt ferrite NPs (~ 35 nm) and assessed their elemental modification (Fe to Co ratio) occurring in mouse fibroblasts.[158] When incorporated at high concentration, the NPs are located in the cell nucleus. Their chemical degradation (accumulation of Co) is related to changes in the cellular morphology and potentially contributes to cell death. Gianoncelli and coworkers investigated the distribution and potential toxicity of magnetic NPs (Fe_2O_3 and $CoFe_2O_4$) of approximately 35 nm and 110 nm, incubated with human glioblastoma-astrocytoma cells, by coupling STXM at 1.1 keV to XRF mapping with a spatial resolution of 650 nm (**Figure 14C**).[159] They revealed different uptakes and distributions for the two types of NPs that can be related to different intracellular interactions and toxicities. A quantitative study coupling soft-STXM with XRF reported the investigation of the cellular uptake and toxicity of luminescent silica 30 nm NPs. The silica NP distribution within human adenocarcinoma cells were mapped with a spatial resolution of 500 nm and the NP average concentration was estimated between $2.04 \times 10^6/\mu m^3$ and $2.22 \times 10^6/\mu m^3$ per cell volume.[160]

When coupled to soft-STXM, XANES provides the distributions of the chemical species composing the sample. Chemical maps at the oxygen and titanium absorption edges were acquired to track the uptake and bioaccumulation of TiO_2 NPs with different hydrodynamic sizes into epithelial cells of Daphnia magna gut.[161] In agreement with TEM results, Kwon and coworkers showed that TiO_2 NPs do not penetrate into the gut epithelial cells. Moreover, XANES enables fine analysis with the aim of investigating the chemical changes of the NPs induced by cell interactions. An in-depth study of the biodistribution and biomodification of iron oxide NPs (~130 nm) of different crystalline phases were performed in the digestive tract of Daphnia magna. An evolution of the XANES spectra on the Fe L-edge was observed revealing a biomodification (oxidative dissolution) of the Fe_3O_4 NPs.[162] With this approach, a quantitative elemental analysis of the sample can also be achieved. The concentration of the elements of interest can be determined by measuring the signal intensity per area, with a high sensitivity to traces (down to parts-per-millions). For instance, Yamamoto *et al.*[163] quantitatively monitored the penetration of organic core-multishell NCs of 10 nm after topical application on human skin and the release of their dexamethasone drug content. They analyzed vertical sections of 350 nm thickness of human skin. Since XANES provides access to the electronic structures, the NCs were distinguished from the drug by the differences in the spectroscopic signatures associated with the different oxygen chemical bounds. STXM enabled to detect 5% drug loading in NCs and revealed that NCs remained in the *stratum corneum* even after 1 000 min exposure.

Most of the above-mentioned studies using hard X-rays suffer from their low spatial resolution (~ 1 µm) not enough to resolve individual NPs. Recently, the improvement of the X-ray focusing systems has led to sub-micron probes.[164] Alternatively, ptychography, a coherent diffraction imaging approach, allows nanometer resolution in cellular maps, including for trace elements.[165] Ptychography uses a STXM setup to record a set of diffraction patterns from the successive illumination of overlapping regions on the sample. An iterative algorithm is then used to reconstruct a 2D image with an amplitude and phase contrast. By coupling XFR with ptychography, Stachnik *et al.*[166] have mapped quantitatively the distribution of antibiotic loaded-iron oxide NCs within macrophages, simultaneously with the identification of the different sub-cellular structures, with a spatial resolution below 100 nm.

5.2.2. 3D imaging by Synchrotron X-ray tomography

As described for electron tomography (see paragraph 2.1.3.), X-ray tomography is based on the acquisition and processing of a series of 2D X-ray images from the sample recorded at different orientations. 2D images can be obtained by the different X-ray microscopy approaches (XRF or XAS). The tilted series are then processed to get a 3D image of the specimen. In Yao *et al.*[167], two tilted series were acquired by STXM at two energies below and above the absorption edge of a specific element (Dual-energy contrast X-ray microscopy) to quantitatively map the 3D distribution of antitumoral $Gd@C_{82}(OH)_{22}$ NPs inside macrophages, with a spatial resolution of 80 nm. The NPs were mainly found in an aggregated state in phagosomes. A high spatial resolution (16.5 nm) was achieved when localizing Fe_3O_4-SiO_2 NPs within HeLa cells, by combining X-ray tomography with ptychography. The high spectral sensitivity of the technique also revealed distinct oxidative states which may result from the natural oxidation of Fe_3O_4 during storage.[168]

Another possible approach, cryo-soft X-ray Tomography (cryo-SXT), lies in the acquisition of tilted series of soft X-ray TM images on cryo-specimens giving access to a full 3D volume at resolutions down to 25 nm.[169] Cryo-SXT exploits the property of soft X-rays in the water-window region which are strongly adsorbed by the carbon-rich structures composing the biological specimens whilst their attenuation by ice is minimal. It is the only imaging approach able to provide 3D maps at high resolution of unstained vitrified whole-cells, thus avoiding chemical treatments and sectioning. It was employed to study the cellular uptake and distribution of gold NP within fibroblasts and macrophages.[170] Recently, Kepsutlu *et al.*[171] investigated the uptake of dendritic polyglycerol sulfate-coated gold NPs in human lung epithelial cells Cryo-SXT was able to detect gold NPs in specific cellular localizations (cytoplasm and lipid droplets) at levels undetectable by confocal light microscopy. Another study assessed the distribution and cytotoxicity of cisplatin-coated gold NPs of tens of nanometers within cutaneous squamous cell carcinoma. In this study, contrary to TEM, cryo-STX enabled to discriminate the different organelles and to visualize the internalized NPs in the perinuclear region. The NPs enhanced the cisplatin delivery inside cancer cells, but did not penetrate inside nucleus.[172] Interestingly, Reineck *et al*.[173] correlated cryo-SXT with confocal fluorescence microscopy, SEM and AFM to monitor the uptake mechanism of fluorescent nanodiamonds inside and on the surface of cancer cells with a spatial resolution of 28 nm.

Moreover, cryo-specimens employed in cryo-SXT are compatible with correlative cryo-epifluorescence microscopy and TEM. By combining cryo-SXT with these two techniques, Chiappi *et al.*[174] investigated the interaction of 15 nm-sized SPIONs with breast cancer cells, at a spatial resolution of 60 nm. They demonstrated that SPIONs accumulate near the cell nucleus, inside endocytic vesicles whose number and size increased with the incubation time, representing 1% of the cell volume after 12h incubation. More recently, correlative cryo-epifluorescence microscopy and cryo-SXT were employed to visualize the cellular uptake of plasmid DNA-loaded MOFs within human prostate cancer cells.[175]

Tomography can also be coupled with XAS in order to get a 3D chemical information. For instance, near-edge absorption soft X-ray nanotomography (NEASXT) was used to determine the distribution of cubic SPIONs of around 14 nm within human adenocarcinoma cells, at a 50 nm resolution (**Figure 14D**).[176] Tilt-series were acquired at 700 eV and 709 eV, corresponding to the iron L_3 absorption edge, to specifically detect the absorption changes corresponding to SPIONs, as the absorption of cellular components was constant at these two energies.

Despite the high potential of X-ray approaches, the huge majority of studies undertake correlative investigations. For instance, cryo-SXT has been combined with Surface Enhanced Raman Scattering (SERS) spectroscopy to determine the NCs-cell interactions from their specific vibrational signature. With this approach, the uptake mechanism of silver NPs was monitored within fibroblasts and macrophages with a resolution of 36 nm.[177] While cryo-SXT demonstrated the formation of NPs ring-shape structures inside endosomes, SERS revealed its relation with the specific interactions between the NPs surface and biomolecules surrounding them. Recently, Szekeres *et al.*[178] combined cryo-soft X-ray nanotomography, SERS and MS to monitor the formation of a protein corona around gold NPs (30 nm) when internalized within epithelial cells. It was demonstrated that the uptake mechanism and intracellular fate of the NPs depend on their protein corona composition.

This summary offers a quick insight of the X-rays spectromicroscopy techniques that can be employed to characterize NCs and assess their interactions with biological systems. Although non-exhaustive (other examples can be found in [179]), it reveals the high potential of these techniques which were limited for a long time by their poor spatial resolution but have recently undergone notable improvements. Noteworthy, the large majority of the present examples used a multimodal approach by combining X-ray and electron spectromicroscopies. Both are complementary: the first has high spectral resolution and sensitivity, and requires minimal sample preparation, while the last provides structural and chemical information with a higher spatial resolution.

6. PERSPECTIVES

The analytical tools to characterize NCs on an individual basis attract a growing interest. It is more and more acknowledged that accurate measurements of size distributions should be based on tracking individual NPs. In the case of TRPS, engineered functionalized membranes are under development, whereas for NTA, data analysis methods are adjusted to take into account polydisperse samples.[180] Archimedes® (Malvern) is a highly innovative instruments which use the technique of resonant mass measurement to detect and accurately count particles (particle concentration) in the size range 50 nm – 5 µm, and reliably measure their buoyant mass, dry mass and size,[181] but which, to the best of our knowledge has not been used yet in the field of nanomedicine.

For many years, TEM has been the method of choice to investigate biological systems. The possibilities offered by cryo-TEM to study NC samples in 2D and 3D at HR in their hydrated environment have not been fully exploited so far. The recent introduction of direct electron detectors that enable HR imaging in cryo-conditions down to nearly atomic scales is revolutionary. Remarkably, this approach makes it possible to address the dynamic aspects of processes such as the conformational variation of flexible objects or their assembly pathways. In Zhang *et al*.[182], individual-particle electron tomography was applied to image DNA-nanogold conjugates allowing to obtain the density maps with a resolution of about 2 nm. Using these maps as constraints, the authors deduced the dsDNA conformations by molecular dynamics simulations and determined the DNA-assembling and flexible protein structure and dynamics. Another very interesting example is the analysis of the structural evolution of hybrid albumin-MOF (BSA-ZIF-8, ZIF standing for Zeolite imidazolate framework) assemblies during their formation revealing a mechanism based on the dissolution-recrystallization of highly hydrated amorphous particles and on the solid-state transformation of a protein-rich amorphous phase.[183]

Despite its analytical capabilities and usefulness for 2D and 3D imaging, STEM is still underutilized for NCs' investigations. It has been used mainly for HAADF 2D imaging. A very promising STEM approach is integrated differential phase contrast (iDPC) imaging, an emergent HR-STEM approach enabling direct imaging of the phase of the specimen transmission function.[184] iDPC contrast allows a better detection of light elements among heavy ones compared with conventional HAADF imaging. Moreover, this technique has a signal-to-noise ratio better than other STEM modes (for instance ADF and HAADF) and also phase contrast HR-TEM imaging. As a result, beam-sensitive specimens can be imaged with a sub-Å resolution at ultra-low electron doses ($< 40\ e^{-}\ Å^{-2}$) 2-3 orders of magnitude lower than that used in conventional STEM. In three recent studies,[69][185][186] the 3D architecture of the beam-sensitive zeolite ZSM-5 (ZSM standing for Zeolite Socony Mobil) crystals was determined at atomic-resolution by iDPC-STEM but also light-element aromatics were directly visualized in the ZSM-5 crystal cages.

Another major interest of STEM lies in the possibility to characterize the chemical species by EELS spectromicroscopy at very high spatial resolution, down to the atomic scale.[42][80][187] EELS has been used in few NC studies to obtain elemental maps, but the edge fine structure has rarely been exploited so far to distinguish between chemical species. This is also true for XANES that has been scarcely used for NC analysis[188] and very rarely for species mapping. For instance, based on the analysis of the fine structures of carbon, nitrogen and oxygen edges, XANES can provide a complete identification of organic compounds[189] that can give very valuable information for organic NC identification in biological environments, without need of labelling. Compared to EELS, XANES presents the advantage of a better spectral resolution, a high sensitivity to trace elements and a reduced specimen damage that is a decisive factor for sensitive specimens. However, it has the disadvantage of a more limited spatial resolution for chemical mapping. Both X-ray and electron spectromicroscopies can be combined advantageously to overcome their respective limitations.[190] Besides, recent advances are pushing back the limits of both techniques. For instance, sub-10 nm resolutions are now achieved by cryo-soft X-ray ptychography.[191] For EELS, advances in STEM monochromators have improved the energy resolution below 5 meV and, novel spectrometers and direct detections have increased notably the sensitivity of the analysis which should make it possible to strongly reduce the electron doses needed for acquisitions on sensitive materials.[192]

Concerning 3D-imaging, FIB-SEM is undeniably the method of choice to image very large volumes. A very recent study shows that FIB-SEM technology can be extended for the analysis of volumes up to 10^7 µm^3 with a high isotropic resolution (voxel sizes of 8 x 8 x 8 nm) compatible with the imaging of the smallest cellular organelles.[193] In this study, the central brain of an adult drosophila was analyzed providing information for most of the brain on the detailed circuits consisting of neurons and their chemical synapses. In most of the cases, FIB-SEM is employed on chemically fixed, resin embedded specimens whose contrast is enhanced with high concentrations of staining agents. 3D-SEM can be applied to vitrified, hydrated and unstained specimens[194][195] but cryo-3D-STEM investigations remain extremely delicate and were limited to rare studies and, to the best of our knowledge, never for NC analysis. Cryo-SXT constitutes a very promising alternative approach for 3D investigations of NCs in relatively thick samples (~µm). An important feature of SXT is that 3D image contrast is directly related to the X-ray absorption coefficient and it can be interpreted quantitatively as local variations in carbon densities.[196] Hence, no contrast enhancement is required to image samples avoiding chemical treatments. Moreover, vitrified specimens are compatible with cryogenic-fluorescence microscopy (cryo-FM) that can locate tagged molecules of interest. This correlative cryo-SXT and cryo-FM is a powerful tool to investigate the relation between a specific cellular function and the 3D sub-cellular architecture of whole cells.[197]–[199]

Compared to EM, near-field microscopies (STM, AFM, s-SNOM and PTIR) offer a simplified sample preparation since staining or chemical fixation are not needed. Nevertheless, when observed in air, samples are usually dried which can be the source of sample distortion and damage. For instance, dehydration of liposomes or organic NPs can affect their size and drug distribution. As an alternative, AFM can be operated within fluid cells to characterize NPs in their native state. Both the probe and the sample are then immersed in a liquid (e.g. water). Nevertheless, it is difficult to achieve a good fixation of NCs on their support during investigations in liquid state. Moreover, this strategy leads to a more complex analysis because cantilever oscillations are prone to be dampened by water.[200] In addition, for optical analysis with s-SNOM and PTIR, water generates a background signal due to its strong IR absorption and thermal expansion. To prevent water IR absorption, the specimen can be illuminated from the bottom by total internal reflection though an IR-transparent prism (e.g. zinc selenide) used as a substrate. Alternatively, deuterated water can also be used since it displays a lower IR absorption in the amide I and amide II regions. With these approaches, nanoscale resolved *in liquid* s-SNOM and PTIR have been demonstrated for living cell,[201] thin poly(methyl methacrylate) films,[202] amyloid peptide fibrils,[203] catalase nanocrystals and biomimetic peptoid nanosheets.[204] In contrast, *in liquid* TERS is not limited by the presence of water since it is a weak Raman scatterer. Few studies have already been performed by TERS in water to image and analyze organic monolayers[205][206] and bilayers,[207] single-wall carbon nanotubes,[208] functionalized gold triangles,[209] and chemical reactions at the solid-liquid interface.[210][211]

Regarding the PTIR technique, further perspectives are intended to extend the IR spectral range to enlarge the NC detection possibilities in biological media. Ortega *et al.*[212] have demonstrated the possibility to image hybrid NPs in the far IR domain, outside the biological window. Further investigations are needed to improve the relatively weak spatial resolution of this promising approach.

Another important challenge in nanomedicine is the quantitative analysis of the NC components (drugs, shells, targeting ligands) on an individual NCs basis. This would be of main interest in terms of quality assessment of drug formulations, as the drug loading would be determined ion an individual NC basis. Despite an attempt made on a poly-methyl-methacrylate films,[213] quantification by PTIR remains an arduous task. While the relatively recent PTIR technique is still in progress, it is a promising tool that increasingly attracts attention.

Although near-field optical microscopies are able to identify and characterize NCs and their interactions with biomaterials, their spatial resolution cannot compete with EM. Correlative studies are then crucial to overcome this limitation and deeply analyze the samples. A pioneer study correlated PTIR and TEM results to analyze the structure of bacterial amyloidogenic proteins at high resolution.[214] Other studies also reports on correlative TEM/s-SNOM and TEM/TERS approaches to characterize phase change materials[215] and tobacco mosaic virus particles, respectively.[216] Even farther, complementary techniques can be integrated to the setup of a near-field optical microscopes. For instance, ultrasonic sources were integrated into the AFM set-up to image single-walled carbon nanohorns of 70 – 110 nm embedded in mice blood and cells[217] and SiO_2 NPs of 95 nm and 87 nm in alveolar macrophages and red blood cells.[218][219] More recently, confocal microscopy was also coupled with s-SNOM to image membranes.[220] These interesting improvements can particularly be used to unambiguously identify the intracellular compartments where the NCs are located.

7. CONCLUSION

Nanomedicines gain increasing interest in the treatment of severe diseases such as cancer and infections. In the journey from bench to bedside, the comprehensive characterization of nanomedicines and the knowledge of their interaction with the living medium is fundamental but challenging. Indeed, multifunctional NCs possess complex core-shell structures, composed of synergic drugs and engineered coatings bearing targeting ligands. This review highlighted that the methods allowing to characterize the NCs on an individual basis are key in terms of quality control of NC formulations and to study their biological fate.

The design of drug NCs with sizes usually lower than 200 nm necessitates a deep understanding of their supramolecular architecture, composition and interaction with living media, especially targeted cells. The NCs' size distribution is commonly determined by DLS, but this "bulk" technique gives average values and is sensitive to the population with largest sizes. In this context, other techniques (NTA, SPES and TRPS) were developed to measure size distribution and sometimes other properties such as surface charge, based on individual NC analysis. These techniques could be applied whatever the nature (organic, inorganic or hybrid) of the sample.

EM are the principal characterization tools to observe drug NCs and to investigate their interaction with biological systems. Seeing the unseen is the art of microscopy and the examples presented here highlight the usefulness of advanced EM techniques to decipher the structure and composition of individual drug NCs. Vital to scientists, microscopy allows to visualize and interrogate phenomena occurring beyond the reach of the naked eye, while capturing sometimes aesthetic patterns as shown in the images chosen here.

Advantageously, for chemical mapping, EMs have been coupled to analytical tools based on the spectroscopic analysis of electrons (EELS) or photons (EDX). These spectromicroscopies provide information at the nanoscale about the chemical compositions, morphologies, sizes and cellular localizations of a large variety of NCs. However, these approaches are limited to the analysis of a reduced volume that may be not statistically representative of the complete specimen depending of its heterogeneity, and the preparation method which, in certain cases, results in the selection of fractions with particular physico-chemical characteristics. The combination and comparison with bulk approaches giving information on the complete specimen allow to bypass these drawbacks.

However, TEM investigations are limited to NCs below 500 nm compatible with the transmission of the electron beam through the specimen. Thus, biological samples containing NCs in cells or need to be sectioned and dried. 3D investigations on thick samples as whole-cells or small animals can be carried on by recording SEM images on successive sections from the specimen. Cryo-EM methods constitute a good alternative to image NCs in conditions close to their native state. For instance, cryo-TEM allows to localize NCs in cells with sub-nanometric spatial resolution but is more suitable for the detection of electron-dense NCs as compared to organic NCs due to their low contrast.

Near-field microscopy approaches are of peculiar interest in the study of NCs. s-SNOM is well adapted for NCs which strongly scatter the light, such as metal NCs and allow contrast differentiation for species as small as 50 nm, but not well appropriated for poorly scattering samples such as organic NCs. NanoSIMS is also well adapted for metal NCs but the spatial resolution is lower. Besides, investigation of organic samples needs labelling with isotopes. The first technique able to detect unlabelled polymeric NCs in cells was Raman microspectroscopy, offering the possibility to perform imaging together with chemical analysis. However, the resolution was limited by light diffraction to 300 nm - 1 µm and Raman signal is usually overwhelmed by the large cell autofluorescence. In contrast, PTIR enabled detecting unlabelled polymeric NCs as small as 150 nm inside the cells. Moreover, the distribution of the components of individual NCs was unambiguously determined. PTIR is gaining increasing interest for the polymeric soft NC investigation, with potential interest for quantitative analysis. Similar achievements were made by Synchrotron-based X-ray spectromicroscopy which emerged as a highly sensitive approach to map quantitatively sample chemical composition with sub-micron resolution. These characterizations were mostly applied on inorganic NCs. Cartographies were made on unlabeled samples of relatively important thicknesses.

In a nutshell, the methods used to investigate individual NCs allowed: i) studying the morphology and the crystalline structure of the NCs; ii) localizing the components of an individual NC (drugs, coatings, ligands); iii) quantify the constituents in a NCs; iv) detecting NCs in cells and biological samples and v) exploring the fate (degradation, drug release) of a NC in a biological media.

However, all nanoscale approaches are subject to potential artefacts and are limited to the analysis of NCs with a specific size range, chemical nature and morphology. The investigation tools need to be carefully chosen according to the question(s) to be addressed and statistically relevant analyses have to be performed. There is no universal method allowing a full NC characterization and combinatorial approaches are essential. Whereas, the individual NC characterization approaches are expected to gain increasing interest in the near future, their combination with "bulk" approaches is essential to gain in depth information of NCs.

LIST OF ABBREVIATIONS

2D	Two-dimension
3D	Three-dimension
ADF	Annular Dark-Field
AFM	Atomic Force Microscopy
AFM-IR	Atomic Force Microscopy-based Infrared
BF	Bright Field
CNT	Carbon Nanotube
Cryo-FM	Cryogenic-Fluorescence Microscopy
Cryo-SXT	Cryo-Soft X-ray Tomography
CTEM	Conventional Transmission Electron Microscopy
DCS	Differential Centrifugal Sedimentation
DF	Dark-field
DLS	Dynamic Light Scattering
EDX, EDXS, EDS	Energy dispersive X-ray spectroscopy,
EELS	Electron Energy Loss Spectroscopy,
EFTEM	Energy Filter Transmission Electron Microscopy
ELS	Electrophoretic Light Scattering
EM	Electron microscopy
ET	Electron tomography
FDA	Food and Drug Administration

FEG	Field Emission Gun
FFF	Field Flow Fractionation
FIB	Focused Ion Beam
FTIR	Fourier Transform Infrared
HAADF	High-Angle Annular Dark-Field
HPLC	High Performance Liquid Chromatography
HRTEM	High-resolution Transmission Electron Microscopy
JNP	Janus Nanoparticle
MALDI	Matrix Assisted Laser Desorption Ionisation
MIL	Material of Institute Lavoisier
MOF	Metal-Organic Framework
MSN	Mesoporous Silica Nanoparticle
Nano-FTIR spectroscopy	Fourier Transform Infrared Nanospectroscopy
NC	Nanocarrier
NEASXT	Near-Edge Absorption Soft X-ray Nanotomography
NEXAFS	Near Edge X-ray Absorption near edge Fine structure
NMR	Nuclear Magnetic Resonance
NP	Nanoparticle
NTA	Nanoparticle Tracking Analysis
PAA	Poly(acrylic acid)
PEG	Poly(ethylene glycol)
PIP	Pipemidic acid
PLA	Poly(lactic acid)
PLGA	Poly(lactic-co-glycolic acid)
PS	Polystyrene
PTIR	Photothermal Induced Resonances
PVA	Polyvinyl alcohol
SAXS	Small Angle X-rays Scattering
SBF-SEM	Serial Block-Face Scanning Electron Microscopy
SEM	Scanning Electron Microscopy
SERS	Surface Enhanced Raman Scattering
SIMS	Secondary Ion Mass Spectroscopy
SPA	Single Particle Analysis
SPES	Single Particle Extinction and Scattering

SPION	Superparamagnetic Iron Oxide Nanoparticle
s-SNOM	Scattering-type Scanning Near-Field Optical Microscopy
STEM	Scanning Transmission Electron Microscopy
STM	Scanning Tunnelling Microscopy
STXM	Scanning Transmission X-ray Microscopy
TEM	Transmission Electron Microscopy
TERS	Tip-Enhanced Raman Scattering
TGA	Thermogravimetric Analysis
ToF-SIMS	Time-of-flight secondary ion mass spectrometry
TRPS	Tunable Resistive Pulse Sensing
TXM	Transmission X-ray Microscopy
UiO	Universitetet i Oslo
UV-Vis	Ultraviolet-visible Spectrophotometry
XANES	X-ray Absorption Near-Edge Structure
XAS	X-ray Absorption Spectroscopy
XPS	X-ray Photoelectron Spectroscopy
XRD	X-Ray Diffraction
XFM	X-ray Fluorescence Microscopy
XRF	X-Ray Fluorescence spectroscopy
ZIF	Zeolite imidazolate framework
ZSM	Zeolite Socony Mobil

REFERENCES

[1] Z. Zhao, A. Ukidve, V. Krishnan, S. Mitragotri, *Adv. Drug Deliv. Rev.* **2019**, *143*, 3.

[2] J.B. Finean, M.G. Rumsby, *Nature* **1963**, *200*, 1340.

[3] D.J.A. Crommelin, P. van Hoogevest, G. Storm, *J. Controlled Release* **2020**, *318*, 256.

[4] A.C. Anselmo, S. Mitragotri, *Bioeng. Transl. Med.* **2019**, *4*, e10143.

[5] A.-A.D. Jones, G. Mi, T.J. Webster, *Trends Biotechnol.* **2019**, *37*, 117.

[6] *Nat. Nanotechnol.* **2020**, *15*, 963.

[7] E. Sánchez-López, D. Gomes, G. Esteruelas, L. Bonilla, A.L. Lopez-Machado, R. Galindo, A. Cano, M. Espina, M. Ettcheto, A. Camins, A.M. Silva, A. Durazzo, A. Santini, M.L. Garcia, E.B. Souto, *Nanomaterials* **2020**, *10*, 292.

[8] X. Li, E. Porcel, M. Menendez-Miranda, J. Qiu, X. Yang, C. Serre, A. Pastor, D. Desmaële, S. Lacombe, R. Gref, *ChemMedChem* **2020**, *15*, 274.

[9] H. Sharma, P.K. Mishra, S. Talegaonkar, B. Vaidya, *Drug Discov. Today* **2015**, *20*, 1143.

[10] P. Horcajada, T. Chalati, C. Serre, B. Gillet, C. Sebrie, T. Baati, J.F. Eubank, D. Heurtaux, P. Clayette, C. Kreuz, J.-S. Chang, Y.K. Hwang, V. Marsaud, P.-N. Bories, L. Cynober, S. Gil, G. Férey, P. Couvreur, R. Gref, *Nat. Mater.* **2010**, *9*, 172.

[11] A. Ahmad, F. Khan, R.K. Mishra, R. Khan, *J. Med. Chem.* **2019**, *62*, 10475.

[12] R. Gref, A. Domb, P. Quellec, T. Blunk, R.H. Müller, J.M. Verbavatz, R. Langer, *Adv. Drug Deliv. Rev.* **2012**, *64*, 316.

[13] O. Harush-Frenkel, E. Rozentur, S. Benita, Y. Altschuler, *Biomacromolecules* **2008**, *9*, 435.

[14] N. Oh, J.-H. Park, *Int. J. Nanomedicine* **2014**, *9 Suppl 1*, 51.

[15] R.A. Petros, J.M. DeSimone, *Nat. Rev. Drug Discov.* **2010**, *9*, 615.

[16] E. Hinde, K. Thammasiraphop, H.T.T. Duong, J. Yeow, B. Karagoz, C. Boyer, J.J. Gooding, K. Gaus, *Nat. Nanotechnol.* **2017**, *12*, 81.

[17] J. Panyam, V. Labhasetwar, *Adv. Drug Deliv. Rev.* **2003**, *55*, 329.

[18] S.K. Sahoo, J. Panyam, S. Prabha, V. Labhasetwar, *J. Controlled Release* **2002**, *82*, 105.

[19] R. Kalluru, F. Fenaroli, D. Westmoreland, L. Ulanova, A. Maleki, N. Roos, M.P. Madsen, G. Koster, W. Egge-Jacobsen, S. Wilson, H. Roberg-Larsen, G.K. Khuller, A. Singh, B. Nyström, G. Griffiths, *J. Cell Sci.* **2013**, *126*, 3043.

[20] C. He, K. Lu, W. Lin, *J. Am. Chem. Soc.* **2014**, *136*, 12253.

[21] D. Hofmann, S. Tenzer, M.B. Bannwarth, C. Messerschmidt, S.-F. Glaser, H. Schild, K. Landfester, V. Mailänder, *ACS Nano* **2014**, *8*, 10077.

[22] M. Calero, M. Chiappi, A. Lazaro-Carrillo, M.J. Rodríguez, F.J. Chichón, K. Crosbie-Staunton, A. Prina-Mello, Y. Volkov, A. Villanueva, J.L. Carrascosa, *J. Nanobiotechnology* **2015**, *13*, 16.

[23] J.W. Wills, H.D. Summers, N. Hondow, A. Sooresh, K.E. Meissner, P.A. White, P. Rees, A. Brown, S.H. Doak, *ACS Nano* **2017**, *11*, 11986.

[24] Z. Shen, J. Song, Z. Zhou, B.C. Yung, M.A. Aronova, Y. Li, Y. Dai, W. Fan, Y. Liu, Z. Li, H. Ruan, R.D. Leapman, L. Lin, G. Niu, X. Chen, A. Wu, *Adv. Mater.* **2018**, *30*, 1803163.

[25] D. Duchêne, R. Gref, *Int. J. Pharm.* **2016**, *502*, 219.

[26] V. Klang, C. Valenta, N.B. Matsko, *Micron* **2013**, *44*, 45.

[27] J. Kuntsche, J.C. Horst, H. Bunjes, *Int. J. Pharm.* **2011**, *417*, 120.

[28] E. Manaia, B. Chiari-Andréo, B. Silva, J. Oshiro Junior, L. Chiavacci, *Int J Nanomedicine* **2017**, *12*, 4991.

[29] A. Brown, N. Hondow, in *Front. Nanosci.* (Ed: H. Summers), Elsevier**2013**, 95.

[30] M. Reifarth, S. Hoeppener, U.S. Schubert, *Adv. Mater.* **2018**, *30*, 1703704.

[31] S. Wang, C.M. McGuirk, M.B. Ross, S. Wang, P. Chen, H. Xing, Y. Liu, C.A. Mirkin, *J. Am. Chem. Soc.* **2017**, *139*, 9827.

[32] D. Niu, Z. Liu, Y. Li, X. Luo, J. Zhang, J. Gong, J. Shi, *Adv. Mater.* **2014**, *26*, 4947.

[33] K.A. Eid, H.M. Azzazy, *Int. J. Nanomedicine* **2012**, *7*, 1543.

[34] N. Ž. Knežević, J.-O. Durand, *Nanoscale* **2015**, *7*, 2199.

[35] Q. He, J. Shi, F. Chen, M. Zhu, L. Zhang, *Biomaterials* **2010**, *31*, 3335.

[36] H. Li, H. Yu, C. Zhu, J. Hu, M. Du, F. Zhang, D. Yang, *RSC Adv.* **2016**, *6*, 94160.

[37] J.R. Morones, J.L. Elechiguerra, A. Camacho, K. Holt, J.B. Kouri, J.T. Ramírez, M.J. Yacaman, *Nanotechnology* **2005**, *16*, 2346.

[38] N.Q. Yin, P. Wu, T.H. Yang, M. Wang, *RSC Adv.* **2017**, *7*, 9123.

[39] J. Hitchcock, A.L. White, N. Hondow, T.A. Hughes, H. Dupont, S. Biggs, O.J. Cayre, *J. Colloid Interface Sci.* **2020**, *567*, 171.

[40] R. Mahugo, A. Mayoral, M. Sánchez-Sánchez, I. Diaz, *Front. Chem.* **2019**, *7*.

[41] A. Fondell, K. Edwards, L.M. Ickenstein, S. Sjöberg, J. Carlsson, L. Gedda, *Eur. J. Nucl. Med. Mol. Imaging* **2009**, *37*, 114.

[42] A. Gloter, V. Badjeck, L. Bocher, N. Brun, K. March, M. Marinova, M. Tencé, M. Walls, A. Zobelli, O. Stéphan, C. Colliex, *Mater. Sci. Semicond. Process.* **2017**, *65*, 2.

[43] L.L. Félix, B. Sanz, V. Sebastián, T.E. Torres, M.H. Sousa, J. a. H. Coaquira, M.R. Ibarra, G.F. Goya, *Sci. Rep.* **2019**, *9*, 1.

[44] P. Brüggeller, E. Mayer, *Nature* **1980**, *288*, 569.

[45] J. Dubochet, A.W. McDowall, *J. Microsc.* **1981**, *124*, 3.

[46] D. Danino, *Curr. Opin. Colloid Interface Sci.* **2012**, *17*, 316.

[47] H. Friedrich, P.M. Frederik, G. de With, N.A.J.M. Sommerdijk, *Angew. Chem. Int. Ed.* **2010**, *49*, 7850.

[48] V. Lučić, A. Rigort, W. Baumeister, *J. Cell Biol.* **2013**, *202*, 407.

[49] R.F. Thompson, M. Walker, C.A. Siebert, S.P. Muench, N.A. Ranson, *Methods* **2016**, *100*, 3.

[50] L.M. Ickenstein, M.C. Sandström, L.D. Mayer, K. Edwards, *Biochim. Biophys. Acta BBA - Biomembr.* **2006**, *1758*, 171.

[51] J. Barauskas, A. Misiunas, T. Gunnarsson, F. Tiberg, M. Johnsson, *Langmuir* **2006**, *22*, 6328.

[52] R.I. Koning, A.J. Koster, T.H. Sharp, *Ann. Anat. - Anat. Anz.* **2018**, *217*, 82.

[53] Y. Cheng, *Cell* **2015**, *161*, 450.

[54] R. Fernandez-Leiro, S.H.W. Scheres, *Nature* **2016**, *537*, 339.

[55] K.R. Vinothkumar, R. Henderson, *Q. Rev. Biophys.* **2016**, *49*.

[56] K. Murata, M. Wolf, *Biochim. Biophys. Acta BBA - Gen. Subj.* **2018**, *1862*, 324.

[57] P.L. Stewart, *WIREs Nanomedicine Nanobiotechnology* **2017**, *9*, e1417.

[58] S. Guo, M. Vieweger, K. Zhang, H. Yin, H. Wang, X. Li, S. Li, S. Hu, A. Sparreboom, B.M. Evers, Y. Dong, W. Chiu, P. Guo, *Nat. Commun.* **2020**, *11*, 1.

[59] H. Azhari, M. Strauss, S. Hook, B.J. Boyd, S.B. Rizwan, *Eur. J. Pharm. Biopharm.* **2016**, *104*, 148.

[60] J.S. Lengyel, J.L. Milne, S. Subramaniam, *Nanomed.* **2008**, *3*, 125.

[61] C. Bonnaud, C.A. Monnier, D. Demurtas, C. Jud, D. Vanhecke, X. Montet, R. Hovius, M. Lattuada, B. Rothen-Rutishauser, A. Petri-Fink, *ACS Nano* **2014**, *8*, 3451.

[62] O. Le Bihan, P. Bonnafous, L. Marak, T. Bickel, S. Trépout, S. Mornet, F. De Haas, H. Talbot, J.-C. Taveau, O. Lambert, *J. Struct. Biol.* **2009**, *168*, 419.

[63] P. Ercius, O. Alaidi, M.J. Rames, G. Ren, *Adv. Mater.* **2015**, *27*, 5638.

[64] A. Balfourier, N. Luciani, G. Wang, G. Lelong, O. Ersen, A. Khelfa, D. Alloyeau, F. Gazeau, F. Carn, *Proc. Natl. Acad. Sci.* **2020**, *117*, 103.

[65] A. Guven, I.A. Rusakova, M.T. Lewis, L.J. Wilson, *Biomaterials* **2012**, *33*, 1455.

[66] C. Hoskins, Y. Min, M. Gueorguieva, C. McDougall, A. Volovick, P. Prentice, Z. Wang, A. Melzer, A. Cuschieri, L. Wang, *J. Nanobiotechnology* **2012**, *10*, 27.

[67] R. Leapman, in *Transm. Electron Energy Loss Spectrom. Mater. Sci. EELS Atlas*, John Wiley & Sons, Ltd**2005**, 49.

[68] S. Ristig, O. Prymak, K. Loza, M. Gocyla, W. Meyer-Zaika, M. Heggen, D. Raabe, M. Epple, *J. Mater. Chem. B* **2015**, *3*, 4654.

[69] B. Shen, X. Chen, D. Cai, H. Xiong, X. Liu, C. Meng, Y. Han, F. Wei, *Adv. Mater.* **2019**, *32*, 1906103.

[70] L.H. Bryant, S.J. Kim, M. Hobson, B. Milo, Z.I. Kovacs, N. Jikaria, B.K. Lewis, M.A. Aronova, A.A. Sousa, G. Zhang, R.D. Leapman, J.A. Frank, *Nanomedicine Nanotechnol. Biol. Med.* **2017**, *13*, 503.

[71] A.-V. Weiss, M. Koch, M. Schneider, *Int. J. Pharm.* **2019**, *570*, 118650.

[72] L.C. Gontard, A. Fernández, R.E. Dunin-Borkowski, T. Kasama, S. Lozano-Pérez, S. Lucas, *Micron* **2014**, *67*, 1.

[73] A.M. Schrand, J.J. Schlager, L. Dai, S.M. Hussain, *Nat. Protoc.* **2010**, *5*, 744.

[74] R. Di Corato, A. Espinosa, L. Lartigue, M. Tharaud, S. Chat, T. Pellegrino, C. Ménager, F. Gazeau, C. Wilhelm, *Biomaterials* **2014**, *35*, 6400.

[75] X. Li, N. Semiramoth, S. Hall, V. Tafani, J. Josse, F. Laurent, G. Salzano, D. Foulkes, P. Brodin, L. Majlessi, N.-E. Ghermani, G. Maurin, P. Couvreur, C. Serre, M.-F. Bernet-Camard, J. Zhang, R. Gref, *Part. Part. Syst. Charact.* **2019**, *36*, 1800360.

[76] K.L. Mcdonald, *J. Microsc.* **2009**, *235*, 273.

[77] A.-K. Barthel, M. Dass, M. Dröge, J.-M. Cramer, D. Baumann, M. Urban, K. Landfester, V. Mailänder, I. Lieberwirth, *Beilstein J. Nanotechnol.* **2014**, *5*, 1905.

[78] N. Singh, G.J.S. Jenkins, B.C. Nelson, B.J. Marquis, T.G.G. Maffeis, A.P. Brown, P.M. Williams, C.J. Wright, S.H. Doak, *Biomaterials* **2012**, *33*, 163.

[79] E. Allard-Vannier, K. Hervé-Aubert, K. Kaaki, T. Blondy, A. Shebanova, K.V. Shaitan, A.A. Ignatova, M.-L. Saboungi, A.V. Feofanov, I. Chourpa, *Biochim. Biophys. Acta BBA - Gen. Subj.* **2017**, *1861*, 1578.

[80] C. Gay, E. Letavernier, M.-C. Verpont, M. Walls, D. Bazin, M. Daudon, N. Nassif, O. Stéphan, M. de Frutos, *ACS Nano* **2020**, *14*, 1823.

[81] I. Cabezón, E. Augé, M. Bosch, A.J. Beckett, I.A. Prior, C. Pelegrí, J. Vilaplana, *Histochem. Cell Biol.* **2017**, *148*, 3.

[82] V. Mollo, P. Scognamiglio, A. Marino, G. Ciofani, F. Santoro, *Adv. Mater. Technol.* **2020**, *5*, 1900687.

[83] P.K. Hansma, J. Tersoff, *J. Appl. Phys.* **1987**, *61*, R1.

[84] A. Rodríguez-Galván, O. Amelines-Sarria, M. Rivera, M. del P. Carreón-Castro, V.A. Basiuk, *Nano* **2016**.

[85] S. Sadaf, L. Walder, *Adv. Mater. Interfaces* **2017**, *4*.

[86] D.A. Yarotski, S.V. Kilina, A.A. Talin, S. Tretiak, O.V. Prezhdo, A.V. Balatsky, A.J. Taylor, *Nano Lett.* **2009**, *9*, 12.

[87] C.J. Fleming, Y.X. Liu, Z. Deng, G. Liu, *J. Phys. Chem. A* **2009**, *113*, 4168.

[88] C.J. Fleming, N.-N. Yin, S.L. Riechers, G. Chu, G. Liu, *ACS Nano* **2011**, *5*, 1685.

[89] S. Riechers, Q. Zhong, N.-N. Yin, A. Karsai, S.R.P. da Rocha, G. Liu, *J. Drug Deliv.* **2015**, *2015*.

[90] L. Shi, C.J. Fleming, S.L. Riechers, N.-N. Yin, J. Luo, K.S. Lam, G. Liu, *J. Drug Deliv.* **2011**, *2011*.

[91] P. Eaton, P. West, *Atomic Force Microscopy*, Oxford University Press, Oxford, New York **2010**.

[92] R. Gref, Y. Minamitake, M.T. Peracchia, V. Trubetskoy, V. Torchilin, R. Langer, *Science* **1994**, *263*, 1600.

[93] J.R. Smith, T.O.B. Olusanya, D.A. Lamprou, *Expert Opin. Drug Deliv.* **2018**, *15*, 1211.

[94] M.N.V. Ravi Kumar, U. Bakowsky, C.M. Lehr, *Biomaterials* **2004**, *25*, 1771.

[95] S. Sharma, H.I. Rasool, V. Palanisamy, C. Mathisen, M. Schmidt, D.T. Wong, J.K. Gimzewski, *ACS Nano* **2010**, *4*, 1921.

[96] Y. M. Efremov, T. Okajima, A. Raman, *Soft Matter* **2020**, *16*, 64.

[97] A. zur Mühlen, E. zur Mühlen, H. Niehus, W. Mehnert, *Pharm. Res.* **1996**, *13*, 1411.

[98] D.A. Lamprou, V. Venkatpurwar, M.N.V.R. Kumar, *PLOS ONE* **2013**, *8*, e64490.

[99] Y.F. Dufrêne, T. Ando, R. Garcia, D. Alsteens, D. Martinez-Martin, A. Engel, C. Gerber, D.J. Müller, *Nat. Nanotechnol.* **2017**, *12*, 295.

[100] L. Urbina, A. Eceiza, N. Gabilondo, M.Á. Corcuera, A. Retegi, *Int. J. Biol. Macromol.* **2020**, *163*, 1249.

[101] H. Lee, Y. Hong, D. Lee, S. Hwang, G. Lee, J. Yang, D.S. Yoon, *Nanotechnology* **2020**, *31*, 215706.

[102] A. Rodzinski, R. Guduru, P. Liang, A. Hadjikhani, T. Stewart, E. Stimphil, C. Runowicz, R. Cote, N. Altman, R. Datar, S. Khizroev, *Sci. Rep.* **2016**, *6*, 20867.

[103] C. Dong, S. Corsetti, D. Passeri, M. Rossi, M. Carafa, F. Pantanella, F. Rinaldi, C. Ingallina, A. Sorbo, C. Marianecci, *AIP Conf. Proc.* **2015**, *1667*, 020011.

[104] D. Passeri, C. Dong, M. Reggente, L. Angeloni, M. Barteri, F.A. Scaramuzzo, F.D. Angelis, F. Marinelli, F. Antonelli, F. Rinaldi, C. Marianecci, M. Carafa, A. Sorbo, D. Sordi, I.W. Arends, M. Rossi, *Biomatter* **2014**, *4*, e29507.

[105] H. Shen, D. Long, L. Zhu, X.-Y. Li, Y. Dong, N. Jia, H. Zhou, X. Xin, Y. Sun, *Biophys. Chem.* **2006**, *122*, 1.

[106] Z. Wang, A. Cuschieri, *Int. J. Mol. Sci.* **2013**, *14*, 9111.

[107] Y. Zhang, M. Yang, M. Ozkan, C.S. Ozkan, *Biotechnol. Prog.* **2009**, *25*, 923.

[108] G. Pyrgiotakis, C.O. Blattmann, P. Demokritou, *ACS Sustain. Chem. Eng.* **2014**, *2*, 1681.

[109] Y. Dror, R. Sorkin, G. Brand, O. Boubriak, J. Urban, J. Klein, *Sci. Rep.* **2017**, *7*, 45758.
[110] A. Centrone, *Annu. Rev. Anal. Chem.* **2015**, *8*, 101.
[111] R.J. Hermann, M.J. Gordon, *Annu. Rev. Chem. Biomol. Eng.* **2018**, *9*, 365.
[112] X. Chen, D. Hu, R. Mescall, G. You, D.N. Basov, Q. Dai, M. Liu, *Adv. Mater.* **2019**, *31*, 1804774.
[113] Z. Nuño, B. Hessler, J. Ochoa, Y.-S. Shon, C. Bonney, Y. Abate, *Opt. Express* **2011**, *19*, 20865.
[114] D. Kurouski, A. Dazzi, R. Zenobi, A. Centrone, *Chem. Soc. Rev.* **2020**, *49*, 3315.
[115] M. Ashtikar, L. Langelüddecke, A. Fahr, V. Deckert, *Biochim. Biophys. Acta BBA - Gen. Subj.* **2017**, *1861*, 2630.
[116] I. Amenabar, S. Poly, M. Goikoetxea, W. Nuansing, P. Lasch, R. Hillenbrand, *Nat. Commun.* **2017**, *8*, 14402.
[117] L.B. Capeletti, J.F.A. de Oliveira, L.M.D. Loiola, F.E. Galdino, D.E. da S. Santos, T.A. Soares, R. de O. Freitas, M.B. Cardoso, *Adv. Funct. Mater.* **2019**, *29*, 1904216.
[118] A. Dazzi, R. Prazeres, F. Glotin, J.M. Ortega, *Opt. Lett.* **2005**, *30*, 2388.
[119] A. Dazzi, F. Glotin, R. Carminati, *J. Appl. Phys.* **2010**, *107*, 124519.
[120] H. Zhou, Y. Tang, S. Zhang, in *Smart Nanocontainers* (Eds: P. Nguyen-Tri, T.-O. Do, T.A. Nguyen), Elsevier**2020**, 7.
[121] J. Mathurin, E. Pancani, A. Deniset-Besseau, K. Kjoller, C.B. Prater, R. Gref, A. Dazzi, *The Analyst* **2018**, *143*, 5940.
[122] K. Wieland, G. Ramer, V.U. Weiss, G. Allmaier, B. Lendl, A. Centrone, *Nano Res.* **2019**, *12*, 197.
[123] D. Khanal, I. Khatib, J. Ruan, D. Cipolla, F. Dayton, J.D. Blanchard, H.-K. Chan, W. Chrzanowski, *Anal. Chem.* **2020**, *92*, 9922.
[124] N. Piergies, E. Pięta, C. Paluszkiewicz, H. Domin, W.M. Kwiatek, *Nano Res.* **2018**, *11*, 4401.
[125] E. Pięta, C. Paluszkiewicz, W.M. Kwiatek, *Phys. Chem. Chem. Phys.* **2018**, *20*, 27992.
[126] N. Piergies, A. Dazzi, A. Deniset-Besseau, J. Mathurin, M. Oćwieja, C. Paluszkiewicz, W.M. Kwiatek, *Nano Res.* **2020**, *13*, 1020.
[127] N. Piergies, M. Oćwieja, C. Paluszkiewicz, W.M. Kwiatek, *Appl. Surf. Sci.* **2021**, *537*, 147897.
[128] E. Pięta, C. Petibois, C. Paluszkiewicz, W.M. Kwiatek, *Appl. Surf. Sci.* **2020**, *499*, 143975.
[129] E. Pancani, J. Mathurin, S. Bilent, M.-F. Bernet-Camard, A. Dazzi, A. Deniset-Besseau, R. Gref, *Part. Part. Syst. Charact.* **2018**, *35*, 1700457.
[130] K. Kemel, A. Deniset-Besseau, A. Baillet-Guffroy, V. Faivre, A. Dazzi, C. Laugel, *Int. J. Pharm.* **2020**, *579*, 119193.
[131] J. Stetefeld, S.A. McKenna, T.R. Patel, *Biophys. Rev.* **2016**, *8*, 409.
[132] B. Carr, M. Wright, **n.d.**, 33.
[133] V. Filipe, A. Hawe, W. Jiskoot, *Pharm. Res.* **2010**, *27*, 796.
[134] M. a. C. Potenza, T. Sanvito, S. Argentiere, C. Cella, B. Paroli, C. Lenardi, P. Milani, *Sci. Rep.* **2015**, *5*, 18228.
[135] T. Sanvito, P. Bigini, M.V. Cavanna, F. Fiordaliso, M.B. Violatto, L. Talamini, M. Salmona, P. Milani, M.A.C. Potenza, *Nanomedicine Nanotechnol. Biol. Med.* **2017**, *13*, 2597.
[136] M.A. C. Potenza, Ž. Krpetić, T. Sanvito, Q. Cai, M. Monopoli, J.M. de Araújo, C. Cella, L. Boselli, V. Castagnola, P. Milani, K. A. Dawson, *Nanoscale* **2017**, *9*, 2778.
[137] Y. Pei, R. Vogel, C. Minelli, in *Charact. Nanoparticles* (Eds: V.-D. Hodoroaba, W.E.S. Unger, A.G. Shard), Elsevier**2020**, 117.
[138] A. Sikora, A.G. Shard, C. Minelli, *Langmuir* **2016**, *32*, 2216.
[139] C. Colliex, *Comptes Rendus Phys.* **2019**, *20*, 746.
[140] M.T. Proetto, C.R. Anderton, D. Hu, C.J. Szymanski, Z. Zhu, J.P. Patterson, J.K. Kammeyer, L.G. Nilewski, A.M. Rush, N.C. Bell, J.E. Evans, G. Orr, S.B. Howell, N.C. Gianneschi, *ACS Nano* **2016**, *10*, 4046.
[141] I. Lozić, R.V. Hartz, C.A. Bartlett, J.A. Shaw, M. Archer, P.S.R. Naidu, N.M. Smith, S.A. Dunlop, K.S. Iyer, M.R. Kilburn, M. Fitzgerald, *Biomaterials* **2016**, *74*, 200.
[142] P.J. Kempen, C. Hitzman, L.S. Sasportas, S.S. Gambhir, R. Sinclair, *MRS Online Proc. Libr. OPL* **2013**, *1569*, 157.

[143] J. Neunzehn, F. Draude, U. Golla-Schindler, H.F. Arlinghaus, H.-P. Wiesmann, *Surf. Interface Anal.* **2013**, *45*, 1340.
[144] A.V. Singh, H. Jungnickel, L. Leibrock, J. Tentschert, P. Reichardt, A. Katz, P. Laux, A. Luch, *Sci. Rep.* **2020**, *10*, 261.
[145] M.W. Westneat, J.J. Socha, W.-K. Lee, *Annu. Rev. Physiol.* **2008**, *70*, 119.
[146] H.A. Castillo-Michel, C. Larue, A.E. Pradas del Real, M. Cotte, G. Sarret, *Plant Physiol. Biochem.* **2017**, *110*, 13.
[147] A.P. Hitchcock, *J. Electron Spectrosc. Relat. Phenom.* **2015**, *200*, 49.
[148] M. Holt, R. Harder, R. Winarski, V. Rose, *Annu. Rev. Mater. Res.* **2013**, *43*, 183.
[149] C.M. Graf, M.C. Meinke, Q. Gao, S. Hadam, J. Raabe, W.S. M.d, U. Blume-Peytavi, J.M. Lademann, E. Ruhl, A. Vogt, *J. Biomed. Opt.* **2009**, *14*, 021015.
[150] C. Graf, D. Nordmeyer, S. Ahlberg, J. Raabe, A. Vogt, J. Lademann, F. Rancan, E. Rühl, in *Colloidal Nanoparticles Biomed. Appl. X*, International Society For Optics And Photonics**2015**, 93381L.
[151] T. Paunesku, S. Vogt, B. Lai, J. Maser, N. Stojićević, K.T. Thurn, C. Osipo, H. Liu, D. Legnini, Z. Wang, C. Lee, G.E. Woloschak, *Nano Lett.* **2007**, *7*, 596.
[152] T. Liu, I. Kempson, M. de Jonge, D.L. Howard, B. Thierry, *Nanoscale* **2014**, *6*, 9774.
[153] B. Luan, T. Friedrich, J. Zhai, V.A. Streltsov, B.W. Lindsey, J. Kaslin, M.D. de Jonge, J. Zhu, T.C. Hughes, X. Hao, *RSC Adv.* **2016**, *6*, 23550.
[154] L. Pascolo, B. Bortot, N. Benseny-Cases, A. Gianoncelli, G. Tosi, B. Ruozi, C. Rizzardi, E. De Martino, M.A. Vandelli, G.M. Severini, *Int. J. Nanomedicine* **2014**, *9*, 2791.
[155] A. Gianoncelli, R. Delfino, S. Sala, G. Kourousias, S. Giordani, F. Romano, G. Ricci, L. Pascolo, *Nucl. Instrum. Methods Phys. Res. Sect. B Beam Interact. Mater. At.* **2020**, *465*, 79.
[156] F. Cammisuli, S. Giordani, A. Gianoncelli, C. Rizzardi, L. Radillo, M. Zweyer, T. Da Ros, M. Salomé, M. Melato, L. Pascolo, *Sci. Rep.* **2018**, *8*, 706.
[157] A. Gianoncelli, F. Cammisuli, M. Altissimo, M. Salomé, O. Radillo, G. Ricci, S. Giordani, C. Rizzardi, L. Pascolo, *X-Ray Spectrom.* **2019**, *48*, 413.
[158] P. Marmorato, G. Ceccone, A. Gianoncelli, L. Pascolo, J. Ponti, F. Rossi, M. Salomé, B. Kaulich, M. Kiskinova, *Toxicol. Lett.* **2011**, *207*, 128.
[159] A. Gianoncelli, P. Marmorato, J. Ponti, L. Pascolo, B. Kaulich, C. Uboldi, F. Rossi, D. Makovec, M. Kiskinova, G. Ceccone, *X-Ray Spectrom.* **2013**, *42*, 316.
[160] A. Procopio, C. Cappadone, N. Zaccheroni, E. Malucelli, L. Merolle, A. Gianoncelli, A. Sargenti, G. Farruggia, F. Palomba, E. Rampazzo, S. Rapino, L. Prodi, S. Iotti, *Talanta* **2019**, *202*, 251.
[161] D. Kwon, H.W. Nho, T.H. Yoon, *J. Nanosci. Nanotechnol.* **2015**, *15*, 4229.
[162] D. Kwon, H.W. Nho, T.H. Yoon, *Colloids Surf. B Biointerfaces* **2014**, *122*, 384.
[163] K. Yamamoto, A. Klossek, R. Flesch, T. Ohigashi, E. Fleige, F. Rancan, J. Frombach, A. Vogt, U. Blume-Peytavi, P. Schrade, S. Bachmann, R. Haag, S. Hedtrich, M. Schäfer-Korting, N. Kosugi, E. Rühl, *J. Controlled Release* **2016**, *242*, 64.
[164] S. Matsuyama, K. Maeshima, M. Shimura, *J. Anal. At. Spectrom.* **2020**, *35*, 1279.
[165] B.D. Samber, E. Meul, B. Laforce, B.D. Paepe, J. Smet, M.D. Bruyne, R.D. Rycke, S. Bohic, P. Cloetens, R.V. Coster, P. Vandenabeele, T.V. Berghe, *PLOS ONE* **2018**, *13*, e0190495.
[166] K. Stachnik, M. Warmer, I. Mohacsi, V. Hennicke, P. Fischer, J. Meyer, T. Spitzbart, M. Barthelmess, J. Eich, C. David, C. Feldmann, B. Busse, K. Jähn, U.E. Schaible, A. Meents, *Sci. Rep.* **2020**, *10*, 1784.
[167] S. Yao, J. Fan, Z. Chen, Y. Zong, J. Zhang, Z. Sun, L. Zhang, R. Tai, Z. Liu, C. Chen, H. Jiang, *IUCrJ* **2018**, *5*, 141.
[168] M. Gallagher-Jones, C.S.B. Dias, A. Pryor, K. Bouchmella, L. Zhao, Y.H. Lo, M.B. Cardoso, D. Shapiro, J. Rodriguez, J. Miao, *Sci. Rep.* **2017**, *7*, 4757.
[169] R. Carzaniga, M.-C. Domart, L.M. Collinson, E. Duke, *Protoplasma* **2014**, *251*, 449.
[170] D. Drescher, T. Büchner, P. Guttmann, S. Werner, G. Schneider, J. Kneipp, *Nanoscale Adv.* **2019**, *1*, 2937.
[171] B. Kepsutlu, V. Wycisk, K. Achazi, S. Kapishnikov, A.J. Pérez-Berná, P. Guttmann, A. Cossmer, E. Pereiro, H. Ewers, M. Ballauff, G. Schneider, J.G. McNally, *ACS Nano* **2020**.

[172] S. Gil, E. Solano, F. Martínez-Trucharte, J. Martínez-Esaín, A.J. Pérez-Berná, J.J. Conesa, C. Kamma-Lorger, M. Alsina, M. Sabés, *PLOS ONE* **2020**, *15*, e0230022.

[173] P. Reineck, A.N. Abraham, A. Poddar, R. Shukla, H. Abe, T. Ohshima, B.C. Gibson, C. Dekiwadia, J.J. Conesa, E. Pereiro, A. Gelmi, G. Bryant, *Biotechnol. J.* **n.d.**, *n/a*, 2000289.

[174] M. Chiappi, J.J. Conesa, E. Pereiro, C.O.S. Sorzano, M.J. Rodríguez, K. Henzler, G. Schneider, F.J. Chichón, J.L. Carrascosa, *J. Nanobiotechnology* **2016**, *14*, 15.

[175] A. Poddar, J.J. Conesa, K. Liang, S. Dhakal, P. Reineck, G. Bryant, E. Pereiro, R. Ricco, H. Amenitsch, C. Doonan, X. Mulet, C.M. Doherty, P. Falcaro, R. Shukla, *Small* **2019**, *15*, 1902268.

[176] J.J. Conesa, J. Otón, M. Chiappi, J.M. Carazo, E. Pereiro, F.J. Chichón, J.L. Carrascosa, *Sci. Rep.* **2016**, *6*, 22354.

[177] D. Drescher, P. Guttmann, T. Büchner, S. Werner, G. Laube, A. Hornemann, B. Tarek, G. Schneider, J. Kneipp, *Nanoscale* **2013**, *5*, 9193.

[178] G.P. Szekeres, S. Werner, P. Guttmann, C. Spedalieri, D. Drescher, V. Živanović, M. Montes-Bayón, J. Bettmer, J. Kneipp, *Nanoscale* **2020**, *12*, 17450.

[179] Y. Zhu, X. Cai, J. Li, Z. Zhong, Q. Huang, C. Fan, *Nanomedicine Nanotechnol. Biol. Med.* **2014**, *10*, 515.

[180] A. Kim, W.B. Ng, W. Bernt, N.-J. Cho, *Sci. Rep.* **2019**, *9*, 2639.

[181] C.M. Maguire, M. Rösslein, P. Wick, A. Prina-Mello, *Sci. Technol. Adv. Mater.* **2018**, *19*, 732.

[182] L. Zhang, D. Lei, J.M. Smith, M. Zhang, H. Tong, X. Zhang, Z. Lu, J. Liu, A.P. Alivisatos, G. Ren, *Nat. Commun.* **2016**, *7*, 11083.

[183] A.F. Ogata, A.M. Rakowski, B.P. Carpenter, D.A. Fishman, J.G. Merham, P.J. Hurst, J.P. Patterson, *J. Am. Chem. Soc.* **2020**, *142*, 1433.

[184] E. Yücelen, I. Lazić, E.G.T. Bosch, *Sci. Rep.* **2018**, *8*, 2676.

[185] B. Shen, X. Chen, K. Shen, H. Xiong, F. Wei, *Nat. Commun.* **2020**, *11*, 2692.

[186] Y. Zhou, X. Xu, A. Carlsson, S. Lazar, Z. Pan, Y. Ma, O. Terasaki, H. Deng, *Chem. Mater.* **2020**, *32*, 4966.

[187] S.-Y. Chen, A. Gloter, A. Zobelli, L. Wang, C.-H. Chen, C. Colliex, *Phys. Rev. B* **2009**, *79*, 104103.

[188] T. Hidalgo, M. Giménez-Marqués, E. Bellido, J. Avila, M.C. Asensio, F. Salles, M.V. Lozano, M. Guillevic, R. Simón-Vázquez, A. González-Fernández, C. Serre, M.J. Alonso, P. Horcajada, *Sci. Rep.* **2017**, *7*, 43099.

[189] S.C.B. Myneni, *Rev. Mineral. Geochem.* **2002**, *49*, 485.

[190] A.E. Goode, A.E. Porter, M.P. Ryan, D.W. McComb, *Nanoscale* **2015**, *7*, 1534.

[191] D.A. Shapiro, S. Babin, R.S. Celestre, W. Chao, R.P. Conley, P. Denes, B. Enders, P. Enfedaque, S. James, J.M. Joseph, H. Krishnan, S. Marchesini, K. Muriki, K. Nowrouzi, S.R. Oh, H. Padmore, T. Warwick, L. Yang, V.V. Yashchuk, Y.-S. Yu, J. Zhao, *Sci. Adv.* **2020**, *6*, eabc4904.

[192] O.L. Krivanek, N. Dellby, J.A. Hachtel, J.-C. Idrobo, M.T. Hotz, B. Plotkin-Swing, N.J. Bacon, A.L. Bleloch, G.J. Corbin, M.V. Hoffman, C.E. Meyer, T.C. Lovejoy, *Ultramicroscopy* **2019**, *203*, 60.

[193] L.K. Scheffer, C.S. Xu, M. Januszewski, Z. Lu, S. Takemura, K.J. Hayworth, G.B. Huang, K. Shinomiya, J. Maitin-Shepard, S. Berg, J. Clements, P. Hubbard, W. Katz, L. Umayam, T. Zhao, D. Ackerman, T. Blakely, J. Bogovic, T. Dolafi, D. Kainmueller, T. Kawase, K.A. Khairy, L. Leavitt, P.H. Li, L. Lindsey, N. Neubarth, D.J. Olbris, H. Otsuna, E.T. Trautman, M. Ito, J. Goldammer, T. Wolff, R. Svirskas, P. Schlegel, E.R. Neace, C.J. Knecht, C.X. Alvarado, D.A. Bailey, S. Ballinger, J.A. Borycz, B.S. Canino, N. Cheatham, M. Cook, M. Dreher, O. Duclos, B. Eubanks, K. Fairbanks, S. Finley, N. Forknall, A. Francis, G.P. Hopkins, E.M. Joyce, S. Kim, N.A. Kirk, J. Kovalyak, S.A. Lauchie, A. Lohff, C. Maldonado, E.A. Manley, S. McLin, C. Mooney, M. Ndama, O. Ogundeyi, N. Okeoma, C. Ordish, N. Padilla, C. Patrick, T. Paterson, E.E. Phillips, E.M. Phillips, N. Rampally, C. Ribeiro, M.K. Robertson, J.T. Rymer, S.M. Ryan, M. Sammons, A.K. Scott, A.L. Scott, A. Shinomiya, C. Smith, K. Smith, N.L. Smith, M.A. Sobeski, A. Suleiman, J. Swift, S. Takemura, I. Talebi, D. Tarnogorska, E. Tenshaw, T. Tokhi, J.J. Walsh, T. Yang, J.A. Horne, F. Li, R. Parekh, P.K. Rivlin, V. Jayaraman, K. Ito, S. Saalfeld, R. George, I.A. Meinertzhagen, G.M. Rubin, H.F. Hess, V. Jain, S.M. Plaza, *BioRxiv* **2020**, 2020.04.07.030213.

[194] D. Spehner, A.M. Steyer, L. Bertinetti, I. Orlov, L. Benoit, K. Pernet-Gallay, A. Schertel, P. Schultz, *J. Struct. Biol.* **2020**, *211*, 107528.

[195] N. Vidavsky, S. Addadi, A. Schertel, D. Ben-Ezra, M. Shpigel, L. Addadi, S. Weiner, *Proc. Natl. Acad. Sci.* **2016**, *113*, 12637.
[196] M. Elbaum, *Curr. Opin. Microbiol.* **2018**, *43*, 155.
[197] H. Bai, Y. Guan, J. Liu, L. Chen, W. Wei, G. Liu, Y. Tian, *J. Synchrotron Radiat.* **2020**, *27*, 176.
[198] H.-Y. Chen, D.M.-L. Chiang, Z.-J. Lin, C.-C. Hsieh, G.-C. Yin, I.-C. Weng, P. Guttmann, S. Werner, K. Henzler, G. Schneider, L.-J. Lai, F.-T. Liu, *Sci. Rep.* **2016**, *6*, 34879.
[199] N. Varsano, T. Dadosh, S. Kapishnikov, E. Pereiro, E. Shimoni, X. Jin, H.S. Kruth, L. Leiserowitz, L. Addadi, *J. Am. Chem. Soc.* **2016**, *138*, 14931.
[200] T.E. Schäffer, J.P. Cleveland, F. Ohnesorge, D.A. Walters, P.K. Hansma, *J. Appl. Phys.* **1996**, *80*, 3622.
[201] C. Mayet, A. Dazzi, R. Prazeres, F. Allot, F. Glotin, J.M. Ortega, *Opt. Lett.* **2008**, *33*, 1611.
[202] M. Jin, F. Lu, M.A. Belkin, *Light Sci. Appl.* **2017**, *6*, e17096.
[203] G. Ramer, F.S. Ruggeri, A. Levin, T.P.J. Knowles, A. Centrone, *ACS Nano* **2018**, *12*, 6612.
[204] B.T. O’Callahan, K.-D. Park, I.V. Novikova, T. Jian, C.-L. Chen, E.A. Muller, P.Z. El-Khoury, M.B. Raschke, A.S. Lea, *Nano Lett.* **2020**, *20*, 4497.
[205] T. Schmid, B.-S. Yeo, G. Leong, J. Stadler, R. Zenobi, *J. Raman Spectrosc.* **2009**, *40*, 1392.
[206] N. Martín Sabanés, L.M.A. Driessen, K.F. Domke, *Anal. Chem.* **2016**, *88*, 7108.
[207] A. Nakata, T. Nomoto, T. Toyota, M. Fujinami, *Anal. Sci.* **2013**, *29*, 865.
[208] N. Kumar, W. Su, M. Veselý, B.M. Weckhuysen, A.J. Pollard, A.J. Wain, *Nanoscale* **2018**, *10*, 1815.
[209] A. Bhattarai, A.G. Joly, A. Krayev, P.Z. El-Khoury, *J. Phys. Chem. C* **2019**, *123*, 7376.
[210] A. Bhattarai, P.Z. El-Khoury, *J. Phys. Chem. Lett.* **2019**, *10*, 2817.
[211] N. Kumar, C.S. Wondergem, A.J. Wain, B.M. Weckhuysen, *J. Phys. Chem. Lett.* **2019**, *10*, 1669.
[212] J.-M. Ortega, F. Glotin, R. Prazeres, X. Li, R. Gref, *Appl. Opt.* **2017**, *56*, 6663.
[213] G. Ramer, V.A. Aksyuk, A. Centrone, *Anal. Chem.* **2017**, *89*, 13524.
[214] D. Partouche, J. Mathurin, A. Malabirade, S. Marco, C. Sandt, V. Arluison, A. Deniset-Besseau, S. Trépout, *J. Microsc.* **2019**, *274*, 23.
[215] M. Lewin, B. Hauer, M. Bornhöfft, L. Jung, J. Benke, A.-K.U. Michel, J. Mayer, M. Wuttig, T. Taubner, *Appl. Phys. Lett.* **2015**, *107*, 151902.
[216] A. Hermelink, D. Naumann, J. Piesker, P. Lasch, M. Laue, P. Hermann, *Analyst* **2017**, *142*, 1342.
[217] L. Tetard, A. Passian, K.T. Venmar, R.M. Lynch, B.H. Voy, G. Shekhawat, V.P. Dravid, T. Thundat, *Nat. Nanotechnol.* **2008**, *3*, 501.
[218] L. Tetard, A. Passian, R.M. Lynch, B.H. Voy, G. Shekhawat, V. Dravid, T. Thundat, *Appl. Phys. Lett.* **2008**, *93*, 133113.
[219] L. Tetard, A. Passian, R.H. Farahi, T. Thundat, *Ultramicroscopy* **2010**, *110*, 586.
[220] T.F.D. Fernandes, O. Saavedra-Villanueva, E. Margeat, P.-E. Milhiet, L. Costa, *Sci. Rep.* **2020**, *10*, 7098.

Chapter 2 .

Specimen preparation and analytical techniques

2.1 . Metal organic framework drug nanocarriers

Because MOFs are so diverse in composition, the Cambridge Crystallographic Data Centre reports nearly 12,500 structures of three-dimensional frameworks.[99] Ettlinger *et al.*[6] have recently reviewed 95 papers to rank three MOFs as prominent nanocarriers: MIL-100(Fe), UiO-66(Zr) and ZIF-8(Zn), which stand for Materials of Institute Lavoisier, Universitetet i Oslo and Zeolitic Imidazolate Framework, respectively. In particular, MIL-100(Fe) and its isoreticular analogue MIL-100(Al) are the most studied MOFs for drug delivery.[6] They have been shown to be biocompatible by *in vitro* and *in vivo* assays for several human cell lines [20–28], Wistar female rats [23, 30–32] and Danio Rerio zebrafish embryos [29] (see Section 1.1.1).

2.1.1 . Materials of Institute Lavoisier

MIL-100(Al) and MIL-100(Fe) can be obtained by bio-friendly and green syntheses,[22, 47] ensuring that no solvent or toxic unreacted reagent is harmful to the organism. They are formed by the self-assembly of trimesate and aluminium (III) or iron (III) ions. Their chemical formulae are $Al_3O(OH)(C_9O_6H_3)_2(H_2O)_2$ and $Fe_3O(OH)(C_9O_6H_3)_2(H_2O)_2$, respectively. Both have a cubic zeolitic structure (Fd$\bar{3}$m space group) characterised by large ($\sim$ 29 Å) and small ($\sim$ 25 Å) pores that are accessible through hexagonal ($\sim$ 8.6 Å) or pentagonal ($\sim$ 4.7 Å) windows (see Figure 2.1).[100, 101] They display a porosity of about 1,500 – 2,000 $m^2.g^{-1}$,[47] which ensures a high drug payload.

Notably, MIL-100(Al) and MIL-100(Fe) have shown higher anticancer drug loadings than other organic nanocarriers (topotecan: 12 wt% vs. < 6 wt% in lipid nanoparticles;[25] busulfan: $\sim$30 wt% vs. < 6 wt% in lipid and polymeric nanoparticles;[23,26,32] doxorubicin: 27 wt% vs. < 15 wt% in polymeric nanoparticles and commercial liposomal Doxil®[46]). As the incorporated drugs can bond with the framework through host-guest interactions, the drug loading can be further improved. Previous studies have shown that phosphorylated drugs achieve enhanced interactions with the open metal sites[48, 54]. For example, gemcitabine, prednisolone and azidothymidine showed higher loading in MIL-100(Fe) when phosphorylated (gemcitabine monophosphate: 31 wt% vs. 1 wt%,[42] prednisolone monophosphate: 30 wt% vs. 19 wt%,[58] azidothymidine triphosphate: 24 wt% vs. 1 wt%.[49, 50]

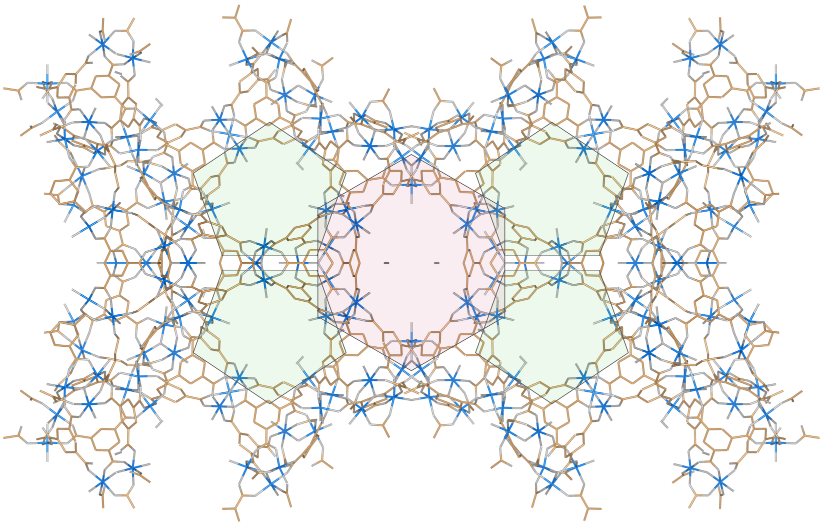

Figure 2.1: Crystal structure of MIL-100 MOFs observed along the [011] direction. Blue, yellow and grey colours represent the metal, carbon and oxygen atoms, respectively. The purple hexagon and green pentagons represent the two different windows for accessing the pores.

2.1.2 . Specimen preparation

In this work, MIL-100(Al) and MIL-100(Fe) were synthesised following the microwave - assisted hydrothermal method described in [22, 44]. The exact procedure can be found in Appendix A. It should be mentioned that the UiO-66 MOFs analysed in the Chapter 3 were provided by the Nanobio team at the Institut des Sciences Moléculaires d'Orsay, Orsay, France. They were synthesised following the procedure described in [102]. Then, two studies were carried out on the biodegradation of MIL-100 and their drug loading.

The biodegradation of MOFs was studied in a physiological mimic medium. Biological media are extremely complex environments in which many molecules can interact with the nanomaterial. The use of simpler media, such as serum or physiological buffer, is more appropriate to gain insights into unknown mechanisms. Here, phosphate-buffered saline (PBS) was used as a simple medium to mimic physiological conditions. It is composed of KCl (2.67 mM), KH_2PO_4 (1.47 mM), NaCl (137.93 mM) and $Na_2HPO_4.7H_2O$ (8.06 mM) and maintains a pH between 7.0 and 7.3. The experimental procedure was adapted from previous work.[44] Prior to biodegradation, the nanoparticles were suspended in deionised water after centrifugation at 11,000g for 15 min. To remove any traces of ethanol, two additional washes in deionised water were performed by successive centrifugations at 11,000g for 10 min, respectively. For biodegradation, 1 mL of commercial PBS was added to the pellet. The mixture was incubated at 37°C for 48h. The final product was recovered by centrifugation at 12,000g for 15 min and redispersed in deionised water. To minimise the aggregation, the degraded nanoparticles were characterised as soon as possible. In this work, the biodegradation process was monitored step by step. Thus, different stages of biodegradation were prepared by varying the concentration of MOFs (from 2.5 mg/mL to 10 mg/mL) and PBS (from

0.3 mM to 10 mM). Chapter 4 provides a detailed discussion.

To assess the drug loading of MOFs, the anti-cancer drug gemcitabine monophosphate was incorporated at 20 %wt. Although MIL-100(Al) has already been studied for the incorporation of drugs, such as adenosine triphosphate[44, 45] and doxorubicin,[46] this work demonstrates for the first time the encapsulation of gemcitabine monophosphate in such a material. The loading procedure was therefore adapted from previous methods using doxorubicin.[46] The loading was achieved by the impregnation method: the MOFs are soaked in a concentrated drug solution, allowing the molecules to diffuse into the pores.[13, 103] To this end, the nanoparticles were first recovered by centrifugation at 11,000g for 15 min, then washed twice in deionised water by successive centrifugations at 11,000g for 10 min. A solution of gemcitabine monophosphate (50 μL, 3.1 mg/mL) was added to the MOFs suspension (105.5 μL, 7.4 mg/mL). The final concentrations were 1 mg/mL of drug and 5 mg/mL of MOFs. The mixture was stirred overnight. The final product was recovered by centrifugation at 10,000g for 10 min.

Each preparation was characterised by *bulk* techniques to assess its quality prior to individual analysis. In particular, Dynamic Light Scattering (DLS), Fourier Transform Infrared spectroscopy (FTIR), porosimetry, UV-vis spectroscopy and Thermogravimetric Analysis (TGA) were used. The experimental procedure is described in detail in Appendix A. The results are presented in Appendix B.1. The MOFs exhibited a hydrodynamic size (around 200 nm), chemical composition and porosity (around 2,000 $m^2.g^{-1}$) in agreement with the literature.[44, 62, 101, 104–106].

As shown in Figure 2.2, the as-prepared suspensions contained unreacted reagents (resi-dues indicated by the yellow arrows), making it difficult to analyse and map the chemical composition of individual MOFs by electron spectromicroscopy. Therefore, several attempts were made to produce high quality specimens. First, successive low-speed centrifugations (< 3,000g for 5 min) were used to remove the chemical residues. Although successful, this method resulted in the loss of valuable amounts of material and the aggregation of the nanoparticles. More efforts were put

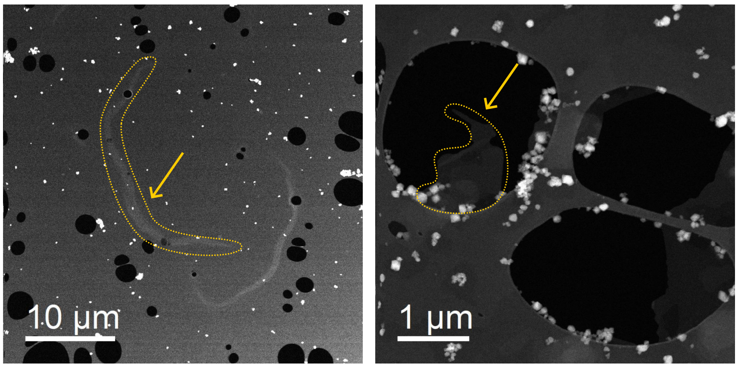

Figure 2.2: HAADF-STEM images of MIL-100(Fe) showing the presence of residues in the as-prepared suspensions. The residues are indicated by the yellow arrows, and are likely to be unreacted reagents. The bright sports are MOFs nanoparticles, while the black rounded shapes are holes in the grid carbon film.

into the suspension drop casting. As the MOFs are intrinsically positively charged, the grids were glow discharged under argon (at 5 mA for 30s) to promote interactions between the two. This left the chemical residues in the drop solution. A simple blotting of the drop allowed them to be removed from the specimen. Therefore, all MOFs specimens were prepared by dropping 4 μL of the suspension onto a TEM grid for 10s before blotting with a filter paper.

Free standing drugs and biomolecules were also analysed. In these cases, the solids were dissolved in deionised water or absolute ethanol and drop cast in the same way as the MOFs, without glow discharge.

2.2 . Electron microscopy

In this thesis, TEM and STEM were used to analyse the specimens. A schematic representation of each technique is given in Figure 2.3.a. TEM is based on a parallel beam illuminating the specimen, while STEM uses a focused raster probe. Their basic operation is explained below. Firstly, both have an illumination system that consists of an electron source and electromagnetic lenses operating in an ultra-high vacuum. The electron source is a tip (tungsten filament, ZrO_2-coated tungsten filament or lanthanum hexaboride crystal), from which the electrons are extracted by thermionic emission (heating), high-temperature field-emission (Schottky effect) or cold field-emission (tunneling effect). Cold field-emission guns (cFEG) exhibit the highest brightness (number of electrons extracted per steradian per time) and coherence (low spatial and energy spread of the electrons).[66, 107] Then, the electrons are accelerated to voltages typically ranging from 80 kV to 300 kV, to reach the specimen. They pass through condenser and objective lenses that shape the incident beam. In STEM, an aperture controls the beam convergence semi-angle to adjust the probe size for high spatial resolution (large angle, small beam size) or conversely, low electron density (small angle, large beam size). Round microscope lenses cannot be manufactures without aberrations (*e.g.* spherical aberration - Cs -, chromatic aberration, astigmatism and coma). These affect the focusing of the incident beam and hence, the resolution of the microscope.[66, 107] By adding multipole correctors to the system, the electron path can be adjusted to achieve the atomic resolution.[108]

TEM and STEM are both based on the transmission mode in which the incident electron beam passes through the specimen. Hence, they require thin specimens (< 500 nm) to allow the electron transmission.[66, 107] During transmission, a fraction of the electrons interact with the specimen. This gives rise to elastic and inelastic scattering events (see Figure 2.3.b). Elastic scattering consists of an electron-nucleus interaction that typically induces a large deviation in the path of the incident electron (> 10 mrad). The heavier the atom, the larger the nucleus, the higher the scattering angle. Conversely, inelastic scattering is an electron-electron interaction involving a transfer of the kinetic energy of the incident electron to the electron cloud of the atom. It usually deviates the path of the

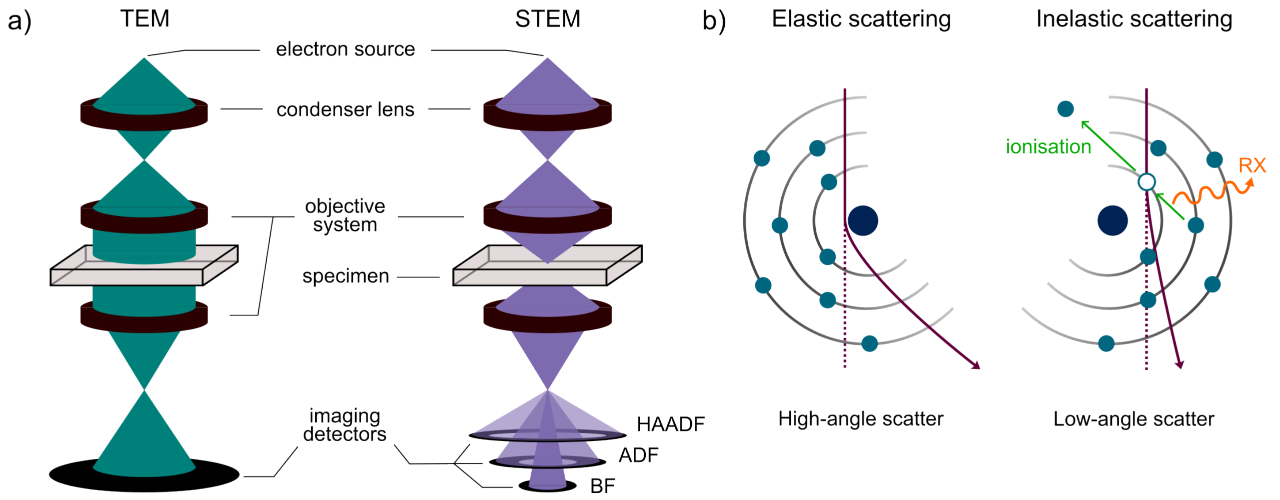

Figure 2.3: a) Schematic representation of the microscope set-ups for TEM (left) and STEM (right). TEM consists of a parallel beam and a single camera detector, while STEM has a focused scanning beam and several disc and annular detectors. b) Schematic representation of the electron-matter interactions occuring through elastic and inelastic scatterings of the incident electron beam.

incident electron only slightly ($<$ 10 mrad).[66, 107] A proportion of the elastically and inelastically scattered electrons are collected with different detectors to analyse the specimen. Note that the scattered electrons represent only a small fraction of the incident beam, the rest being transmitted without interaction. These are referred to as the scattered and unscattered beams, respectively.

For crystalline specimens, such as MOFs, the arrangement of atoms creates a coherent elastic scattering, also known as Bragg diffraction. It produces an electron diffraction pattern that is characteristic of the crystal periodicity. In the imaging mode, part of the Bragg diffraction contributes to the image contrast. Thus, using a Fourier transform, the crystalline information (structure and orientation) can be extracted from the reciprocal space of the collected image.

In TEM (Figure 2.3.a), a camera collects both the scattered and unscattered beams that are out of phase. Since electrons have wave properties, this results in a phase contrast in the image. The images may also exhibit an amplitude contrast, which depends on the crystallinity (Bragg diffraction), composition and thickness of the specimen.

As shown in Figure 2.3.a, STEM is equipped with several different detectors of variable diameter. There are at least two: the Bright-Field (BF) and the Annular Dark-Field (ADF). The BF detector is a relatively small-diameter disc detector. It collects the unscattered, inelastically scattered at small angles and Bragg diffraction beams. Similar to TEM, STEM-BF images display phase and amplitude contrast. The ADF is an annular detector. Due to its shape, it collects mainly the elastically scattered beams. Since the scattering angle depends on the atomic number, the ADF provides a contrast dependent on the composition of the specimen. With different inner and outer radii, it can be more or less sensitive to light and heavy atoms. For example, with large radii, High-Angle ADF (HAADF) is mostly sensitive to heavy atoms that elastically scatter electrons at higher angles.

The HAADF provides a Z-contrast that is proportional to the square of the atomic number of the elements (Z^n, where 1.5 < n < 2.0).

2.2.1 . Radiation damage under the electron beam

As mentioned in Chapter 1, specimens can be damaged during the analysis. Knock-on, radiolysis and beam heating are the main processes that cause loss of mass and chemical changes.[109–111] Knock-on is the displacement or sputtering of an atom by elastic scattering. This creates point defects and changes in the chemical environment. This type of damage occurs when the microscope voltage is higher than the atomic displacement energy. Thus, reducing the microscope voltage can minimise knock-on.

In the case of organic or biological matter, radiolysis and thermal degradation (beam heating) create most damage.[109, 110] These are caused by inelastic scattering that induces atomic vibration and ionisation. This leads to a local increase in temperature and the emission of secondary electrons (electrons ejected from the cloud following the ionisation). In particular, secondary electrons are able to propagate in the specimen over tens of nanometres.[112] Thus, in addition to breaking chemical bonds, they lead to the formation of radical species and chemical recombinations that further damage the specimen. Both radiolysis and beam heating can be reduced by increasing the microscope voltage to reduce the inelastic scattering cross-section and by using cryogenic temperatures (liquid nitrogen or helium) to limit the propagation of free radicals.[67, 68, 110] For example, cryo-TEM imaging of biological specimens is typically performed at 200 kV and at liquid nitrogen temperature.[113] Another strategy to reduce the beam damage is to minimise the electron dose. Biological specimens are typically studied at 10 $\bar{e}$/Å^2 – 15 $\bar{e}$/Å^2.[113] In TEM and STEM, decreasing the electron dose can be achieved by reducing the beam current and the dwell time. In practice, the beam current can be reduced by lowering the extraction voltage or using apertures to shut off part of the beam. As STEM is a scanning technique, decreasing of the electron dose can also be done by reducing the electron density through the increase of the pixel size and of the probe (defocusing or using a small convergence semi-angle). Note however that reducing the electron dose means reducing the collected signal. Hence, new technologies are needed to improve the detection sensitivity. Nowadays, DED allows the collection of weak signals with an improved signal-to-noise ratio.[75]

For both TEM and STEM, good practice can also further minimise the beam damage. This involves avoiding unnecessary high magnifications to observe the specimen and focusing the probe in a sacrificial region, close to the region of interest.[110, 111] All these experimental methods have been used in this thesis work.

2.2.2 . Morphology and crystal structure

Conventional TEM was used to study the morphology of MOFs. The experiments were performed at 100kV on a JEOL JEM-2010 microscope equipped with an LaB_6 electron source and a Gatan Ultrascan 1K CCD camera. The column vacuum was typically 10^{-7} Torr. A picture of the microscope is shown in Figure 2.4.

Due to the radiation sensitivity of the MIL-100 nanomaterials, their structure tended to collapse, resulting in a loss of information. In order to preserve the integrity of the specimens during the analysis, high-resolution imaging required alternative methods, in particular cryo-TEM, using low electron doses and cryogenic temperatures. In collaboration with Jéril Degrouard (Laboratoire de Physique des Solides, Orsay, France), this technique was used to assess the crystallinity of the MOFs. The experiments were performed on a different JEOL JEM-2010 microscope than above, operated at 200 kV and equipped with a Schottky field-emission gun, a Gatan 626 cryo-holder and a Gatan Ultrascan 4K CCD camera. The column vacuum was typically 10^{-8} Torr. Data were collected at a temperature of approximately 100 K, with an estimated electron dose between 10 $\bar{e}$/Å^2 and 15 $\bar{e}$/Å^2. All the TEM and cryo-TEM images presented in this manuscript are raw data.

Another alternative method to perform high-resolution imaging of radiation-sensitive specimens is integrated Differential Phase Contrast (iDPC)-STEM. It uses a single four-quadrant disc detector to measure the beam phase variation induced by the atomic electric field. The image contrast is directly proportional to the atomic number (Z), allowing a sufficient signal-to-noise ratio (SNR) to be obtained even at low electron doses. In this thesis, iDPC-STEM was used in collaboration with Pr. Susana Trasobares (University of Cádiz, Puerto Real, Spain). The data were collected on a double Cs aberration-corrected FEI Cubed Titan Themis microscope, operated at 300 kV and equipped with a high-brightness X-FEG electron gun and a four-quadrant imaging de-

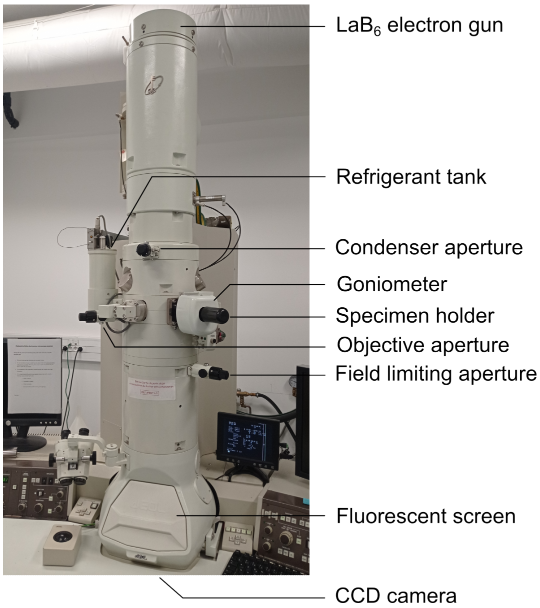

Figure 2.4: Photograph of the JEOL JEM-2010 microscope, equipped with an LaB_6 electron source.

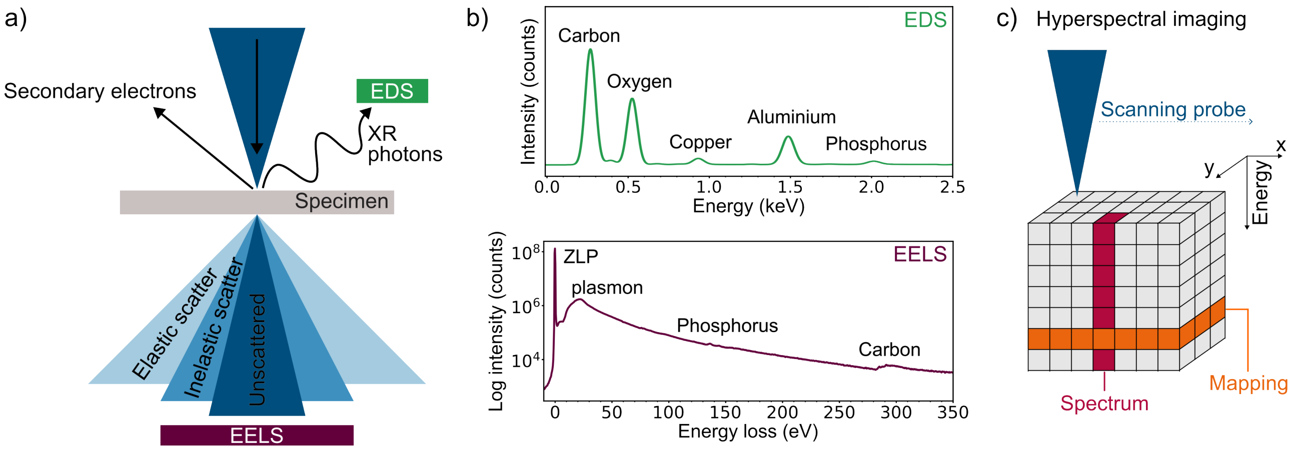

Figure 2.5: a) Schematic representation of the emitted particles during the interaction between the incident electron and the specimen. EDS collects the emitted X-rays while EELS collects the unscattered and inelastically scattered electrons. b) Examples of spectra obtained by EDS (green) and EELS (purple). The prominent ZLP signal results from the unscattered electrons. c) Schematic representation of the 3D data obtained using the hyperspectral mode of electron spectromicroscopy.

tector (FEI DF4). The beam convergence semi-angle was 21.4 mrad, while the camera length was set at 185 mm or 285 mm. To avoid beam damage, the probe current was reduced to about 0.5 pA with a dwell time per pixel of 2.5 μs, and a pixel size of $\sim$ 84 pm, reducing the electron dose to 60 $\bar{e}$/Å^2. The iDPC-STEM images were denoised using the Average Background Subtraction Filter (ABSF) (step: 2, delta: 5%, cycles: 99%). It consists of analysing the reciprocal space of the image to isolate the crystalline information (nanomaterial) from the amorphous background (noise) according to the frequency of each signal (high frequency: noise, low frequency: crystallinity).[114] The algorithm is available online via the HRTEM script that can be installed on the Digital Micrograph®software.[115] To improve the result, the filter was run twice.

2.2.3 . Electron spectromicroscopy

STEM can also be used to analyse the composition of the specimen. For this purpose, the microscopes are equipped with specific spectrometers (Figure 2.5.a-b) to perform EDS or EELS. Both can provide a quantitative analysis. The focused scanning probe of STEM microscopes allows a point-by-point analysis of the specimen with atomic spatial resolution. Thus, a full spectrum is collected at each pixel of the scan. The resulting hyperspectral data, known as spectrum-image or spim,[116] is in three dimensions (x, y and energy, Figure 2.5.c). By extracting the signal from local regions, one or a few pixels, individual spectra can be analysed to determine the chemical composition of the specimen (pink colour in Figure 2.5.c). Chemical maps can also be obtained by integrating the spectrum over specific energy ranges (orange colour in Figure 2.5.c).[66, 107]

2.2.3.1 . Elemental analysis

As mentioned above, the inelastically scattered electrons transfer kinetic energy to the electrons of the specimen. This energy transfer results in the excitation of the specimen electrons.

Different behaviours are then observed depending on the type of excitation occuring in the vibrational, valence or core levels. In the case of core excitations, the electron is ejected from the cloud (ionisation). This creates a vacancy that can be filled by an electron from the upper layers. Its excess in energy induces the emission of a high-energy particle (X-ray or Auger electron). The energy of this particle is characteristic of the atom. The EDS spectrometer identifies the elemental composition of the specimen by collecting the emitted X-rays. This results in a spectrum that displays the number of X-rays as a function of their energy (Figure 2.5.b, green spectrum). Each peak indicates the presence of an atom species in the specimen. For example, carbon and aluminium have peaks at 0.28 keV and 1.49 keV, respectively.

Here, STEM-EDS was used to determine the elemental composition of MOFs. In collaboration with Pr. Susana Trasobares (University of Cádiz, Puerto Real, Spain), two different microscopes were used: an FEI Talos F200X G2 microscope and the aforementioned double Cs aberration-corrected FEI Cubed Titan Themis (used for iDPC-STEM), which are both equipped with a high-brightness X-FEG electron gun and a Super X-EDS spectrometer (ThermoFisher Scientific). The beam convergence semi-angle was 21.4 mrad for the FEI Talos and 7.5 mrad for the FEI Titan microscope. The FEI Talos microscope was operated at 200 kV, with a probe current, pixel dwell time and pixel size of approximately 120 pA, 30 µs and 1.5 nm. The FEI Titan microscope was operated at 300 kV, with a probe current, pixel dwell time and pixel size of approximately 135 pA, 128 μs and 3 nm. The electron dose applied in both cases is estimated to be around 10^2 $\bar{e}$/Å^2. All EDS data were collected with an energy window of 5 keV. Data were acquired and processed using the ThermoFisher Scientific Velox software. The elemental maps were presented as net intensities and without interpolation. An additional Gaussian blur filter (α: 0.8) was applied to denoise the maps. This method consists of smoothing the data contained in neighbouring pixels by combining the information according to a Gaussian distribution. The elemental quantification was performed by fitting the EDS spectra with an empirical model and deconvoluting the elements coming from impurities or components of the microscope (*i.e.* silicon, sulphur, chlorine, potassium, calcium and copper). The quantification, given in atomic percentages, remains estimate as parasitic events were not taken into account.

2.2.3.2 . Chemical analysis

As shown in Figure 2.5.a, the EELS spectrometer is placed after the specimen (it replaces the BF) to collect the inelastically scattered beam and to measure the energy lost during the kinetic transfer. As the energy lost is equal to the excitation energy, EELS can identify the type of transition involved in the process and hence, the electronic configuration of the atom. This results in a spectrum plotting the number of scattered electrons as a function of their energy loss (Figure 2.5.b, purple spectrum). Each peak corresponds to a specific excitation of the electrons in the vibrational or electronic states of the specimen. The broad spectral range of EELS provides a multimodal overview of the chemical structure and properties of the specimen (vibrational modes, optical properties, band gaps, oxidation state, degree of unsaturation, etc). The vibrational excitations occur at low energies (< 2 eV). This region is called the ultralow-loss and probes excitations similar to IR or Raman spectroscopy (< 16,000 cm^{-1}). The valence electron excitations occur at an intermediate energy (2 – 50 eV). This region is called the low-loss and covers the UV-vis region (25 – 620 nm). Finally, the core electron excitations occur at high energies (> 50 eV). This region is called the core-loss and covers the extreme UV and soft XR domain (100 eV – 5 keV). Note that the spectrum is dominated by a prominent peak at 0 eV, also known as the Zero-Loss Peak (ZLP). It mainly corresponds to the unscattered beam, which is also collected during the analysis due to its close proximity to the low-energy inelastically scattered electrons.

The energy spread of the electron gun and the chromatic aberrations limit the spectral resolution of the microscope. This can impede the analysis in the far and mid-infrared (1 meV – 500 meV) and the discrimination between electronic excitations that are close in energy. This is the case even when equipped with a cFEG (energy spread 300 meV, measured at the full width half maximum of the ZLP). In order to access the three spectral regions, STEM microscopes must be equipped with a monochromator. This recent technology is able to narrow the energy spread of the electron source by selecting the electrons in a specific energy range (Figure 2.6.a). The monochromator shuts-off part of the electron beam to improve the spectral resolution of EELS down to 5 meV.[80]

As shown in the EELS spectrum of Figure 2.5.b, the low-loss signals have a relatively high intensity, which is due to a higher cross-section. Conversely, the ultralow and core-losses exhibit weaker signals due to lower cross-sections, overlap with the tail of the ZLP or with the increasing background of multiple inelastic scattering events. As a result, these signatures are more difficult to detect, especially at low electron doses. The development of DED for EELS has enabled to improve the detection sensitivity and collect these weak signals with a sufficient SNR. In the case of radiation-sensitive specimens, DED allows for efficient analysis at extremely low electron doses (> 10 $\bar{e}$/Å^2, see Chapter 3).

In this thesis, STEM-EELS was performed on a monochromated Cs aberration-corrected Nion Hermes 200-S microscope. A photograph of this microscope can be found in Figure 2.6.b. This unique instrument is equipped with a cFEG, a Nion Iris spectrometer, a Quantum Detectors Merlin DED EELS camera and a HennyZ cryoholder (temperature of approximately 120K). All the experiments were performed at 100 kV, with a column vacuum of approximately 10^{-10} Torr and a beam convergence semi-angle of 10 mrad. This sub-nanometre probe size allowed to reduce the electron density and thus the beam damage. Thanks to the monochromation and the DED, the chemical signature of the specimens was studied in the three spectral regions (the ultralow-loss, the low-loss and the core-loss). The ultralow-loss spectra were collected with an entrance aperture of 300 μm and an energy dispersion of 1.6 meV/ch, resulting in a spectral resolution of about

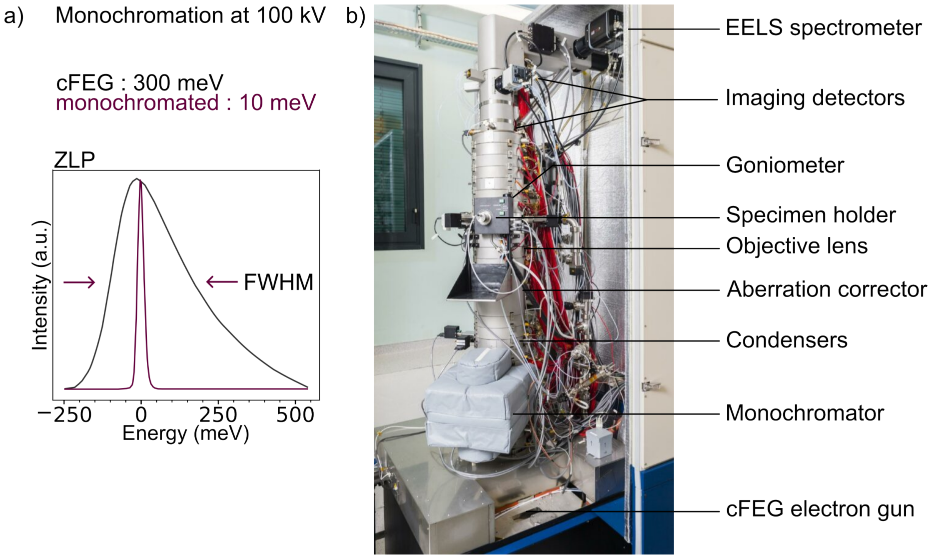

Figure 2.6: a) Example of the monochromation: before monochromation, the energy spread of the cFEG reaches 300 meV, while it is narrowed to 10 meV after monochromation (measured at the Full Width Half Maximum, FWHM). b) Photograph of the Cs aberration-corrected Nion Hermes 200-S microscope, equipped with a monochromated cFEG electron gun.

12 meV. The low and core-losses were studied with an entrance aperture of 1 – 2 mm and an energy dispersion ranging from 15 meV/ch to 389 meV/ch (spectral resolution 40 – 800 meV). The electron dose was varied from 10 $\bar{e}/\text{Å}^2$ to 10^4 $\bar{e}/\text{Å}^2$. To this end, the beam current was adjusted with the monochromator slit from 8 pA to 50 pA, the pixel size was set from 3 nm to 10 nm and the dwell time per pixel was varied between 2 – 50 ms. Note that all the experiments were carried out in the direct beam mode, which unlike the aloof mode, ensures spatial resolution.

All the data were acquired using the open-source Nion Swift software and processed using the Gatan Digital Micrograph ®software. Different calibrations were used in this work. First, the EELS spectra were acquired with a small dispersion (0.389 eV/ch) to acquire simultaneously the ZLP and the carbon K-edge and to calibrate the peaks (ZLP at 0 eV, peak of amorphous carbon at 285.0 eV). Then, in Chapter 3, the calibration of the oxygen K- and iron L- edges was performed using published data on MOFs obtained by X-ray absorption spectroscopy. In Chapter 4 and Chapter 5, the oxygen K-edge was typically acquired simultaneously with the carbon K-edge so that the spectra could be calibrated using the dispersion measured between the ZLP and carbon K-edge. For all the data, the background was subtracted with different functions depending on the energy range concerned, either a power-law, a first or second-order polynomial function. The Principal Component Analysis (PCA) was used as a denoising method for low signal spectra. It is a multivariate statistical analysis that describes correlated variations of a data set with orthogonal variables called components. The principal components are those resulting from the stronger variations that best illustrate the data set.[117] The algorithm, available in the Hyperspy Python library,[118] was typically run with 3 to 6 components. In the ultralow-losses, the spectra were deconvolved using the Richardson-Lucy algorithm (10 iterations) to improve the spectral resolution (from 12 meV to 7 meV). This algorithm, also available in the Hyperspy Python library,[118] is an iterative process that corrects the aberrations estimated from the microscope's point spread function (defined by the ZLP for data obtained at high spectral resolution in the ultralow-loss).[119] All the chemical maps were obtained using the Gatan Digital Micrograph®software. For the huge majority of them, they were obtained by integrating the corresponding signal after background subtraction (and PCA where necessary). This method was however not suitable for mapping the low-loss signature of the two MOFs mixed in the same specimen (in Chapter 3). In this case, a multi-Gaussian fit was performed using the Non-Linear Least Squares (NLLS) method in the Gatan Digital Micrograph®software. This consists of fitting the data with a non-linear function that minimises the squares of the residual errors.

Chapter 3 .

Damage-free multimodal analysis of MOFs by monochromated STEM-EELS

MOFs are mainly composed of organic matter (see the molecular structure of MIL-100 in Chapter 2) and hence, are extremely sensitive to electron irradiation. When analysed by electron microscopy, these organic-inorganic nanomaterials undergo a rapid degradation under the beam. The nanostructures are progressively destroyed, resulting in the loss of crystallinity, particle shrinkage and changes in the chemical composition. MOFs have previously been reported to lose their integrity for electron doses < 30 $\bar{e}$/Å^2.[120] Thus, classical modes of imaging and spectroscopy are not suitable for their analysis. Further instrumental developments and alternative methods are needed for the damage-free study of these nanomaterials.

As discussed in Section 2.2, the beam damage can be reduced by drastically decreasing the electron dose and using cryogenic temperatures. However, decreasing the electron dose means reducing the signals and therefore requires an increase in detection sensitivity. The recent development of DED has opened up new possibilities for the analysis at low electron doses. The high sensitivity of DED allows the collection of a weak signal with an improved SNR.[75]

DED can be used for both imaging and spectroscopy. In September 2021, the monochromated Nion Hermes 200-S microscope (used in this thesis) was equipped with a DED camera for EELS studies. Since then, this thesis work has shown that the combination of direct electron detection and monochromation has enabled impressive breakthroughs in deciphering the chemical structure of complex nanomaterials. With a monochromated beam, the microscope was able to cover a wide spectral range, from the ultralow-loss (< 2 eV, < 16,000 cm^{-1}), through the low-loss (2 – 50 eV, 25 – 620 nm), to the core-loss regions (> 50 eV). Then, using the high sensitivity of the DED, undamaged signatures could be obtained at extremely low electron doses, down to 10 $\bar{e}$/Å^2, in the three spectral regions.

3.1 . An innovative acquisition strategy for radiation-sensitive systems

Based on the instrumentation described above, this section presents an innovative acquisition strategy for the damage-free multimodal analysis of MOFs by monochromated STEM-EELS. This study shows the elucidation of the undamaged chemical signature of MIL-100(Al) and MIL-100(Fe) in the IR, UV-vis and soft XR regions. To enrich the analysis, the signatures of MIL-100(Al) and MIL-100(Fe) were compared with another type of MOF, namely UiO-66(Zr).

This section also demonstrates the possibility of analysing the chemical changes induced by the electron beam. By gradually increasing the electron dose up to 10^4 $\bar{e}$/Å^2, the spectral changes were monitored step by step. A complete understanding of each spectral evolution was then achieved thanks to the high dynamic range of the DED, which allowed the simultaneous acquisition of the low intensity signatures (typically core-loss, see Section 2.2) with higher intensity features (*e.g.* low-loss signals, see Section 2.2). Note that, in this section, the structures named intact and degraded refer to the signatures obtained at low and high electron doses, respectively.

This work is the result of a collaboration with Jéril Degrouard (Laboratoire de Physique des Solides, Orsay, France) and has been published in the journal ACS Nano. Note that the supplementary information can be found in Appendix C.

Article published in:
Chaupard, M.; Degrouard, J.; Li, X.; Stéphan, O.; Kociak, M.; Gref, R.; de Frutos, M. Nanoscale Multimodal Analysis of Sensitive Nanomaterials by Monochromated STEM-EELS in Low-Dose and Cryogenic Conditions. *ACS nano*, **2023**, 17, 4 , 3452-3464. doi: 10.1021/acsnano.2c09571.

In this work, Jéril Degrouard carried out the cryoTEM experiments. I synthesised the MOFs nanoparticles, under the supervision of Dr Ruxandra Gref. With the help of Dr Xiaoyan Li and Dr Marta de Frutos, I carried out the EELS experiments. With the help of Pr Odile Stéphan and Dr Mathieu Kociak, I performed the data processing. Finally, I was the main contributor to the writing of the article, under the supervision of Dr Marta de Frutos, Pr Odile Stéphan and Dr Mathieu Kociak.

NANOSCALE MULTIMODAL ANALYSIS OF SENSITIVE NANOMATERIALS BY MONOCHROMATED STEM-EELS IN LOW-DOSE AND CRYOGENIC CONDITIONS

Maeva Chaupard, Jéril Degrouard, Xiaoyan Li, Odile Stéphan, Mathieu Kociak, Ruxandra Gref, Marta de Frutos

To cite this version:

Maeva Chaupard, Jéril Degrouard, Xiaoyan Li, Odile Stéphan, Mathieu Kociak, et al.. NANOSCALE MULTIMODAL ANALYSIS OF SENSITIVE NANOMATERIALS BY MONOCHROMATED STEM-EELS IN LOW-DOSE AND CRYOGENIC CONDITIONS. ACS Nano, 2023, 17 (4), pp.3452-3464. 10.1021/acsnano.2c09571 . hal-04184364

HAL Id: hal-04184364
https://hal.science/hal-04184364
Submitted on 21 Aug 2023

Nanoscale Multimodal Analysis of Sensitive Nanomaterials by Monochromated STEM-EELS in Low-Dose and Cryogenic Conditions

Maeva Chaupard,[a,b] Jéril Degrouard,[a] Xiaoyan Li,[a] Odile Stéphan,[a] Mathieu Kociak,[a]
*Ruxandra Gref,[b] Marta de Frutos[a]**

[a]Laboratoire de Physique des Solides, CNRS, UMR 8502, Université Paris-Saclay, F-91405 Orsay, France
[b]Institut des Sciences Moléculaires d'Orsay, CNRS, UMR 8214, Université Paris-Saclay, F-91405 Orsay, France

*****Marta de Frutos
Email: marta.de-frutos@universite-paris-saclay.fr

KEYWORDS: Radiation-sensitive nanomaterials, multimodal analysis, monochromated STEM-EELS, low-dose analysis, high-resolution spectromicroscopy, organic-inorganic nanoparticles, metal-organic frameworks.

ABSTRACT: Scanning Transmission Electron Microscopy coupled with Electron Energy Loss Spectroscopy (STEM-EELS) provides spatially resolved chemical information down to the atomic scale. However, studying radiation-sensitive specimens such as organic-inorganic composites remains extremely challenging. Here, we analysed metal-organic framework nanoparticles (nanoMOFs) at low-dose (10 ē/Å^{2}) and liquid nitrogen temperatures similar to cryo-TEM conditions, usually employed for high-resolution imaging of biological specimens. Our results demonstrate that monochromated STEM-EELS enables damage-free analysis of nanoMOFs, providing in a single experiment, signatures of intact functional groups comparable with infrared, ultraviolet and X-ray data, with an energy spectral resolution down to 7 meV. The signals have been mapped at the nanoscale (< 10 nm) for each of these energy spectral ranges, including the chemical features observed for high energy losses (X-ray range). By controlling beam irradiation and monitoring spectral changes, our work provides insights into the possible pathways of chemical reactions occurring under electron exposure.

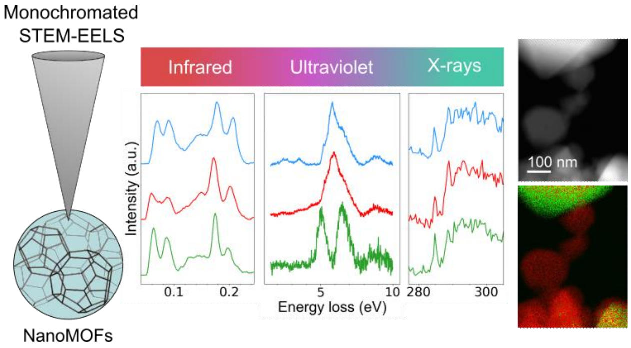

These results demonstrate the possibilities for characterising at the nanoscale the chemistry of sensitive systems such as organic and biological materials.

INTRODUCTION

Nanosized metal-organic frameworks (nanoMOFs) are organic-inorganic nanomaterials with a three-dimensional structure created by the self-assembly of organic linkers and metal clusters. With their versatile compositions and high porosity, nanoMOFs are of great interest for gas storage,[1] wastewater treatment,[2] catalysis,[3] sensing[4] and drug delivery.[5] Providing comprehensive and reliable characterisation of such materials is a significant step in the development of applications but remains challenging due to their nanometric sizes together with their complex structures and compositions. In this regard, spectromicroscopies have been developed, constantly pushing the limits of spatial and energy resolutions. These analytical techniques exploit photons, ions or electrons interactions[6] to explore nanomaterial local physical and chemical properties. Among them, Scanning Transmission Electron Microscopy coupled with Electron Energy Loss Spectroscopy (STEM-EELS) offers the possibility of a deep chemical analysis down to the atomic scale.[7] In this approach, hyperspectral data are acquired by a point-by-point rastering of the electron probe over the area of interest, providing simultaneously imaging and local information on the electronic and vibrational transitions induced by the interaction of the incident electrons with the specimen. The last generation microscopes equipped with monochromated electron guns cover excitations over a wide energy range from tens of meV (far infrared -IR-range) to hundreds of eV (soft X-rays) with an energy resolution (δE) reaching $\lesssim$ 10 meV.[7]

However, studying organic and organic-inorganic nanomaterials remains a delicate task, as they are extremely sensitive to radiation damage. Beam-induced-radiolysis and knock-on may result in structural (shrinking, amorphisation) and chemical damages (loss of mass and bond breakage), affecting the nanomaterial's integrity.[8–10] Noticeably, by employing damage preventive conditions (cryo-holder, low-dose or aloof configuration), recent papers have shown the powerful possibilities offered by EELS for deep characterisation of organic molecules, polymers, MOFs and MOF glass composites in the energy ranges corresponding to IR,[11–14] UV[15–17] and X-rays.[10,18] But to date, none of them has coupled the analysis in the three energy windows. Yet, exploiting the entire energy range would provide a signal complementarity allowing an in-depth characterisation of the nanomaterial composition but also monitoring reactional mechanisms.

With the aim of using the full potential of STEM-EELS, we report in the following a nanoscale multimodal spectroscopic analysis of nanoMOFs. Among their large family, we selected MIL-100(Fe), MIL-100(Al) and UiO-66 nanoparticles, where MIL and UiO stand for Material of Institute Lavoisier and Universitetet i Oslo, respectively. MIL-100 are self-assembled from benzene tricarboxylic acid (BTC) and iron or aluminium ions, while UiO-66 consist of the coordination of zirconium ions with benzene dicarboxylic acid (BDC). For the three of them, the metal-linker coordination bond involves carboxylate functions. As previously reviewed by Liu *et al.*,[19] MOFs are generally highly sensitive to the electron beam. The authors indicated a beam tolerance dose ranging from 5 $\bar{e}/\text{Å}^2$ to 30 $\bar{e}/\text{Å}^2$ for several widely studied MOFs (MIL-101, MOF-5, NU-1000, UiO-66 and ZIF-8 where NU and ZIF stand for Northwestern University and Zeolitic Imidazolate Framework), by monitoring the diffraction spot fading with exposure. Others have also demonstrated the structural and molecular modification of ZIF-L by monitoring the diffraction spot fading and EELS signatures above tens of $\bar{e}/\text{Å}^2$.[10] Although few in number, these studies suggest that MOF materials exhibit a different beam tolerance dose depending on their nature. Because of the extreme radiation sensitivity of MIL-100(Fe) and UiO-66, high-resolution STEM imaging was only possible with low-dose conditions, of the order of 10 $\bar{e}/\text{Å}^2$.[20,21] On the opposite, to the best of our knowledge, MIL-100(Al) have not been studied yet by STEM. At last, none of the three nanoMOFs has been carefully characterised by EELS. The main reason for the lack of damage-free EELS analysis is the difficulty of getting a measurable signal at low doses. Therefore, many questions still need unravelling for a better understanding of these nanoMOFs properties.

Here, we present intact nanoMOFs data obtained from monochromated STEM-EELS measurements at cryogenic temperatures and low-dose (10 ē/$Å^2$), by using a direct detection camera allowing the detection of very weak signals.[22] By exploring the three energy ranges (corresponding to IR, UV and X-ray intervals), we provide a comprehensive study of the nanoMOFs' chemical signatures with an energy resolution down to 7 meV. First, we investigate the local chemical reactions occurring under controlled beam irradiation with a systematic approach revealing complex mechanisms. Then, we demonstrate the possibility of characterising intact nanoMOFs at low-dose. Each feature was compared with infrared, ultraviolet and X-ray data to be assigned to specific functional groups. Finally, by extracting the corresponding spectral features, we map the nanoMOFs' signature over the three energy ranges with a nanoscale spatial resolution. By exploiting the whole EELS energy range, our results provide damage-free analysis of these sensitive specimens and offer a better understanding of their complex nanostructures.

RESULTS AND DISCUSSION

NanoMOFs crystal structure

We performed cryo-transmission electron microscopy (cryo-TEM) imaging of the three nanoMOFs. This technique has the advantage of assessing the crystallinity of the specimens on a single-particle basis. As shown in **Figure 1a-c**, the nanoparticles display well-faceted morphologies typical of MIL-100(Al),[23] MIL-100(Fe)[24] and UiO-66.[25] Their sizes range from 40 nm to 300 nm for MIL-100, and from 100 nm to 1.2 µm for UiO-66. The images show the crystal structures with a spatial resolution of 6 Å along the [112], [110] and [532] directions for MIL-100(Al), MIL-100(Fe), and UiO-66, respectively. These results are in good agreement with previous studies, showing the cubic structure (Fd-3m space group) of MIL-100[20] and UiO-66.[21] However, the observation of the UiO-66 structure, which has previously revealed details below 2 Å,[21] was partially hampered here by the TEM spatial resolution. Because the present cryo-TEM images were obtained in low-dose conditions (total dose estimated between 10 and 15 ē/$Å^2$) no structural damage was observed for a single image acquisition. However, due to the extreme radiation sensitivity of the nanoMOFs, the high-resolution information tended to disappear after consecutive image acquisitions over the same area. The observed loss of crystallinity in TEM gives a rough estimation of the beam tolerance dose of these nanoMOFs. Hence, similar low-doses have been applied in STEM acquisitions for a damage-free analysis of the specimens.

Figure 1d provides a schematic representation of the nanoMOF chemical structures. Since the three specimens exhibit different structures, it depicts a simplified model composed of the metal (labelled M) coordinated to the linkers but does not describe the minor specificities of each system. To help the reading, the chemical bonds described in this manuscript are indicated. We will refer to this schema throughout the manuscript.

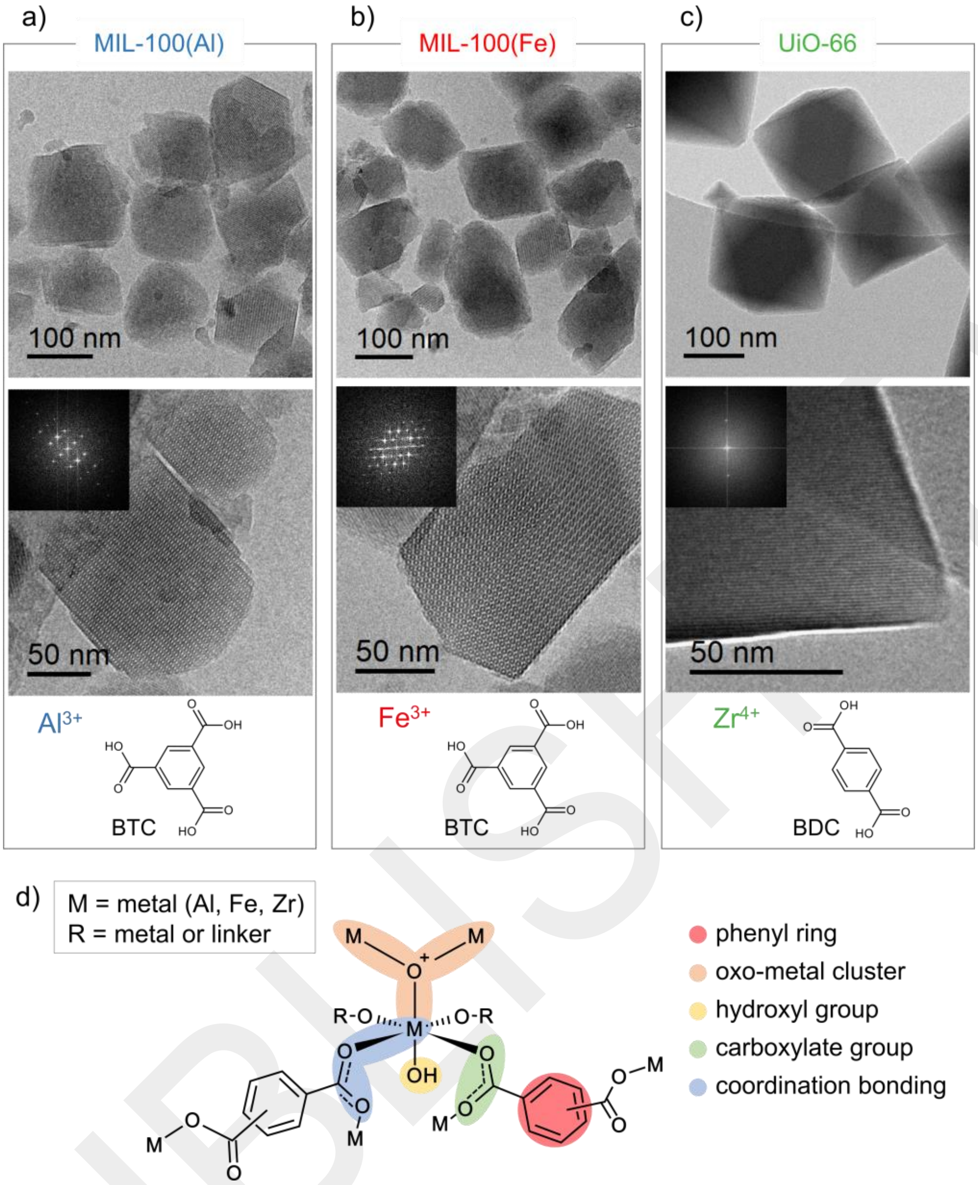

Figure 1. Cryo-TEM images of (a) MIL-100(Al), (b) MIL-100(Fe), and (c) UiO-66 nanoparticles. The top row images illustrate their well-faceted morphologies. At higher magnification, the middle row images show their crystal planes with a spatial resolution of 6 Å along the (a) [112], (b) [110] and (c) [532] directions, respectively. The corresponding fast Fourier transforms are shown on the inset. The chemical components of each nanoMOFs are indicated in the bottom row. (d) Schematic representation of the molecular structure of the three nanoMOFs. For simplicity, the different MIL-100 and UiO-66 structures have been generalised using atom labelling (M for metals and R for metals or linkers). OH groups represent hydroxyl groups found in the three nanoMOFs or MIL-100 structural water. The colours relate the chemical groups to their designation employed in the main text.

EELS: a multimodal analysis for radiation-sensitive material

STEM-EELS was used for an in-depth analysis of the three nanoMOFs. **Figure 2a** shows a schematic representation of the microscope setup. The focused electron beam is scanned over the area of interest (typically 400 x 400 nm^2) giving hyperspectral data (the so-called Spectrum Imaging mode[26]). At each beam position, an image of the specimen is acquired on the High Angle Annular Dark Field (HAADF) detector and simultaneously, the EEL spectrometer measures the energy lost by the electrons, providing spatially resolved chemical information. In the present work, we used a highly monochromated Nion Hermes 200-S microscope fitted with a Nion Iris spectrometer and a Quantum Detectors Merlin direct electron detector. This combination provides ultimate energy resolution ($\delta E \lesssim 10$ meV) and high energy range (from far IR to soft X-rays) together with a high sensitivity that is crucial for dose-limited measurements (see Experimental section). As shown in **Figure 2b**, EELS data cover a wide energy range: the ultralow-loss (ULL) region (below 2 eV, < 16000 cm^{-1}) associated with vibrational excitations down to the far IR; the low-loss (LL) region involving valence excitations from the visible to the vacuum UV energy range (2 – 50 eV, equivalent to 25 – 620 nm); and the core-loss (CL) region (above 50 eV) that, similarly to soft X-ray absorption spectroscopies, reveals the electronic structure of the material through the analysis of their atomic ionisation edges. With a wide energy window spanning 400 eV, we collected simultaneously the LL and CL signals (energy resolution $\delta E = 800$ meV). A closer look at the individual LL and CL features was achieved with a higher energy resolution ($\delta E = 40$ meV for 16 eV energy window or $\delta E = 220$ meV for 116 eV energy window). Because the ULL features are located at very small energy losses (hundreds of meV), they appear as weak signals superimposed on the intense zero-loss peak (ZLP), corresponding to unscattered electrons transmitted with no energy loss through the specimen. Hence, ULL analysis requires an even higher energy resolution corresponding to a narrower energy window (1.6 eV energy window, $\delta E = 12$ meV). For each energy window, the energy resolution δE was measured on the EELS detector from the full-width at half-maximum of the ZLP (see SI for an extensive discussion of the energy resolution and its dependence with acquisition and detection conditions). It should be highlighted that our observations were only possible thanks to the use of a direct detection camera whose high sensitivity and very low noise improve the signal-to-noise ratio (SNR) and whose high dynamic range allows the simultaneous collection of the huge ZLP along with the weak CL signal with no saturation nor loss of sensitivity.[22]

As nanoMOFs are extremely sensitive to the electron beam, their analysis requires special care to prevent degradation under electron irradiation. Therefore, the study was carried out by using i) a cryo-specimen holder cooled down to 125 K; ii) a 10 mrad convergence semi-angle enabling sub-nanometer beam sizes (far from the ultimate microscope performance) to decrease the electron current density; and iii) low electron dose conditions (see details in SI). By adjusting the probe current, the acquisition time and image pixel size, we reached total doses down to 10 $\bar{e}/Å^2$, as low as those employed for cryo-TEM imaging of biological specimens.[27] Then, the beam-induced damage effect was studied by increasing the dose up to 10^4 $\bar{e}/Å^2$ (details on total dose and dose rate calculations are given in SI). To do so, data were collected either by a single acquisition on different areas or several successive acquisitions on the same area. In the following, the corresponding total doses are named *single acquisition dose* or *cumulative dose*, respectively (more details in SI). At least six hyperspectral images were acquired for each electron dose condition on different nanoparticles to provide statistical analysis. Note that, to adjust the electron dose, the study was performed with relatively large pixel sizes, restraining the spatial resolution: the lowest electron dose was obtained with a pixel of 10 nm while higher doses were reached for pixels of 1 nm.

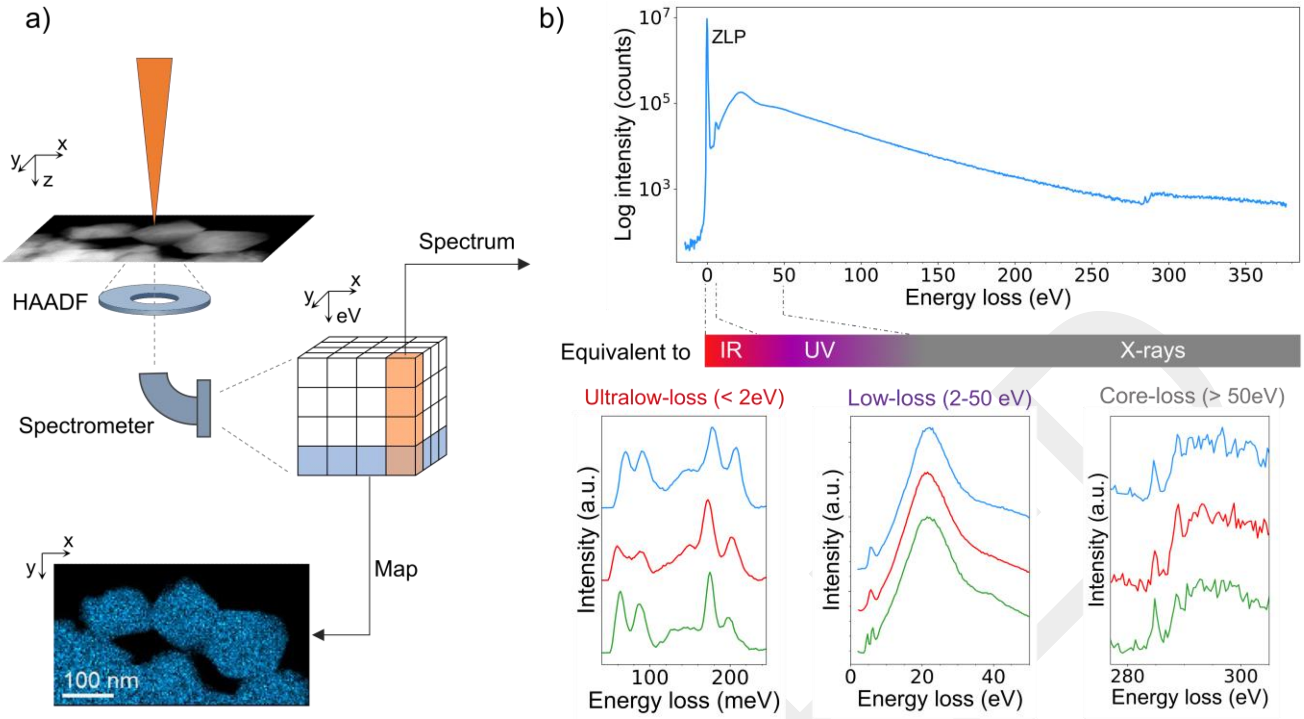

***Figure 2**. Schematic representation of STEM-EELS. (a) The scanning electron probe acquires hyperspectral images with a nanoscale spatial resolution. It offers a multimodal analysis ranging from the vibrational to the soft X-ray energy window. (b) At the top, the widest energy window (spanning 400 eV, δE = 800 meV) enables simultaneously analysing of the LL and CL signals. ULL was not distinguishable at this energy resolution. Here, the signature of MIL-100(Al) is shown at low-dose. At the bottom: enlarged views of the LL (on the middle) and CL signals (on the right) obtained at low-dose for the three nanoMOFs. ULL spectra (on the left) were acquired at 120 $\bar{e}/\text{Å}^2$ with a narrower energy window (spanning 1.6 eV, δE = 12 meV). Blue, red and green colours represent the spectra obtained for MIL-100(Al), MIL-100(Fe) and UiO-66, respectively.*

Core-loss excitations

We first analysed the inner electron shell excitations of the nanoMOFs on the carbon and oxygen K-edges (**Figures 3a and 3c**). The two spectra show changes in the chemical signatures as a function of the electron dose. The carbon K-edge evolution of MIL-100(Al) is presented in **Figure 3a** (blue lines). Similar evolutions are observed for MIL-100(Fe) and UiO-66 in Figure S1. All spectra were calibrated by setting the ZLP at 0 eV and the characteristic peak of amorphous carbon (grey line in **Figure 3a**) at 285.0 eV.[28] In **Figure 3a**, the spectrum of MIL-100(Al) obtained at low-dose (10 $\bar{e}/\text{Å}^2$), reveals two intense peaks, at 285.0 eV (denoted CL_1) and 288.7 eV (denoted CL_3), and a weak signal at 291.1 eV (denoted CL_4). EELS CL spectra are directly comparable to the corresponding X-ray absorption data obtained in the same energy range.[29,30] Nonetheless, the carbon K-edge of these nanoMOFs has never been studied with such techniques. Hence, we compare our EELS results with the Near-Edge X-ray Absorption Fine Structure (NEXAFS) spectra of the free-standing organic linkers (black line in **Figure 3a**, grey line in Figure S2). As shown in **Figure 3a**, CL_1, CL_3 and CL_4 features of MIL-100(Al) are compatible with those previously reported for BTC by NEXAFS.[31] This good agreement demonstrates that low-dose EELS features of nanoMOFs are damage-free signatures. They are respectively related to $1s–\pi^*_{C=C}$ transitions in phenyl rings (CL_1), $1s–\pi^*_{COO}$ transitions in carboxyl groups (CL_3) and $1s–\sigma^*_{C-C}$ transitions in phenyl rings (CL_4).[31,32] A similar comparison between low-dose EELS and NEXAFS for MIL-100(Fe), UiO-66, BTC and BDC can be found in Figure S2. The similarities between nanoMOFs entities and their linkers are consistent since the organic part of the nanoparticles is the only contribution to the carbon K-edge, the data having been recorded above vacuum, on the grid carbon holes. Besides, it should be mentioned that the lack of influence from the metal coordination is not surprising since it is achieved through oxygen atoms of carboxyl groups. One could expect additional 1s–$\sigma^*_{C\text{-}H}$ transitions in phenyl rings near 287 eV, as previously demonstrated by NEXAFS and EELS studies on BDC,[32] BTC (see NEXAFS data in Figure S2) and other benzene derivatives.[18,33–35] Here, its absence is probably due to instantaneous dehydrogenation under electron irradiation.[36] Except for beam-induced dehydrogenation, our low-dose EELS results are similar to linkers NEXAFS data, revealing spectral features characteristic of intact functional groups.

When increasing the electron dose, spectral changes illustrate the evolution of the specimen's chemical composition as a result of radiolysis. First, a slight reduction and broadening of peak CL_1 are observed with an enhancement of peak CL_4. The decrease of peak CL_1 reflects the breakage of C=C bonds, while its broadening outlines the formation of new types of chemical bonds induced by irradiation. Upon irradiation, its shape tends to be similar to amorphous carbon (grey line in **Figure 3a**). In the meantime, the peak CL_4 increase is associated with the formation of C-C bonds, which can be closely related to the radiolysis of benzene double bonds. More significantly, an intense peak (denoted CL_2) rises at 287.6 eV along with a drastic reduction of the peak CL_3. It indicates the formation of a new species and the breakage of the -COO bonds of the carboxyl groups. According to the literature, the peak CL_2 can be attributed to 1s–$\pi^*_{C=O}$ transitions of the carbonyl groups (-CO).[33,35] This evolution indicates that, under beam-induced radiolysis, the carboxyl species are presumably converted into carbonyl by the reduction of the organic linkers. For higher electron doses (above 310 ē/Å^2), the same trend continues without further changes illustrating the robustness of the carbonyl (-CO) composite created under irradiation (shown in Figure S1 for electron doses up to 780 ē/Å^2).

By monitoring the chemical evolution under irradiation, our study enables us to relate the features observed at high electron doses (usually employed for the EELS analysis) with the chemical functions of the original intact nanomaterial. For instance, previous EELS studies of biominerals performed above 100 ē/Å^2 have systematically reported a peak at 287 eV, similar to CL_2, as a fingerprint of the organic fraction.[37–40] Here, we show that this feature can correspond to the degraded signature of components containing carboxyl functions, which in the case of biominerals could correspond to fatty acids or proteins.

In **Figure 3b**, we mapped the distribution of carbonyl components produced under the beam with a nanoscale spatial resolution, across the same scanned area, as a function of the electron dose (see SI for details and Figure S3). To do so, the intensities of peaks CL_2 and CL_3 were integrated, after background subtraction and processing with principal component analysis (PCA). At low-dose, carboxyl groups (-COO) are homogeneously distributed across the nanoparticles, as expected from the nanoMOFs molecular structure. At 310 ē/Å^2, a uniform reduction of the linker into carbonyl (-CO) is observed at this spatial resolution. Note that for such electron doses, the nanoparticle morphology remains unchanged, as observed in the corresponding HAADF image (left side). These results demonstrate the possibility of damage-free mapping at the nanoscale of specific chemical groups. Moreover, it should be mentioned that, to the best of our knowledge, intact organic component mapping has never been performed at an electron dose as low as employed here (10 ē/Å^2).

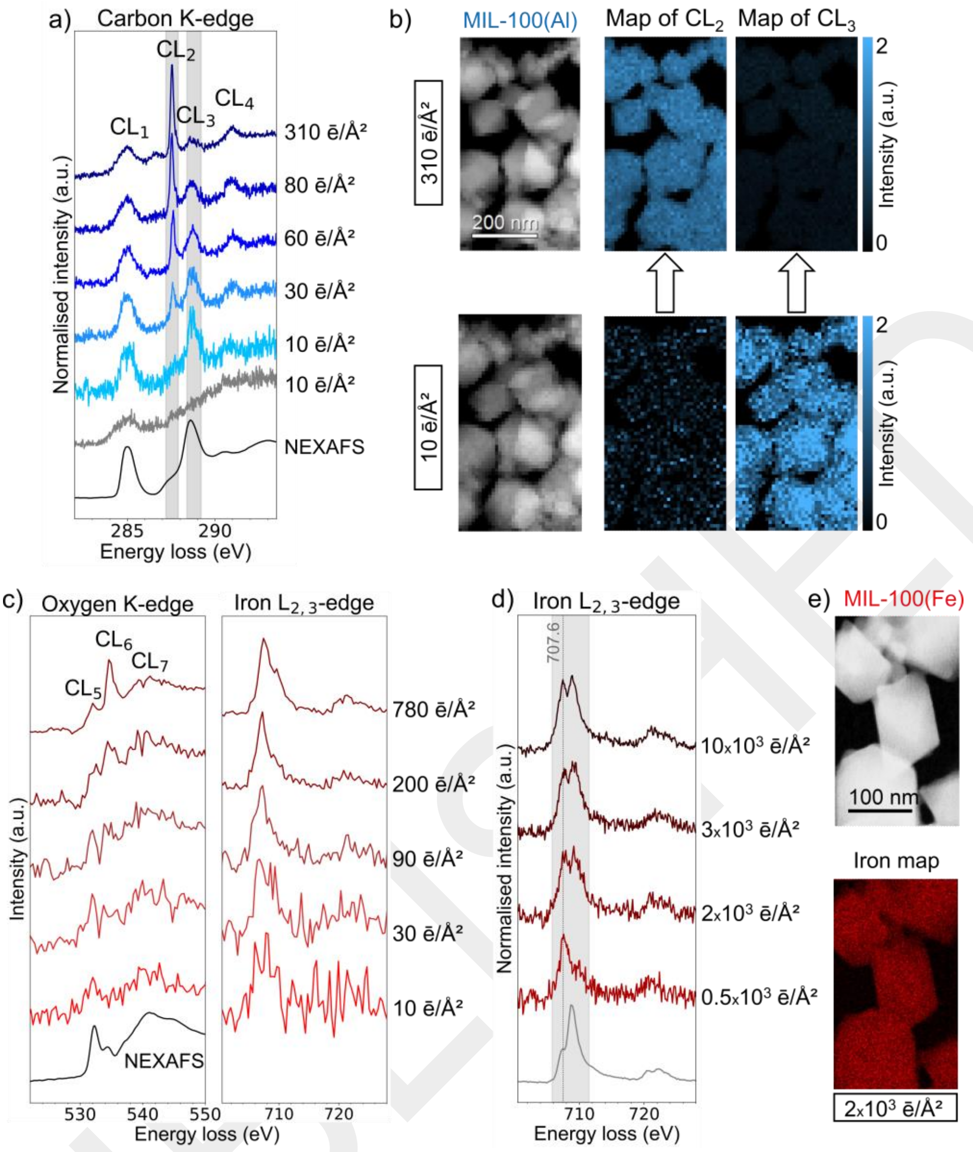

***Figure 3**. Core-loss analysis of MIL-100 nanoparticles as a function of the electron dose. All spectra are average features obtained by extracting and summing the signal over the whole hyperspectral image. (a) Evolution of the carbon K-edge of MIL-100(Al) with the electron dose (cumulated doses, see SI); (b) the corresponding HAADF-STEM images and chemical maps obtained for peaks CL$_2$ and CL$_3$ at 10 ē/Å^2 and 310 ē/Å^2. Evolution with the electron dose for MIL-100(Fe) of (c) the oxygen K-edge (on the left) and iron L$_{2,3}$-edge (on the right) from 10 ē/Å^2 to 780 ē/Å^2 (single acquisition doses) and (d) the iron L$_{2,3}$-edge obtained for higher electron doses between 500 ē/Å^2 and 10^4 ē/Å^2(cumulated doses, see SI). (e) HAADF-STEM image (at the top) of MIL-100(Fe) and the corresponding elemental map (at the bottom) showing the spatial distribution of iron at 2x10^3 ē/Å^2. The grey lines are EEL spectra obtained for amorphous carbon in (a) and iron (III) oxide in (d), while the black spectrum in (a) and (c) corresponds to BTC analysed by near-edge X-ray absorption fine structure (Buck, M.; Zharnikov, M. personal communication, 2022). All spectra are unprocessed. The energy resolution is about $\delta E = 40$ meV for (a) $\delta E = 800$ meV for (c) and $\delta E = 220$ meV for (d). NanoMOFs spectra in (a) and (d) have been normalised to the integrated signal (details in SI). Chemical maps were obtained as described in SI, after denoising by principal component analysis. (b) and (e) are intensity maps of the corresponding features integrated over the grey areas in (a) and (d). The intensity scale has been normalised to compare chemical maps at a given dose in (b). The spatial resolution is 10 nm in (b) and 2 nm in (e). More details are provided in SI.*

To correlate the linker's and metal's behaviour induced by the electron beam, we used a 400 eV energy window to acquire simultaneously the oxygen K-edge and Fe L$_{2,3}$-edge of MIL-100(Fe). The spectra were calibrated according to a previous X-ray Absorption Near-Edge Structure (XANES) study on MIL-100(Fe).[41] In agreement with the carbon K-edge, the oxygen K-edge of MIL-100(Fe) shows the degradation of the organic part under irradiation (**Figure 3c**, left side, red lines). At low-dose (10 ē/Å^2), it displays two peaks at 532.2 eV (denoted CL$_5$) and ~ 540 eV (denoted CL$_7$). These features are in agreement with XANES data obtained from MIL-100(Fe)[41,42] and with NEXAFS measurements from free-standing BTC (comparison shown in **Figure 3c, black line**), where authors attributed the peaks to 1s–π*$_{C=O}$ (CL$_5$) and 1s–σ*$_{C\text{-}O}$ (CL$_7$) transitions of carboxyl groups, respectively.[31] As the metal-linker coordination bond is achieved through oxygen elements of carboxylate groups, one could expect additional features related to iron coordination. Indeed, the Fe*(3d)*-O*(2p)* orbital hybridisation[43] should be detected near 531.5 eV, as typically observed in EELS for iron (III) oxide (whose oxygen K-edge is shown in Figure S2). Here, its absence for MIL-100(Fe) is probably due to the lower concentration of iron-oxo clusters compared to carboxylic linkers (two linkers per cluster as indicated by the molecular formula $Fe_3O(OH)(BTC)_2(H_2O)_2$). Moreover, the oxygen K-edge analysis at low-dose (10 ē/Å^2) remains limited by its low cross-section, as observed in **Figure 3c,** where the fine structure analysis is hindered by the low SNR.

Upon irradiation, peak CL$_5$ decreases attesting to the damage of the -COO bonds. In the meantime, the asymmetric peak CL$_6$ appears near 534.2 eV. The identification of this peak is not straightforward. Previous studies based on NEXAFS and EELS have attributed a similar peak to 1s–π*$_{C=O}$, 1s–π*$_{C\text{-}OH}$ or 1s–σ*$_{C=O}$ transitions in BDC,[32] amino-acids,[44] oxidised multi-walled carbon nanotubes[45] and poly(ethylene terephthalate).[46] These multiple assignments make it difficult to identify the peak CL$_6$ reliably. Nonetheless, our present results on the carbon K-edge strongly suggest that the peak CL$_6$ is associated with the reduction of carboxylic groups into carbonyl. Indeed, we observe a concurrent increase of the peaks CL$_2$ and CL$_6$ above 30 ē/Å^2. As we assign the CL$_2$ peak to carbonyl groups (-CO), the CL$_6$ peak could also highlight the degradation of the linkers' -COO groups.

Thereafter, we studied the metal part of nanoMOFs and first kept focused on MIL-100(Fe) (**Figures 3c and 3d**). **Figure 3c (right side, red lines)** depicts the typical dose evolution observed for the iron L$_{2,3}$-edge on MIL-100(Fe). The L-edges of transition metals provide information on their electronic environment such as oxidation state and crystal-field splitting.[43] Unfortunately, the signal was found to be too low in low-dose conditions for any fine analysis. Iron's low cross-section and low concentration in the nanoMOFs make the signal tens of times weaker than the carbon K-edge one. A quantifiable signal was only detected for higher electron doses starting from 90 ē/Å^2. As aforementioned, these conditions imply that the organic part is already degraded. At this dose, MIL-100(Fe) exhibit a main peak at 707.6 eV, followed by a small shoulder at 708.9 eV observable for higher electron doses (i.e. 780 ē/Å^2). These data agree with previous XANES measurements on MIL-100(Fe) where authors attributed the signature to surface Fe^{2+} species produced by reduction under vacuum.[41,42] These authors also detected a peak at 534.2 eV similar to CL$_6$, which we assign here to degraded organic linkers. Herein, the combined systematic study of the iron, oxygen and carbon edges as a function of the electron dose provides supplementary information on this phenomenon. This dose-effect study suggests that the linkers' reduction induced by radiolysis can also affect the coordination structure of iron and hence, its valency. Nonetheless, the iron behaviour under high electron irradiation remains unclear. **Figure 3d** shows the evolution of the iron L$_{2,3}$-edge of MIL-100(Fe) compared to an iron(III) oxide reference (grey line) for higher doses between 500 ē/Å^2 and 10^4 ē/Å^2. Starting from 2x10^3 ē/Å^2, the peak of MIL-100(Fe) located at 708.9 eV drastically increases revealing changes in electronic configuration. For this high dose range, the organic fraction is drastically degraded and may involve a complex chemical evolution which is not straightforward to disentangle.

Figure 3e shows the elemental iron map achieved by integrating the L$_3$-edge signal after PCA processing (details in SI). It attests to a homogeneous distribution of iron across the nanoMOFs, with a spatial resolution of 2 nm. Iron valency distribution could not be mapped at low doses because of its weak SNR features and, for higher electron doses, its distribution analysis is irrelevant since the nanoMOFs are degraded. Other metallic edges of nanoMOFs were also detected in the same conditions. Figure S4 shows the iron M$_{2,3}$-edge of MIL-100(Fe) and zirconium M$_{2,3,4,5}$ and N$_{2,3}$-edges of UiO-66. For MIL-100(Al), the aluminium K and L$_{2,3}$-edges typically located at 1560 eV and 77 eV were not detected, probably due to their low cross-section and low aluminium concentration in the specimen.

Our results provide insights into the nanoscale analysis of intact complex organic assemblies. Compared to the commonly used soft X-ray absorption spectromicroscopies,[30] EELS provides a similar fine structure analysis with high energy resolution features, closely similar to the XANES and NEXAFS studies, but also enables a low-dose chemical mapping of the linkers functions with an improved spatial resolution[6] down to 10 nm (**Figure 3b**). These results demonstrate the possibility of characterising intact sensitive specimens at the nanoscale.

Low-loss excitations

Thereafter, we focus on analysing the LL region, where the excitations of valence electrons are visible. First, we used a large energy window of 400 eV to simultaneously monitor the LL and CL evolutions with the electron dose (**Figure 4a-c**, δE = 800 meV). Then, we used a smaller energy window, spanning 16 eV, to achieve a better energy resolution (**Figure 4d**, δE = 40 meV). The more significant LL contribution shared for the three nanoMOFs is a huge bulk plasmon peak standing out near 22 eV, which is due to the electrons' collective oscillations (observed in **Figure 2b**). As shown in **Figure 4a-c**, other molecular are also observable in the UV energy range below 10 eV. Unlike the carbon K-edge that is similar for the three systems, distinct LL features are found for each nanoMOF. **Figure 4d** shows the low-loss response of nanoMOFs obtained at low (10 ē/Å^{2}) and higher (above 130 ē/Å^{2}) electron doses with a closer look between 2 eV and 10 eV. At low-dose, MIL-100(Al) displays an intense peak centred around 5.8 eV with shoulders at 5.2 eV and 6.6 eV. For MIL-100(Fe), a similar feature is exhibited with a slight blue shift of the intense peak to 5.9 eV and less pronounced shoulders at 5.3 eV and 6.6 eV. Both MIL-100 exhibit two weak features at 2.5 eV and 3.5 eV and an additional very weak peak near 4.5 eV. Conversely, only two intense and asymmetric peaks are found for UiO-66 near 5.1 eV and 6.5 eV. The aforementioned signals of the three nanoMOFs agree reasonably well with UV-vis experiments between 2 eV and 6 eV.[47–49] They have been usually related to π–π^* transitions but barely assigned to specific chemical functions. To get more insights, we compared the signature of nanoMOFs with their free-standing organic linkers, focusing on the shaded area LL$_2$ in **Figure 4a-d**. The two organic linkers (BTC and BDC) show two peaks at 5.3 eV and 6.8 eV (see Figure S5 for the comparison of nanoMOFs, BTC and BDC spectra). They were attributed to the designated benzoic and local-excitation bands of functionalised phenyl groups, respectively.[50] These bands seem to be slightly red-shifted for nanoMOFs, where the linkers are coordinated with metals (e.g. shifted to 5.1 eV and 6.5 eV for UiO-66). Hence, we assume that the metal bonding affects the LL$_2$ features of the coordinated organic molecules. This is in agreement with previous UV-vis studies that related the 5.1 eV peak of UiO-66 to linker-to-metal charge transfer.[51–53] In addition, the peak observed for MIL-100 around 5.8/5.9 eV is not detected for the organic linkers. Thus, this intense peak may also be related to metal bonding. In a nutshell, our results suggest the LL$_2$ feature may be considered as a spectral fingerprint of the coordination bonding between the organic and metal parts of the nanoMOFs. In the absence of UV-vis data from the literature, the weak features observed for MIL-100 below 4 eV are not straightforward to interpret and theoretical studies are required in order to elucidate their origin.

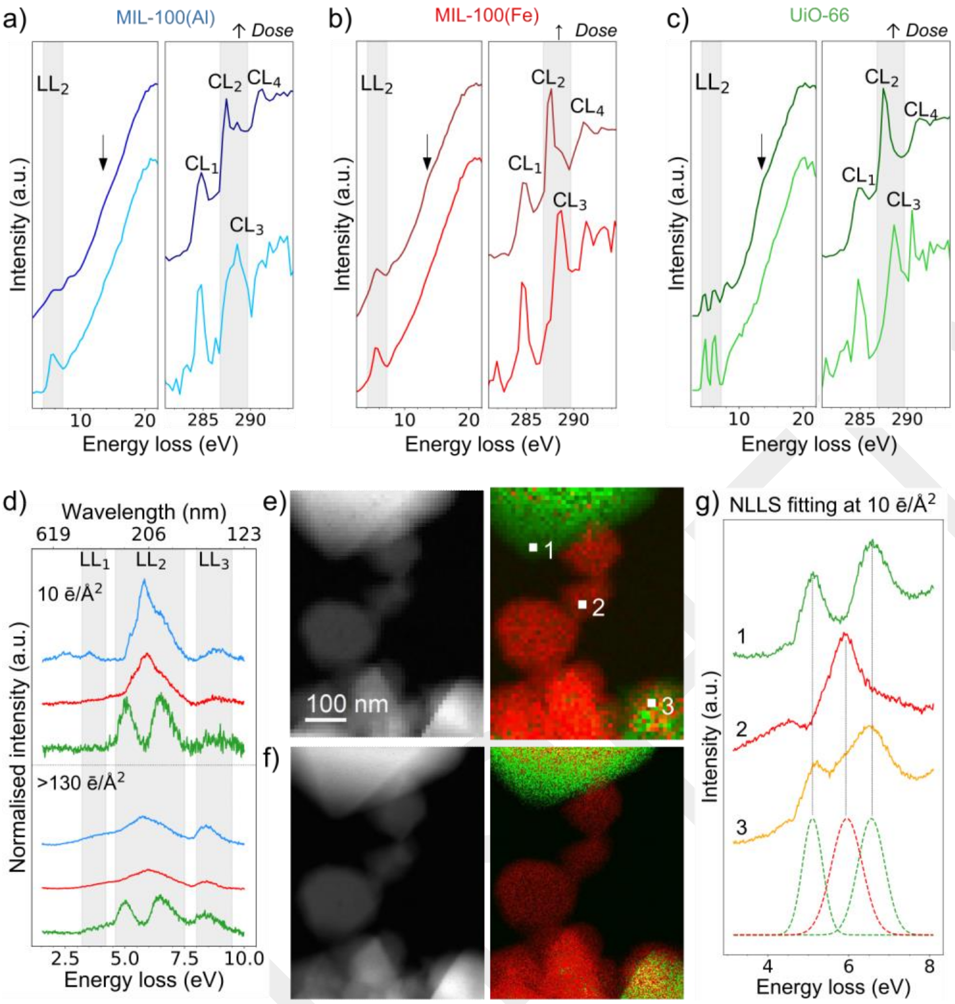

***Figure 4**. Low-loss analysis of MIL-100 and UiO-66 nanoparticles as a function of the electron dose. (a-c) Evolution with the electron dose of the low-loss signal acquired simultaneously with the carbon K-edge using the 400 eV energy window. The energy resolution is about δE = 800 meV. The electron doses are 10 ē/Å^2 for light colours and >750 ē/Å^2 for dark colours (single acquisition doses, see SI). Black arrows near 14 eV indicate the H K-edge revealing H_2 production under irradiation. (d) Comparison of the low-loss signal obtained at electron dose of 10 ē/Å^2 (top row) and above 130 ē/Å^2 (bottom row) (cumulated doses, see SI) with a smaller energy window spanning 16 eV (energy resolution of about δE = 40 meV). Spectra are normalised to the integrated signal (see SI). (e-f) HAADF-STEM images (left) and the corresponding maps (right) of UiO-66 (green) and MIL-100(Fe) (red) obtained at (e) 10 ē/Å^2 and (f) 210 ē/Å^2 after PCA processing. The pixel size is 10 nm in (e) and 2 nm in (f). (g) Spectra obtained after PCA (solid lines) from the areas labelled 1, 2, and 3 in (e) and the NLLS components (dashed lines) used to map their distribution. Spectra of (a-d) are average raw data obtained by extracting and summing the signal over hundreds of square nanometres. Blue, red and green represent MIL-100(Al), MIL-100(Fe), UiO-66 in (a-g) while orange line stands for the superimposed signal of the latter two in (g). SI provides more details.*

As already noticed in the carbon K-edge study, the LL signal displays particular changes upon electron irradiation. As shown in **Figure 4a-d**, all the LL$_2$ features decrease with the electron dose. A more detailed evolution with the electron dose can be found in Figure S5. Considering our assignment, this can reveal the loss of coordination bonds between metal clusters and organic linkers that are progressively degraded. In the meantime, a peak near 4 eV (denoted LL$_1$) rises with the electron dose. Previous EELS and UV-vis studies of the polymethylmethacrylate degradation induced by irradiation have attributed this peak to the formation of carbonyl functions (n–$\pi^*_{C=O}$ transitions).[54,55] The simultaneous acquisition of the LL and CL signals (400 eV energy window) allows us to compare their evolution. **Figures 4a-c**, S1 and S5 show the concurrent formation of peaks LL_1 and CL_2 with the decrease of LL_2 features for doses above 130 ē/Å^2. These observations suggest that the loss of coordination bonds is related to the reduction of carboxylic groups (-COO) into carbonyl moieties (-CO). Indeed, as the nanoMOFs assembly is conducted by the coordination of the carboxylic functions, their reduction into carbonyl species weakens the coordination bond, inducing the decrease of the features LL_2.

Interestingly, the three nanoMOFs display a similar peak near 9 eV (denoted LL_3, **Figure 4d**), which is red-shifted to 8.4 eV upon irradiation (see Figure S5). Such a peak has previously been attributed to water exciton.[36,56] Its presence for MIL-100 could be related to structural water as indicated by the chemical formula ($Al_3O(OH)(BTC)_2(H_2O)_2$ and $Fe_3O(OH)(BTC)_2(H_2O)_2$). But, considering water molecules to be prone to beam degradation,[57] it could also be attributed to hydroxyl groups (-OH), also present in the three nanoMOFs (UiO-66 chemical formula: $Zr_6O_4(OH)_4(BDC)_6$). Another peak near 14 eV is also observable for electron doses above 80 ē/Å^2 (**Figure 4a-c**). As previously reported,[36,58] it is associated with the hydrogen K-edge, attesting to the production of H_2 upon electron irradiation. Since we assume direct dehydrogenation of the organic linkers even at low-dose (no $1s–\sigma^*_{C\text{-}H}$ transitions are observed in our carbon K-edge data), the dihydrogen signal certainly comes from the hydroxyl groups or structural water of nanoMOFs. Noteworthy, it suggests that irradiation of hydroxyl groups and structural water may enhance the beam-induced degradation effect as (i) it could produce reactive species such as radicals, which may increase the radiolysis of the organic linkers[36] and (ii) lead to complex chemical evolution affecting the metal environment (e.g. change of the iron $L_{2,3}$-edge for high electron doses in Figure 3d).

Recent studies have reported about damage-free LL EELS signatures of organic specimens[11,17] but none of them provides maps of the signals. Conversely, other authors used higher electron doses to map the signal of MOF glass blends,[16] probably inducing beam damages. Here, a specimen was prepared by mixing MIL-100(Fe) with UiO-66 and LL maps were recorded at low-dose to ensure nanoMOFs being intact (**Figure 4e-f**). As shown in **Figures 4e and 4g**, each nanoMOF specific feature was mapped at 10 ē/Å^2, using PCA processing and Nonlinear Least-Squares (NLLS) Gaussian fitting (details on the NLLS Gaussian fitting are provided in SI, Figure S6). To assess the possibility of localising the two signals at higher electron doses, the study was repeated at 210 ē/Å^2 (**Figure 4f**). In the two conditions, MIL-100(Fe) (in red) was successfully distinguished from UiO-66 (in green). This result demonstrates that the chemical information can still be localised despite degradation under electron irradiation. The main difference between the two conditions lies in the spatial resolution: the lowest electron dose, associated with no degradation, imposes a large pixel size of 10 nm, whereas fixing a higher dose allows an increase of the pixel size to 1 nm but induces beam damage. This highlights the general trend that the chemical imaging of sensitive nanomaterials is a trade-off between spatial resolution and induced degradation. Our results illustrate the possibility of distinguishing organic molecules in the LL energy range and mapping their features with a nanoscale resolution.

By correlating the CL and LL energy ranges, our results enable deciphering the chemical changes induced by electron irradiation. To a lesser extent, the chemical changes under irradiation have previously been studied for MOFs in the LL and CL.[10] Here, with low-dose conditions and an improved energy resolution, we further demonstrate that it is possible to distinguish the direct beam effect (reduction of carboxylic moieties, radiolysis of hydroxyl groups and H_2 production) from the secondary reactions implied (loss of coordination bond and iron reduction). Nonetheless, since EELS allows one to reach energy ranges that are arduously covered by conventional techniques (e.g. VUV, XUV), all our assignments remain assumptions that need to be confirmed with theoretical studies.

Ultralow-loss excitations

The three nanoMOFs and their free-standing organic linkers were analysed in the vibrational energy window with conventional attenuated total reflection (ATR) – Fourier Transform (FT) IR and ULL STEM-EELS. The energy resolution was equal to 4 cm^{-1} for FTIR and 12 meV (97 cm^{-1}) for EELS. By applying the Richardson-Lucy deconvolution (details in SI and Figure S7), the EELS ZLP was narrowed to reach an energy resolution of $\delta E = 7$ meV (55 cm^{-1}). **Figure 5a** compares the resulting spectra obtained with the two techniques. The full spectra ranging from 70 meV to 500 meV are given in Figures S8 and S9. Here, we briefly describe the main vibrational modes denoted from ULL$_1$ to ULL$_6$ (grey areas in **Figures 5a**, S5 and S6) but a complete assignment based on the literature can be found in Table S1.

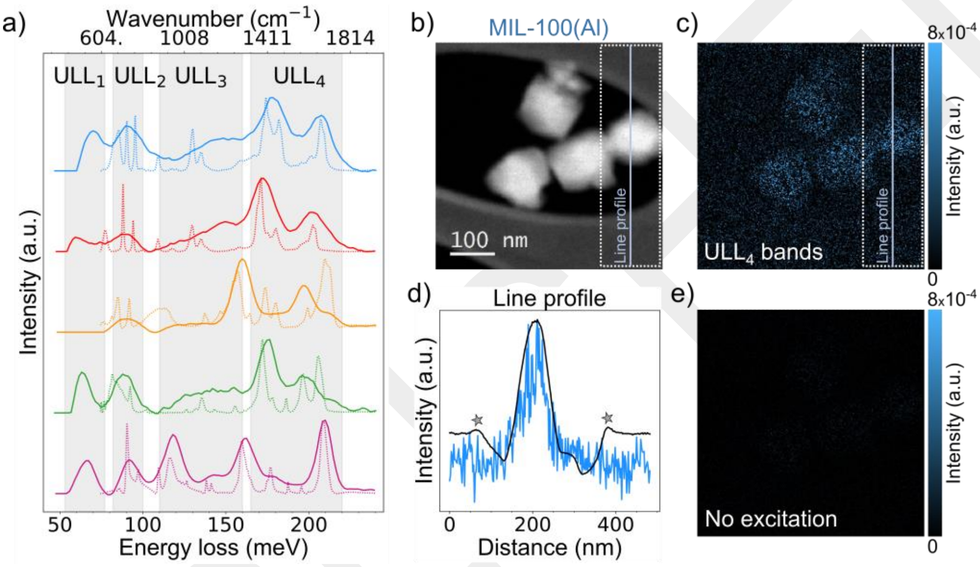

***Figure 5**. Ultralow-loss analysis of nanoMOFs and their free-standing organic linkers acquired at about 120 ē/Å^2 (single acquisition dose, beam current = 4 pA, total acquisition time ~ 100s). (a) Comparison of the ultralow-loss EELS (solid line) with conventional FTIR (dotted line) for MIL-100(Al) in blue, MIL-100(Fe) in red, BTC in yellow, UiO-66 in green and BDC in pink. All EEL spectra are averages obtained by extracting and summing the signal over the whole hyperspectral image. They have been collected in an energy window of 2 eV and deconvolved using the Richardson-Lucy Algorithm (details in SI). The EEL energy resolution is about $\delta E = 7$ meV (55 cm^{-1}), and the FTIR one is about 4 cm^{-1} (0.5 meV). (b) HAADF image of MIL-100(Al) nanoparticles and (c) the corresponding chemical map of the CO vibration modes (shaded ULL$_4$ area in (a)). (d) Intensity profiles acquired along the indicated line of the HAADF image (black line profile) and the chemical map (blue line profile) from (b-c). To increase the SNR, several line profiles were added, as illustrated by the white dotted rectangle in (b-c). It shows a localised signal on the nanoparticles. Grey stars indicate the amorphous carbon film signal. (e) Chemical map obtained on an area where no excitation was detected (450 – 495 meV). It attests thickness does not contribute to the signal map of MIL-100(Al) in (b). The pixel size is 2 nm in (b-c) and (e). Chemical maps were obtained as described in SI. They have been normalised to the ZLP to exclude the thickness variations. For comparison, their intensity scale is also normalised (see SI).*

FTIR spectra display the features specific to the specimen's functional groups (**Figure 5a**). In the ULL$_2$ area, characteristic bands of the metal part are observed for MIL-100(Fe) and UiO-66. For MIL-100(Fe), the asymmetric Fe$_3$-μ_3-O stretching band is located at 624 cm^{-1} (77 meV). Noticeably, this band carries information on the oxidation state of iron: a previous FTIR study has demonstrated that the partial reduction of iron induces a blue shift of this band from 618 cm^{-1} to 597 cm^{-1}.[59] Here, our FTIR data indicate that non-irradiated MIL-100(Fe) contain Fe^{3+} ions, in agreement with previous Mössbauer studies.[60] Likewise, the Zr$_3$-μ_3-O stretching bands of UiO-66 are observed at 620 – 745 cm^{-1} (80 - 90 meV), where they are mixed with the vibration modes of the organic part. The five specimens display significant bands in the ULL$_4$ area. They are attributed to CO stretching modes of carboxylic groups. By comparing the nanoMOFs with their organic linkers, these bands seem to shift upon coordination. Whereas the BTC CO bands are located at 1326 cm^{-1} (164 meV) and 1691 cm^{-1} (210 meV), they are found at 1405 cm^{-1} (174 meV), 1672 cm^{-1} (207 meV) for MIL-100(Al) and 1380 cm^{-1} (171 meV), 1632 cm^{-1} (202 meV) for MIL-100(Fe). Similarly, CO bands are red-shifted from 1287 cm^{-1} (160 meV) and 1682 cm^{-1} (209 meV) in BDC to 1387 cm^{-1} (172 meV) and 1584 cm^{-1} (196 meV) in UiO-66 (see Table S1). This comparison also highlights the distinct features of BDC, which exhibits additional bands in the ULL3 area corresponding to CC, CO and CH bending modes. In the three nanoMOFs spectra, residual solvents (water, ethanol and N,N-dimethylformamide, DMF) are also detected. More details are given in Figure S8.

In EELS data, the main specific ULL features observed for the five specimens are in agreement with the FTIR results (**Figure 5a**). Given the lower energy resolution, all the peaks cannot be observed, but the metal and carboxylic main features were readily detected. The CH bending (ULL$_2$ area) and CO stretching modes (ULL$_4$ area) match the FTIR experiments for all the specimens except BTC. Indeed, the EELS intensity of the BTC CO band (215 meV, 1734 cm^{-1}) seems reduced compared to FTIR. Such spectral differences between the two techniques may be explained by distinct excitation mechanisms following photons absorption (FTIR) and electrons inelastic scattering (EELS). Nevertheless, a complete understanding will need the help of theoretical calculations. At high energy losses, the features detected in EELS as in FTIR can be attributed to the remaining solvents (adsorbed DMF, ethanol and structural water). A more detailed discussion is provided in Figure S9. Beyond the similarities with the FTIR signal, EELS reveals additional vibrational excitations at low energy (ULL$_1$ peaks) that were not reached with the conventional technique (**Figure 5a**). Al-O, Fe-O and Zr-O stretching modes of MIL-100(Al), MIL-100(Fe) and UiO-66 were recorded in the far IR region at 71 meV (573 cm^{-1}), 60 meV (484 cm^{-1}) and 64 meV (516 cm^{-1}), respectively (assignment based on the literature as cited in Table S1).

Despite the generally good agreement between FTIR and EELS data (**Figure 5a**), minor differences were observed. Indeed, the ULL study was performed at electron doses around 120 ē/Å^2 to increase the SNR and, based on the carbon K-edge analysis (**Figure 3a**), these conditions induce chemical damage to the specimens. Effective evidence lies in the peak found in EELS at 291 meV (2347 cm^{-1}) for the nanoMOFs (indicated in Figure S9 with an arrow) that was not detected in FTIR (Figure S8) and can correspond to degraded products. Moreover, it must be mentioned that all the aforementioned bands (**Figure 5a**) may be slightly shifted from their initial positions due to partial degradation of the chemical functions. For instance, the CO stretching modes (ULL$_4$ peaks) could correspond to degraded carboxylic (COO) groups, or even carbonyl (CO) groups, as demonstrated in the carbon K-edge study. Given the EELS' limited energy resolution, such subtle differences cannot be discriminated.

Recent studies have suggested a possible damage-free analysis of sensitive specimens in the ULL energy range using the aloof configuration.[11–13,61,62] By focusing the electron probe a few nanometers away from the specimen, the authors recorded an intact signal. This configuration leverages the long-range interactions associated with the phonon excitations to collect a signal without direct impact on the specimen.[7] Here, measurements were repeated in transmission and aloof configurations, and no differences were observed apart from a lower SNR (see Figure S10). This points out an interesting fact: here, EELS performed in the transmission (bulk excitation) and the aloof modes give peaks at sensibly the same energy revealing an absence of dispersion effect. Collective excitations (e.g. surface phonon polaritons) would implied a dispersion effect, and its absence here indicates the excitation of very localised vibrational modes associated with molecular vibrations. As a further evidence, we did not observe the rapid surface signal intensity modulation characteristic of confined surface phonon polaritons in phononic nanomaterials.[63] Thereafter, the transmission configuration was chosen for our experiments because, compared to the aloof one, it offers the possibility of a spatially resolved analysis, allowing chemical mapping.

By using the transmission configuration, previous studies have mapped the linker signature of MOF crystal-glass composites, notably constituted of BDC.[14] Yet, while employing higher electron doses (below 5x10^3 ē/Å^2), their analysis was still affected by the difficulty of ZLP tail removal. Herein, with lower electron doses (~120 ē/Å^2), we provide a chemical map of the MIL-100(Al) linkers' distribution at a pixel size of 2 nm. To do so, we chose the MIL-100(Al)'s CO stretching modes since they are the most intense features of the spectra. Despite their possible degradation, they remain an appropriate and robust spectral fingerprint of the nanoMOFs vibrational excitations. **Figure 5b-c** displays the HAADF image and chemical map obtained by integrating the intensity of the two CO bands (ULL$_4$ peaks) after background subtraction and PCA processing (see SI). To exclude any contribution from the nanoparticles thickness, the chemical map has been normalised by the ZLP intensity. An enhanced signal is detected on the nanoMOFs. **Figure 5d** provides averaged intensity line profiles of the HAADF (in black) and chemical map images (in blue) measured in the white dotted rectangle. The HAADF and chemical signals are clearly correlated. A weaker signal is also found on the amorphous carbon film (grey area in the HAADF image of **Figure 5b**, and indicated by grey stars in the line profile of **Figure 5d**) due to excitations in the ULL$_4$ area (Figure S9).[64] Finally, a map was obtained with a similar data processing from an energy range with no excitations (450 – 495 meV) and no signal was detected (**Figure 5e**). All together, these results attest to the effective localisation of the CO vibrational modes on the nanoMOFs. They demonstrate the possibility of mapping the vibrational excitations of sensitive nanoMOFs with high energy and spatial resolution. Compared to IR spectromicroscopy, EELS provides similar information on the molecular vibrational modes, but it also allows mapping their distribution with an improved spatial resolution (at the nanoscale).

Monitoring beam-induced chemical reactions.

The present study has allowed us to monitor the chemical degradation of three sensitive nanoMOFs under electron irradiation. Thanks to the multimodal approach, we have assigned all the vibrational and electronic transitions observed in the IR, UV and soft X-ray energy ranges to specific functional groups. In **Figure 6**, we resume the schematic representation of the nanoMOFs chemical structure given in **Figure 1d** and we indicate the corresponding peaks described in this manuscript according to the electron dose. The multimodal information was cross-correlated between the three energy windows to obtain a deep characterisation of nanoMOFs. For instance, at low-dose, while the metal-linker coordination bonding is not observed in the CL, it is well documented in the LL and ULL regions (peaks LL$_2$, ULL$_1$ and ULL$_2$). Upon irradiation, LL and CL features illustrate radiolysis damages to the organic linkers through (i) instantaneous dehydrogenation of the benzene ring, (ii) breakage of the benzene double bonds (peak CL$_1$) leading to the formation of single bonds (peak CL$_4$) and (iii) reduction of the carboxylic groups (-COO, peaks CL$_3$ and CL$_5$) into carbonyl composites (-CO, peak CL$_2$) causing the loss of coordination bond (peak LL$_2$). We suppose this linker vacancy leads to metal reduction. H_2 production under irradiation suggests (i) hydrogen loss from hydroxyl groups and remaining solvents (structural water, ethanol or DMF) and (ii) the formation of reactive species, such as radicals, that could enhance the beam-induced degradation effect through complex reactions. This mechanism remains an assumption that would need further investigations to be clarified.

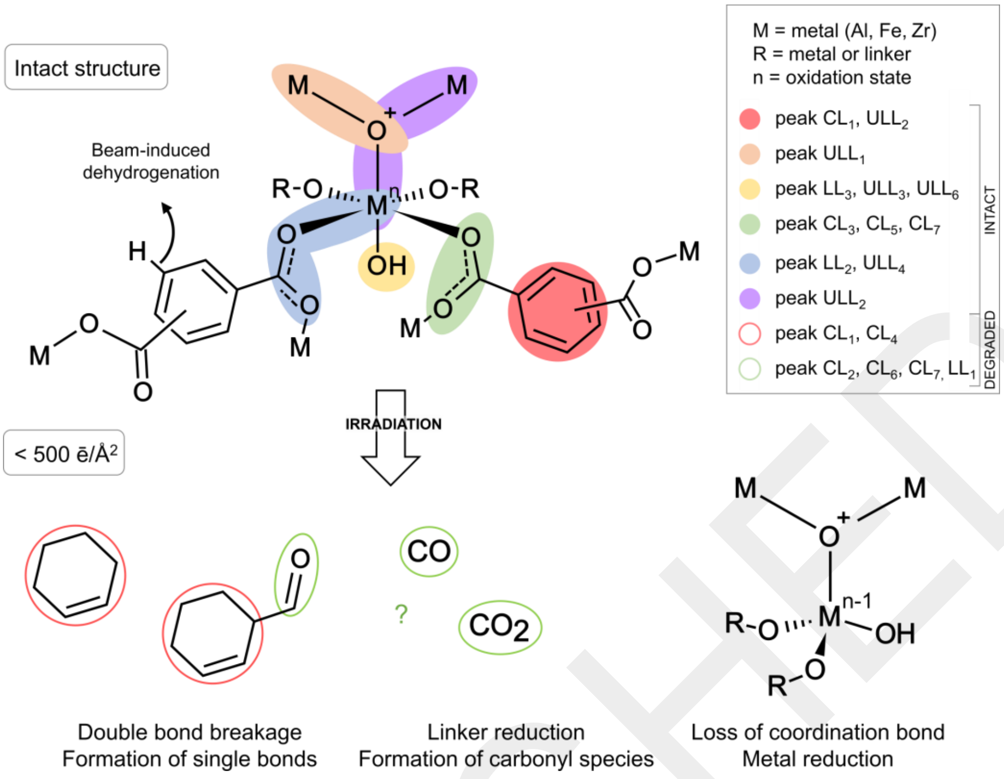

***Figure 6**. Schematic representation of the main irradiation effects on the molecular structure of nanoMOFs. The different MIL-100 and UiO-66 structures have been simplified using general atom labels (M for metals and R for metals or linkers). At the top, the intact molecular structure of nanoMOFs depicts their characteristic chemical functions. The colours relate them to the peak assignment described in this manuscript and Table S1 for intact signatures, assuming that beam alteration is not detected in ULL EELS due to the energy resolution. At the bottom, the possible degraded structures are illustrated according to the observed alterations in EELS for doses below 500 ē/Å^2.*

CONCLUSION

This study presents a damage-free multimodal analysis of nanoMOFs at the nanoscale. Our results underline the powerful possibilities offered by STEM microscopes equipped with a monochromated beam and a direct electron detection in terms of energy resolution (down to 12 meV) and sensitivity for studying beam-sensitive specimens. The detector high dynamic range enables the analysis of very low signals obtained in low-dose conditions[22] and a multimodal analysis with the simultaneous acquisition of the LL and CL signals without saturation from the ZLP. With low-dose (10 ē/Å^2) and cryogenic conditions, as employed for cryo-TEM high-resolution imaging of biological specimens, we successfully revealed the intact signatures of nanoMOFs and related them to specific electronic transitions. In these conditions, we outlined the spectral similarities between EELS and photon-based spectroscopic techniques. In the IR window, the vibration modes agreed with FTIR data acquired on the same specimens, albeit less energy resolved. In the X-ray window, the fine structure analysis revealed features very similar to the X-ray absorption spectroscopy data described in the literature. Besides, since EELS covers a broader energy range compared to photon-based spectroscopies, it has access to energy domains that are arduously reached by other techniques such as vacuum UV (100 – 200 nm, 6 – 12 eV) and extreme UV (10 – 100 nm, 12 – 120 eV) and are of main interest for investigating the valence electron excitations. Namely, we revealed valuable information on the metal-linker coordination bond in the vacuum-

UV range, which precise identification needs to be specified by theoretical studies. Furthermore, at low-dose, we successfully mapped the distribution of the nanoMOFs' intact chemical groups in the three energy ranges, with a 10 nm spatial resolution. Then, since low-dose constrained the analysis spatial resolution, we demonstrated that higher electron doses could be employed to map the LL signal of MIL-100(Fe) and UiO-66 with a smaller pixel size (2 nm), without impeding the localisation of the chemical signature. By increasing the electron dose from 10 $\bar{e}/Å^2$ to 10^4 $\bar{e}/Å^2$, we monitored the irradiation-induced effect on these sensitive specimens in the three energy ranges and identified the chemical groups of intact and degraded signatures.

This study demonstrates STEM-EELS as a key technique for understanding the complexity of highly sensitive nanostructures, offering the possibility of a deep characterisation in a wide energy range, spanning from IR through UV to soft X-rays, in a single experiment. Our results outline that this multimodal approach allows the identification and mapping of the functional groups of organic-inorganic specimens. Similar procedures could also be used to study other hybrid specimens of various compositions such as organic blend components, organic-inorganic interfaces or nanoparticles embedded in organic matrices or in the cellular context, but also pure organic materials as biological macromolecules or cellular organelles. Not only can products be identified, but chemical reactions can also be monitored to decipher complex mechanisms. Therefore, chemical reactions in nanosystems, including the most sensitive ones as hybrid or organic materials, could also be investigated *in situ* when changing the temperature (heating/cooling chip devices), the environment (liquid or gas reaction cells) or under irradiation (photons or electrons). In the following, we aim to investigate nanoMOFs as drug nanocarriers by characterising the drug loading and distribution and unveiling the cellular fate of single nanoparticles.

EXPERIMENTAL SECTION

NanoMOFs preparation. MIL-100(Fe) and MIL-100(Al) were synthesised following the previously reported microwave-assisted hydrothermal method.[65] UiO-66 nanoparticles were synthesised following the procedure described in [[25]]. In order to assess their purity, the three nanoMOFs were analysed after their synthesis and prior to nanoscale characterization, by Fourier Transform IR Spectroscopy (FTIR) in the attenuated total reflection (ATR) mode (Figure S8). Synthesis and specimen preparations are detailed in SI.

Cryogenic Transmission Electron Microscopy (cryo-TEM). The experiments were performed at 200kV on a JEOL JEM-2010 transmission electron microscope equipped with a *Schottky* field emission gun, a Gatan 626 cryo-holder and a Gatan Ultrascan 4K CCD camera. The specimens were imaged with a magnification of 50kx and 80kx using a minimal dose system estimated between 10 and 15 $\bar{e}/Å^2$. Images were collected between 1000 nm and 2500 nm nominal defocus. All the results presented here are unprocessed.

Scanning Transmission Electron Microscopy and Electron Energy Loss Spectroscopy (STEM-EELS). STEM-EELS experiments were carried out on a monochromated Cs-corrected Nion Hermes 200-S microscope operated at 100kV, equipped with a single tilt cryo-specimen holder (HennyZ), a Nion Iris spectrometer and a Merlin Direct Electron Detector camera (Quantum Detectors, UK) for spectroscopic analysis. The convergence semi-angle was set to 10 mrad, enabling a sub-nanometer beam size. The spectra were recorded for each characteristic feature in different energy windows by adjusting the range to either 2 eV (dispersion of 1.6 meV/channel) or 16 eV (15.2 meV/channel) or 116 eV (112 meV/channel) or 400 eV (389 meV/channel). The entrance aperture for EELS was set to 300 µm for the 2 eV energy window and to 1 mm for the others. For each dispersion, the energy resolution δE was measured from the full-width at half-maximum of the ZLP. It reached

12 meV for the lowest energy window spanning 2 eV. Electron dose effects were analysed for a total dose from $10\ \bar{e}/\text{Å}^2$ to $10^4\ \bar{e}/\text{Å}^2$ and dose rates ranging from $4\text{x}10^3\ \bar{e}/\text{Å}^2/\text{s}$ to $10^6\ \bar{e}/\text{Å}^2/\text{s}$ (details on total dose and dose rates are given in SI). This study has been performed by either a single acquisition on different areas or several successive acquisitions on the same area. The increasing single acquisition doses have been obtained by raising the probe current (from 6 pA to 40 pA), the dwell time (from 2 ms to 3 ms) and reducing the pixel size (from 10 nm to 3 nm). The cumulated doses of successive acquisitions have been obtained at a constant beam current (6 pA or 15 pA), by varying the pixel size (from 10 nm to 1 nm) and dwell time (from 2 ms to 80 ms). More details are given in SI. As EELS imposes a maximum thickness to collect a signal, we limited the analysis to small nanoparticles (< 150 nm). Apart from the LL mapping, we selected those above the grid carbon film holes to avoid the carbon contribution to the measurements. All EELS data were acquired in the conventional transmission mode, except for the organic linkers in the ULL energy range, which were analysed in the aloof configuration due to their large thickness. Additional EELS for iron (III) oxide reference spectra was performed on a Nion Ultrastem 200 operating at 100 kV with a probe semi-angle of 25 mrad, an EELS aperture of 2 mm and an EELS energy window of 200 eV. Details on data processing are given in SI.

Fourier-Transform Infrared (FTIR) spectroscopy. Conventional FTIR spectra were collected for each type of nanoMOFs, and their corresponding organic linkers with a Vertex 70 spectrometer (Bruker, Germany) equipped with an ATR device. Data were collected between 4000 cm^{-1} and 600 cm^{-1} with a 1.5 mm spectral aperture averaging 128 scans. The spectral resolution was equal to 4 cm^{-1} (0.5 meV). SI provides details on the data processing.

SUPPORTING INFORMATION

The Supporting Information is available free of charge at https://pubs.acs.org/doi/10.1021/acsnano.XXX. Additional experimental details of the nanoMOFs synthesis and sample preparation, the dose-effect experiment and data processing, additional FTIR and EELS spectra in the three energy ranges and the table of assignments (PDF).

ACKNOWLEDGMENTS

This work has been partly supported by the National Agency for Research under the program of future investment TEMPOS CHROMATEM (Reference no. ANR-10-EQPX-50) and the European Union’s Horizon 2020 research and innovation program (Grant no. 823717, ESTEEM3). For the cryo-TEM experiments, the authors acknowledge the financial support from the « Investissements d’Avenir » of the LabEx PALM (ANR-10-LABX-0039-PALM). We thank the STEM team at the Laboratoire de Physique des Solides, particularly M. Tencé, M. Walls, S. Y. Woo and L. H. G. Tizei for discussions and help with the EELS experiments. We are grateful to X. Li and all the NanoBio team from Institut des Sciences Moléculaires d’Orsay for kindly providing the UiO-66 specimen and helping with the synthesis, and to the CPSysBio team at the Institut Chimie Physique, in particular A. Dazzi, A. Deniset-Besseau and J. Mathurin, for allowing us access to the ATR-FTIR equipment. We sincerely thank T. Okajima from the Aichi Synchrotron Radiation Center, M. Zharnikov from Heidelberg University and M. Buck from University of St Andrews for sharing their NEXAFS data on the free-standing organic linkers.

REFERENCES

(1) Vaghasia, R.; Savani, M.; Saini, B. Metal Organic Frameworks (MOFs) as an Adsorbent Material for CO2 Capture. In *Metal Nanocomposites for Energy and Environmental Applications*; Singh, S. P., Agarwal, A. K., Kumar, K., Srivastav, S. K., Eds.; Energy, Environment, and Sustainability; Springer: Singapore, 2022; pp 157–186. https://doi.org/10.1007/978-981-16-8599-6_7.

(2) Ahmad, S.; Abbasi, B. bin K.; Nazir, M. S.; Abdullah, M. A. Metal Organic Frameworks (MOFs) as Formidable Candidate for Pharmaceutical Wastewater Treatment. In *Inorganic-Organic Composites for Water and Wastewater Treatment: Volume 2*; Lichtfouse, E., Muthu, S. S., Khadir, A., Eds.; Environmental Footprints and Eco-design of Products and Processes; Springer: Singapore, 2022; pp 37–63. https://doi.org/10.1007/978-981-16-5928-7_2.

(3) Qin, Y.; Hao, M.; Li, Z. Chapter 17 - Metal–Organic Frameworks for Photocatalysis. In *Interface Science and Technology*; Yu, J., Jaroniec, M., Jiang, C., Eds.; Surface Science of Photocatalysis; Elsevier, 2020; Vol. 31, pp 541–579. https://doi.org/10.1016/B978-0-08-102890-2.00017-8.

(4) Sacchetti, A.; Rossetti, A.; Martí-Rujas, J. Chapter Three - Metal-Organic Frameworks (MOFs) for Sensing. In *Advances in Chemical Engineering*; Magagnin, L., Rossi, F., Eds.; Soft Robotics; Academic Press, 2021; Vol. 57, pp 91–122. https://doi.org/10.1016/bs.ache.2021.03.002.

(5) He, S.; Wu, L.; Li, X.; Sun, H.; Xiong, T.; Liu, J.; Huang, C.; Xu, H.; Sun, H.; Chen, W.; Gref, R.; Zhang, J. Metal-Organic Frameworks for Advanced Drug Delivery. *Acta Pharm. Sin. B* **2021**. https://doi.org/10.1016/j.apsb.2021.03.019.

(6) Chaupard, M.; de Frutos, M.; Gref, R. Deciphering the Structure and Chemical Composition of Drug Nanocarriers: From Bulk Approaches to Individual Nanoparticle Characterization. *Part. Part. Syst. Charact.* **2021**, *38* (9), 2100022. https://doi.org/10.1002/ppsc.202100022.

(7) Colliex, C. From Early to Present and Future Achievements of EELS in the TEM. *Eur. Phys. J. Appl. Phys.* **2022**, *97*, 38. https://doi.org/10.1051/epjap/2022220012.

(8) Egerton, R. F. Radiation Damage to Organic and Inorganic Specimens in the TEM. *Micron* **2019**, *119*, 72–87. https://doi.org/10.1016/j.micron.2019.01.005.

(9) Ilett, M.; S'ari, M.; Freeman, H.; Aslam, Z.; Koniuch, N.; Afzali, M.; Cattle, J.; Hooley, R.; Roncal-Herrero, T.; Collins, S. M.; Hondow, N.; Brown, A.; Brydson, R. Analysis of Complex, Beam-Sensitive Materials by Transmission Electron Microscopy and Associated Techniques. *Philos. Trans. R. Soc. Math. Phys. Eng. Sci.* **2020**, *378* (2186), 20190601. https://doi.org/10.1098/rsta.2019.0601.

(10) Ghosh, S.; Yun, H.; Kumar, P.; Conrad, S.; Tsapatsis, M.; Mkhoyan, K. A. Two Distinct Stages of Structural Modification of ZIF-L MOF under Electron-Beam Irradiation. *Chem. Mater.* **2021**, *33* (14), 5681–5689. https://doi.org/10.1021/acs.chemmater.1c01332.

(11) Rez, P.; Aoki, T.; March, K.; Gur, D.; Krivanek, O. L.; Dellby, N.; Lovejoy, T. C.; Wolf, S. G.; Cohen, H. Damage-Free Vibrational Spectroscopy of Biological Materials in the Electron Microscope. *Nat. Commun.* **2016**, *7* (1), 10945. https://doi.org/10.1038/ncomms10945.

(12) Haiber, D. M.; Crozier, P. A. Nanoscale Probing of Local Hydrogen Heterogeneity in Disordered Carbon Nitrides with Vibrational Electron Energy-Loss Spectroscopy. *ACS Nano* **2018**, *12* (6), 5463–5472. https://doi.org/10.1021/acsnano.8b00884.

(13) Hachtel, J. A.; Huang, J.; Popovs, I.; Jansone-Popova, S.; Keum, J. K.; Jakowski, J.; Lovejoy, T. C.; Dellby, N.; Krivanek, O. L.; Idrobo, J. C. Identification of Site-Specific Isotopic Labels by Vibrational Spectroscopy in the Electron Microscope. *Science* **2019**, *363* (6426), 525–528. https://doi.org/10.1126/science.aav5845.

(14) Collins, S. M.; Kepaptsoglou, D. M.; Hou, J.; Ashling, C. W.; Radtke, G.; Bennett, T. D.; Midgley, P. A.; Ramasse, Q. M. Functional Group Mapping by Electron Beam Vibrational Spectroscopy from Nanoscale Volumes. *Nano Lett.* **2020**, *20* (2), 1272–1279. https://doi.org/10.1021/acs.nanolett.9b04732.

(15) Guo, C.; Allen, F. I.; Lee, Y.; Le, T. P.; Song, C.; Ciston, J.; Minor, A. M.; Gomez, E. D. Probing Local Electronic Transitions in Organic Semiconductors through Energy-Loss Spectrum Imaging in the Transmission Electron Microscope. *Adv. Funct. Mater.* **2015**, *25* (38), 6071–6076. https://doi.org/10.1002/adfm.201502090.

(16) Collins, S. M.; Kepaptsoglou, D. M.; Butler, K. T.; Longley, L.; Bennett, T. D.; Ramasse, Q. M.; Midgley, P. A. Subwavelength Spatially Resolved Coordination Chemistry of Metal–Organic Framework Glass Blends. *J. Am. Chem. Soc.* **2018**, *140* (51), 17862–17866. https://doi.org/10.1021/jacs.8b11548.

(17) Das, P. P.; Guzzinati, G.; Coll, C.; Gomez Perez, A.; Nicolopoulos, S.; Estrade, S.; Peiro, F.; Verbeeck, J.; Zompra, A. A.; Galanis, A. S. Reliable Characterization of Organic & Pharmaceutical Compounds with High Resolution Monochromated EEL Spectroscopy. *Polymers* **2020**, *12* (7), 1434. https://doi.org/10.3390/polym12071434.

(18) Pal, R.; Bourgeois, L.; Weyland, M.; Sikder, A. K.; Saito, K.; Funston, A. M.; Bellare, J. R. Chemical Fingerprinting of Polymers Using Electron Energy-Loss Spectroscopy. *ACS Omega* **2021**, *6* (37), 23934–23942. https://doi.org/10.1021/acsomega.1c02939.

(19) Liu, L.; Zhang, D.; Zhu, Y.; Han, Y. Bulk and Local Structures of Metal–Organic Frameworks Unravelled by High-Resolution Electron Microscopy. *Commun. Chem.* **2020**, *3* (1), 1–14. https://doi.org/10.1038/s42004-020-00361-6.

(20) Mayoral, A.; Mahugo, R.; Sánchez-Sánchez, M.; Díaz, I. Cs-Corrected STEM Imaging of Both Pure and Silver-Supported Metal-Organic Framework MIL-100(Fe). *ChemCatChem* **2017**, *9* (18), 3497–3502. https://doi.org/10.1002/cctc.201700519.

(21) Zhang, D.; Zhu, Y.; Liu, L.; Ying, X.; Hsiung, C.-E.; Sougrat, R.; Li, K.; Han, Y. Atomic-Resolution Transmission Electron Microscopy of Electron Beam–Sensitive Crystalline Materials. *Science* **2018**. https://doi.org/10.1126/science.aao0865.

(22) Hart, J. L.; Lang, A. C.; Leff, A. C.; Longo, P.; Trevor, C.; Twesten, R. D.; Taheri, M. L. Direct Detection Electron Energy-Loss Spectroscopy: A Method to Push the Limits of Resolution and Sensitivity. *Sci. Rep.* **2017**, *7* (1), 8243. https://doi.org/10.1038/s41598-017-07709-4.

(23) Li, X.; Porcino, M.; Qiu, J.; Constantin, D.; Martineau-Corcos, C.; Gref, R. Doxorubicin-Loaded Metal-Organic Frameworks Nanoparticles with Engineered Cyclodextrin Coatings: Insights on Drug Location by Solid State NMR Spectroscopy. *Nanomaterials* **2021**, *11* (4), 945. https://doi.org/10.3390/nano11040945.

(24) Li, X.; Semiramoth, N.; Hall, S.; Tafani, V.; Josse, J.; Laurent, F.; Salzano, G.; Foulkes, D.; Brodin, P.; Majlessi, L.; Ghermani, N.-E.; Maurin, G.; Couvreur, P.; Serre, C.; Bernet-Camard, M.-F.; Zhang, J.; Gref, R. Compartmentalized Encapsulation of Two Antibiotics in Porous Nanoparticles: An Efficient Strategy to Treat Intracellular Infections. *Part. Part. Syst. Charact.* **2019**, *36* (3), 1800360. https://doi.org/10.1002/ppsc.201800360.

(25) Morris, W.; Wang, S.; Cho, D.; Auyeung, E.; Li, P.; Farha, O. K.; Mirkin, C. A. Role of Modulators in Controlling the Colloidal Stability and Polydispersity of the UiO-66 Metal–Organic Framework. *ACS Appl. Mater. Interfaces* **2017**, *9* (39), 33413–33418. https://doi.org/10.1021/acsami.7b01040.

(26) Jeanguillaume, C.; Colliex, C.; Ballongue, P.; Teneé, M. New STEM Multisignal Imaging Modes, Made Accessible through the Evaluation of Detection Efficiencies. *Ultramicroscopy* **1992**, *45* (2), 205–217. https://doi.org/10.1016/0304-3991(92)90510-Q.

(27) Dubochet, J.; Lepault, J.; Freeman, R.; Berriman, J. A.; Homo, J.-C. Electron Microscopy of Frozen Water and Aqueous Solutions. *J. Microsc.* **1982**, *128* (3), 219–237. https://doi.org/10.1111/j.1365-2818.1982.tb04625.x.

(28) Mangolini, F.; Li, Z.; Marcus, M. A.; Schneider, R.; Dienwiebel, M. Quantification of the Carbon Bonding State in Amorphous Carbon Materials: A Comparison between EELS and NEXAFS Measurements. *Carbon* **2021**, *173*, 557–564. https://doi.org/10.1016/j.carbon.2020.11.021.

(29) Hitchcock, A. P.; Dynes, J. J.; Johansson, G.; Wang, J.; Botton, G. Comparison of NEXAFS Microscopy and TEM-EELS for Studies of Soft Matter. *Micron* **2008**, *39* (6), 741–748. https://doi.org/10.1016/j.micron.2007.09.010.

(30) Goode, A. E.; Porter, A. E.; Ryan, M. P.; McComb, D. W. Correlative Electron and X-Ray Microscopy: Probing Chemistry and Bonding with High Spatial Resolution. *Nanoscale* **2015**, *7* (5), 1534–1548. https://doi.org/10.1039/C4NR05922K.

(31) Cebula, I.; Lu, H.; Zharnikov, M.; Buck, M. Monolayers of Trimesic and Isophthalic Acid on Cu and Ag: The Influence of Coordination Strength on Adsorption Geometry. *Chem. Sci.* **2013**, *4* (12), 4455–4464. https://doi.org/10.1039/C3SC52137K.

(32) Okajima, T.; Teramoto, K.; Mitsumoto, R.; Oji, H.; Yamamoto, Y.; Mori, I.; Ishii, H.; Ouchi, Y.; Seki, K. Polarized NEXAFS Spectroscopic Studies of Poly(Butylene Terephthalate), Poly(Ethylene Terephthalate), and Their Model Compounds. *J. Phys. Chem. A* **1998**, *102* (36), 7093–7099. https://doi.org/10.1021/jp981164t.

(33) Varlot, K.; Martin, J. M.; Quet, C. EELS Analysis of PMMA at High Spatial Resolution. *Micron* **2001**, *32* (4), 371–378. https://doi.org/10.1016/S0968-4328(00)00017-2.

(34) Kolczewski, C.; Püttner, R.; Martins, M.; Schlachter, A. S.; Snell, G.; Sant'Anna, M. M.; Hermann, K.; Kaindl, G. Spectroscopic Analysis of Small Organic Molecules: A Comprehensive near-Edge x-Ray-Absorption Fine-Structure Study of C6-Ring-Containing Molecules. *J. Chem. Phys.* **2006**, *124* (3), 034302. https://doi.org/10.1063/1.2139674.

(35) Hitchcock, A. P.; Urquhart, S. G.; Rightor, E. G. Inner-Shell Spectroscopy of Benzaldehyde, Terephthalaldehyde, Ethylbenzoate, Terephthaloyl Chloride and Phosgene: Models for Core Excitation of Poly(Ethylene Terephthalate). *J. Phys. Chem.* **1992**, *96* (22), 8736–8750. https://doi.org/10.1021/j100201a015.

(36) Leapman, R. D.; Sun, S. Cryo-Electron Energy Loss Spectroscopy: Observations on Vitrified Hydrated Specimens and Radiation Damage. *Ultramicroscopy* **1995**, *59* (1), 71–79. https://doi.org/10.1016/0304-3991(95)00019-W.

(37) Kłosowski, M. M.; Friederichs, R. J.; Nichol, R.; Antolin, N.; Carzaniga, R.; Windl, W.; Best, S. M.; Shefelbine, S. J.; McComb, D. W.; Porter, A. E. Probing Carbonate in Bone Forming Minerals on the Nanometre Scale. *Acta Biomater.* **2015**, *20*, 129–139. https://doi.org/10.1016/j.actbio.2015.03.039.

(38) Nitiputri, K.; Ramasse, Q. M.; Autefage, H.; McGilvery, C. M.; Boonrungsiman, S.; Evans, N. D.; Stevens, M. M.; Porter, A. E. Nanoanalytical Electron Microscopy Reveals A Sequential Mineralization Process Involving Carbonate-Containing Amorphous Precursors. *ACS Nano* **2016**, *10* (7), 6826–6835. https://doi.org/10.1021/acsnano.6b02443.

(39) Kim, E.; Agarwal, S.; Kim, N.; Hage, F. S.; Leonardo, V.; Gelmi, A.; Stevens, M. M. Bioinspired Fabrication of DNA–Inorganic Hybrid Composites Using Synthetic DNA. *ACS Nano* **2019**, *13* (3), 2888–2900. https://doi.org/10.1021/acsnano.8b06492.

(40) Gay, C.; Letavernier, E.; Verpont, M.-C.; Walls, M.; Bazin, D.; Daudon, M.; Nassif, N.; Stéphan, O.; de Frutos, M. Nanoscale Analysis of Randall's Plaques by Electron Energy Loss Spectromicroscopy: Insight in Early Biomineral Formation in Human Kidney. *ACS Nano* **2020**, *14* (2), 1823–1836. https://doi.org/10.1021/acsnano.9b07664.

(41) Hidalgo, T.; Giménez-Marqués, M.; Bellido, E.; Avila, J.; Asensio, M. C.; Salles, F.; Lozano, M. V.; Guillevic, M.; Simón-Vázquez, R.; González-Fernández, A.; Serre, C.; Alonso, M. J.; Horcajada, P. Chitosan-Coated Mesoporous MIL-100(Fe) Nanoparticles as Improved Bio-Compatible Oral Nanocarriers. *Sci. Rep.* **2017**, *7* (1), 43099. https://doi.org/10.1038/srep43099.

(42) Giménez-Marqués, M.; Bellido, E.; Berthelot, T.; Simón-Yarza, T.; Hidalgo, T.; Simón-Vázquez, R.; González-Fernández, Á.; Avila, J.; Asensio, M. C.; Gref, R.; Couvreur, P.; Serre, C.; Horcajada, P. GraftFast Surface Engineering to Improve MOF Nanoparticles Furtiveness. *Small* **2018**, *14* (40), 1801900. https://doi.org/10.1002/smll.201801900.

(43) Chen, S.-Y.; Gloter, A.; Zobelli, A.; Wang, L.; Chen, C.-H.; Colliex, C. Electron Energy Loss Spectroscopy and Ab Initio Investigation of Iron Oxide Nanomaterials Grown by a Hydrothermal Process. *Phys. Rev. B* **2009**, *79* (10), 104103. https://doi.org/10.1103/PhysRevB.79.104103.

(44) Zubavichus, Y.; Shaporenko, A.; Grunze, M.; Zharnikov, M. Innershell Absorption Spectroscopy of Amino Acids at All Relevant Absorption Edges. *J. Phys. Chem. A* **2005**, *109* (32), 6998–7000. https://doi.org/10.1021/jp0535846.

(45) Babaa, M.-R.; Bantignies, J.-L.; Alvarez, L.; Parent, P.; Normand, F. L.; Gulas, M.; Mane, J. M.; Poncharal, P.; Doyle, B. P. NEXAFS Study of Multi-Walled Carbon Nanotubes Functionalization with Sulfonated Poly(Ether Ether Ketone) Chains. *J. Nanosci. Nanotechnol.* **2007**, *7* (10), 3463–3467. https://doi.org/10.1166/jnn.2007.816.

(46) Varlot, K.; Martin, J. M.; Quet, C.; Kihn, Y. Towards Sub-Nanometer Scale EELS Analysis of Polymers in the TEM. *Ultramicroscopy* **1997**, *68* (2), 123–133. https://doi.org/10.1016/S0304-3991(97)00019-3.

(47) Andrade, P. H. M. Synthesis of TiO2@MOF Composites for the Photodegradation of Organic Pollutants. Master dissertation, Universidade Federal de Minas Gerais, Brasil, 2021. https://repositorio.ufmg.br/handle/1843/38408 (accessed 2022-03-11).

(48) Shih, Y.-H.; Chien, C.-H.; Singco, B.; Hsu, C.-L.; Lin, C.-H.; Huang, H.-Y. Metal–Organic Frameworks: New Matrices for Surface-Assisted Laser Desorption–Ionization Mass Spectrometry. *Chem. Commun.* **2013**, *49* (43), 4929–4931. https://doi.org/10.1039/C3CC40934A.

(49) Nivetha, R.; Gothandapani, K.; Raghavan, V.; Jacob, G.; Sellappan, R.; Bhardwaj, P.; Pitchaimuthu, S.; Kannan, A. N. M.; Jeong, S. K.; Grace, A. N. Highly Porous MIL-100(Fe) for the Hydrogen Evolution Reaction (HER) in Acidic and Basic Media. *ACS Omega* **2020**, *5* (30), 18941–18949. https://doi.org/10.1021/acsomega.0c02171.

(50) Scott, A. I. *Interpretation of the Ultraviolet Spectra of Natural Products: International Series of Monographs on Organic Chemistry*; Elsevier, 2013.

(51) Subudhi, S.; Mansingh, S.; Swain, G.; Behera, A.; Rath, D.; Parida, K. HPW-Anchored UiO-66 Metal–Organic Framework: A Promising Photocatalyst Effective toward Tetracycline Hydrochloride Degradation and H2 Evolution via Z-Scheme Charge Dynamics. *Inorg. Chem.* **2019**, *58* (8), 4921–4934. https://doi.org/10.1021/acs.inorgchem.8b03544.

(52) Man, Z.; Meng, Y.; Lin, X.; Dai, X.; Wang, L.; Liu, D. Assembling UiO-66@TiO2 Nanocomposites for Efficient Photocatalytic Degradation of Dimethyl Sulfide. *Chem. Eng. J.* **2022**, *431*, 133952. https://doi.org/10.1016/j.cej.2021.133952.

(53) Leloire, M.; Walshe, C.; Devaux, P.; Giovine, R.; Duval, S.; Bousquet, T.; Chibani, S.; Paul, J.-F.; Moissette, A.; Vezin, H.; Nerisson, P.; Cantrel, L.; Volkringer, C.; Loiseau, T. Capture of Gaseous Iodine in Isoreticular Zirconium-Based UiO-n Metal-Organic Frameworks: Influence of Amino Functionalization, DFT Calculations, Raman and EPR Spectroscopic Investigation. *Chem. – Eur. J.* **2022**, *28* (14), e202104437. https://doi.org/10.1002/chem.202104437.

(54) Ritsko, J. J.; Brillson, L. J.; Bigelow, R. W.; Fabish, T. J. Electron Energy Loss Spectroscopy and the Optical Properties of Polymethylmethacrylate from 1 to 300 EV. *J. Chem. Phys.* **1978**, *69* (9), 3931–3939. https://doi.org/10.1063/1.437131.

(55) Vinu, R.; Madras, G. Photocatalytic Degradation of Methyl Methacrylate Copolymers. *Polym. Degrad. Stab.* **2008**, *93* (8), 1440–1449. https://doi.org/10.1016/j.polymdegradstab.2008.05.018.

(56) Yakovlev, S.; Libera, M. Dose-Limited Spectroscopic Imaging of Soft Materials by Low-Loss EELS in the Scanning Transmission Electron Microscope. *Micron* **2008**, *39* (6), 734–740. https://doi.org/10.1016/j.micron.2007.10.019.

(57) Schneider, N. M.; Norton, M. M.; Mendel, B. J.; Grogan, J. M.; Ross, F. M.; Bau, H. H. Electron–Water Interactions and Implications for Liquid Cell Electron Microscopy. *J. Phys. Chem. C* **2014**, *118* (38), 22373–22382. https://doi.org/10.1021/jp507400n.

(58) Sousa, A.; Aitouchen, A.; Libera, M. Water Mapping in Hydrated Soft Materials. *Ultramicroscopy* **2006**, *106* (2), 130–145. https://doi.org/10.1016/j.ultramic.2005.06.059.

(59) Leclerc, H.; Vimont, A.; Lavalley, J.-C.; Daturi, M.; Wiersum, A. D.; Llwellyn, P. L.; Horcajada, P.; Férey, G.; Serre, C. Infrared Study of the Influence of Reducible Iron(III) Metal Sites on the Adsorption of CO, CO2, Propane, Propene and Propyne in the Mesoporous Metal–Organic Framework MIL-100. *Phys. Chem. Chem. Phys.* **2011**, *13* (24), 11748–11756. https://doi.org/10.1039/C1CP20502A.

(60) Horcajada, P.; Surblé, S.; Serre, C.; Hong, D.-Y.; Seo, Y.-K.; Chang, J.-S.; Grenèche, J.-M.; Margiolaki, I.; Férey, G. Synthesis and Catalytic Properties of MIL-100(Fe), an Iron(Iii) Carboxylate with Large Pores. *Chem. Commun.* **2007**, *0* (27), 2820–2822. https://doi.org/10.1039/B704325B.

(61) March, K.; Venkatraman, K.; Truong, C. D.; Williams, D.; Chiu, P.-L.; Rez, P. Protein Secondary Structure Signatures from Energy Loss Spectra Recorded in the Electron Microscope. *J. Microsc.* **2021**, *282* (3), 215–223. https://doi.org/10.1111/jmi.12995.

(62) Jokisaari, J. R.; Hachtel, J. A.; Hu, X.; Mukherjee, A.; Wang, C.; Konecna, A.; Lovejoy, T. C.; Dellby, N.; Aizpurua, J.; Krivanek, O. L.; Idrobo, J.-C.; Klie, R. F. Vibrational Spectroscopy of Water with High Spatial Resolution. *Adv. Mater.* **2018**, *30* (36), 1802702. https://doi.org/10.1002/adma.201802702.

(63) Li, X.; Haberfehlner, G.; Hohenester, U.; Stéphan, O.; Kothleitner, G.; Kociak, M. Three-Dimensional Vectorial Imaging of Surface Phonon Polaritons. *Science* **2021**, *371* (6536), 1364–1367. https://doi.org/10.1126/science.abg0330.

(64) Rodil, S. E. Infrared Spectra of Amorphous Carbon Based Materials. *Diam. Relat. Mater.* **2005**, *14* (8), 1262–1269. https://doi.org/10.1016/j.diamond.2005.01.044.

(65) Agostoni, V.; Horcajada, P.; Noiray, M.; Malanga, M.; Aykaç, A.; Jicsinszky, L.; Vargas-Berenguel, A.; Semiramoth, N.; Daoud-Mahammed, S.; Nicolas, V.; Martineau, C.; Taulelle, F.; Vigneron, J.; Etcheberry, A.; Serre, C.; Gref, R. A “Green” Strategy to Construct Non-Covalent, Stable and Bioactive Coatings on Porous MOF Nanoparticles. *Sci. Rep.* **2015**, *5* (1), 7925. https://doi.org/10.1038/srep07925.

3.2 . Conclusion and prospects

This study demonstrates the powerful capabilities of monochromated STEM-EELS for the analysis of radiation-sensitive specimens, when combined with DED. On the one hand, the intact chemical structure of MOFs was successfully recorded without beam damage. On the other hand, the broad spectral range of EELS has provided a multimodal approach to unravel the complex structure of MOFs in the IR, UV-vis and soft XR regions. This all-in-one technique has allowed to characterise not only the organic and inorganic parts of MOFs, but also their non-covalent interactions (coordination bonds).

Then, with a gradual increase of the electron dose up to $10^4\ \bar{e}/\text{Å}^2$, monochromated STEM-EELS was used to monitor the beam effect on MOFs and to identify the species generated by radiolysis. The multimodality of EELS has allowed to obtain reliable chemical mechanisms by combining a spectral analysis from the three domains.

These results form the basis for the study of the biodegradation (Chapter 4) and drug uptake of MOFs (Chapter 5), as they have enabled to define damage-free conditions and to study the behaviour of MOFs under irradiation. In the following studies, similar conditions were used to assess the interactions of MOFs with their surrounding environment. The signature of the composite specimen (biodegraded or drug-loaded MOF) is often compared with the bare material characterised in this chapter.

These results also pave the way for the nanoscale characterisation of other organic and organic-inorganic nanomaterials, such as molecules, polymers or biomaterials. In the cellular context, STEM-EELS could be used as a label-free technique to unravel complex mechanisms at the nanoscale.

Finally, this work also demonstrates the possibility of monitoring *in situ* chemical reactions. Here, chemical changes induced by electrons were monitored. Other external stimuli, such as light, temperature changes or environmental changes (in gas or liquid cells), could also be studied using appropriate set-ups.

Chapter 4 .

Study of the biodegradation of MOFs

The therapeutic efficacy of MOFs nanocarriers is determined by their interactions not only with the drug but also with the biological media. Changes in the composition and pH of the surrounding medium are responsible for the uncontrolled drug release through the weakening of the host-guest interactions and the biodegradation of the MOFs. Previous studies have linked burst release to drug protonation at acidic pH [27,37] and to competitive complexations of surrounding anions with the metal clusters at neutral pH.[33,42,48,53] As discussed in Section 1.1.3, phosphate biomolecules present in physiological media have been shown to be responsible for the dissolution of MOFs and hence, drug leakage.[56,58,62,63] To achieve a local sustained drug release, the biodegradation of the framework should be fully understood and controlled. This would allow the optimisation of the nanocarrier design to avoid undesirable behaviours such as aggregation, premature leakage and burst release of the drug. In addition, it could also provide more insight into the cellular fate of MOFs. Therefore, this chapter provides an overview of the biodegradation mechanisms of MOFs in a medium that mimics physiological conditions, a phosphate-buffered saline (PBS) solution.

4.1 . A correlative approach to elucidate complex mechanisms

This section is presented as an article, to be submitted soon. Unlike previous studies that have only focused on the early and final stages of biodegradation, this work provides a detailed step-by-step understanding of the process. As the biodegradation drives the drug release, this work would also help to optimise the nanocarrier for sustained drug delivery.

While Chapter 3 has described STEM-EELS as a powerful technique for the analysis of organic-inorganic nanomaterials, this work reveals the limits of the approach and shows that it is sometimes insufficient for the analysis of complex composites. Here, a combination of electron (spectro)microscopy techniques has been used to unravel the complex chemical processes at the nanoscale. In particular, TEM, iDPC-STEM, STEM-EDS and STEM-EELS were used to monitor each step of the biodegradation process. While each of these techniques provides valuable information on the changes in the morphology, crystal structure and chemical composition of the MOFs, their combination has allowed to shed new light on the complex mechanisms at the nanoscale. In particular, this work reveals highly heterogeneous mechanisms. This highlights the need for an individual characterisation of nanomaterials, especially for biomedical applications.

MIL-100(Al) nanoparticles were selected for this study because of their smaller size compared to MIL-100(Fe) (see DLS results in Appendix B.1, Figure B.1). Their reduced thickness allows for more efficient electron transmission and hence, a higher signal for STEM-EELS analysis. In addition, high-resolution imaging has shown better results on MIL-100(Al) nanoparticles than on MIL-100(Fe). Figure 4.1 displays the best iDPC-STEM images obtained for the two MOFs. The framework crystal structure is observed with a higher spatial resolution for MIL-100(Al), down to 2 Å. Thereby, the following studies focus on MIL-100(Al) only.

The iDPC-STEM and STEM-EDS studies were carried out in collaboration with Pr. Susana Trasobares (University of Cádiz, Puerto Real, Spain). I synthesised the MOFs nanoparticles and performed the EELS experiments. We both did the data processing. Finally, I was the main contributor to the writing of the article, under the supervision of Dr Marta de Frutos, Pr Susana Trasobares and Dr Ruxandra Gref. Note that the supplementary information can be found in Appendix C.

In the following, the nanoparticles designated as intact and biodegraded refer to the state of MOFs obtained before and after contact with PBS, while damaged and original structures correspond to the signatures obtained at low and high electron doses, respectively.

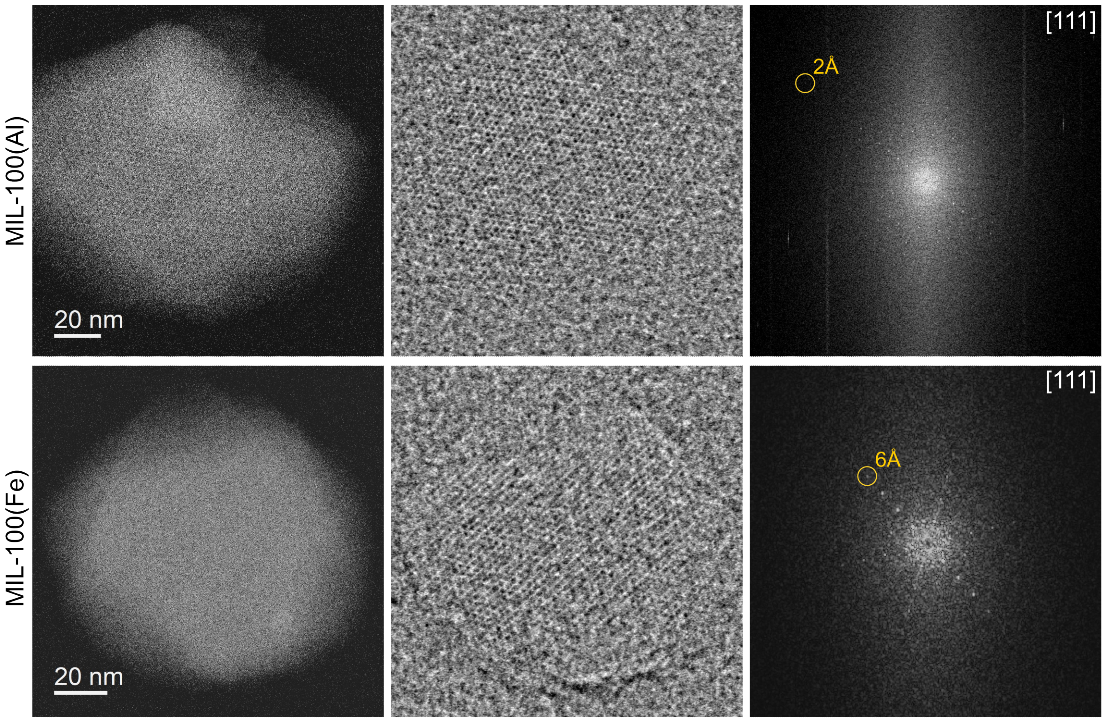

Figure 4.1: HAADF-STEM (left), iDPC-STEM (middle) and the corresponding Fast-Fourier Fransform (FFT, right) images of MIL-100(Al) (top row) and MIL-100(Fe) nanoparticles (bottom row) obtained at 300 kV with an estimated electron dose of 60 $\bar{e}/\text{Å}^2$. The crystal structures are observed along the [111] direction for both MOFs. The spatial resolution reaches 2 Å for MIL-100(Al) and 6 Å for MIL-100(Fe).

Insight into the Nanoscale Biodegradation Mechanisms of MOFs by Electron Spectromicroscopy

Maeva Chaupard,[a,b] *Susana Trasobares,*[c] *Ruxandra Gref,*[b] *Marta de Frutos*[a]*

[a]Laboratoire de Physique des Solides, CNRS, UMR 8502, Université Paris-Saclay, F-91405 Orsay, France
[b]Institut des Sciences Moléculaires d'Orsay, CNRS, UMR 8214, Université Paris-Saclay, F-91405 Orsay, France
[c]Departamento de Ciencia de los Materiales e Ingeniería Metalúrgica y Química Inorgánica, Facultad de Ciencias, Universidad de Cádiz, 11510 Cádiz, Spain

*Marta de Frutos
Email: marta.de-frutos@universite-paris-saclay.fr

ABSTRACT: Metal-organic frameworks (MOFs) reveal to be promising nanocarriers for drug delivery. After administration in the body, they allow local drug release into specific tissues. The drug release rate is controlled by the progressive biodegradation of the MOFs. Therefore, understanding the interactions of MOFs with the physiological medium is of utmost importance to improve the efficiency of the treatment. To gain more insight, this study combines a variety of electron spectromicroscopy techniques. Each of them provides complementary information on changes in the morphology, crystal structure and chemical composition of individual nanoparticles to elucidate the detailed chemical process. This study provides a comprehensive overview of the complexity and heterogeneity of the biodegradation by analysing not only the usual early and late stages of biodegradation, but also the intermediates. In particular, it shows that MOFs are sparsely eroded by phosphate molecules to create an amorphous metal phosphate phase that gradually replaces the framework. Finally, this work addresses systematic and combinatorial methods that could be applied to study the behaviour of MOFs in more complex media and inside cells.

KEYWORDS: metal-organic frameworks, drug delivery, biodegradation, advanced electron spectromicroscopy, iDPC-STEM, STEM-EDS, STEM-EELS

INTRODUCTION

Metal-organic frameworks have recently attracted an increasing interest for drug delivery. Composed of metal clusters and organic linkers, their composition is tuneable, resulting in a variety of properties.[1] In particular, a wise choice of building blocks can ensure biocompatibility and biodegradability. Their versatile composition can also tune their permanent porosity and pore size. A high surface area allows MOFs to achieve a high drug payload. Encapsulated in the pores of MOFs, the drug is protected from enzymatic activity. Then, MOFs allow for slow and controlled release of the drug by their biodegradability. The framework gradually disassembles by interactions with the surrounding biological environment (change in pH or composition), weakening the retention of the drug.[2]

As MOFs biodegradation and drug release are inextricably linked, a major interest lies in the study of the biological triggers responsible for the MOF structural disassembly. However, the complexity of biological media hampers the deciphering of unknown chemical mechanisms. Instead of using such complex media, numerous papers report the use of buffers, culture cell media or serum for *in-vitro* degradation experiments.[3,4] One of the most commonly used is phosphate buffered saline (PBS), as it closely mimics the pH and osmotic concentration of the biological medium. Its effect on the fate of MOFs has been studied for several nanoparticles such as ZIF-8,[3,5] UiO-66[4,6,7] and MIL-100[8–10] (which stand for Zeolitic Imidazolate Framework, Universitetet i Oslo and Material of Institute Lavoisier, respectively). As described elsewhere,[11] they all undergo changes in morphology, crystal structure and chemical composition when exposed to phosphate ions. Although these studies have focused on different MOFs, similar behaviours have been observed: the release of the linkers,[4,6,8–10] the MOF amorphisation[4,8,9] and the formation of amorphous metal phosphates.[3,5,8,10] Some of the studies have also shown a surface erosion by *in-situ* Atomic Force Microscopy[5,9] and Transmission Electron Microscopy (TEM).[10,12] Taken together, these observations show that MOF degradation is driven by competitive phosphate complexation with the metal ions. Recently, Vuong et al.[10] showed that for MIL-100(Al), phosphate ions first replace constitutive water molecules and then, organic linkers.

Although numerous studies have already investigated the degradation process of various MOFs in PBS, none of them has reported a detailed step-by-step mechanism. Several questions remain regarding the amorphisation of the framework and the homogeneity of the process. Answering these questions could provide clues for optimising the design of MOFs to maximise their therapeutic efficacy.

Here, we provide further insights into the nanoscale degradation mechanisms of MIL-100(Al) in PBS. With a progressive increase in the phosphorus/aluminium trimer ratio (P/Al_3), the process is monitored through the intermediate stages of degradation by using a combination of advanced electron spectromicroscopies. This study reveals the changes in morphology, crystal structure and chemical composition that individual nanoparticles undergo.

RESULTS AND DISCUSSION

1) Biodegradation of MIL-100(Al) in PBS.

Prior to biodegradation, the synthesised nanoparticles were characterised by dynamic light scattering, porosimetry, thermogravimetric analysis and Transmission Electron Microscopy (TEM) to analyse their morphology, crystal structure and chemical purity. The details are given in SI **(Figure S1)**. MIL-100(Al) were then chemically degraded in PBS. In contrast to previous studies, here the degree of degradation of the MOFs was gradually increased in order to follow the chemical process step by step. **Table 1** summarises the different concentrations of MOFs and PBS used for these experiments. For each of them, the P/Al_3 molar ratio is provided (the Experimental section gives more details on the degradation procedure and the calculation of the P/Al_3 ratio). In the following, we will refer to this ratio to distinguish the different specimens. Note that as no solids could be recovered for $P/Al_3 = 22.8$, no data were collected for this specimen.

Two series of P/Al$_3$ were prepared, with a MOF concentration of 2.5 mg/mL and 10 mg/mL (the latter marked with * hereafter). Since the reaction rate can depend not only on the ratio of the reagents but also on their absolute concentrations, these experimental conditions could correspond to different reaction kinetics.

For each P/Al$_3$ ratio, the resulting degraded nanoparticles were analysed by Fourier Transform Infrared spectroscopy (FTIR) in order to monitor the compositional evolution of MIL-100(Al) throughout the degradation process. The resulting spectra are shown in **Figure 1**. Prior to biodegradation, the intact MIL-100(Al) are characterised by benzene ring deformation and aromatic CH bending modes (δ_{CH}) at 690-770 cm^{-1}; and CC and CO stretching modes of aromatic and coordinated carboxylic groups (ν_{CC}, ν_{CO}) at 1400-1670 cm^{-1} (black curve in **Figure 1**). A broader spectral interval is provided in **Figure S2**, showing the OH stretching modes of water molecules (ν_{OH}) at around 3300 cm^{-1}. These results are in agreement with previous studies.[13–15] After biodegradation, a band near 1030 cm^{-1} appears and increases strongly with the P/Al$_3$ ratio. It has been previously observed in degraded MIL-100(Al) and indicates the PO stretching vibration modes (ν_{PO}).[13] On the contrary, the δ_{CH}, ν_{CC} and ν_{CO} vibration modes decrease as the P/Al$_3$ ratio increases. Since these bands are chemical fingerprints of the organic linkers, this suggests a loss of the linkers. For the nanoparticles degraded at higher MOF and PBS concentrations, FTIR shows a similar result at P/Al$_3$ =0.1* and P/Al$_3$ =0.6*.

Table 1. *Experimental conditions used for the MIL-100(Al) biodegradation study. For each of them, the MOFs and PBS concentrations were varied while keeping a constant volume of 1mL. The P/Al$_3$ molar ratios were calculated as described in the Experimental section. The * indicates the conditions carried out at higher MOFs and PBS concentrations. No solids could be recovered at P/Al$_3$ = 22.8.*

P/Al$_3$	MIL-100(Al) concentration (mg/mL)	PBS concentration (mM)
0.1	2.5	0.3
0.1*	10.0	1.0
0.2	2.5	0.7
0.6	2.5	2.5
0.6*	10.0	10.0
1.0	2.5	4.4
1.5	2.5	6.6
2.3	2.5	10.0
22.8	0.3	10.0

The increase of the ν_{PO} band demonstrates the progressive interaction of phosphate molecules with the MOFs throughout the degradation process. In addition, the observed loss of linkers agrees with previous chromatographic measurements on UiO-66 and MIL-100.[4,6,8–10] Taken together, these observations are consistent with the previously proposed mechanisms in which the organic linkers are progressively replaced by phosphate molecules.[13] However, while some of the studies reported a steady state of linker loss after tens of hours in PBS, [4,6,8–10] here, a continuous loss of the linkers is observed during the process. This suggests that phosphates are able to completely dissolve MIL-100(Al).

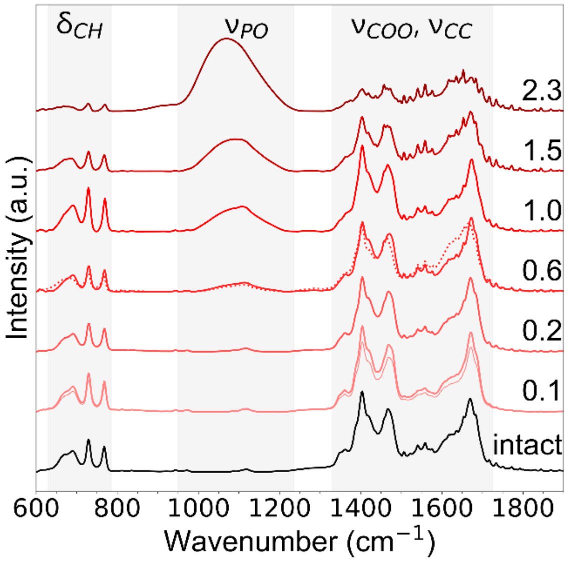

***Figure 1**. FTIR spectra of intact (black) and degraded MIL-100(Al) (red) in PBS at different P/Al_3 molar ratios. The dotted lines represent P/Al_3 = 0.1* and P/Al_3 = 0.6*. The shaded areas highlight the spectral fingerprints of the organic linkers (ν_{CH}, ν_{COO} and ν_{CC}) and phosphate molecules interacting with the MOFs (ν_{PO}). The spectral resolution is about 4 cm^{-1}.*

Although FTIR provides valuable information on the change in chemical composition of MIL-100(Al) during biodegradation, the results remain bulk average measurements of the nanomaterial preparations. A complete understanding of the biodegradation chemical mechanisms can only be achieved by analysing individual nanoparticles. Therefore, electron microscopy was used to probe further changes at the nanoscale spatial resolution. Complementary techniques were used to fully characterise the morphology, crystal structure and chemical composition of biodegraded MOFs.

2) *Monitoring the erosion and amorphisation by electron microscopy.*

Figure 2 shows TEM images of intact and biodegraded MIL-100(Al) for different P/Al_3 ratios, obtained at a MOF concentration of 2.5 mg/mL. These results illustrate the morphological changes of the nanoparticles while exposed to PBS. First, the intact MIL-100(Al) exhibit facetted morphologies, as reported elsewhere.[13,14] The observed nanoparticle sizes range between 40 and 200 nm. Then, after contact with PBS, the first stages of biodegradation (P/Al_3 = 0.1 and P/Al_3 = 0.2) show only slight changes. The nanoparticles remain well facetted, while some of them have holes in the structure, as indicated by the yellow arrows in **Figure 2**. This local mass loss is consistent with the surface erosion previously observed by *in-situ* Atomic Force Microscopy and TEM for ZIF-8 and MIL-100.[5,9,10,12] Thanks to the progressive degradation of MIL-100(Al), we can further specify that the erosion tends to increase with the P/Al_3 ratio. Since a continuous loss of linkers was also observed by FTIR, our results indicate that the erosion is associated with the linkers' substitution by phosphates, leaving missing linker defects in the MOF structure.

Then, starting from P/Al_3 = 0.6, the growth of an amorphous phase around the MIL-100(Al) nanoparticles is observed. This leads to the formation of spherical deposits of tens of nanometres. Their size and density increase with the P/Al_3 ratio until recovering the nanoparticles. At P/Al_3 = 1.0 and P/Al_3 =1.5, some of the amorphous structures appear to move away from the degraded MOFs (enlarged views in **Figure S3a**). This results in the progressive fragmentation of the nanoparticles. Interestingly, no significant change in the nanoparticle size is noticed for these P/Al_3 ratios (TEM size measurements shown in **Figure S4**).

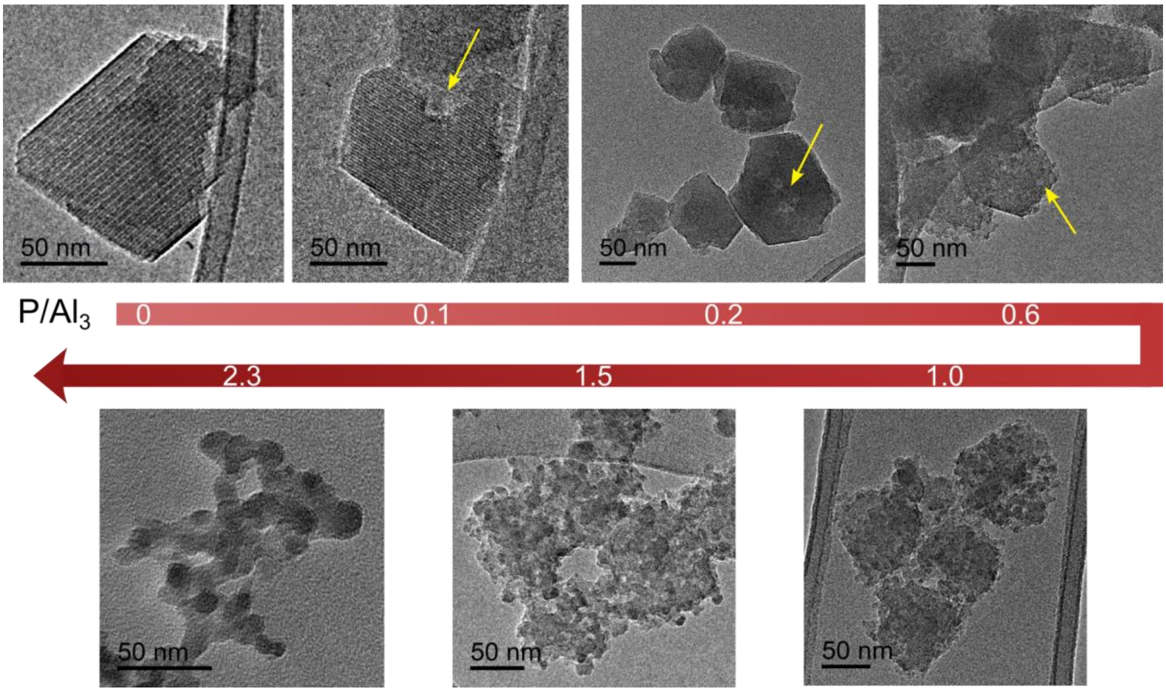

Figure 2. *TEM images of intact and biodegraded MIL-100(Al) at different P/Al*$_3$ *ratios. The yellow arrows indicate erosion of the framework, which tends to increase with the degree of biodegradation. Amorphous deposits are observed around the MOFs at P/Al*$_3$ *= 0.6, 1.0 and 1.5. At P/Al*$_3$ *= 2.3, the MOFs are completely dissolved, leaving only an amorphous phase.*

At high stages of biodegradation (P/Al$_3$ = 2.3), no MIL-100(Al) nanoparticles are observed. The specimen contains only amorphous rounded structures of about 20 nm. These structures appear to be aggregated with residues, which could be the released linkers remaining in suspension. This suggests that by interacting with phosphate ions, linker substitution and erosion occur until the complete disassembly of the MOFs. The amorphous phase, which gradually replaces the MOFs during biodegradation, is the only fraction left.

The rate of biodegradation appears to be faster at higher concentrations of MOFs and PBS (**Figure S3b**). For instance, the morphology of the nanoparticles at P/Al$_3$ = 0.6* (MOFs at 10 mg/mL) are similar to those observed at P/Al$_3$ = 1 (MOFs at 2.5 mg/mL). This suggests that the kinetics of the process are influenced by both the ratios and concentrations of the reagents.

Overall, the imaging of individual MIL-100(Al) nanoparticles at each stage of biodegradation reveals a highly heterogeneous process. In contrast to previous bulk studies based on electron and X-ray diffraction showing the amorphisation of the entire MOFs,[4,8,9] our results reveal the heterogeneity of the process. In the early stages of biodegradation (P/Al$_3$ < 1), erosion and amorphous deposits are observed sparsely throughout the specimen. However, it was not possible to extract a clear distribution pattern or information about the site of erosions at the spatial resolution of **Figure 2** and **Figure S3**. It could be hypothesised that they occur at sites of structural defects, but only high-resolution imaging could provide more insight.

Therefore, high-resolution imaging was performed at the sub-nanometre scale in order to observe the effect of phosphate ions on the MOF crystallinity. Due to the beam sensitivity of MOFs, this requires the use of dedicated techniques operating at low electron doses, hence using sensitive detectors.[16] Here, we used the integrated Differential Phase Contrast Scanning Transmission Electron Microscopy (iDPC-STEM) technique to study the crystal structure of MIL-100(Al). Based on a four-quadrant detector, this technique provides an image contrast directly proportional to the atomic electronic potential. It is therefore highly sensitive to both light and heavy atoms (e.g. carbon, oxygen and aluminium). This allows MOFs to be imaged at high resolution with minimal electron dose while preserving the integrity of the specimen structure.[17]

Figure 3 compares the iDPC-STEM images of intact and degraded MIL-100(Al) at $P/Al_3 = 0.1^*$, along the [111] direction. Due to the low signal-to-noise ratio (SNR), the images were denoised by average background subtraction filtering. Here, the material is displayed in white and the vacuum in dark grey due to the phase contrast. The structure of the intact MOFs is observed with a spatial resolution of 2 Å. Its crystallinity is consistent with the cubic structure first described by Volkringer et al.[18], also shown in **Figure 3a**. After biodegradation, the nanoparticles exhibit a similar crystalline organisation, as highlighted by the Fast Fourier Transform (FFT). This same FFT pattern was found for both specimens on the explored areas suggesting that the phosphate molecules do not disrupt the global crystallinity of the nanoparticles, but only affect specific sites that are difficult to localize at the first stages of biodegradation. However, it should be noted that the images of the degraded MIL-100(Al) have a lower spatial resolution (3 Å). This could be the result of a beam misalignment but can also reflect the effect of phosphates that reduce the crystallinity fraction of the nanomaterial.

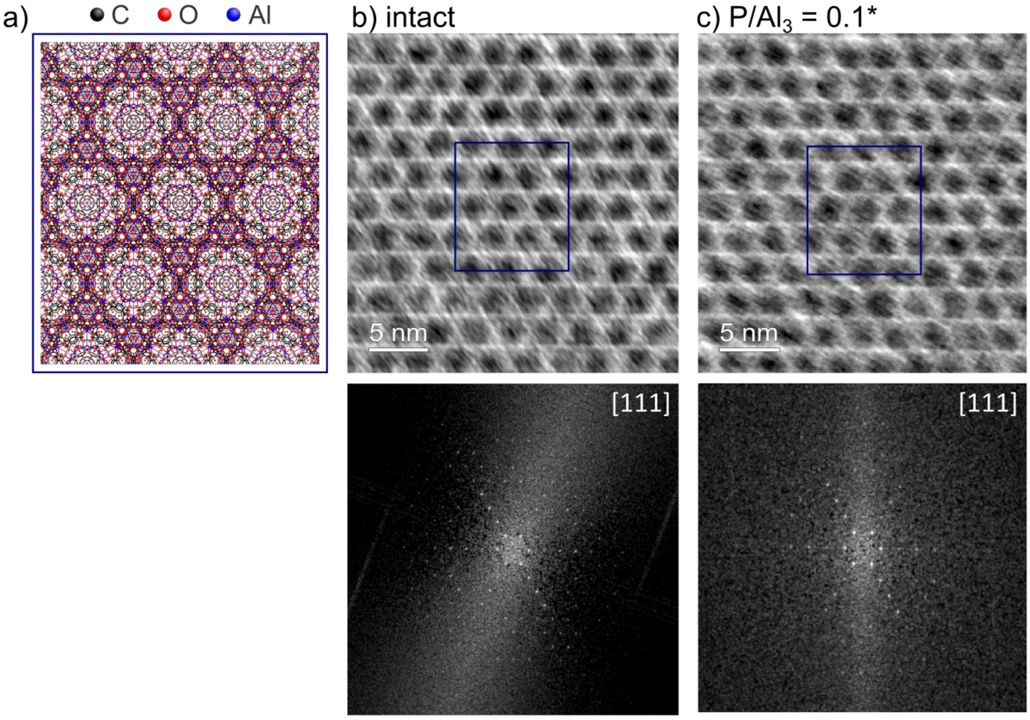

Figure 3. *(a) Structural model of MIL-100(Al). (b-c) Average background subtraction filtered (ABSF) iDPC-STEM image (top row) and the corresponding FFT pattern (bottom row) of (b) intact MIL-100(Al) and (c) biodegraded MIL-100(Al) at* $P/Al_3 = 0.1^*$. *Both MOFs are observed along the [111] direction. The spatial resolution reaches 2 Å for (b) and 3 Å for (c).*

The higher stages of biodegradation ($P/Al_3 > 0.1$) were more difficult to image at high-resolution (see **Figure S5**): the crystalline fraction of material decreases as the amorphous phase replaces the MOFs structure resulting in a poor SNR. Therefore, the crystal structure of degraded MIL-100(Al) at $P/Al_3 = 1.5$ was investigated by TEM at lower spatial resolution. As shown by the FFT, **Figure 4** shows a TEM image obtained along the [112] direction with a spatial resolution of 5 Å. In this case, the phase contrast displays the nanomaterial in dark and the vacuum in light grey (reverse contrast than Figure 3). Interestingly, only the inner part of the nanoparticle is crystalline. The outer part of the nanoparticle consists only of the amorphous deposits.

This suggests that the degraded MIL-100(Al) remain partially crystalline during their fragmentation. It is likely that the amorphous phase progressively spreads over the nanoparticle (**Figure 4**, P/Al_3 = 1.5), until complete disassembly of the framework (**Figure 2**, P/Al_3 = 2.3). Elemental and chemical analyses were then carried out to identify the chemical composition of the amorphous phase and to understand the mechanisms of its sparse formation.

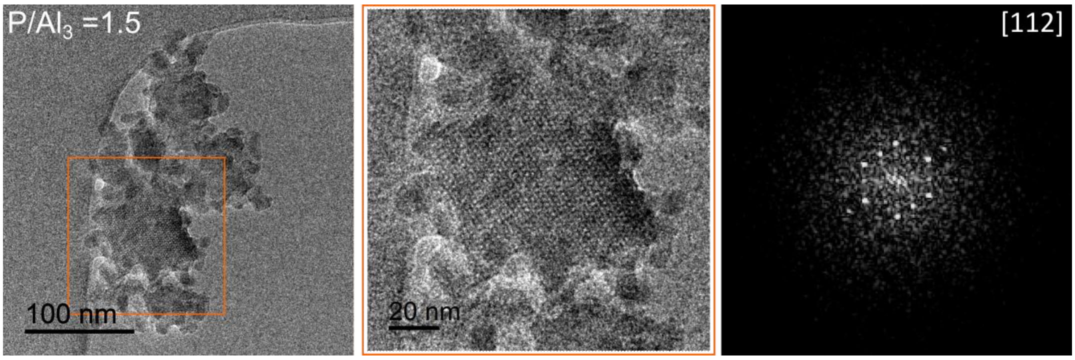

Figure 4. *TEM image of degraded MIL-100(Al) at P/Al_3 = 1.5, observed along the [112] direction, and the corresponding diffraction pattern. The spatial resolution is 5 Å.*

3) Local chemical heterogeneities observed by STEM-EDS and STEM-EELS.

The changes in the chemical composition of MIL-100(Al) were assessed by STEM-Energy Dispersive X-Ray Spectroscopy (EDS) and STEM-Electron Energy Loss Spectroscopy (EELS). STEM-EDS allows the elemental analysis of the specimen whereas STEM-EELS is able to provide information on its chemical structure. Both techniques require adjusting the electron dose depending on the nature and concentration of the chemical species composing the specimen to obtain measurable spectral signatures.

For STEM-EDS, the data were collected with electron doses ranging from 100 $\bar{e}/Å^2$ to 450 $\bar{e}/Å^2$. **Figure 5 and S6** summarises the results obtained on MIL-100(Al) for an increasing degree of biodegradation. The intact MIL-100(Al) were found to mainly contain carbon (55 at.%), oxygen (30 at.%) and aluminium (9 at.%), which originate from their trimesate linkers and aluminium oxo-clusters, respectively. The oxygen content was lower than the theoretical formula of MIL-100(Al) (49 at.% C, 43 at.% O and 8 at.% Al, not counting hydrogen that is not detected in EDS). Given the extreme radiation sensitivity of MOFs, this probably results from a beam-induced loss of mass (see SI for more details, **Figure S6a**). Despite the beam damage, the three elements were detected on all the nanoparticles and as expected, their distribution appears homogeneous at the spatial resolution chosen for the acquisitions (< 3 nm) (**Figure 5,** top row). Consequently, the use of quite high electron doses seems to have little incidence on the elemental distributions at this spatial resolution.

For a better comparison of the evolution, **Figure 6** resumes the elemental maps of phosphorus and carbon superimposed throughout the process. For the intact nanoparticles, a very low signal of phosphorus is detected corresponding to acquisition noise. The amount of phosphorus increases with the biodegradation degree, and the distributions of phosphorus and carbon become more heterogeneous. For MIL-100(Al) biodegraded at P/Al_3 = 0.1* and P/Al_3 = 0.2, the contact with PBS did not induce strong changes in the elemental distributions of carbon, oxygen and aluminium (**Figure 5)**. They were detected in similar quantities than for the intact MOFs

(58 at.%, 33 at.% and 10 at.%, respectively). Phosphorus were also detected in traces < 1 at.%, in all the nanoparticles (**Figure S6b**). At this spatial resolution, the phosphorus distribution presents a granular appearance (**Figure 5,** middle row, and **Figure 6**). This granularity may result from the low phosphorus signal (at the detection limit) but also from a local heterogeneous distribution that would require a higher spatial resolution to be characterise.

At high biodegradation stages ($P/Al_3 = 0.6$* and $P/Al_3 = 1.0$), the four elements were detected in variable amounts with a strongly heterogeneous distribution (**Figure 5,** bottom row, and **Figure 6a**). The profile of the elemental distributions are provided in **Figure 6b.** Some regions showed concentrations of carbon, oxygen, aluminium and phosphorus that appear to be correlated (highlighted by the black arrow in **Figure 6b**) and their elemental abundancies are similarly to intact nanoparticles at the slight degradation stages (53 at.%, 30 at.%, 10 at.% and 1 at.%, respectively). In contrast, other regions were found deficient in carbon and highly concentrated in oxygen, aluminium and phosphorus (3 at.%, 71 at.%, 16 at.% and 10 at.%, respectively, **Figure S6c**). They are relatively small with sizes ranging from 20 nm to 30 nm. The corresponding profile shows high concentrations of phosphorus, aluminium and oxygen and a lack of carbon (indicated by the black arrow in **Figure 6b**). These areas co-localise with the amorphous deposits previously observed in TEM images (**Figures 5**, **6** and **S6**). These observations indicate that the amorphous phase contains aluminium phosphate mineral. Since the carbon comes only from the linkers, the lower carbon content also suggests that phosphorus is concentrated in areas where organic moieties are depleted. This is consistent with the gradual replacement of organic linkers (carbon based) by phosphate molecules, as suggested by FTIR measurements. However, the stoichiometry of the elements (71 at.% O, 16 at.% Al and 10 at.% P) also reveals that oxygen is in excess compared to pure aluminium phosphate ($AlPO_4$, 66 at.% O, 17 at.% Al and 17 at.% P) suggesting the presence of aluminium oxide.

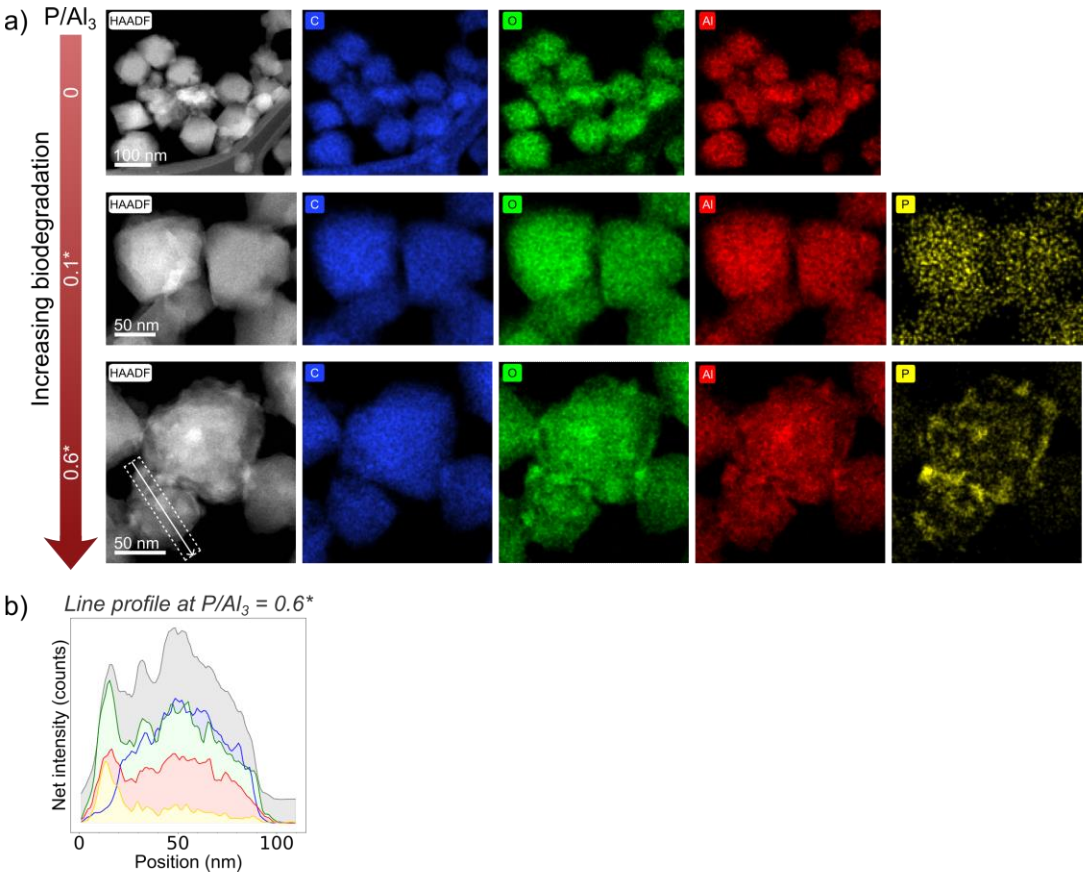

Figure 5. *a) Evolution of the elemental composition for MIL-100(Al) with increasing biodegradation stage. HAADF-STEM images (left) and the corresponding STEM-EDS elemental maps of carbon (blue), oxygen (green), phosphorus (yellow) and aluminium (red) from intact (top row) to P/Al*$_3$ *= 0.6* (bottom row). b) Line profile of the elemental distributions for biodegraded MIL-100(Al) at P/Al*$_3$ *= 0.6*, obtained along the white arrows indicated on the corresponding HAADF-STEM image. Data were collected between 100 ē/Å*^{2} *and 450 ē/Å*^{2}*, with a pixel size < 3 nm. Additional EDS spectra are shown in Figure S6.*

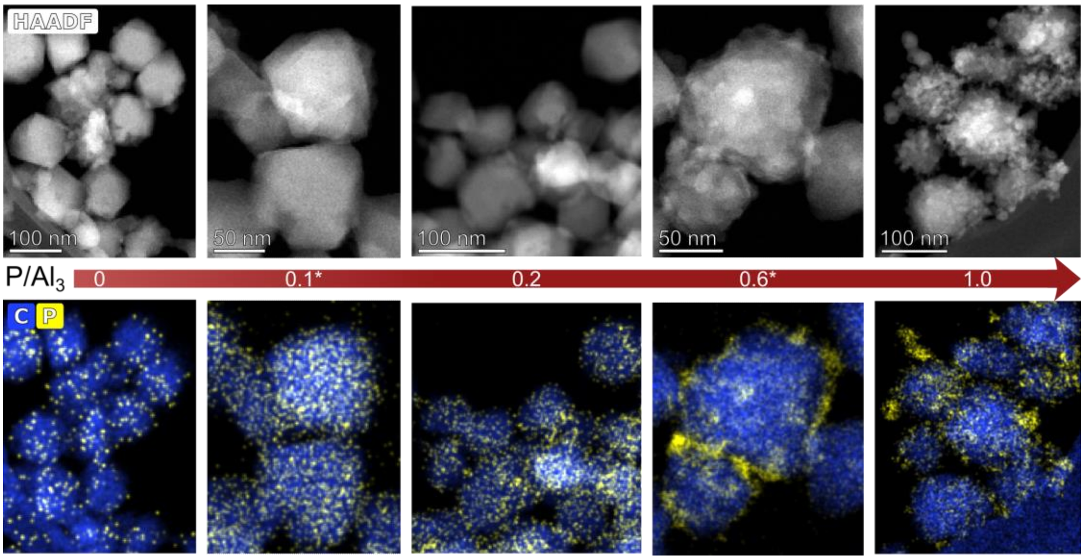

Figure 6. *HAADF-STEM images (top row) and the corresponding superimposed EDS elemental maps (bottom row) of carbon (in blue) and phosphorus (in yellow) for intact and degraded MIL-100(Al) at increasing P/Al*$_3$ *ratios (from left to right). For intact nanoparticles, the detected phosphorus signal results from the acquisition noise. At P/Al*$_3$ *= 0.6* and P/Al*$_3$ *= 1.0, the distribution of carbon and phosphorus is anti-colocalised. Data were collected between 100 ē/Å*^{2} *and 450 ē/Å*^{2}*, with a pixel size < 3 nm.*

STEM-EELS was then used to gain further insight into the compositional changes observed at high stages of biodegradation. The chemical signature of the intact MIL-100(Al) was used as a reference to compare with that of degraded MOFs. A recent study has shown that low doses (~10 ē/Å^2) provide the undamaged signatures of MOFs, but at the cost of a very low signal and a reduced spatial resolution (10 nm).[15] In the present study, electron doses higher than 400 ē/Å^2 were applied to increase the detected signal and to improve the spatial resolution (< 3 nm). Such conditions imply radiolysis damage of the organic fraction of the MOFs. Therefore, the spectral signatures collected correspond to damaged linkers, affected by bond breakage and chemical rearrangement. Nonetheless, the results remain valuable if complemented by a beam-effect study on the specimen.[15] Here, a beam-effect study was carried out to attribute the damaged spectral signatures of biodegraded MIL-100(Al) to specific functional groups from their original chemical structure (see SI for more details).

Both the low-loss and core-loss ranges were analysed as a function of the biodegradation degree. **Figure 7a** shows a typical spectrum covering the two regions (y-axis in log scale). The low-loss region has an intrinsic high cross-section (see SI for more details). Thus, it was studied first to get a measurable signal at limited electron doses. However, this region was not sensitive to the changes induced by biodegradation (**Figure S9a**). The analysis was then conducted in the core-loss region, where features have a lower cross-section (see SI for more details). They cover the spectral region from the aluminium $L_{2,3}$-edge (at 75 eV) to the oxygen K-edge at 535 eV).

a) Typical EELS spectrum

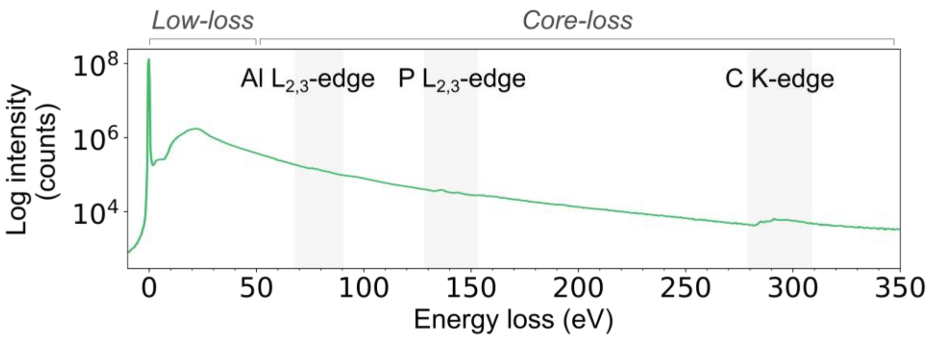

b) Fine structure analysis

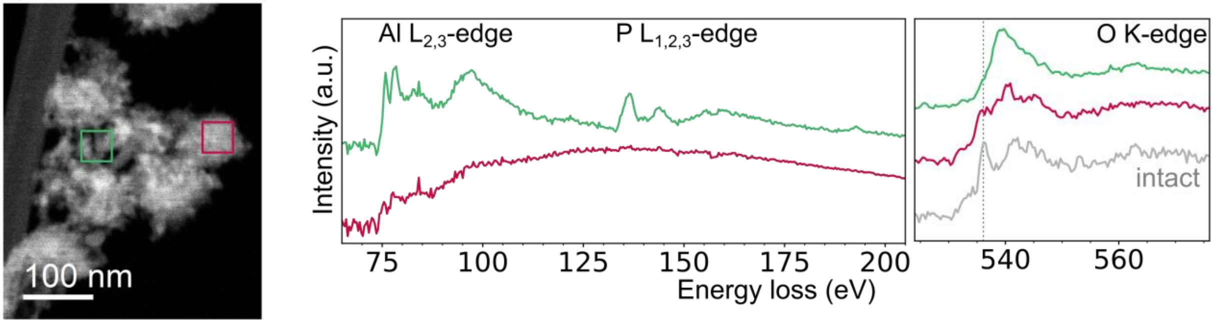

***Figure 7**. a) Typical EELS spectrum obtained for biodegraded MIL-100(Al) at P/Al$_3$ = 1.5. The spectral range covers the low-loss and core-loss region. The low-loss has the highest SNR. Then in the core-loss, the carbon displays a more intense signal than the aluminium and phosphorus due to its higher concentration in the specimen. b) STEM-HAADF image of degraded MIL-100(Al) at P/Al$_3$ = 1.5, and the corresponding EELS spectra obtained in the red and green regions. The red region indicates a MOF-like morphology, while the green region focuses on the amorphous deposits. The aluminium and phosphorus L-edge spectra were obtained at 2.10^3 ē/Å^2, while the oxygen K-edge was obtained at 400 ē/Å^2. For comparison with the intact MIL-100(Al), a spectrum obtained at 300 ē/Å^2 is shown in grey. The spatial resolution is 3 nm. The spectral resolution is 0.8 eV in (a) and (b).*

The carbon K-edge displays the highest signal (and SNR) due to its relatively high concentration in the MOFs and high ionization cross section. It is therefore more reliable for detecting change in the composition of the specimens. It was collected on the intact and biodegraded MIL-100(Al) at $P/Al_3 < 1.5$. All the specimens display similar signatures at low (10 ē/Å^2) and high doses (700 ē/Å^2) (**Figure S9b**). At low dose, three peaks were observed at 285.0 eV, 288.6 eV and 290.9 eV that correspond to the $1s\text{-}\pi^*_{C=C}$, $1s\text{-}\pi^*_{C=O}$ and $1s\text{-}\sigma^*_{C\text{-}O}$ transitions of the organic linkers, respectively.[15] At high dose, a peak appears at 287.5 eV describing the damaged linkers (see details in SI). These similarities suggest that linkers remain present until $P/Al_3 = 1.5$. This agrees with FTIR that detected fingerprints of the linkers for these stages of biodegradation (δ_{CH}, ν_{CC} and ν_{CO}, **Figure 1**).

Then, as the oxygen is the second most abundant element in the MOFs, its K-edge displayed a relatively high signal. Like for the carbon, the oxygen K-edge was collected on the intact and biodegraded MIL-100(Al) at $P/Al_3 < 1.5$, at low (10 ē/Å^2) and high doses (700 ē/Å^2) (**Figure S9b**, beam-effect study). At 10 ē/Å^2, the intact and biodegraded MOFs at $P/Al_3 = 0.1$* and $P/Al_3 = 0.6$) show a peak at 534.0 eV. It was attributed to the $1s\text{-}\pi^*_{C=O}$ transitions of the organic linkers.[15] At electron doses higher than 300 ē/Å^2, this peak is shifted to 536.5 eV due to the beam damage of the linkers (see details in SI). Despite beam damage, this shifted peak can still be used as a chemical fingerprint for assessing the presence of the linkers in biodegraded MIL-100(Al) at $P/Al_3 = 1.5$. **Figure 7b** shows the oxygen K-edge of degraded MIL-100(Al) at $P/Al_3 = 1.5$, obtained at a spatial resolution of 3 nm by applying a dose of 400 ē/Å^2. The specimen presents a heterogeneous morphology and two different regions were identified and analysed: a region with a MOF-like morphology (red) and another with amorphous deposits (green). The green and red regions display quite different features. The green spectrum shows a single broad contribution at 540 eV, while the red spectrum shows two peaks at 536.5 eV (indicated by the dotted line) and 541.0 eV. The red spectrum has a signature close to that of the intact MIL-100(Al) (grey line in **Figure 7b**) obtained at an equivalent electron dose (300 ē/Å^2). The peak at 536.5 eV reveals linkers are still present in the red region. In the green region, the broad feature centred around 540 eV, without thin peaks is typical from metal phosphates.[19,20] This indicates that the amorphous deposits are composed of aluminium phosphates. The absence of the peak at 536.5 eV points out that no linkers remain in the amorphous phase. This is eventually consistent with the elemental maps of **Figure 6**, as no carbon is detected on the amorphous deposits.

At last, **Figure 7b** shows the aluminium and phosphorus $L_{1,2,3}$-edges of degraded MIL-100(Al) at $P/Al_3 = 1.5$. Compared to carbon and oxygen, these elements are less concentrated in the specimens and display very low signals. Thus, higher electron doses ~10^3-10^4 ē/Å^2 were required to efficiently detect the corresponding features. The aluminium $L_{2,3}$-edge displays three specific features at 76.0 eV, 78.5 eV and near 98 eV and the phosphorus $L_{1,2,3}$-edge exhibits three peaks at 136.8 eV, 144.2 eV and 193.0 eV. The aluminium $L_{2,3}$-edge was detected in both the red and green regions, with a weaker signal in the red region. This difference in signal intensity is probably due to the concentration of aluminium that is higher in the inorganic phase (16 at.%) than in the MOF-like structure (10 at.%), as measured by EDS (**Figure S6c**). Nonetheless, it should be noted that the signal attenuation may also be due to the greater thickness of the specimen in the red region (about one hundred) than in the green region (20-30 nm). Signal attenuation with sample thickness is a well-known phenomenon in EELS spectroscopy.[21] Conversely, phosphorus was only detected in the green region and not in the red one. This indicates a high concentration of phosphorus located in the amorphous deposits. The corresponding EELS elemental mapping (**Figure S10**) are consistent with the EDS elemental distribution in **Figure 6**. Despite the relatively high electron doses, the identification of the mineral phase in the amorphous deposits remains possible as inorganic components are less sensitive to beam damage than organic matter. Both aluminium and phosphorus fine structures can be compared with previous EELS studies carried out on $AlPO_4$.[22,23] The spectral similarities with $AlPO_4$ of the green region data confirm that the amorphous deposits are composed of aluminium phosphates.

Overall, our electron spectromicroscopy study has revealed localised chemical changes that occur at the nanoscale during the biodegradation of MIL-100(Al). STEM-EDS has shown that at early stages of biodegradation ($P/Al_3 < 0.2$), carbon, oxygen, aluminium and phosphorus are homogeneously distributed throughout the nanoparticles. This suggests that phosphate molecules interact at different positions homogeneously distributed over the framework. At higher stages of biodegradation ($P/Al_3 > 0.2$), a more heterogeneous distribution was observed. In particular, aluminium, oxygen and phosphorus were found concentrated in amorphous regions around the MOFs. STEM-EELS unambiguously showed that these amorphous deposits are made of aluminium phosphates. Some aluminium oxide was also detected. The analysis of the carbon and oxygen K-edges revealed that the amorphous inorganic deposits do not contain any organic content, so no organic linkers are still present. This agrees with previous studies showing the formation of metal phosphate deposits at the late stages of biodegradation of ZIF-8 and MIL-100.[3,5,8,10] By analysing the intermediate stages of biodegradation, these results additionally show the progressive substitution of the linkers by phosphate and the formation of a mineral phase.

4) Heterogeneous biodegradation mechanisms.

Combining the results of the different techniques provides an overview of the biodegradation mechanisms. At early stages of biodegradation, phosphorus is only detected inside of the MIL-100(Al) (STEM-EDS, **Figure 5 and S6**). This suggests that phosphate molecules diffuse through the pores and interact with the framework. Phosphates are then assumed to substitute the linkers and they are gradually released during the process (FTIR, **Figure 1**). This agrees with previous studies from litterature.[10] The loss of the linkers creates missing linker defects (TEM, **Figure 2**). These crystal defects are highly reactive sites that are prone to further interact with phosphate molecules and promotes the erosion of the framework. At $P/Al_3 = 0.6$, these interactions lead to the formation of amorphous aluminium phosphate deposits around the nanoparticles (STEM-EDS, STEM-EELS, **Figures 5, 7 and S6**). They are purely inorganic as they do not contain organic linkers (STEM-EDS, absence of carbon in **Figure 5 and S6**; STEM-EELS absence of carbon and linker's oxygen in **Figure 7**). Their sizes and density increase with the P/Al_3 ratio, resulting in a continuous crystal growth promoted by the contact with PBS (TEM, **Figure 2**). This may be related to the continuous erosion of the framework (FTIR, **Figure 1**) that feeds the deposits with the constant release of both organic linkers and aluminium ions.

In contrast to previous electron and X-ray diffraction studies which focused only on the early and late stages of the degradation of UiO-66 and MIL-100 in PBS,[4,8,9] our results describe a progressive degradation involving the constant erosion of the framework promoted by phosphate molecule release. As the building blocks of the MOF are gradually released from certain areas, it is not surprising that MIL-100(Al) remain partially crystalline during the process. As a result, we observe an amorphous phase that gradually replaces the MOFs crystals (TEM, **Figure 4**). The erosion being continuous, it occurs until the complete dissolution of the framework, leaving a completely amorphous structure in the late stages of biodegradation ($P/Al_3 = 2.3$, TEM, **Figure 2**).

CONCLUSION

By combining a variety of electron microscopy and spectroscopy techniques, this study provides an overview of the nanoscale biodegradation mechanisms of MIL-100(Al) in physiological medium. In particular, we used TEM and iDPC-STEM imaging coupled with STEM-EDS and STEM-EELS to monitor the changes in morphology, crystal structure and chemical composition of MOFs in contact with PBS. While each of these techniques described distinct degradation features, their combination has allowed to reveal the complexity and heterogeneity of the process. In particular, it was shown that phosphate molecules of PBS induce a sparse and continuous erosion of MIL-100(Al), which feeds the progressive growth of an amorphous aluminium phosphate phase.

In addition, this study highlights the need to monitor complex reactions step by step in order to gain a full understanding. Unlike previous studies that focused on the early and final stages of biodegradation to report the formation of metal phosphates, this work focused on the intermediate stages to reveal the heterogeneity of the process. Further studies would be required to identify the source of the heterogeneity. Given the high reactivity of defect sites, we suggest that free metal sites are nests for nucleation of the amorphous deposits.

Finally, this work describes an efficient strategy that could be applied to the study the biodegradation mechanisms of MOFs in more complex media close to *in-vivo* condition, such as culture cell media, blood. The behaviour of MOFs could thus be analysed for variable pH and composition (ions and proteins). These *in-vitro* studies are essential prerequisites for understanding the degradation mechanisms inside cells. The approaches and methodologies used in our present work are also compatible with the study of *in-vivo* mechanisms in cells.

MATERIALS AND METHODS

Synthesis of MIL-100(Al)

MIL-100(Al) nanoparticles were synthesized by a microwave assisted hydrothermal method, as previously reported in [24]. Prior biodegradation, the original MIL-100(Al) nanoparticles were characterised to assess their morphology, crystal structure and purity by dynamic light scattering, porosimetry, thermogravimetric analysis, FTIR and TEM. More details are given in SI.

Degradation of nanoparticles

Prior to degradation, the nanoparticles were recovered by centrifugation at 11,000g for 15 min, then washed twice in water by two successive centrifugations at 10,000g for 10 min. For degradation, 1 mL of PBS was added to the pellet, and incubated at 37°C for 48h (WiseCube® WIF incubator, Witeg Labortechnik GmbH, Germany). The final product was recovered by centrifugation at 12,000g for 15 min and redispersed in water, except for the $P/Al_3 = 22.8$, which was analysed as-is. Table 1 summarises the different concentrations used for MIL-100(Al) suspension and PBS. The P/Al_3 molar ratio was calculated as follows:

$$\frac{[PBS] \text{ x } V_{PBS} \text{ x } M_{MIL-100(Al)}}{[MIL-100(Al)]}$$

where [PBS], V_{PBS}, $M_{MIL-100(Al)}$ and [MIL-100(Al)] are the concentration of PBS in $mol.L^{-1}$, the volume of PBS in L, the molecular weight of MIL-100(Al) in $g.mol^{-1}$ and the concentration of MIL-100(Al) in $mg.mL^{-1}$, respectively.

High resolution imaging and elemental composition.

Sample preparation. 4µL of each suspension were deposited onto glow-discharged TEM carbon grids during 10 s and blotted with filter paper. Lacey carbon 300 mesh and holey carbon 200 mesh (Agar Scientific) were used for STEM-EELS and iDPC-STEM-EDS, respectively.

iDPC-STEM and STEM-EDS experiments were performed on two microscopes: a FEI Cubed Titan Themis and a FEI Talos F200X G2 microscope. The former is equipped with a four-quadrant imaging detector (FEI DF4) for iDPC-STEM experiments, a double Cs aberration energy filter (Gatan Quantum ERS). The two microscopes are also equipped with a high brightness X-FEG electron gun and a Super X-EDS spectrometer (ThermoFisher Scientific). The iDPC experiments were performed at 200 kV with a probe current of 0.5 pA, a dwell time of 2.5 µs, and a pixel size of < 1Å, reducing the electron dose below 60 $\bar{e}$/Å^2. The obtained images were processed using the average background subtraction filter (ABSF), available online in the HRTEM script for Digital Micrograph software.[25] To improve the result, the filter was run twice with the following parameters: step of 2, delta of 5% and cycles of 99%. For the EDS experiments, the Titan Themis was operated at 300 kV with a beam convergence semi-angle of 21.4 mrad and a camera length of 115 mm, while the Talos F200X was used at 200 kV with a beam convergence of 7.5 mrad and a camera length of 125 nm. The probe current was around 130 pA, the dwell time < 128 µs and the pixel size between 1 and 9 nm, for both microscopes. The applied electron dose is estimated to be of the order of 10^2 $\bar{e}$/Å^2. All EDS data were collected with a dispersion of 5 eV and analysed with the ThermoFisher Scientific Velox software. The elemental quantification provided in atomic percentage was obtained by fitting the spectra with an empirical model and deconvolving the elements coming from impurities or components of the microscope (*i.e.* silicon, sulphur, chlorine, potassium, calcium and copper). The elemental maps were obtained in net intensities after filtering with a Gaussian blur (α 0.8).

STEM-EELS measurements were performed on a monochromated Cs-corrected Nion Hermes 200-S microscope operated at 100kV, equipped with a single tilt cryo-specimen holder (HennyZ), a Nion Iris spectrometer and a Merlin Direct Electron Detector camera (Quantum Detectors, UK) for spectroscopy. The convergence semi-angle was 10 mrad. For EELS, the entrance aperture was 1 mm or 2 mm and the energy dispersion was 0.015 eV/channel for low-loss experiments and 0.270 eV/ch or 0.398 eV/channel for simultaneous acquisition of low and core-loss signals. The data were collected at different electron doses ranging from 10 $\bar{e}$/Å^2 to 3.10^4 $\bar{e}$/Å^2. To do so, the beam current, dwell time and pixel size were set between 6 – 60 pA, 2 – 30 ms, and 0.5 – 10 nm. The data were analysed in the Gatan Digital Micrograph® software. The spectral resolution, mentioned in each figure, was measured at the full width at half maximum of the zero-loss peak (ZLP). The spectra were calibrated using the ZLP (0 eV) and the carbon K-edge (first peak at 285.0 eV). All the presented spectra were processed by background subtraction with a power law, in front of every edge of interest. The elemental maps were obtained by integrating the corresponding edges after background subtraction. To distinguish the oxygen from the mineral and organic phases, the oxygen K-edge was denoised by principal component analysis (6 components) using the Hyperspy Python library.[26]

ACKNOWLEDGMENTS

This project has received funding from the European Union's Horizon 2020 research and innovation programme under grant agreement No 823717 – ESTEEM3.

This work has been partly supported by the National Agency for Research under the program of future investment TEMPOS CHROMATEM (Reference no. ANR-10-EQPX-50) and the European Union's Horizon 2020 research and innovation program (Grant no. 823717, ESTEEM3).

REFERENCES

(1) He, S.; Wu, L.; Li, X.; Sun, H.; Xiong, T.; Liu, J.; Huang, C.; Xu, H.; Sun, H.; Chen, W.; Gref, R.; Zhang, J. Metal-Organic Frameworks for Advanced Drug Delivery. *Acta Pharm. Sin. B* **2021**, *11* (8), 2362–2395. https://doi.org/10.1016/j.apsb.2021.03.019.

(2) Ding, M.; Liu, W.; Gref, R. Nanoscale MOFs: From Synthesis to Drug Delivery and Theranostics Applications. *Adv. Drug Deliv. Rev.* **2022**, *190*, 114496. https://doi.org/10.1016/j.addr.2022.114496.

(3) Luzuriaga, M. A.; Benjamin, C. E.; Gaertner, M. W.; Lee, H.; Herbert, F. C.; Mallick, S.; Gassensmith, J. J. ZIF-8 Degrades in Cell Media, Serum, and Some—but Not All—Common Laboratory Buffers. *Supramol. Chem.* **2019**, *31* (8), 485–490. https://doi.org/10.1080/10610278.2019.1616089.

(4) Bůžek, D.; Adamec, S.; Lang, K.; Demel, J. Metal–Organic Frameworks vs. Buffers: Case Study of UiO-66 Stability. *Inorg. Chem. Front.* **2021**, *8* (3), 720–734. https://doi.org/10.1039/D0QI00973C.

(5) Velásquez-Hernández, M. de J.; Ricco, R.; Carraro, F.; Limpoco, F. T.; Linares-Moreau, M.; Leitner, E.; Wiltsche, H.; Rattenberger, J.; Schröttner, H.; Frühwirt, P.; Stadler, E. M.; Gescheidt, G.; Amenitsch, H.; Doonan, C. J.; Falcaro, P. Degradation of ZIF-8 in Phosphate Buffered Saline Media. *CrystEngComm* **2019**, *21* (31), 4538–4544. https://doi.org/10.1039/C9CE00757A.

(6) Wang, L.; Wen, X.; Li, J.; Zeng, P.; Song, Y.; Yu, H. Roles of Defects and Linker Exchange in Phosphate Adsorption on UiO-66 Type Metal Organic Frameworks: Influence of Phosphate Concentration. *Chem. Eng. J.* **2021**, *405*, 126681. https://doi.org/10.1016/j.cej.2020.126681.

(7) Abánades Lázaro, I.; Haddad, S.; Sacca, S.; Orellana-Tavra, C.; Fairen-Jimenez, D.; Forgan, R. S. Selective Surface PEGylation of UiO-66 Nanoparticles for Enhanced Stability, Cell Uptake, and PH-Responsive Drug Delivery. *Chem* **2017**, *2* (4), 561–578. https://doi.org/10.1016/j.chempr.2017.02.005.

(8) Li, X.; Lachmanski, L.; Safi, S.; Sene, S.; Serre, C.; Grenèche, J. M.; Zhang, J.; Gref, R. New Insights into the Degradation Mechanism of Metal-Organic Frameworks Drug Carriers. *Sci. Rep.* **2017**, *7* (1), 13142. https://doi.org/10.1038/s41598-017-13323-1.

(9) Christodoulou, I.; Bourguignon, T.; Li, X.; Patriarche, G.; Serre, C.; Marlière, C.; Gref, R. Degradation Mechanism of Porous Metal-Organic Frameworks by In Situ Atomic Force Microscopy. *Nanomaterials* **2021**, *11* (3), 722. https://doi.org/10.3390/nano11030722.

(10) Le Vuong, M. D.; Christodoulou, I.; Porcino, M.; Dong, S.-T.; Lassalle-Kaiser, B.; Haouas, M.; Gref, R.; Martineau-Corcos, C. Degradation Mechanism of Metal–Organic Framework Drug Nanocarriers Studied by Solid-State Nuclear Magnetic Resonance and X-Ray Absorption Near-Edge Structure Spectroscopy. *Chem. Mater.* **2022**, *34* (18), 8178–8189. https://doi.org/10.1021/acs.chemmater.2c01190.

(11) Bunzen, H. Chemical Stability of Metal-Organic Frameworks for Applications in Drug Delivery. *ChemNanoMat* **2021**, *7* (9), 998–1007. https://doi.org/10.1002/cnma.202100226.

(12) Christodoulou, I.; Lyu, P.; Soares, C. V.; Patriarche, G.; Serre, C.; Maurin, G.; Gref, R. Nanoscale Iron-Based Metal–Organic Frameworks: Incorporation of Functionalized Drugs and Degradation in Biological Media. *Int. J. Mol. Sci.* **2023**, *24* (4), 3362. https://doi.org/10.3390/ijms24043362.

(13) Vuong, D. L. M. Degradation mechanism of nanoparticle-based drug delivery systems: the case of polymer conjugate and metal-organic framework. PhD thesis, Université Paris-Saclay, France, 2022.

(14) Li, X.; Porcino, M.; Qiu, J.; Constantin, D.; Martineau-Corcos, C.; Gref, R. Doxorubicin-Loaded Metal-Organic Frameworks Nanoparticles with Engineered Cyclodextrin Coatings: Insights on Drug Location by Solid State NMR Spectroscopy. *Nanomaterials* **2021**, *11* (4), 945. https://doi.org/10.3390/nano11040945.

(15) Chaupard, M.; Degrouard, J.; Li, X.; Stéphan, O.; Kociak, M.; Gref, R.; de Frutos, M. Nanoscale Multimodal Analysis of Sensitive Nanomaterials by Monochromated STEM-EELS in Low-Dose and Cryogenic Conditions. *ACS Nano* **2023**, *17* (4), 3452–3464. https://doi.org/10.1021/acsnano.2c09571.

(16) Wang, H.; Liu, L.; Wang, J.; Li, C.; Hou, J.; Zheng, K. The Development of IDPC-STEM and Its Application in Electron Beam Sensitive Materials. *Molecules* **2022**, *27* (12), 3829. https://doi.org/10.3390/molecules27123829.

(17) Mejías, F. J. R.; Trasobares, S.; Varela, R. M.; Molinillo, J. M. G.; Calvino, J. J.; Macías, F. A. One-Step Encapsulation of Ortho-Disulfides in Functionalized Zinc MOF. Enabling Metal–Organic Frameworks in Agriculture. *ACS Appl. Mater. Interfaces* **2021**, *13* (7), 7997–8005. https://doi.org/10.1021/acsami.0c21488.

(18) Volkringer, C.; Popov, D.; Loiseau, T.; Férey, G.; Burghammer, M.; Riekel, C.; Haouas, M.; Taulelle, F. Synthesis, Single-Crystal X-Ray Microdiffraction, and NMR Characterizations of the Giant Pore Metal-

Organic Framework Aluminum Trimesate MIL-100. *Chem. Mater.* **2009**, *21* (24), 5695–5697. https://doi.org/10.1021/cm901983a.

(19) Tourtin, F.; Armand, P.; Ibanez, A.; Tourillon, G.; Philippot, E. Gallium Phosphate Thin Solid Films: Structural and Chemical Determination of the Oxygen Surroundings by XANES and XPS. *Thin Solid Films* **1998**, *322* (1), 85–92. https://doi.org/10.1016/S0040-6090(97)00961-9.

(20) Kłosowski, M. M.; Friederichs, R. J.; Nichol, R.; Antolin, N.; Carzaniga, R.; Windl, W.; Best, S. M.; Shefelbine, S. J.; McComb, D. W.; Porter, A. E. Probing Carbonate in Bone Forming Minerals on the Nanometre Scale. *Acta Biomater.* **2015**, *20*, 129–139. https://doi.org/10.1016/j.actbio.2015.03.039.

(21) Egerton, R. F. *Electron Energy-Loss Spectroscopy in the Electron Microscope*; Springer Science & Business Media, 2011.

(22) Jiang, N.; Spence, J. C. H. In Situ EELS Study of Dehydration of Al(OH)3 by Electron Beam Irradiation. *Ultramicroscopy* **2011**, *111* (7), 860–864. https://doi.org/10.1016/j.ultramic.2010.11.004.

(23) Kruse, J.; Leinweber, P.; Eckhardt, K.-U.; Godlinski, F.; Hu, Y.; Zuin, L. Phosphorus L2,3-Edge XANES: Overview of Reference Compounds. *J. Synchrotron Radiat.* **2009**, *16* (2), 247–259. https://doi.org/10.1107/S0909049509000211.

(24) Agostoni, V.; Horcajada, P.; Noiray, M.; Malanga, M.; Aykaç, A.; Jicsinszky, L.; Vargas-Berenguel, A.; Semiramoth, N.; Daoud-Mahammed, S.; Nicolas, V.; Martineau, C.; Taulelle, F.; Vigneron, J.; Etcheberry, A.; Serre, C.; Gref, R. A “Green” Strategy to Construct Non-Covalent, Stable and Bioactive Coatings on Porous MOF Nanoparticles. *Sci. Rep.* **2015**, *5* (1), 7925. https://doi.org/10.1038/srep07925.

(25) Mitchell, D. R. G. *HRTEM Filter*. Dave Mitchell’s DigitalMicrograph^{TM} Scripting Website. http://www.dmscripting.com/hrtem_filter.html (accessed 2023-03-29).

(26) Peña, F. de la; Prestat, E.; Fauske, V. T.; Burdet, P.; Lähnemann, J.; Furnival, T.; Jokubauskas, P.; Nord, M.; Ostasevicius, T.; MacArthur, K. E.; Johnstone, D. N.; Sarahan, M.; Aarholt, T.; Taillon, J.; pquinn-dls; Migunov, V.; Eljarrat, A.; Caron, J.; Poon, T.; Mazzucco, S.; Francis, C.; Martineau, B.; actions-user; Somnath, S.; Slater, T.; Tappy, N.; Walls, M.; Cautaerts, N.; Winkler, F.; DENSmerijn. Hyperspy/Hyperspy: Release v1.6.5, 2021. https://doi.org/10.5281/zenodo.5608741.

4.2 . Conclusion and prospects

This study has shown that correlating TEM, iDPC-STEM, STEM-EDS and STEM-EELS is a powerful strategy for elucidating complex chemical processes at the nanoscale. While each of these techniques characterises a single property (*e.g.* crystal structure or chemical composition), their combination allows a complete understanding of the different interactions involved in the process.

This work has also demonstrated that the use of both low and high electron doses can provide complementary information to describe complex nanomaterials. For example, although low-dose STEM-EELS provided the undamaged structure of biodegraded MOFs, it was limited by a low signal and low spatial resolution (10 $\bar{e}$/Å^{2}, 10 nm). Conversely, performed at higher electron doses (> 10^{2} $\bar{e}$/Å^{2}), STEM-EELS has allowed to assess the chemical composition of biodegraded MOFs with a spatial resolution of less than 3 nm. However, due to the beam damage, high-dose experiments only describe damaged structures. This could lead to a misunderstanding of the specimen features. This work shows that, by monitoring the spectral changes as a function of the electron dose, the beam-effect study helps to relate the damaged signatures to the original structure of the nanomaterial. Thus, despite the extreme radiation sensitivity of MOFs, their analysis should not be limited to low-dose conditions.

By establishing alternative strategies for the analysis of radiation-sensitive and complex nanostructures, this work further paves the way for the study of organic matter and life-related materials.

Chapter 5 .

MOF drug loading and interest for studying biological systems

Finally, the therapeutic efficacy of MOFs nanocarriers was studied by investigating the drug loading, drug distribution and the MOF-drug interactions. This chapter first presents the analysis of the drug-loaded MOFs by STEM-EELS and STEM-EDS. It adresses the abilities of these techniques to characterise the free drug and arises their limitations in the case of organic molecules at low concentrations. As MOFs are inherently designed to interact with biological matter, this chapter then pushes the boundaries of electron spectromicroscopy by analysing biomolecules.

As discussed in Chapter 4, the analysis of radiation-sensitive nanomaterials should not be limited to damage-free conditions at the cost of misinterpretation and misunderstanding of complex structures and mechanisms. Therefore, all the characterisations were performed at low and high electron doses. By studying the beam-effect of different molecules, this work also provides more insight into the radiation damage of beam-sensitive nanomaterials. In particular, gemcitabine monophosphate and naphthazarin (drugs), deoxyribonucleic acid and bovine serum albumin (protein) are within the scope of this study.

5.1 . Drug-loaded MOFs and detection limits for low concentrations

The high drug payload capacity of MIL-100 is not only due to their porosity but also to their amphiphilic character. Drugs can be physically incorporated into the pores and also interact with the open metal sites (hydrophilic) or the organic linkers (more hydrophobic) through electrostatic interactions, coordination bonding, $\pi - \pi$ stacking, van der Waals interactions, hydrogen bonding or hydrophobic interactions.[13, 103] This results in relatively strong host-guest interactions between the drug and the MOFs. These interactions are essential to regulate both the drug uptake in MOFs and the drug release in tumours. Previous studies have shown that phosphorylated drugs achieve enhanced host-guest interactions[48, 54] due to the high affinity of the strong PO_4^{3-} base for the strong Fe^{3+}/Al^{3+} acid.[121] Consistently, gemcitabine monophosphate, prednisolone monophosphate and azidothymidine triphosphate showed higher loading in MIL-100(Fe) (> 20 wt% vs. 1 wt%)[42, 49, 50] and more sustained release than the free drug.[48, 58]

Therefore, the anticancer drug gemcitabine monophosphate (GMP) was selected for encapsulation at 20 wt% in MIL-100(Al) nanoparticles (see the Chapter 2 for more details on the experimental procedure). This hydrophilic drug has a nucleoside-like structure that allows it to be easily incorporated into the DNA chain to stop its synthesis (replication, transcription or repair) and induce cell death.[122] The phosphorylated form of the drug enhances the interactions with the MOFs for efficient incorporation (see Section 1.1.2). This has previously resulted in a drug loading efficiency > 80% for MIL-100(Fe) under these conditions.[42, 123]

Althrough well designed, the drug distributions and loadings of MOFs must be assessed to determine the therapeutic capacity of drug-loaded MIL-100(Al). As their properties can vary from a particle to another, such investigation should be carried out at the nanoscale, on an individual basis. Due to the radiation sensitivity of MOFs that requires minimising the applied electron dose, these techniques may be limited. The following section discusses the detection limits of electron spectromicroscopy in the analysis of low concentration organic materials, in the case of drug-loaded MIL-100(Al).

Prior to individual characterisation, the drug loading and MOF integrity were demonstrated by FTIR and TEM. Appendix B.2 shows the detection of the characteristic IR signature of GMP and the preserved crystallinity of the MOFs after loading.

5.1.1 . STEM-EELS: detection vs. damage

Monochromated STEM-EELS was then used to analyse the chemical signature of the drug-loaded MIL-100(Al). To do so, the fingerprints of the drug-loaded MOFs were compared with that of the free-standing GMP and of the empty MIL-100(Al). The three nanomaterials were studied at low (10 $\bar{e}$/Å^2) and higher electron doses (up to 2.10^4 $\bar{e}$/Å^2) to both characterise the undamaged structures and increase the detection sensitivity and spatial resolution (1 nm), respectively (see Chapter 3). Since the empty MOFs have already been described in Chapter 3, the discussion focuses first on the free-standing GMP.

Figure 5.1 shows the low-loss and core-loss spectra of GMP. According to the chemical composition of GMP (Figure 5.1.a), the analysis in the core-loss region was performed on the phosphorus L-, carbon K-, nitrogen K-, oxygen K- and fluorine K- edges. The features obtained at low dose (10 $\bar{e}$/Å^2) are discussed first. Only the low-loss and carbon K-edge showed a sufficient SNR to be analysed under these conditions (Figure 5.1.b). In the low-loss region, three main peaks are observed at 5.0 eV, 6.2 eV and 8.7 eV. The first two peaks correspond to π-π^* and n-π^* transitions, but would require additional theoretical calculations for a more specific assignment. The third peak results from the presence of water or hydroxyl groups.[124] In the core-loss region, the carbon K-edge exhibits two main peaks at 285.0 eV (peak A) and 287.5 eV (peak C). They correspond to 1s-$\pi^*_{C=C}$ and 1s-$\pi^*_{C=N}$ transitions of the cytosine group, respectively.[97] Another weak contribution is found at about 288.7 eV (peak D), associated with the 1s-$\pi^*_{C=O}$ transitions of the cytosine group.[97, 124]

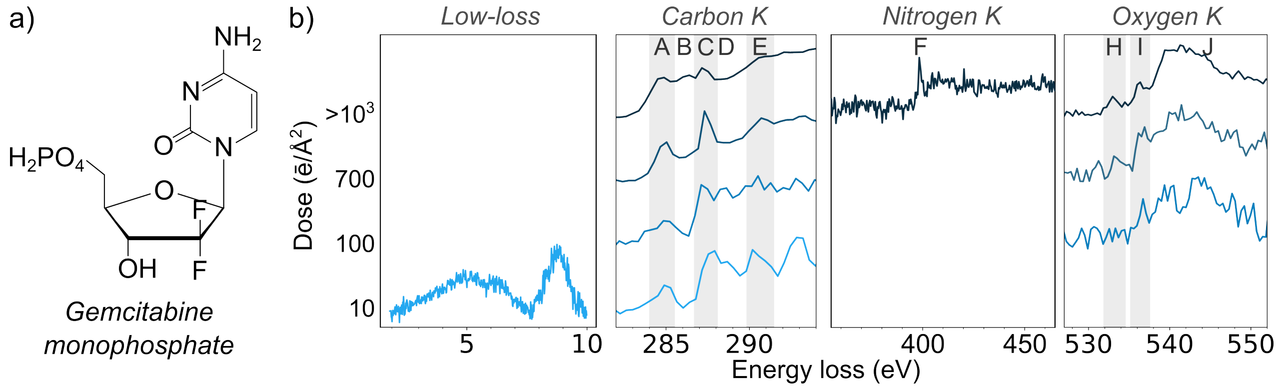

Figure 5.1: a) Molecular structure of GMP. b) EELS spectra of GMP in the low-loss and core-loss regions (carbon K-, nitrogen K- and oxygen K-edges). The spectra are cumulated over hundreds of nanometres. Data were acquired at electron doses ranging from 10 $\bar{e}$/Å^2 to 2.10^4 $\bar{e}$/Å^2. The spectral resolution is 0.04 eV for the low-loss and 0.8 eV for the core-loss.

Higher electron doses (> 10^3 $\bar{e}$/Å^2) were then used to improve the detection sensitivity, in particular for the phosphorus, nitrogen and oxygen. No low-loss data were acquired as the features tended to disappear at high doses due to beam damage. On the carbon K-edge, peaks A and C become prominent and other peaks appear at 286.5 eV (peak B) and near 290.7 eV (peak E). The nitrogen K-edge shows a single peak at 398.6 eV (peak F). The oxygen K-edge displays three peaks at 533.2 (peak H), 536.5 (peak I) and near 541 eV (peak J). These high-dose signals describe a damaged structure. Their assignement is discussed in detail below (see Section 5.2.2). Note that the fluorine K- and phosphorus L- edges were not detected at either low or high electron doses.

Then, the spectra of GMP, MIL-100(Al) and drug-loaded MOFs were compared to detect and localise the drug loaded in the MOFs. In order to discriminate each specific signature, the analysis was focused on spectral features characteristic of the GMP that are not present in the MOFs. These are the low-loss signatures, the fluorine K-edge (685 eV), the phosphorus L-edge (135 eV) and the nitrogen K-edge (400 eV). However, as discussed above, only the low-loss and nitrogen K-edge were detected for the free-standing GMP.

Figure 5.2 (bottom) shows the low-loss spectra of GMP, MIL-100(Al) and loaded-MIL-100(Al) obtained at low dose. GMP (blue line) and MIL-100(Al) (red line) display distinct signatures. This suggests the possibility of distinguishing the two materials in the loaded MIL-100(Al). However, the low-loss spectrum of the loaded MOFs (purple line) is similar to that of the empty MOFs. This could be due to the insufficient sensitivity of STEM-EELS to detect the low concentration of the loaded drug. To improve the detection sensitivity, higher electron doses were used. Unfortunately, the results do not provide any further information as all the low-loss signatures disappear due to beam damage. Similarly, in the core-loss region, the nitrogen K-edge of GMP was not detected in the drug-loaded MIL-100(Al). Again, this is probably due to the low concentration of nitrogen in the loaded MOFs. Overall, these results show that STEM-EELS is not sensitive enough to detect

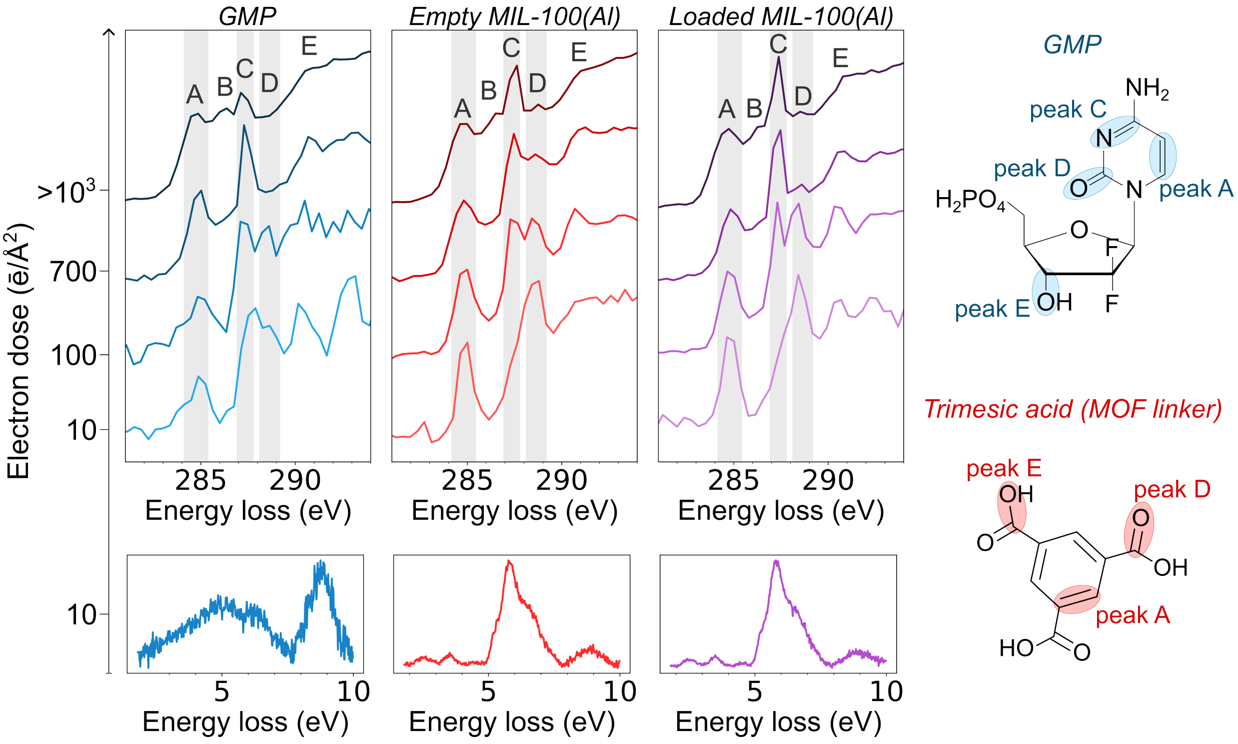

Figure 5.2: Spectral signatures of the bare GMP (blue), the empty MIL-100(Al) nanoparticles (red) and the drug-loaded MIL-100(Al) nanoparticles (purple) obtained in the low-loss (bottom) and core-loss regions (top). The extracted spectra were cumulated over hundreds of nanometres. Data were obtained with electron doses ranging from 10 $\bar{e}$/Å^2 to 2.10^4 $\bar{e}$/Å^2. The spectral resolution is 0.04 eV in the low-loss and 0.8 eV in the core-loss. For clarity, the molecular structure and peak assignement is provided for GMP and MOF linker (trimesic acid).

the characteristic elements of the GMP. To improve the detection efficiency, the analysis was then focused on edges with more favourable edge shapes for their analysis.

The carbon K- and oxygen K-edges showed a suitable SNR due to their higher concentrations in the specimens, compared to the other elements. As both the drug and the MOFs contain these two elements, the two signals overlap and a fine structure analysis was required to distinguish their contributions from their specific signatures. Figure 5.2 (top) displays the carbon K-edge obtained for the three specimens. At low-dose, the carbon K-edge of the GMP shows a distinct feature compared to MIL-100(Al): the peak C. This peak is however not detected in the loaded MIL-100(Al). The carbon K-edge of the loaded MOFs remains similar to that of the empty MOFs. Higher electron doses (up to 2.10^4 $\bar{e}$/Å^2) could not provide any further information. Due to the beam damage, the carbon K-edge becomes similar for the three specimens. Therefore, the signature of the drug could not be detected in the loaded MOFs by analysing the carbon K-edge. For the oxygen K-edge, the signals were found too weak at 100 $\bar{e}$/Å^2 for fine structure analysis. Higher electron doses were required to obtain a measurable signal. Figure 5.3 presents the oxygen K-edge of the three specimens obtained at 700 $\bar{e}$/Å^2. Unfortunately, all the signals becomes similar due to beam damage. Therefore, there are no spectral features specific to the drug to analyse the MOF loading.

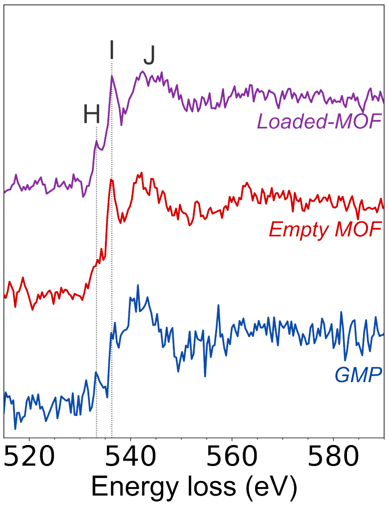

Figure 5.3: a) Comparison of the oxygen K-edge of the bare GMP in blue, the empty MIL-100(Al) in red and the drug-loaded MIL-100(Al) in purple. Data were obtained at 700 $\bar{e}$/Å^2. The spectral resolution is 0.8 eV.

According to the literature (see Section 1.1.2), the drug interacts with the framework through coordination of the phosphate groups with the aluminium sites. Thus, analysis of the aluminium L-edges (76 eV) could provide information on the drug uptake. However, it was not detected neither in the empty nor the loaded MIL-100(Al), at low and high electron doses (up to 1.10^4 $\bar{e}$/Å^2). This is probably due to the unfavourable shape of the aluminium L-edge making it difficult to extract and the too high thickness of the specimen that attenuates the signal.

In a nutshell, despite exploring all available EELS signals in the low-loss and core-loss regions, no chemical fingerprint was found to provide information on the drug load. At low-dose, the signal was probably too low, while higher electron doses hampered to discriminate specific features due the beam damage. We assume that we have reached the EELS detection limits, probably due to the low concentration of the drug and the unfavourable edge shape of its elements. It is also possible that the signal from the GMP is obscured by that of the MOFs, which overlap particularly in the low-loss region and on the carbon K-edge. Note that the specimen thickness could also be involved, as EELS signals are attenuated above $\sim$ 100 nm.

5.1.2 . STEM-EDS: a low reliability

Since EELS and EDS have different cross-sections for the detection of elements, the drug loading study may be successfully achieved by STEM-EDS, where STEM-EELS failed. Therefore, STEM-EDS was used to assess the drug loading in MIL-100(Al). Here, electron doses of about 10^2 $\bar{e}$/Å^2 were used. As shown in Chapter 4, these conditions have a little incidence on the elemental distribution of the specimens, at this spatial resolution.

Figure 5.4 and Figure 5.5 show the EDS spectra and elemental maps of the empty and drug-loaded MOFs. Both display a homogeneous distribution of aluminium, carbon and oxygen, as

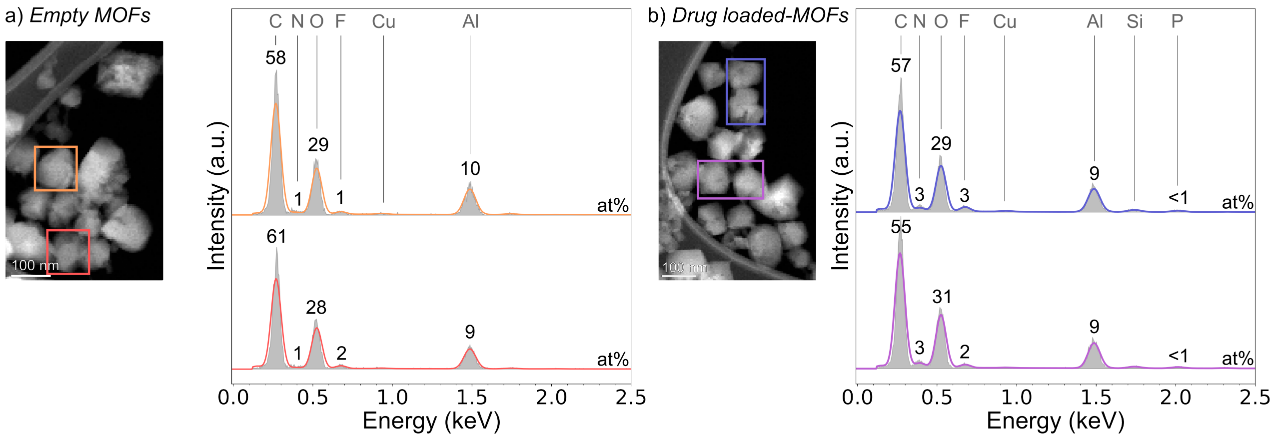

Figure 5.4: EDS elemental spectra obtained for (a) empty and (b) GMP-loaded MIL-100(Al). The electron dose is estimated to be around 10^2 $\bar{e}$/Å^2. The solid line and the shaded area represent the modelled and raw spectra. The modelled spectra were obtained by deconvolution of the silicon, sulphur, chlorine, potassium, calcium and copper elements. Carbon, nitrogen, oxygen, fluorine, aluminium and phosphorus were quantified. The corresponding values are given above each edge, in atomic percent (at%).

expected. In the drug-loaded MOFs, nitrogen, fluorine and phosphorus were used as indicators for the presence of GMP since they are specific to the drug. However, as observed in Figure 5.4.a, nitrogen and fluorine are also detected in the empty MOFs. These impurities could originate from the synthesis, where aluminium nitrate and nitric acid (nitrogen source) were mixed in a microwave Teflon reactor (fluorine source). Comparing the empty and loaded MOFs, the concentration of nitrogen and fluorine seems to slightly increase, from < 2 at% in the empty MOFs to about 3 at% in the loaded ones. This could suggest the detection of the incorporated drug. Figure 5.5 also shows a heterogeneous distribution of fluorine (cyan colour), where hot spots could indicate the accumulation of a cargo in specific regions (drug or impurities). The nitrogen map (orange colour) does not reveal such local accumulations, suggesting that there is no correlation between the two elements. This could indicate, for example, the presence of two different impurity species. Overall, as it is difficult to distinguish the nitrogen and fluorine elements coming from the drug or from the impurities, only phosphorus can be used as a drug indicator. As shown in Figure 5.4.b, the drug-loaded MOFs have a relatively low phosphorus content, below 1 at%. The phosphorus map reveals a roughly uniform distribution (Figure 5.5), but the low signal may misrepresents the effective distribution of the loaded drug.

Further analyses would be required to quantify the concentration of loaded drug. Here, the EDS results only provide qualitative information. However, they are poorly reliable due to the low signal of phosphorus. Like STEM-EELS, STEM-EDS is probably also limited by the low drug concentration in MIL-100(Al). Therefore, a possible strategy would be to further increase the electron dose, at the risk of damaging the specimen integrity and losing the signal.

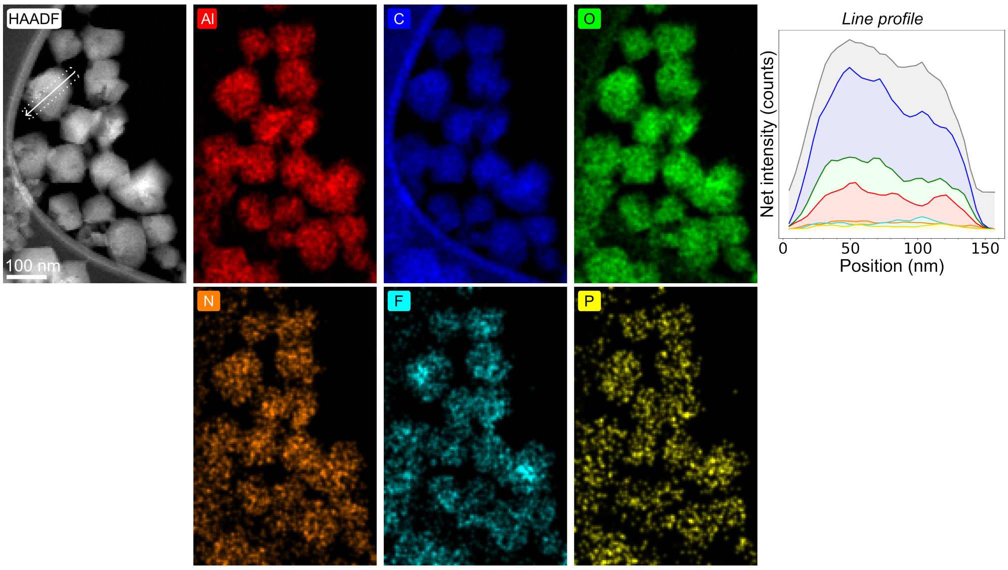

Figure 5.5: HAADF image and EDS elemental maps obtained for GMP-loaded MIL-100(Al). The line profile outlines the homogeneous distribution of the elements, for this spatial resolution. The electron dose is estimated to be around 10^2 $\bar{e}/\text{Å}^2$ and the pixel size is < 5 nm.

5.2 . Outlooks for the study of biological systems

Once administrated in the living body, MOFs inherently interact with biomolecules. With the aim of investigating the MOFs-biomolecule interactions within cells, this section provides references of two of the main macromolecules composing the organism. In particular, STEM-EELS was used to analyse deoxyribonucleic acid (DNA) and bovine serum albumin protein (BSA) in the low-loss and core-loss regions. Low (10 $\bar{e}/\text{Å}^2$) and higher electron doses (up to 2.10^3 $\bar{e}/\text{Å}^2$) were used to collect undamaged signatures and to increase the detection sensitivity of the core-loss features, respectively. In the following, the features obtained at low-dose are first discussed to assign each peak. Then, for high electron doses, the spectral changes were monitored and discussed. Notably, a better understanding of the species produced under the electron beam is provided by comparing the beam-effect studies of DNA and BSA to three other organic moieties: trimesate (MOFs linkers), GMP and naphthazarin.

5.2.1 . Monochromated STEM-EELS of biomolecules

Figure 5.6 display the low and core-loss spectra of DNA. According to its composition (phosphate groups, sugars and nitrogenous bases), the analysis of the core-loss region was focused on the phosphorus L-, carbon K-, nitrogen K- and oxygen K- edges. All the features were acquired at low (10 $\bar{e}/\text{Å}^2$) and high electron doses (up to 2.10^3 $\bar{e}/\text{Å}^2$). At low dose, the DNA spectra show several features in the low and core-losses. In the low-loss, three peaks are observed at 4.7 eV, 6.3 eV and 8.7 eV. The first two peaks correspond to the n-π^* and $\pi - \pi^*$ transitions of DNA,[125, 126] while the last peak indicates the presence of water or hydroxyl groups.[124] In the core-loss, the carbon, nitrogen and oxygen K-edges exhibit a low SNR, while the phosphorus L-edge is not de-

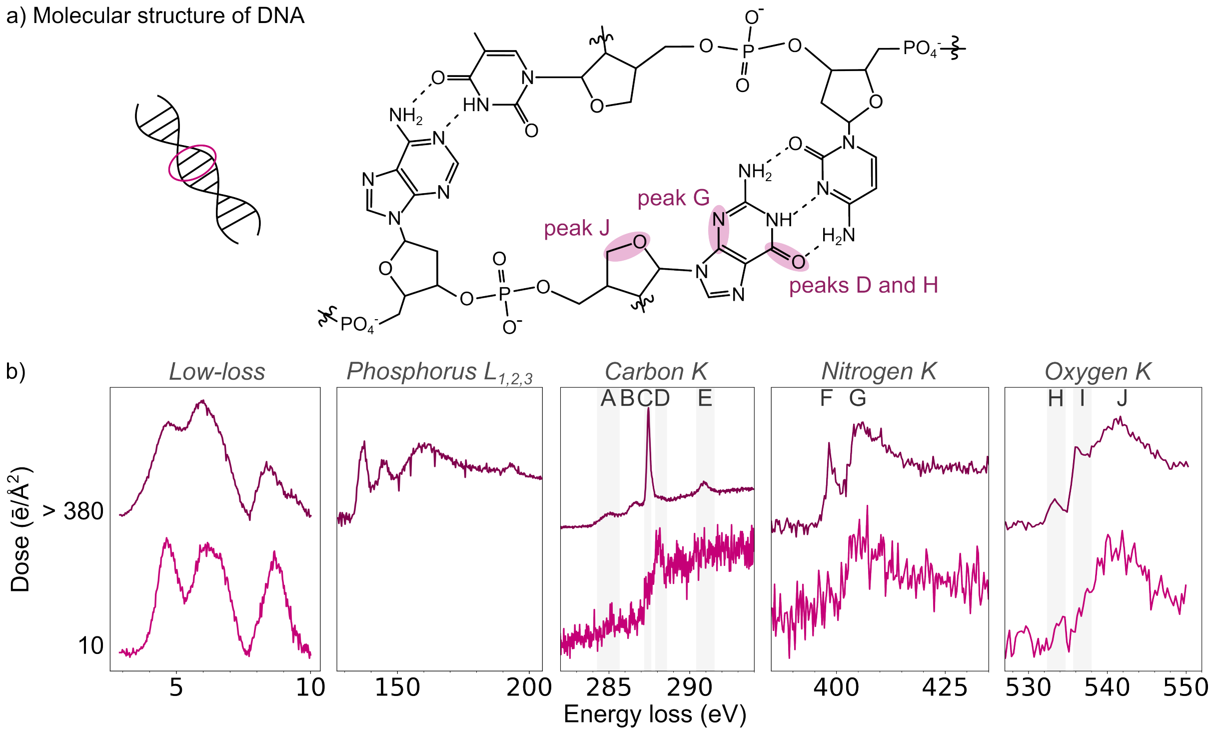

Figure 5.6: a) Example of the molecular structure and b) EELS spectra of DNA obtained in the low and core-loss regions (phosphorus $L_{1,2,3}$-edge, carbon K, nitrogen K and oxygen K-edges). The spectra are cumulated over hundreds of nanometres. Data were acquired at 10 $\bar{e}$/Å^2 (light colours), at 380 $\bar{e}$/Å^2 (dark colours for the low-loss, carbon, nitrogen and oxygen K-edges) and 2.10^3 $\bar{e}$/Å^2 (dark colour for the phosphorus L-edge). The spectral resolution is 0.04 eV for the low-loss and carbon K-edge; and 0.5 eV for the others.

tected. On the carbon K-edge, two peaks can be distinguished at 287.4 eV (weak, peak C), 288.1 eV (prominent, peak D) and 289.3 eV (shoulder). The peak C can be assigned to the 1s-σ^*_{C-H} or 1s-$\pi^*_{C=N}$ transitions.[127, 128] The peaks at 288.1 eV and 289.3 eV indicate 1s-$\pi^*_{C=O}$ transitions involved in the amide and urea groups of the nitrogenous bases.[127, 128] For the nitrogen K-edge, only a weak bump is observed near 405 eV (peak G). It is assigned to the 1s-σ^*_{N-C} transitions of the nitrogenous bases.[128] On the oxygen K-edge, a peak at about 534.0 eV (peak H), followed by a large contribution around 541 eV (peak J) are detected. They correspond to 1s-$\pi^*_{O=C}$ and 1s-$\sigma^*_{O=C}$ transitions of sugar and nitrogen bases, respectively.[127, 128] For each low-loss and core-loss feature, spectral changes are observed as the electron dose is increased up to 380 $\bar{e}$/Å^2. In the low-loss, the first peak is broadened, while the last two peaks are red-shifted to 6.0 eV and 8.5 eV. On the carbon K-edge, peak C increases at 287.5 eV, while several other peaks appear at 285.0 eV (peak A), 286.6 eV (peak B) and 290.9 eV (peak E). On the nitrogen K-edge, a peak at 398.5 eV (peak F) followed by a large contribution at 405 eV (peak G) is clearly distinguishable. Finally, on the oxygen K-edge, the peaks H and J observed at low-dose remain, while another asymmetric peak appears at 536.3 eV (peak I). At 2.10^3 $\bar{e}$/Å^2, the phosphorus $L_{1,2,3}$-edge was also detected, showing three peaks at about 138 eV, 146 eV and 194 eV. These features well describe the 2p-σ^* transitions of the phosphate groups.[127]

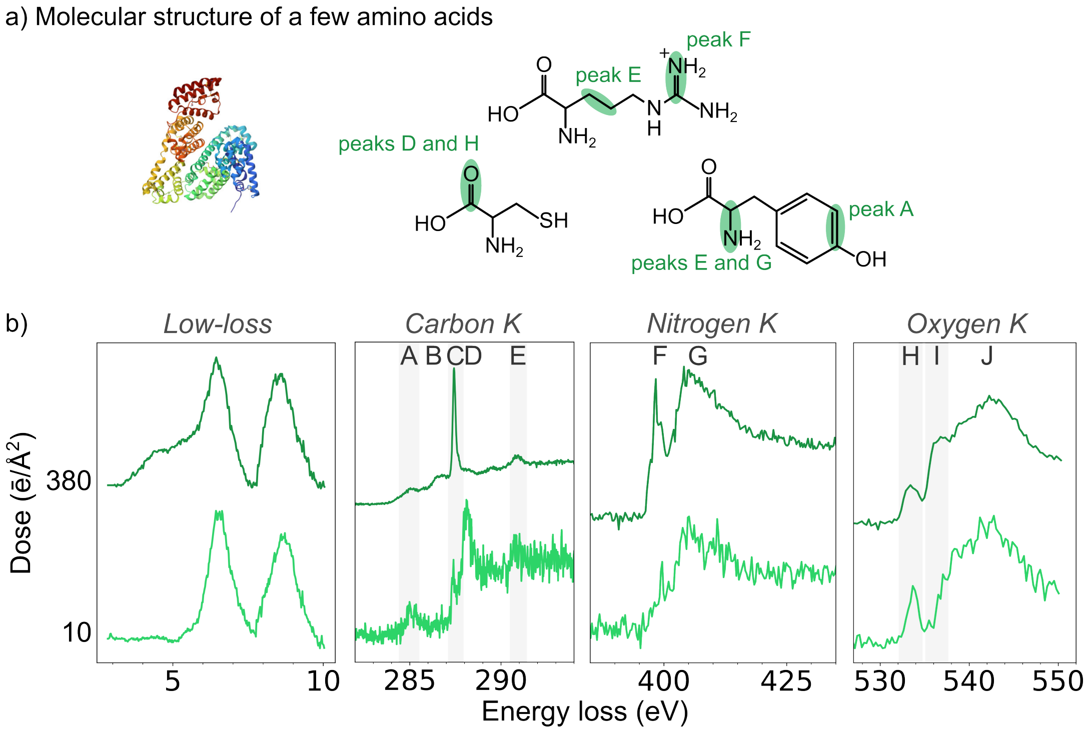

Figure 5.7: a) Example of the molecular composition and b) EELS spectra of BSA obtained in the low and core-loss regions (carbon, nitrogen and oxygen K-edges). The spectra are cumulated over hundreds of nanometres. Data were acquired at 10 $\bar{e}$/Å^2 (light colours) and 380 $\bar{e}$/Å^2 (dark colours). The spectral resolution is 0.04 eV for the low-loss and carbon K-edge; and 0.5 eV for the others.

The low and core-loss spectra of BSA are shown in Figure 5.7. In the core-loss region, the signal was acquired on the carbon K-, nitrogen K- and oxygen K- edges. Under low-dose conditions, the low-loss shows two peaks at 6.5 eV and 8.7 eV. They indicate $\pi - \pi^*$ transitions of BSA[129] and the presence of water or hydroxyl groups,[124] respectively. On the carbon K-edge, four peaks are observed at 285.0 eV (peak A), 287.4 eV (peak C), 288.1 eV (peak D) and 290.9 eV (peak E). The peaks A and D are assigned to 1s-$\pi^*_{C=C}$ and 1s-$\pi^*_{C=O}$ transitions of aromatic and amide groups of proteins.[128, 130] The peak C may correspond to the 1s-σ^* transitions of C-H, C-N or C-S bonds. The peak E may correspond to the 1s-σ^* transitions of C-C, C-N or C-O bonds.[128,130] The nitrogen K-edge shows two contributions at about 399 eV (peak F) and 405 eV (peak G). They correspond to 1s-$\pi^*_{N=C}$ and 1s-σ^*_{N-C} transitions, respectively.[128, 130] The oxygen K-edge displays a peak at 534.0 eV (peak H) followed by a bump around 541 eV (peak J). These are assigned to the 1s-$\pi^*_{O=C}$ and 1s-σ^*_{O-C} transitions of the amide and carboxylic groups.[128, 130] At high electron doses, the spectral evolution of BSA tends to be similar to that of DNA. In the low-loss region, the first peak remains, the last peak is red-shifted to 8.5 eV, and another peak arises near 4.5 eV. On the carbon K-edge, the peaks A and E remain, while the peak C increases at 287.5 eV. Two other peaks appear at 286.6 eV (peak B) and 289.5 eV. On the nitrogen K-edge, the peaks F and G observed at low-dose are enhanced. On the oxygen K-edge, the peaks H and J remain and another appears at 536.5 eV (peak I).

5.2.2 . Overview on the radiolysis of organic and biological matter

Although higher electron doses allow an increase in detection sensitivity, especially for low cross-section edges (*i.e.* phosphorus L-, nitrogen K- and oxygen K- edges), these conditions should be applied with caution when studying organic and biological materials. Beam damage inevitably leads to loss of mass, radiolysis and chemical rearrangement. In order to provide a complete understanding of the chemical changes, the spectral evolution of trimesate (MOFs linkers), GMP, DNA, BSA and naphthazarin is discussed here. The diversity of functional groups in these molecules allows to identify general mechanisms.

For clarity, the reader is referred to Table 5.1 and Table 5.2, which summarise the EELS signatures of the five components observed on the low-loss region, the carbon K-, nitrogen K- and oxygen K-edges, at low and high electron doses (10 $\bar{e}$/Å^{2}and > 10^2 $\bar{e}$/Å^2). The naming and assignment of the peaks is similar to those mentioned above. The trimesate, GMP, DNA and BSA were discussed in Section 3.1, Section 5.1.1 and Section 5.2.1, respectively. Note that for trimesate, the core-loss signatures were obtained directly on the MOFs, but as the carbon and oxygen only come from the linker, they are similar.

Figure 5.8 shows the carbon K-edge of the five specimens. The changes in their spectral signatures fairly illustrate the chemical reactions that occur as the electron dose increases. Fine structure analysis allows each signature to be assigned to a chemical species produced under the electron beam. The first observation of radiation damage is the absence of the signature of hydrogen and fluorine. As discussed in Chapter 3 and Section 5.1.1, the 1s-σ^*_{C-H} transition was not observed on the carbon K-edge of MOFs and GMP, even at low-dose. Although such a signal has already been detected by EELS near 287 eV for small benzene derivatives and polymers,[97,131,132] and at 287.4 eV (peak C) for BSA and DNA in Section 5.2.1, its analysis is not so simple. For the five specimens, the C-H bonds are in low concentration, compared to the unsaturated groups, resulting in a low signal (4 hydrogens for 10 carbon atoms in naphthazarin). Furthermore, the detection of the 1s-σ^*_{C-H} transition can be confused by other transitions, such as the 1s-σ^*_{C-N} transitions of DNA and BSA, which overlap in the peak C (see Section 5.2.1 and Table 5.1).

Similarly, the 1s-σ^*_{C-F} transition (295 eV) was not observed for GMP, despite the robustness of the C-F bonds. Consistently, the fluorine K-edge was also not detected. This suggests a rapid desorption under electron irradiation, similar to hydrogen. Indeed, a previous work has demonstrated the beam-induced fluorine loss in saturated and unsaturated molecules.[133] Nonetheless, it should be mentioned that the detection of fluorine in GMP may be hampered by its unfavourable edge shape and low concentration in the specimen (fluorine represents less than 6 at% of the molecule).

By comparing the five specimens, Figure 5.8 shows similar spectral changes as the electron dose increases. First, peak A at 285.0 eV is broadened. As it is assigned to 1s-$\pi^*_{C=C}$ transitions, this

Table 5.1: Summary of the EELS signatures obtained at low-dose (10 $\bar{e}$/Å^2) for trimesate (MOFs linkers), GMP, DNA, BSA and naphthazarin.

Peak naming	Trimesate		GMP		DNA		BSA		Naphthazarin	
n.a.	5.3 eV	$\pi - \pi^*$	5.0 eV	$\pi - \pi^*$	4.7 eV	n–π^*				
n.a.	6.8 eV	$\pi - \pi^*$	6.2 eV	n–π^*	6.3 eV	$\pi - \pi^*$	6.5 eV	$\pi - \pi^*$		
n.a.	8.6 eV	H_2O ex.	8.7 eV	H_2O ex.	8.7 eV	H_2O ex.	8.7 eV	H_2O ex.		
peak A	285.0 eV	1s-$\pi^*_{C=C}$	285.0 eV	1s-$\pi^*_{C=C}$			285.0 eV	1s-$\pi^*_{C=C}$	285.0 eV	1s-$\pi^*_{C=C}$
peak C			287.5 eV	1s-$\pi^*_{C=N}$	287.4 eV	1s-$\sigma^*_{CH,CN}$	287.4 eV	1s-$\sigma^*_{CH,CN,CS}$	287.5 eV	1s-π^*_{COH}
peak D	288.7 eV	1s-$\pi^*_{C=O}$	288.7 eV	1s-$\pi^*_{C=O}$	288.1 eV	1s-$\pi^*_{C=O}$	288.1 eV	1s-$\pi^*_{C=O}$		
n.a.					289.3 eV	1s-$\pi^*_{C=O}$				
peak E	290.8 eV	1s-σ^*_{C-O}					290.9 eV	1s-$\sigma^*_{CC,CN,CO}$		
peak F							$\sim$ 399 eV	1s-$\pi^*_{N=C}$		
peak G					405 eV	1s-σ^*_{N-C}	405 eV	1s-σ^*_{N-C}		
peak H	534 eV	1s-$\pi^*_{O=C}$			534 eV	1s-$\pi^*_{O=C}$	534 eV	1s-$\pi^*_{O=C}$		
peak J	543 eV	1s-σ^*_{O-C}			541 eV	1s-σ^*_{O-C}	541 eV	1s-σ^*_{O-C}	542 eV	1s-σ^*_{O-C}

H_2O ex. means water exciton and n.a. stands for not applicable.

Table 5.2: Summary of the EELS signatures obtained at high dose (> 10^2 $\bar{e}$/Å^2) for trimesate (MOFs linkers), GMP, DNA, BSA and naphthazarin.

Peak naming	Trimesate		GMP		DNA		BSA		Naphthazarin	
n.a.	5.3 eV				4.7 eV		4.5 eV			
n.a.	6.8 eV				6.0 eV		6.5 eV			
n.a.	8.4 eV	H_2O irr.			8.5 eV	H_2O irr.	8.5 eV	H_2O irr.		
peak A	285.0 eV	1s-$\pi^*_{C=C}$	285.0 eV	1s-$\pi^*_{C=C}$	285.0 eV	1s-$\pi^*_{C=C}$	285.0 eV	1s-$\pi^*_{C=C}$	285.0 eV	1s-$\pi^*_{C=C}$
peak B	286.7 eV	1s-$\pi^*_{C\equiv C}$	286.5 eV	1s-$\pi^*_{C\equiv C}$	286.6 eV	1s-$\pi^*_{C\equiv C}$	286.6 eV	1s-$\pi^*_{C\equiv C}$	286.5 eV	1s-$\pi^*_{C\equiv C}$
peak C	287.6 eV	1s-$\pi^*_{C\equiv O}$	287.5 eV	1s-$\pi^*_{C\equiv O}$	287.5 eV	1s-$\pi^*_{C\equiv O}$	287.5 eV	1s-$\pi^*_{C\equiv O}$	287.5 eV	1s-$\pi^*_{C\equiv O}$
peak D	288.7 eV	1s-$\pi^*_{C=O}$								
n.a.							289.5 eV	n.a.		
peak E	291.0 eV	1s-$\pi^*_{CO_2}$	290.7 eV	1s-$\pi^*_{CO_2}$	290.9 eV	1s-$\pi^*_{CO_2}$	290.9 eV	1s-$\pi^*_{CO_2}$		
peak F			398.6 eV	1s-$\pi^*_{N\equiv C}$	398.5 eV	1s-$\pi^*_{N\equiv C}$	$\sim$ 399 eV	1s-$\pi^*_{N\equiv C}$		
peak G					$\sim$ 405 eV	1s-σ^*_{N-C}	$\sim$ 405 eV	1s-σ^*_{N-C}		
peak H	534.0 eV	1s-$\pi^*_{O\equiv C}$	533.2 eV	1s-$\pi^*_{O\equiv C}$	534.0 eV	1s-$\pi^*_{O\equiv C}$	534.0 eV	1s-$\pi^*_{O\equiv C}$	533.7 eV	1s-$\pi^*_{O\equiv C}$
peak I	536.5 eV	1s-$\pi^*_{CO_2}$	536.5 eV	1s-$\pi^*_{CO_2}$	536.3 eV	1s-$\pi^*_{CO_2}$	536.5 eV	1s-$\pi^*_{CO_2}$	536.8 eV	1s-$\pi^*_{CO_2}$
peak J	$\sim$ 543 eV	1s-σ^*_{O-C}	$\sim$ 541 eV	1s-σ^*_{O-C}	$\sim$ 541 eV	1s-σ^*_{O-C}	$\sim$ 541 eV	1s-σ^*_{O-C}	$\sim$ 542 eV	1s-σ^*_{O-C}

H_2O irr. means the signature of irradiated water and n.a. stands for not applicable.

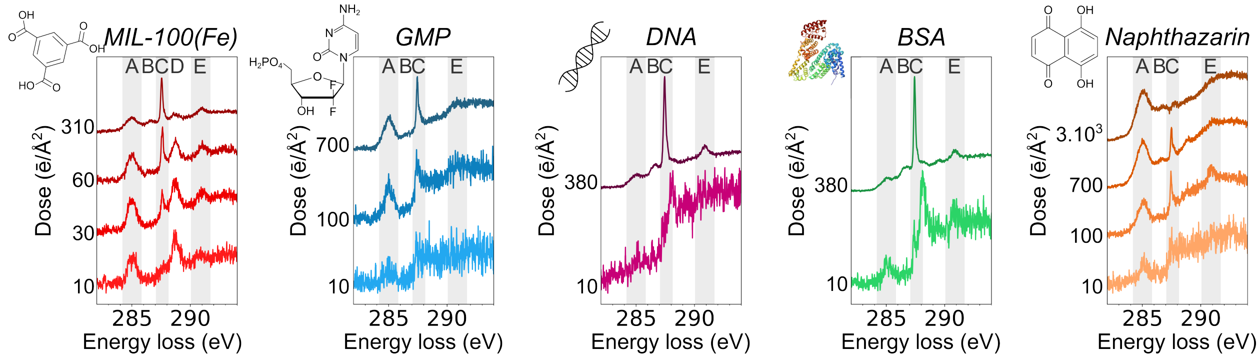

Figure 5.8: EELS carbon K-edge of MIL-100(Al), GMP, DNA, BSA and naphthazarin as a function of the electron dose. Spectra are cumulated over hundreds of nanometres. The spectral resolution is 0.04 eV.

suggests the formation of new bonds with a π^* character. As clearly observed for GMP, the peak becomes more intense with the electron dose, reflecting the formation of double bonds (C=C, sp^2 carbon). At higher electron doses (> 380 $\bar{e}$/Å^2), peak B appears at 286.6 eV. It was previously assigned to 1s-$\pi^*_{C\equiv C}$[134] and highlights the formation of triple bonds (sp carbon). These two observations suggest radical recombination under irradiation to produce unsaturated compounds. Note that concerning nitrogen compounds (GMP, BSA and DNA), the nitrogen K-edge shows a new peak F at about 399 eV for electron doses above 380 $\bar{e}$/Å^2 (Figure 5.6 and Figure 5.7). It is assigned to 1s-$\pi^*_{N=C}$ or 1s-$\pi^*_{N\equiv C}$ transitions [135] and has already been observed in damaged proteins.[130] It is also likely to result from radical recombination and unsaturated compounds.

Then, starting from 100 $\bar{e}$/Å^2, peaks C and E arise at 287.5 eV and 290.9 eV, respectively (Figure 5.8). They have already been described as the 1s-π^* transitions of carbon monoxide and carbon dioxide produced by radiolysis, respectively.[98, 136] To confirm the formation of carbon oxide gases, the carbon and oxygen K-edges were acquired simultaneously. Figure 5.9 displays the corresponding spectral evolution with the electron dose for the five specimens. On the oxygen K-edge, all of them show a peak H at about 534 eV and a peak I at 536.5 eV (Figure 5.9). They are assigned to the 1s-π^* transition of carbon monoxide and carbon dioxide, respectively.[136] A closer look at the five spectra shows that the CO and CO_2 formation is not evenly distributed throughout the specimens. Based on the oxygen K-edge of Figure 5.9, the radiolysis of naphthazarin mainly produces CO (peak H), whereas trimesate is preferentially degraded to CO_2 (peak I). This is probably due to their different chemical composition, where carboxylic acids of trimesate are easily converted to carbon dioxide, whereas the phenol of quinone functions of naphthazarin are closer to the oxidation state of carbon monoxide. Note that the carbon K-edge is more difficult to analyse due to the increasing background obscuring peak E.

Taking advantage of the multimodality offered by EELS, the formation of carbon dioxide can be further confirmed by analysing the ultralow regions. Figure 5.10 shows the superposition of ultralow-loss EELS and FTIR spectra obtained on MIL-100(Al). The shaded area outlines a signature detected near 290 meV ($\sim$ 2,340 cm^{-1}) by both techniques, which in FTIR, is assigned to the

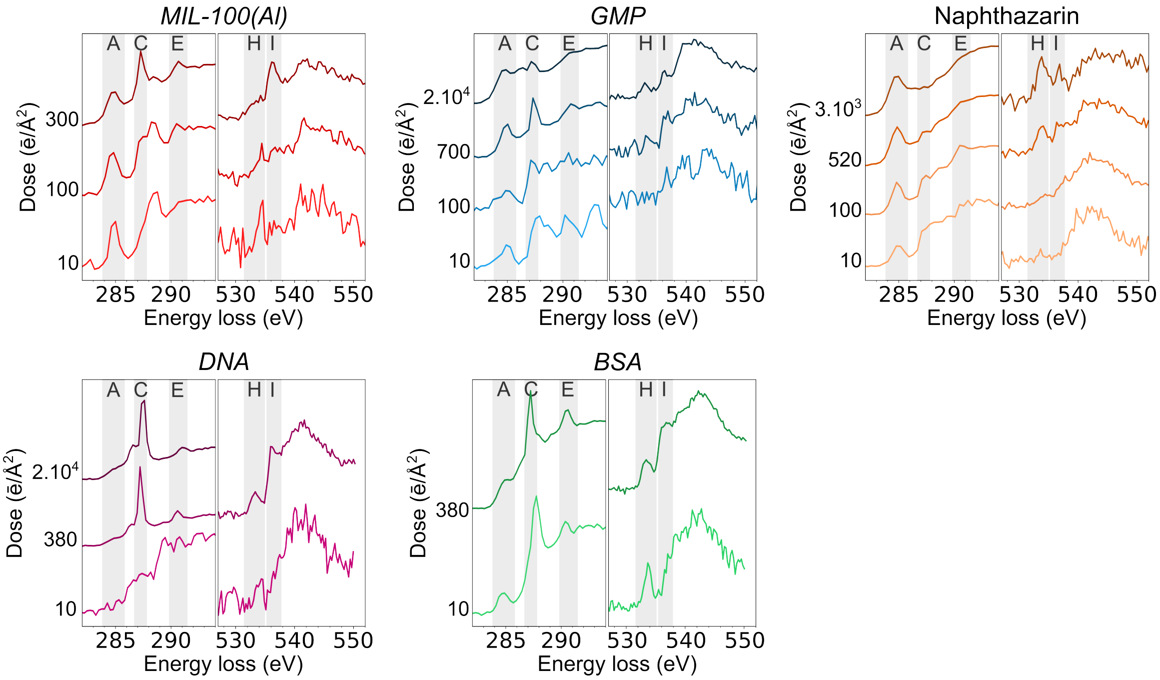

Figure 5.9: EELS carbon and oxygen K-edges acquired simultaneously on MIL-100(Al), GMP, DNA, BSA and naphthazarin as a function of the electron dose. Spectra are cumulated over hundreds of nanometres. The spectral resolution is 0.5 eV for DNA and BSA and 0.8 eV for the others.

well-documented CO_2 vibrational band (atmospheric gas). These results suggest the detection of carbon dioxide in the ultralow-loss EELS. Indeed, this EELS spectrum was obtained at relatively high electron dose (120 $\bar{e}$/Å^2), as required for the collection of the low SNR ultralow-losses. These conditions therefore imply that the organic content of the specimen is partially damaged by the irradiation. Hence, this peak confirms the formation of CO_2 by radiolysis. Note that for MOFs and BSA, the low-loss EELS also shows a new feature near 4 eV with increasing electron dose above 130 $\bar{e}$/Å^2 (see Section 3.1 and Section 5.2.1). By the simultaneous acquisition of the low and core-losses on MOFs, Section 3.1 has revealed its concomitant appearance with peak C at 287.5 eV, which indicates the production of carbon monoxide. Therefore, it could be suggested that the peak at 4 eV is also related to the formation of CO under irradiation.

EELS also describes the formation of other gases under electron irradiation. The low-loss signature of MOFs displays the hydrogen K-edge at about 14 eV (Section 3.1), highlighting the formation of H_2. The gas trapping capacity of MOFs may explain why H_2 is only detected for this specimen, and not for the other molecules. As discussed in [69,137], H_2 formation is due to radiolysis of the water present in the specimen and radical recombination with the aliphatic moieties (-CH, CH_2). Interestingly, the water exciton, initially detected at 8.7 eV for all the specimens, was observed redshifted to 8.4 eV with the electron dose (see Table 5.2, Chapter 3, subsection 5.1.1 and subsection 5.2.1). This observation could also reflect the radiolysis of water and the formation of ·OH radicals.

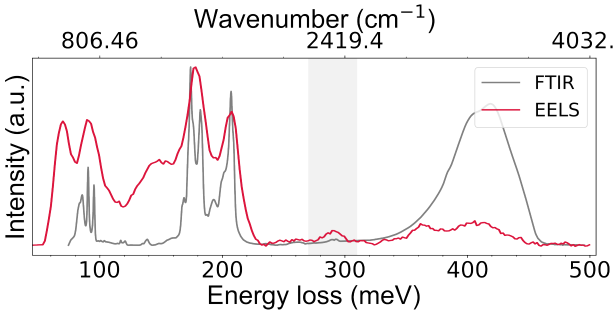

Figure 5.10: FTIR and ultralow-loss EELS spectra of MIL-100(Al) obtained after Richardson-Lucy deconvolution (10 iterations). The shaded area highlights the signature of CO_2 present in ambient air for FTIR and generated under electron irradiation in EELS. The EELS spectra were obtained at 120 $\bar{e}$/Å^2. The spectral resolution is 4 cm^{-1} (0.5 meV) for FTIR and 7 meV (55 cm^{-1}) for EELS.

Table 5.3: Estimation of the carbon and oxygen atom losses in naphthazarin as a function of electron dose. The data were obtained from successive spims performed on the same area (cumulative electron dose). Spectra were cumulated over 300 nm. The number (nb) of counts was determined by integrating the elemental K-edges, and then normalised to the electron dose. The atomic loss calculation assumes that we collect an intact signature at 10 $\bar{e}$/Å^2 (0 % mass loss).

Electron dose	Carbon K-edge		Oxygen K-edge	
($\bar{e}$/Å^2)	Nb of counts	Atomic loss (%)	Nb of counts	Atomic loss (%)
10	6,530	0	297	0
100	6,071	7	426	-43
520	4,761	27	135	55
3.10^3	3,921	40	80	73

Finally, the formation of gas suggests a loss of mass in the specimen. For examples, the production of carbon oxide gases converts organic matter into volatile species that desorb from the nanomaterials. As EELS is a quantitative technique, this mass loss can be estimated. Table 5.3 shows an estimate of the carbon and oxygen losses in the irradiated naphthazarin compound. The measurement was performed by integrating the carbon and oxygen K-edges to determine the number of counts (normalised to the electron dose). This study was only possible because the data were collected on the same areas as the electron dose was increased. By acquiring successive spims on the same region, the electron dose could be increased by cumulative irradiation. In order to accelerate the dose increase, the pixel size and dwell time were also varied (decreasing the pixel size and increasing the pixel dwell time leads to and increase in dose). The results indicate a loss of carbon of (40%), and a higher loss of oxygen (73%) compared to carbon. One could see a good agreement with the stoechiometry of the produced CO_2. However, these results remain rough estimates and can only be used to confirm the loss of mass and carbon oxide gas production. The quantification is poorly reliable: the multiple scattering was not considered and the uncertainty of the measurement seems to be high, as suggested by the negative value obtained on the oxygen K-edge at 100 $\bar{e}$/Å^2.

5.3 . Conclusion and prospects

By analysing encapsulated molecules in low concentration and the behaviour of several free-standing organic and biological molecules under irradiation, this chapter highlights the limitations of electron spectromicroscopy and provides clues for the analysis of radiation-sensitive nanocomposites in the most complex cases.

For low concentration materials (loaded drug in MIL-100(Al)), EELS was unable to detect traces of the organic molecules at both low and high electron doses. At high electron doses, STEM-EDS was probably able to detect and localise the incorporated drug in MIL-100(Al), but the data obtained were unreliable because the drug signal was too low. In this case, the detection limit was reached, due to the low concentration of drug and its low ratio compared to the MOFs. It should be noted that the specimen thickness may also be responsible, as it can affect the electron transmission, resulting in a loss of signal.

Conversely, for the free-standing materials, STEM-EELS was able to detect the distinct signatures of different molecules. At low-dose, it provided information on the low-loss, carbon and oxygen structures of free GMP, DNA, BSA and MIL-100(Al). Only higher electron doses enabled to detect low cross-sections elements (i.e. phosphorus L- and nitrogen K- edges). With the aim of distinguishing different species in a composite material, such as cells, the different elemental compositions could be used (for example phosphorus can be detected at high dose for DNA) as well as the different chemical compositions (carboxyl or amide, obtained at low-dose). However, as a wide majority of organic and biological molecules contain similar chemical groups (carbonyl, carboxyl, amide), fine structure analysis can sometimes be useless. This chapter has demonstrated that, as the electron dose increases, the species undergo different types of reactions, which could allow discrimination. Although all molecules eventually produced unsaturated compounds and carbon oxide gases, the carboxylic groups of the trimesate were more likely to produce CO_2, while the quinone in the naphthazarin created mainly carbon monoxide. Future experiments could provide more insight into the detailed mechanisms of beam damaging. One could also expect different reaction rates, that could also be used to discriminate composite materials.

Chapter 6 .

Conclusion

This work has demonstrated the impressive capabilities of monochromated STEM-EELS for the analysis of various radiation-sensitive specimens. It describes an innovative acquisition strategy to collect undamaged chemical structures at a spatial resolution of 10 nm. The robustness of the methodology has been demonstrated by studying several specimens, either organic-inorganic MOF nanomaterials, organic molecules or biological components. These results were made possible by the use of cryogenic temperatures, extremely low electron doses (10 $\bar{e}$/Å^2) and DED. Together, these features allowed to minimise the beam damage, while collecting a signal with a sufficient SNR for fine structure analysis. Furthermore, complex nanostructures, such as MOFs, can be fully deciphered thanks to the multimodality offered by the monochromated beam. This powerful tool has allowed the study of the signatures of both inorganic entities (metal oxo-clusters and coordination bonds) and organic moieties (linkers) in the IR, UV-vis and soft XR regions. In the future, this methodology could be applied to the study of other radiation-sensitive systems such as polymer blends or biological systems.

This thesis work has also shown that despite the extreme radiation sensitivity of the specimens, their analysis should not be limited to low-dose conditions and reduced spatial resolution, at the cost of misinterpretation. On the contrary, the experimental conditions must be adapted according to the goal of the study. Therefore, in some cases, the electron dose should be increased in order to improve the detection sensitivity of low cross-section edges or to improve the spatial resolution of the analysis. It has notably been shown that electron doses > 10^3 $\bar{e}$/Å^2 were necessary to detect the aluminium and phosphorus L-edges in biodegraded MOFs and to achieve a spatial resolution < 3 nm, more appropriate for the study of local chemical mechanisms.

At high electron doses, the organic moieties are completely damaged. This work has shown that radiolysis inevitably produces carbon oxide gases (CO and CO_2) and unsaturated components (C=C, C≡C, C=N and C≡N). By studying the beam-effect over the three spectral range of EELS, reliable damage mechanisms have been revealed, which appear to be common to the different organic and biological molecules studied here. Although this suggests similarities in the high-dose signatures of molecules, the composition of organic composites, such as polymer blends or cells, could still be distinguished thanks to the tendency to create more or less damaged species. In the case of hybrid organic-inorganic materials, the beam-effect study was shown to be useful to relate the damaged signature to the original chemical structure of the organic component. For example, in the biodegradation study of MOFs performed at > 300 $\bar{e}$/Å^2, it was still possible to distinguish the oxygen signature of the linker from that of the aluminium oxide.

Overall, this thesis work opens up new possibilities for the identification of various radiation - sensitive nanostructures, from the simplest molecules to the more complex composite structures. STEM-EELS was demonstrated to be able to monitor *in situ* chemical reactions. Here, electron-induce chemical changes (radiolysis) was investigated by studying the spectral evolution of nanomaterials over the three spectral ranges under the irradiation, but other stimuli-induce dynamic processes could be analysed (light, temperature, gas adsorption,...). This technique has also provided an overview of the biodegradation mechanisms of MOFs in PBS by monitoring the process *ex situ*. Applied to biological studies, monochromated STEM-EELS could be used as a label-free technique to probe the interactions between nanomaterials and cells and to unravel cellular processes at the nanoscale.

However, STEM-EELS was found to be limited in the analysis of some specific features. For example, it could not reliably characterise the C-H bonds of MOFs, GMP, DNA and BSA, nor could it detect their aluminium, phosphorus, nitrogen and fluorine edges. The study of drug-loaded MOFs was also hampered by the low concentration of GMP. To overcome these limitations, a powerful method lies in the correlative strategy used to study the biodegradation of MOFs. By combining the different observations obtained by TEM, iDPC-STEM, STEM-EDS and STEM-EELS, the complex chemical mechanisms could be elucidated.

Chapter 7 .

Prospects

This chapter presents a few leads for the continuation of this thesis work. It discusses first the optimisation of experimental conditions for STEM-EELS studies, which could improve the damage-free analysis of sensitive materials. Secondly, it presents the different types of investigations that could be carried out on various materials and chemical reactions of interest.

7.1 . Damage-free analysis at higher spatial resolution

By further reducing beam damage, the original chemical structures of radiation-sensitive materials could be studied at higher electron doses and hence, at higher spatial resolution (< 10 nm). To this end, various acquisition strategies could be considered to further preserve the integrity of the irradiated material. In particular, operating at extremely low temperatures and reducing dose accumulation have previously been demonstrated to extend the lifetime of sensitive materials. Firstly, the use of liquid helium has been shown to be more effective than liquid nitrogen in reducing mass loss.[68] In addition, faster scanning probes could also help to reduce damage by minimising exposure time. In this work, a dwell time per pixel of a few milliseconds was the minimum limit, imposed by the frame-based-DED readout. However, the novel event-based detectors would allow faster readout (hundreds of nanoseconds) and therefore, faster scanning.[138] Such an acquisition strategy could be tested since a time-resolved Timepix3 detector will soon be installed on the Nion Hermes 200-S microscope. In certain cases, the use of a pulsed electron beam or a random scanning has also previously shown a reduction in damage compared with the raster scanning of a continuous electron beam under the same conditions.[96, 139, 140] This was attributed to self-healing of the material between each irradiation by rapid radical recombination of broken chemical bonds.

Although these different acquisition strategies would theoretically enable to extend the lifetime of sensitive materials under irradiation, practice shows that each structure behaves differently. Depending on their composition and the degree of conjugation of the systems, the accumulation of charges and the relaxation capacity of the materials can vary greatly. For example, graphene is known to be less sensitive to irradiation than aliphatic chains because of its ability to delocalise charges.[141] However, to date, no clear pattern has been revealed. This highlights the need of understanding the behaviour of the materials under irradiation. Consequently, each of the above strategies needs to be verified for each kind of specimen analysed.

7.2 . A label-free analysis of cells at the nanoscale

Based on this thesis work, interesting prospects are opening up for the study of biological systems. STEM-EELS would provide valuable information about cellular processes and chemical regulations. It is the only technique that would enable to localise specific biomolecules and map the intracellular species, in their native state, at the nanoscale, without chemical labelling. By analysing proteins and DNA, Chapter 5 provides the signatures of two of the main components of cells. These can be used as references in the study of biological specimens. While low electron doses could be used to locally identify the composition of organelles, higher electron doses would be more efficient for detecting endogenous ions in cells, such as phosphorus, calcium or iron.

However, to effectively discriminate the chemical signatures specific to the different cellular components, STEM-EELS requires thin specimens (< 100 nm) prepared without chemical modification. Consequently, the chemical fixations and resin embedding commonly used to prepare biological specimens for cryo-TEM imaging are not suitable. Other methods such as cryogenic fixation could be considered (for instance high-pressure freezing).[74, 142]

7.3 . Monitoring chemical reactions

Chapter 4 showed that monochromated STEM-EELS enables to monitor chemical reactions observed under *ex situ* conditions (here, the MOF biodegradation). This could also be used to study various phenomenon such as oxydo-reduction, chemical substitution, thermal or chemical decomposition, host-guest recognition or molecular sorption in specimens. Therefore, the mode of operation of numerous nanomaterials could be studied, whether semi-conductors, chemical sensors, catalysts, energy materials, biochemical components or pharmaceutical systems. In the case of complex mechanisms, the correlative strategy used in Chapter 4 would provide more insight into the chemical interactions and induced changes in the nanostructures.

Chapter 3 has also highlighted the possibility of analysing the chemical reaction under *in situ* conditions. The dynamic processes and their reversibility could therefore be investigated, upon exposure to various stimuli such as light, temperature, electrical biasing or environmental change (liquid or gas). Obviously, these would require the implementation of specific set-ups such as laser injection, holder equipped with microelectromechanical systems or environmental cells. Note that, in the case of environmental cells, the interactions of electrons with the media should also be investigated since they could disturb the original chemical reaction. For example, it is well known that irradiation of water produces reactive species (H_2O_2, $^{\cdot}H$, $^{\cdot}OH$, etc) that enhance the radiolysis of the specimen.[110]

Appendix A .

Experimental section

A.1 . Synthesis of MIL-100(Al) and MIL-100(Fe)

To avoid the use of toxic catalysts, such as hydrofluoric acid, a green hydrothermal synthesis was developed.[143, 144] It produces nanoparticles with similar physico-chemical properties to those obtained by historical methods, but carried out in water, it is simpler and safer. By using microwave assistance to heat the preparation, the crystal nucleation and growth processes are accelerated[103] from tens of hours to less than half an hour.

Starting from this microwave-assisted hydrothermal synthesis procedure, Dr. Gref's team has over time optimised the experimental conditions (temperature, power, duration, activation and washing steps) to obtain relatively small MIL-100 nanoparticles ($\sim$ 200 nm).[62, 145] Thus, MIL-100(Al) and MIL-100(Fe) were synthesised by this optimised microwave-assisted hydrothermal method, also described in [22, 44]. For safety reasons, the dedicated microwave Teflon reactors were used to contain the high temperatures and pressures of the reaction.

MIL-100(Al) were first prepared by dissolving aluminium nitrate nonahydrate (3.82 mmol, 1.43 g) and trimethyl trimesate (4.81 mmol, 1.21 g) in 20 mL of deionised water. After stirring for 5 min, 4 mL of a nitric acid solution (4 M) was added. The mixture was stirred at room temperature for 5 min before being heated at 210°C (microwave power 1,600 watts, 50%) for 30 min with stirring. The reactors were then cooled to around 80°C and placed in an ice bath for 15 min to stop the crystal growth. The resulting yellow product was recovered by centrifugation at 10,500g for 30 min and activated overnight in 50 mL of methanol with stirring. The final nanoparticles were recovered by centrifugation at 12,000g for 15 min and washed four times in absolute ethanol by centrifugation at 11,000g for 12 min. A size separation step was performed to select the smallest nanoparticles. It consisted of two successive centrifugations of the supernatant at 6,000g for 1min40s.

For MIL-100(Fe), iron chloride hexahydrate (9.02 mmol, 2.43 g) and trimesic acid (4.00 mmol, 0.84 g) were dissolved in 20 mL of deionised water. After heating for 6 min at 130°C with stirring (microwave power 800 watts, 100%), the suspension was cooled for 1h in an ice bath. The resulting orange-red product was recovered by centrifugation at 10,000g for 10 min and washed six times in absolute ethanol by successive centrifugations at 10,000g for 15 min. The size separation step involved two further centrifugations of the supernatant at 1,000g for 1 min.

For both MIL-100, the final suspensions were stored as-is, in absolute ethanol. Prior cellular incubation, the solvant was substitute with deionised water by two succesive centrifugations at 10,000g for 20 min.

A.2 . Quality control by *bulk* techniques

After each preparation, MIL-100 nanoparticles were characterised using *bulk* techniques. These analyses validated the quality of the products by providing average information on their physico-chemical properties. Depending on the technique, the nanoparticles were studied either in suspension or in powder form, after drying at 60°C for 1 to 5 days.

Dynamic light scattering (DLS) was used to measure the hydrodynamic size of the nanoparticles suspended in absolute ethanol at a concentration of 0.5 mg/mL. The experiments were carried out on a Zetasizer Nano (ZS90, Malvern, United Kingdom) by averaging three successive measurements with a stabilisation time of 60s to 120s.

The Bunauer-Emmett-Teller (BET) surface area of the dried MOFs was determined using an Accelerated Surface Area and Porosimetry System (ASAP 2020, Micromeritics, USA). Approximately 60 mg of powder was degassed overnight at 100°C under secondary vacuum and then subjected to nitrogen sorption at liquid nitrogen temperature.

To assess the purity of the MOFs, thermogravimetric analyses were performed on the dried powders using a TGA 4000 (PerkinElmer, USA). Approximately 20 mg of product was heated from 30°C to 600°C, at a temperature rate of 3°C/min and under an O_2 flow rate of 20 mL/min. Weight losses (wt%) were determined by calculating the first-derivative of the TGA curves, smoothed with a second order polynomial Savitzky-Golay filter in Orange[146] (window width of 23 points).

UV-visible spectrometry (Cary 300, Agilent Technologies, USA) was used to measure the optical properties of MIL-100 nanoparticles suspended in absolute ethanol. Data were collected between 200 nm and 800 nm at a scan rate of 100 nm/min, a spectral bandwidth of 2 nm and a collection interval of 0.167 nm.

In collaboration with Pr. Ariane Deniset-Besseau, Pr. Alexandre Dazzi and Dr. Jérémie Mathurin (Institut de Chimie Physique, Orsay, France), Fourier-Transform Infrared (FTIR) spectroscopy was used to determine the chemical composition of MIL-100. The experiments were performed on a Vertex 70 spectrometer (Bruker, Germany) in the attenuated total reflection (ATR) mode. To avoid the inhalation of nanoparticles, only wet products were handled: the suspensions were centrifuged at 10,000g for 5 min, allowing to deposit the wet pellet on the ATR crystal. The solvent was evaporated under an ambient air flow. Data were collected between 4,000 cm^{-1} and 600 cm^{-1} with a spectral aperture of 1.5 mm. To increase the SNR, each acquisition is an average of 128 scans. The spectral resolution is 4 cm^{-1}. The obtained spectra were analysed and processed using Orange, an open source software suite [146] A rubber band baseline correction was applied to remove the solvent signal and allow a better comparison between the different specimens. For the benzene terephthalate spectrum, an additional Kramers-Kronig transformation was applied in Brukers OPUS 6.5 software to suppress the distortion due to the reflectance of the powder.

Note that since DLS and FTIR require only a small amount of product, this technique was systematically used as a quality control for the two MOFs. The other techniques were only used on MIL-100(Al) nanoparticles as they were used in more complex studies.

Appendix B .

Routine characterisation of MOFs

B.1 . The original MOFs

Prior to performing the individual nanoparticle analysis, the MOFs were systematically characterised using *bulk* techniques to assess their quality. Figure B.1 provides the measured physicochemical properties of the two MOFs.

First, DLS and FTIR analyses were applied on both MIL-100(Al) and MIL-100(Fe). DLS measured a hydrodynamic diameter of 171.4 $\pm$ 2.1 nm for MIL-100(Al) and 241.5 $\pm$ 4.6 nm for MIL-100(Fe). The two MOFs have different sizes due to the different synthesis conditions. As observed in Figure B.1.a, the mean intensity-based size distribution shows a unique size population for the two MOFs. Indeed, their polydispersity index is about 0.07, indicating a relatively uniform suspension.

Next, FTIR spectroscopy confirmed the formation of MIL-100(Al) and MIL-100(Fe). As observed in Figure B.1.b, the shaded areas indicate the chemical fingerprints of both the coordinated organic linkers and the metal oxo-clusters, as previously shown in [62]. The aromatic CH bending modes (δ_{CH}) and benzene ring deformation are located at about 690-770 cm^{-1}, whereas the aromatic CC and symmetric CO stretching modes (ν_{CC}, ν_{CO}) of the coordinated linkers are found between 1,400-1,670 cm^{-1}. At last, the ethanol solvent molecules are also detected at about 1,060 cm^{-1} (ν_{CO} stretching and δ_{CH} bending), 2,900 cm^{-1} (ν_{CH} stretching) and 3,300 cm^{-1} (ν_{OH} stretching). A more detailed discussion is given in Chapter 3.

As MIL-100(Al) were used to study complex processes, they were further characterised by porosimetry, UV-vis spectroscopy and TGA analysis. Figure B.1.c shows the typical N_2 isotherm of MIL-100(Al) obtained by porosimetry. Its Bunauer-Emmett-Teller (BET) surface area is about 1930 m^2.g^{-1}. This value agrees with previous studies.[101]

The optical properties of MIL-100(Al) were measured by UV-visible spectroscopy (Figure B.1 .d). The measurements reveal the $\pi - \pi^*_{C=C}$ transitions of the coordinated linkers around 210 nm. Such transitions have already been described in [104–106].

TGA was then used to determine the purity of the synthesised MIL-100(Al). As shown in Fig-

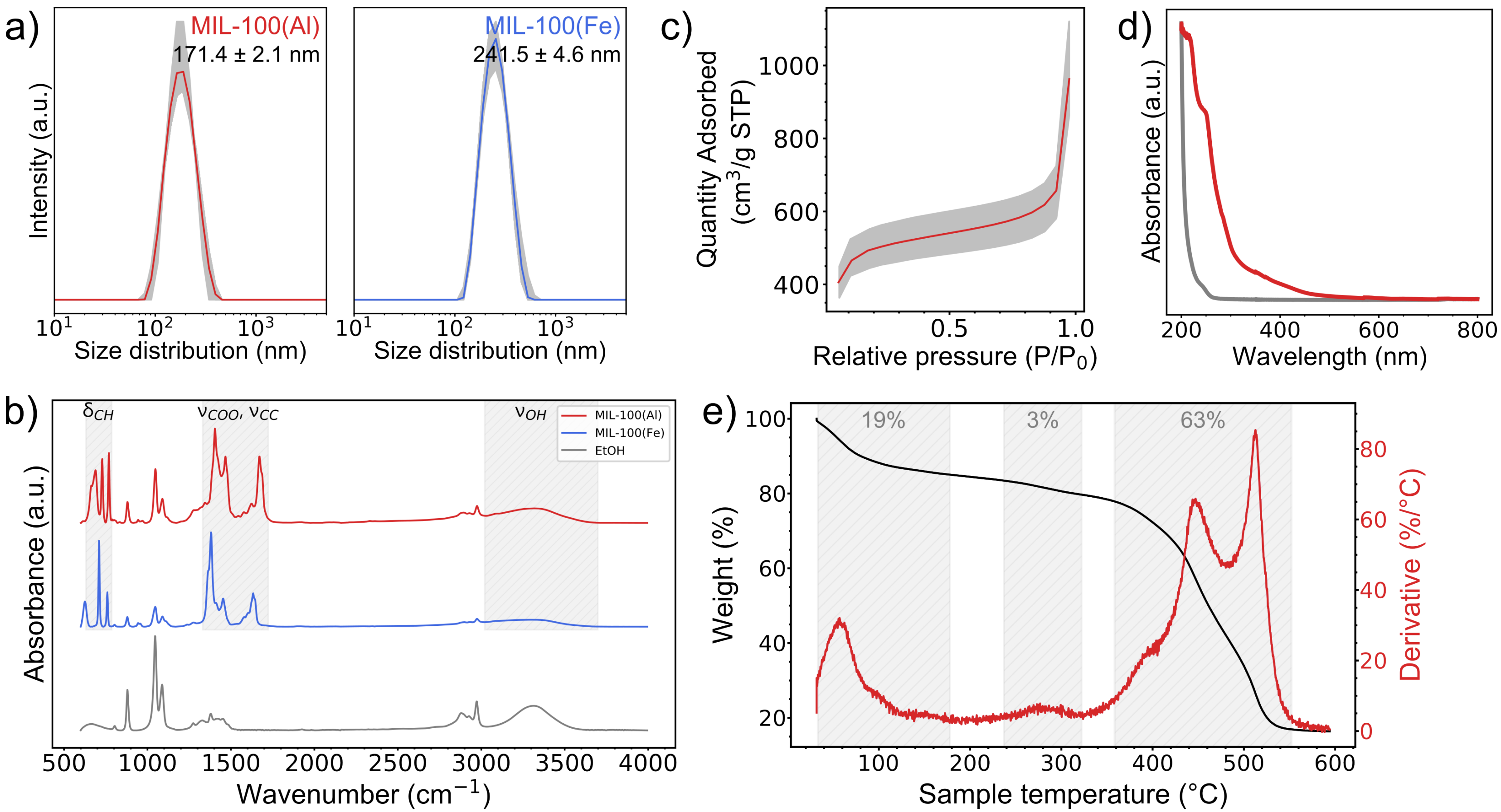

Figure B.1: Bulk characterisation of MIL-100(Al) and MIL-100(Fe) nanoparticles. a) Mean intensity-based size distribution obtained by DLS for MIL-100(Al) in red and MIL-100(Fe) in blue. b) FTIR spectral signature of MIL-100(Al) in red and MIL-100(Fe) in blue along with the solvent reference (ethanol in grey). The data were acquired between 4,000 cm^{-1} and 600 cm^{-1}, with a spectral resolution of 4 cm^{-1}. c) Typical N_2 adsorption isotherm of MIL-100(Al) obtained by porosimetry. c) UV-vis spectra of MIL-100(Al) along with the solvent reference (ethanol in grey). d) Typical TGA curve (black) of MIL-100(Al) and the corresponding first derivative (red) obtained after a second-order Savitzky-Golay smoothing. The data were acquired from 30 °C to 60 °C at a temperature rate of 3 °C/min under an O_2 flow of 20 mL/min. The median weight losses are indicated in grey at the top of the plot. In (a) and (c), the results are presented as the mean of three experiments. The shaded area and solid line represent the raw and median data.

ure B.1.e, the typical thermogram of the MOFs displays three main weight loss steps. As demonstrated in previous studies, they correspond to the evaporation of the solvent (30–150°C, around 19 wt% loss), the removal of coordinated water (230–330°C, around 3 wt% loss) and the thermal degradation of the organic linkers (360–550°C, around 63 wt% loss).[44, 101] Finally, about 15 wt% of inorganic metal oxides remain after heating to 600°C.

Note that FTIR was also used to analyse the chemical composition of the biodegraded and drug-loaded MIL-100(Al). For the biodegraded, a detailed description is given in Section 4.1. For the drug-loaded MOFs, the reader is referred to Appendix B.2.

B.2 . The drug-loaded MOFs

The drug-loaded MIL-100(Al) were characterised by FTIR and TEM to assess their composition and crystallinity. Figure B.2 compares the results obtained before and after the drug loading.

In FTIR, the loaded MIL-100(Al) display additional vibration modes between 995 cm^{-1} and 1,320 cm^{-1} (shaded area). They correspond to the stretching vibration modes of C–F (1,025 cm^{-1}), P–O (1,085 cm^{-1}) and C–N (1,290 cm^{-1}) bonds.[147–149] These results confirm the uptake of the drug. Then, TEM images show that the nanoparticles remain well faceted and crystalline after the drug loading. This suggests that the drug uptake does not affect the integrity of the specimen.

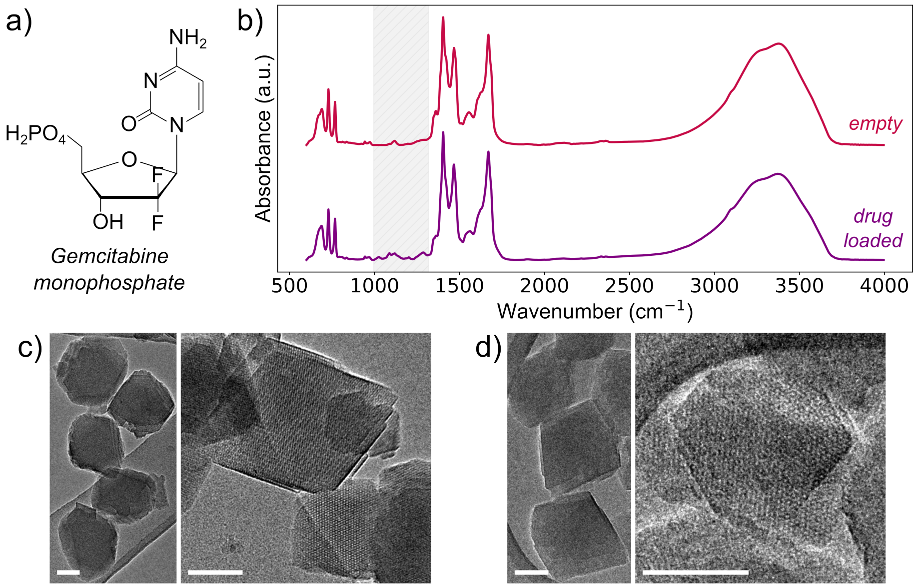

Figure B.2: (a) Molecular structure of gemcitabine monophosphate. (b) FTIR spectra and (c-d) TEM images of (c) empty and (d) GMP-loaded MIL-100(Al) nanoparticles. The shaded area in (b) indicates the spectral differences between MIL-100(Al) and the drug. FTIR data were obtained between 4,000 cm^{-1} and 600 cm^{-1} with a spectral resolution of 4 cm^{-1}. TEM images were acquired at a 40 kx and 50 kx magnification. The scale bar is 50 nm.

Appendix C .

Supporting information on inserted articles

This section contains supplementary information to the scientific articles presented in Chapter 3 and Chapter 4. It presents detailed experimental procedures, data acquisition and processing and complementary results.

Nanoscale Multimodal Analysis of Sensitive Nanomaterials by Monochromated STEM-EELS in Low-Dose and Cryogenic Conditions

Maeva Chaupard,[a,b] *Jéril Degrouard,*[a] *Xiaoyan Li,*[a] *Odile Stéphan,*[a] *Mathieu Kociak,*[a]
Ruxandra Gref,[b] *Marta de Frutos*[a]*

[a]Laboratoire de Physique des Solides, CNRS, UMR 8502, Université Paris-Saclay, F-91405 Orsay, France
[b]Institut des Sciences Moléculaires d'Orsay, CNRS, UMR 8214, Université Paris-Saclay, F-91405 Orsay, France

Corresponding author: marta.de-frutos@universite-paris-saclay.fr

Supplementary Information

NanoMOFs synthesis

Chemicals and material

Iron (III) chloride hexahydrate (97%), aluminium (III) nitrate nonahydrate (98%), trimethyl trimesate (98%) and N,N-dimethylformamide (DMF, 99%) were purchased from Alfa Aesar. 1,3,5-benzene tricarboxylic acid (trimesic acid, BTC, 95%), nitric acid (puriss. > 65%) and zirconyl (IV) chloride octahydrate (98%) were purchased from Sigma-Aldrich. Aluminium oxide and 1,4-benzene dicarboxylic acid (terephthalic acid, BDC, 98%) was purchased from Aldrich. Zirconium oxide was purchased from Prolabo. Absolute ethanol (99%) was purchased from Carlo Erba, methanol (HPLC grade) from Fisher Chemical and acetic acid (≥ 99%) from VWR Chemicals. Deionised water was purified through a Milli-Q system (18.2 MΩ.cm).

Synthesis procedure

For MIL-100(Al), aluminium nitrate nonahydrate (3.82 mmol) and trimethyl trimesate (5.82 mmol) were dissolved with nitric acid (4mL, 4M) in 20mL deionised water. The mixture was heated under stirring for 30 min at 210°C (800 Watts) and then cooled in an ice bath for 1h. After centrifugation for 10 min at 10 000g, the MIL-100(Al) supernatant was replaced by absolute methanol. The mixture was left overnight under stirring and purified by centrifugation for 15 min at 10 000g. The nanoparticles were stored in absolute ethanol. Their chemical formula is $Al_3O(OH)(BTC)_2(H_2O)_2$.

MIL-100(Fe) nanoparticles were obtained from a mixture of iron chloride (5.41 mmol) and trimesic acid (4.03 mmol), dissolved in 20mL of deionised water. After heating under stirring for 6 min at 130°C (800 Watts), the suspension was cooled in an ice bath for 1h and centrifuged for 10 min at 10 000g to replace the supernatant with absolute ethanol. The nanoparticles were finally collected after six washing steps with absolute ethanol by centrifugation for 15 min at 10 000g. To remove aggregates from the suspension, two more centrifugation steps were carried out at 1000g for 1min. The final suspension was stored in absolute ethanol. The chemical formula of MIL-100(Fe) is $Fe_3O(OH)(BTC)_2(H_2O)_2$.

For UiO-66, two solutions of zirconyl chloride octahydrate (0.90mmol) and terephthalic acid (3.02mmol) were prepared in 30mL and 10mL of N,N-dimethylformamide (DMF), respectively and then mixed. An acetic acid solution (17.4M) was added to the mixture to reach a final concentration of 6.5M. After heating at 90°C for 18h, the final nanoparticles were purified by three centrifugation steps with DMF. The solvent was replaced by absolute ethanol after four centrifugations at 10 000g for 10 min. The final suspension was stored as it was. The nanoparticle chemical formula is $Zr_6O_4(OH)_4(BDC)_6$.

After synthesis, the three nanoMOFs were analysed by Fourier Transform IR Spectroscopy (FTIR) in the attenuated total reflection (ATR) mode, to assess their purity, (Figure S8).

Specimen preparation

For the three nanoMOFs, the specimen preparation was adapted to each technique. In electron microscopy, we selected the smallest MIL-100 nanoparticles, below 300 nm, by subsequent centrifugation steps. Since MIL-100(Al) and MIL-100(Fe) display different kinetics of aggregation, the duration and speed of centrifugations were adjusted as follows: the smallest MIL-100(Al) and MIL-100(Fe) nanoparticles were collected from the supernatant after five centrifugation at 1000g for 5 min and four centrifugation at 3000g for 5min, respectively. Concerning UiO-66, its high polydispersity was sufficient to enable focusing the analysis on nanoparticles as small as a hundred nanometers. After that, we further purified the suspensions with high-speed centrifugation. This step is crucial for STEM-EELS since it is sensitive to trace elements such as residual products. Hence, MIL-100(Al) and MIL-100(Fe) were recovered after four centrifugations of 5 min at respectively 3000g and 4000g.

For cryo-TEM, each suspension was centrifuged at 10000g for 15 min to replace ethanol with deionised water. Then, two different preparation methods were used for MIL-100 and UiO-66 because of the aggregation of the latter ones. First, 4µL of each MIL-100 suspension was deposited onto holey carbon grids (Quantifoil® R2/2) ionised by glow discharge. The grids were blotted with a filter paper for 2 seconds and directly plunged into liquid ethane cooled down by liquid nitrogen using a Vitrobot Mark IV (Thermo Fisher Scientific) operated at 22°C and 100% relative humidity. The grids were stored in liquid nitrogen until use. Conversely, the vitrification of UiO-66 was revealed to cause aggregation of the nanoparticles. Hence, they were prepared without vitrification by directly dropping onto a glow-discharged lacey carbon grid (300 mesh, Agar scientific).

For STEM-EELS, a 4µL drop of each nanoMOF suspended in absolute ethanol was deposited during 10s onto a glow-discharged carbon grid (holey carbon 300 mesh, Agar Scientific for MIL-100; lacey carbon 300 mesh, Agar Scientific for UiO-66, BTC and BDC) and blotted with filter paper. The mixed specimen exploited for the LL mapping was obtained using the same method, by a successive dropping of the MIL-100(Fe) and UiO-66 suspensions onto a holey carbon 300 mesh grid (Agar Scientific).

Finally, ATR-FTIR experiments were carried out with dried specimens. First, the nanoMOFs suspensions were concentrated by centrifugation. The resulting aggregated nanoparticles were found as wet pellets. Then, they were delicately transferred onto the crystal and dried under an ambient airflow.

The water and absolute ethanol references were simply dropped onto the crystal. The ATR hammer was used to prevent the evaporation of absolute ethanol. Concerning the organic linkers, the purchased powder products were directly flattened with the ATR hammer. In contrast, for the STEM-EELS study, they were simply suspended in absolute ethanol and dropped into a lacey carbon 300 mesh TEM grid (Agar Scientific). For aluminium and zirconium oxide, each powder was suspended in deionised water by sonication (20 min) and finally dropped into a holey carbon TEM grid (300 mesh, Agar Scientific). For amorphous carbon and iron(III) oxide EELS references, we used respectively pristine holey carbon TEM grids (300 mesh, Agar Scientific) and flower-like Fe_2O_3 by-products found in the MIL-100(Fe) specimen.

EELS energy window and energy resolution

For EELS, we substituted in the main text the usual term in EELS “energy dispersion” with the more reachable term “energy window”. Then, for each energy window used for the acquisitions, the manuscript indicates the corresponding spectral resolution achieved (denoted ΔE), measured on the EELS detector from the full-width at half-maximum (FWHM) of the zero loss peak (ZLP, electrons transmitted with no energy loss through the specimen).

For the sake of clarity, we should highlight that in EELS, the spectral resolution results from the energy spread of the electron beam (narrowed by the monochromator slit) and the point-spread function (PSF). The PSF depends on the selected monochromation strength, the monochromator and spectrometer aberrations, the chosen energy dispersion and the detector characteristics that are improved by using a direct detection camera.

Therefore, the ULL features, analysed with an energy dispersion of 1.6 meV/channel (1.6 eV energy window), display a spectral resolution of δE = 12 meV (FWHM= 7 pixels) corresponding to the PSF. On the opposite, the spectral resolution of the LL and CL spectra observed simultaneously with a dispersion of 398 meV/channel (400 eV energy window) is restrained to δE = 800 meV (FWHM= 2 pixels) by the pixel size.

Electron dose-effect study

The electron dose was adjusted between 10 ē/Å^2 and 10^4 ē/Å^2 by raising the probe current (by opening the monochromator slit), the dwell time and reducing the pixel size. Note that to minimise the electron irradiation before EELS acquisitions, regions of interest were surveyed with fields-of-view as large as possible (2 - 4 µm) and image pixel numbers as small as possible (typically below 512 pixels).

We performed two types of dose-effect studies, cumulative and single acquisitions. For the cumulative study, subsequent hyperspectral images were acquired successively on the same area (Figures 3a-e, 4d-f, S4 and S5). Data were collected at a constant beam current (15 pA for Figure 3d and 6 pA for the other Figures) by varying the pixel size (1-10 nm) and dwell time (2-80 ms, total acquisition time of 2-630s). The total electron dose was then calculated by summing the successive acquisition doses, and is named *"cumulated dose"* in the manuscript. For the single acquisition dose study (Figures 3c, 4a-c, S1, S3 and S4), hyperspectral images were acquired in different areas by varying the beam current (6-40 pA), the pixel size (3-10 nm) and the dwell time (2-3 ms, total acquisition time of about 1-30s). The total electron dose is directly equal to the *single acquisition dose*, as indicated in the manuscript. To ensure repeatability, we acquired at least 6 collections of hyperspectral images for each condition.

Because the three parameters (current, dwell time and pixel size) are adjusted to achieve different dose conditions, the dose rate (ē/Å^2/s) is not constant for the different measurements. Data in Figures 3a-b and S3 have been collected at a constant dose rate (4x10^3 ē/Å^2/s), while in Figure 3c, 4a-c, S1, S2 and S4, dose rates are between 4x10^3 ē/Å^2/s and 3x10^5 ē/Å^2/s. Higher values were used in Figure 3d, from 10^5 ē/Å^2/s to 10^6 ē/Å^2/s. At last, data in Figures 4d and S5 were collected with dose rates ranging from 4x10^3 ē/Å^2/s to 4x10^4 ē/Å^2/s.

For accuracy, we performed a dosimetry study to determine the real current detected by the EELS camera for each dose condition. For this purpose, we defined a calibration scale by counting the electrons/event ratio detected by the EELS direct detection camera as a function of the incident current. This counting mode requires low exposure conditions to discriminate each electron individually (~150 events) that correspond to defocused ZLP and a fast acquisition rate (a few µs). Then, the total number of detected electrons is then used to calculate the total current.

The following formula have been applied for our calculations:

$$\text{Electron dose (ē/Å}^2\text{):} \quad \frac{current \times\ dwell\ time}{(pixel\ size)^2}$$

$$\text{Dose rate (ē/Å}^2\text{/s):} \quad \frac{electron\ dose}{dwell\ time}$$

Data processing

EELS spectra

All EELS spectra have been obtained by summing and extracting the signal over the whole hyperspectral image with a typical size of 400 x 400 nm^2. When possible, hyperspectral images were aligned by the ZLP maximum. The background was removed by subtracting a power-law model or a second-order polynomial function using Gatan Digital Micrograph® software (see Figure S6). Spectra were calibrated using the ZLP (0 eV peak). For CL experiments, where the ZLP is not detected, we used for calibration the features from X-ray absorption spectroscopy and EELS references found in the literature, as detailed in the manuscript.

The spectra intensity in Figures 3a, 3d, 4d and S4 were normalised by the total signal collected for each spectrum. For the other spectra, the intensity is divided by the maximum value.

For vibrational EEL spectra, the spectra are summed over the entire region of interest, including the hole area surrounding the nanoMOFs. This summing is convenient since the aloof signal is analogous to the transmission one (see Figure S9).

In Figures 2b, 5a, S6 and S8, data were deconvolved with the Richardson-Lucy Algorithm (10 iterations) using the Hyperspy Python library[1] (http://hyperspy.org/). Deconvolution allows a resolution improvement based on an iterative process that takes the ZLP as a reference for the point spread function to remove the spectral resolution decrease caused by aberrations.[2] Here, it enabled us to narrow the ZLP and reach 7 meV of spectral resolution (see Figure S6).

EELS maps

For the chemical maps of Figures 2a, 3b, 3e, 4e, 4f, 5c and 5e, raw hyperspectral images were first denoised using PCA (3 components) in Hyperspy,[1] as a denoising method.

Figures 2a, 3b, 3e, 5c and 5e were then built by integrating the intensity of each spectroscopic feature after background subtraction with a first-order polynomial function. For figures 4e and 4f, a multi-Gaussian fitting was applied using the NLLS (non-linear least squares) method under Gatan's Digital Micrograph® software. A typical example of a multi-Gaussian fit is presented in Figure S5. The background was subtracted using a second-order polynomial function, while the three peaks of MIL-100(Fe) and UiO-66 were fitted with Gaussian functions. Maps were then collected from the Gaussian model amplitude, providing the relative abundance of each valence feature of MIL-100(Fe) and UiO-66. Note that the spectral features are not Gaussian, but the intensity variation provides a clear description of the distributions. Nonetheless, in the thick areas, the fitting is not well appropriated, showing an unreal mixing of the contributions. Besides, since the analysis was performed above the carbon layer of the TEM grid, some signals are increased (i.e. 4.4 eV).

The scale intensity of the chemical maps has been normalised by the maximum value in the pair of images in Figures 3b, 5c and 5e, respectively, allowing comparison. In addition, maps of Figures 5c and 5e have been normalised by the ZLP intensity to exclude the thickness variations.

FTIR spectra

FTIR data were acquired with Brukers' OPUS 6.5 software, analysed and baseline corrected with Orange,[3] an open-source software suite. The Kramers-Kronig transformation was applied in the OPUS 6.5 software for the BDC specimen.

Correlation of the LL and CL signals

Figure S1 shows the LL and carbon K-edge signal window for MIL-100(Al), MIL-100(Fe) and UiO-66. These features were acquired simultaneously with the 400 eV energy window as a function of electron dose. This correlation enables deciphering the degradation mechanisms by comparing the concurrent evolution of each signature. For instance, the decrease of peak LL_2 along with the increase of peak CL_2 suggests that the reduction of the carboxylic groups (-COO) into carbonyl (-CO) weakens the metal-linker coordination bond. Above 80 ē/Å^2, H_2 formation is indicated by the rising of the hydrogen K-edge (black arrows) due to the radiolysis of hydroxyl groups.

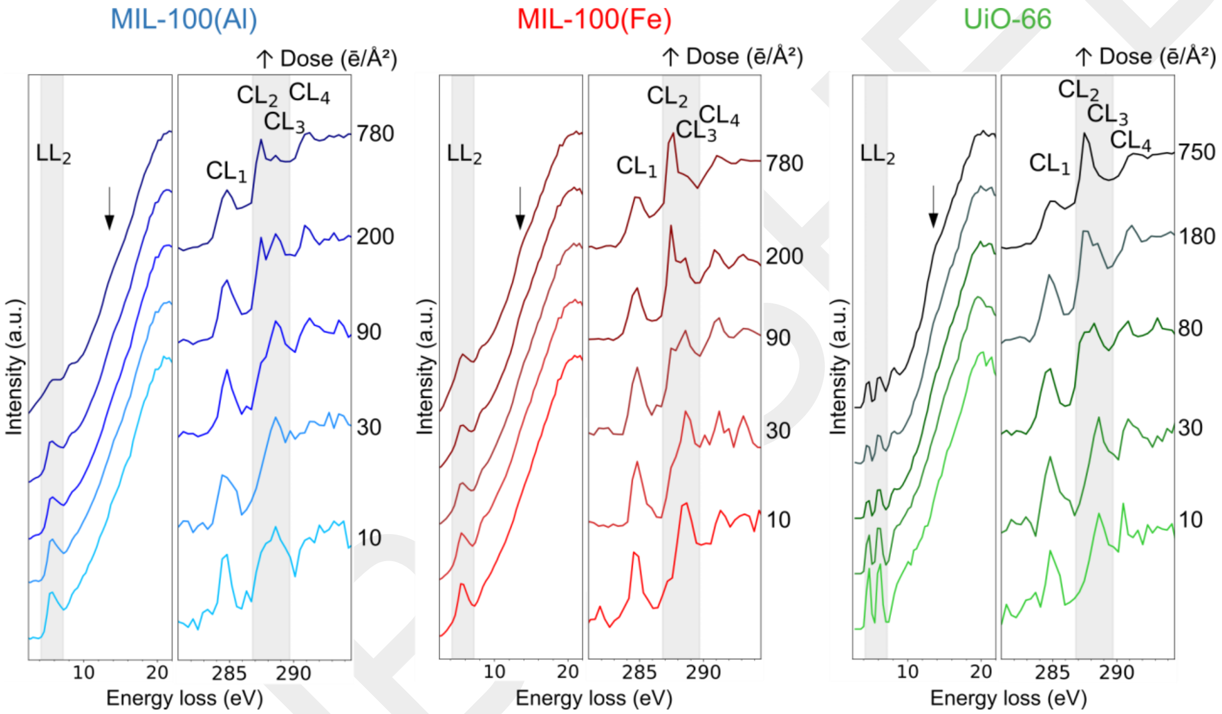

Figure S1. *Evolution with the electron dose of the low-loss signal along with the carbon K-edge acquired simultaneously with the 400 eV energy window. The energy resolution is about δE = 800 meV. The electron doses are indicated on the right of each spectrum and correspond to single acquisition doses. Data were collected at 6 pA with a total acquisition time of 1s (low-dose) or at 40 pA with a total acquisition time of about 5-20s. All spectra are averages, obtained by extracting and summing the signal over the whole hyperspectral image. The black arrows near 14 eV indicate the H K-edge revealing* H_2 *production under irradiation. Blue, red and green colours represent MIL-100(Al), MIL-100(Fe) and UiO-66, respectively.*

Comparison of low-dose EELS CL and NEXAFS data

Figure S2 highlights the similarities between the carbon and oxygen K-edges of BTC, MIL-100(Fe), BDC and UiO-66.

The BTC and BDC spectra were obtained by NEXAFS performed on different equipment.[4,5] Hence, the observed slight changes in the fine features might be explained by a different spectral resolution, which has been estimated to be close to 0.3 eV in the carbon K-edge.[4,5] At the carbon K-edge, the BTC and BDC spectra show 1s–σ*$_{\text{C-H}}$ transitions in phenyl rings near 287.5 eV.[4,5] Surprisingly, they are not detected in the nanoMOFs, which we attribute to beam-induced dehydrogenation.

At the oxygen K-edge, the features displayed by MIL-100(Fe) are more similar to the organic linkers than iron(III) oxide. The nanoMOFs organic linkers seem to be the main contributors to the signal, which is probably related to their higher concentration in the material (two linkers per cluster).

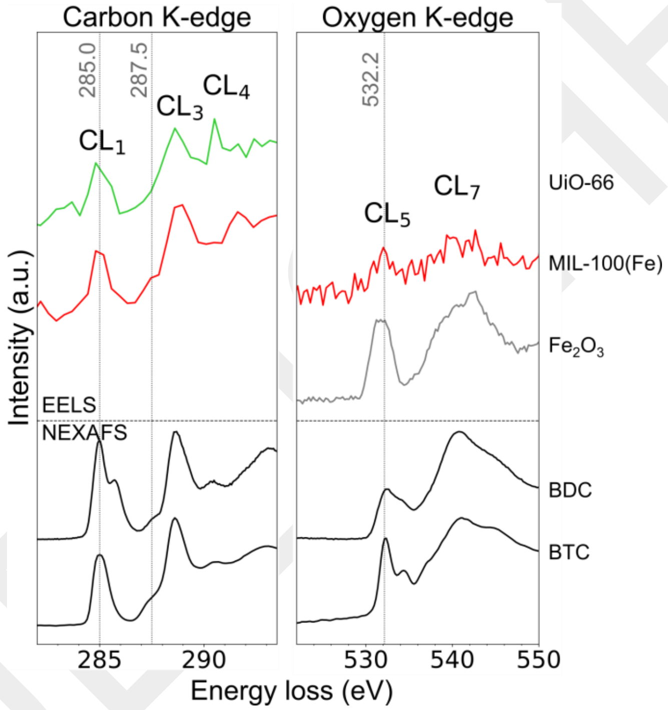

Figure S2. *Comparison of the low-dose EELS spectra of UiO-66, MIL-100(Fe) and iron (III) oxide with the NEXAFS spectra of the free-standing organic linkers. The carbon (left) and oxygen (right) K-edges of UiO-66, MIL-100(Fe) and* Fe_2O_3 *obtained by EELS (in green, red and grey, respectively) are compared with the one obtained for BTC and BDC (black) by NEXAFS (Okajima, T.; Buck, M.; Zharnikov, M. personal communication, 2022). EEL spectra were acquired with an energy window of 400 eV (δE = 800 meV).*

PCA processing at the carbon K-edge

Figure S3 displays the carbon K-edges of MIL-100(Al), before and after PCA processing. Additionally, we provide the spectrum extracted from a single pixel and from the entire region-of-interest (ROI) for the two conditions. As observed, the weak SNR achieved at such relatively low doses impedes a direct investigation. The fine structure analysis requires the spectra to be summed over a large ROI. Besides, PCA processing provides valuable denoising that enables to map the chemical information.

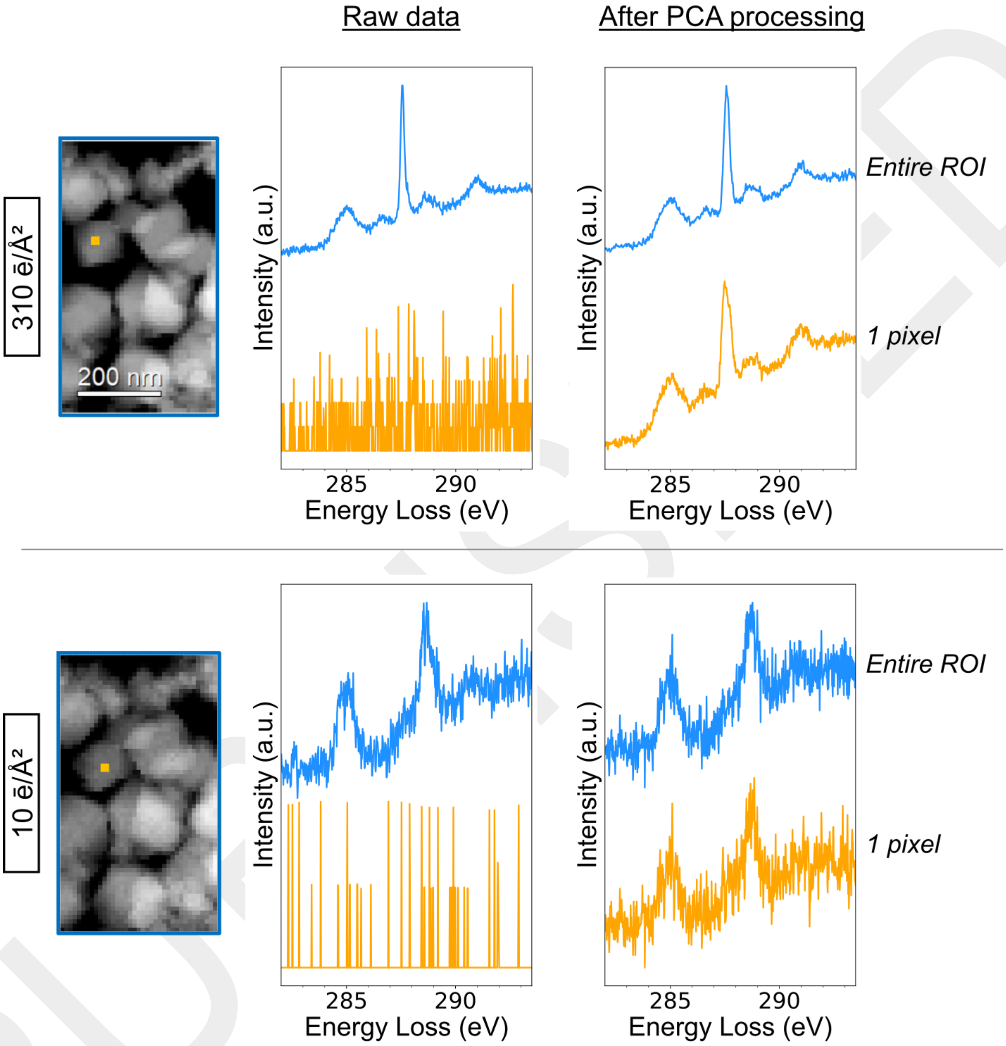

Figure S3. *Comparison of the carbon K-edge spectra of MIL-100(Al) obtained at low (10 ē/Å^2) and higher dose (310 ē/Å^2), before and after PCA processing (3 components). Orange and blue colours represent the spectra extracted from a single pixel, or the entire region-of-interest (ROI), respectively. The energy resolution is about δE = 40 meV. The indicated electron doses are cumulated doses resulting from successive acquisitions over the same area. Data were collected with a total acquisition time of 6s (low-dose) or 60s (higher dose) at a constant beam current of 6 pA.*

Metal edges of MIL-100(Fe) and UiO-66

Figure S4 provides additional information on the metal edges of MIL-100(Fe) and UiO-66, briefly mentioned in the main text. For MIL-100(Fe), in addition to the iron L_3-edge described in the manuscript, a weak signal corresponding to the iron $M_{2,3}$-edges was observed near 55 eV (Figure S4a). Likewise, the zirconium $N_{2,3}$-edges of UiO-66 were detected at ~ 40 eV (Figure 2b, green spectrum) and its $M_{2,3,4,5}$-edges were found between 210 eV and 350 eV (Figure S4b). For these last structures, no apparent changes were monitored with the electron dose (apart from the SNR increase) but again, the analysis was limited by the very weak signal.

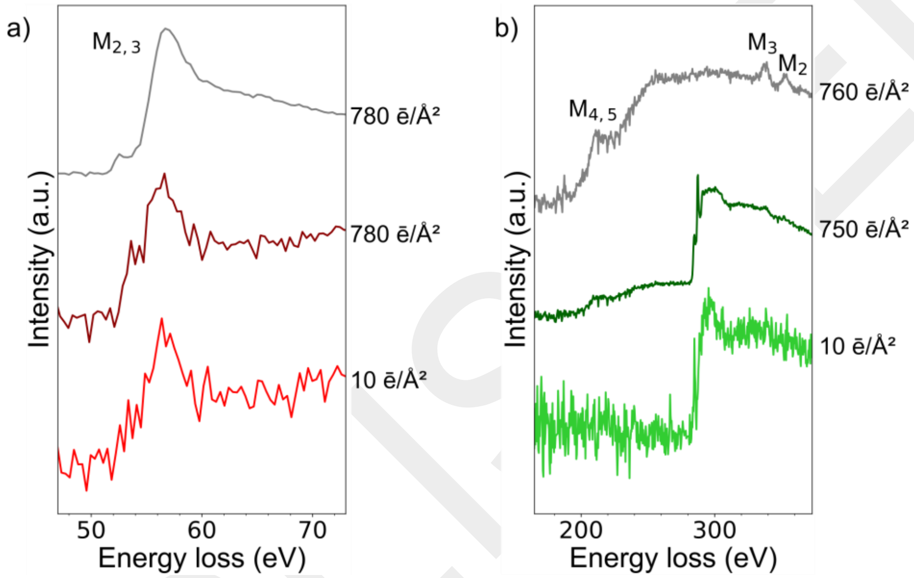

Figure S4. *(a) Iron $M_{2,3}$-edges of MIL-100(Fe) in red compared to Fe_2O_3 in grey. (b) Zirconium $M_{2,3,4,5}$-edges of UiO-66 in green compared to ZrO_2 in grey. Spectra were acquired with an energy window of 400 eV to reach an energy resolution of δE = 800 meV. The indicated electron doses correspond to single acquisition doses. NanoMOFs data were collected at 6 pA with a total acquisition time of 1s (low-dose) or at 40 pA with a total acquisition time of 10-20s (higher dose).*

Low-loss signatures of the three nanoMOFs and their organic linkers

Figure S5 compares the low-loss signatures obtained for the three nanoMOFs with the free-standing organic linkers and amorphous carbon. The nanoMOFs features are discussed in the manuscript. For BTC and BDC, the 5.3 and 6.8 eV peaks indicate the benzoic band and the local-excitation band of benzene.[6] For amorphous carbon, the 6.4 eV peak is related to π–π^* transitions of unsaturated bonds (C=C).[6] It is reduced and broadened with the electron dose.

The manuscript relates peak LL$_3$ to structural water molecules or hydroxyl groups of nanoMOFs. For reference compounds (organic linkers and amorphous carbon), adsorbed water is unlikely because of the electron microscope ultra-high vacuum and water irradiation.[7] Hence, we could relate peak LL$_3$ of reference compounds to surface hydroxyl groups (-OH).

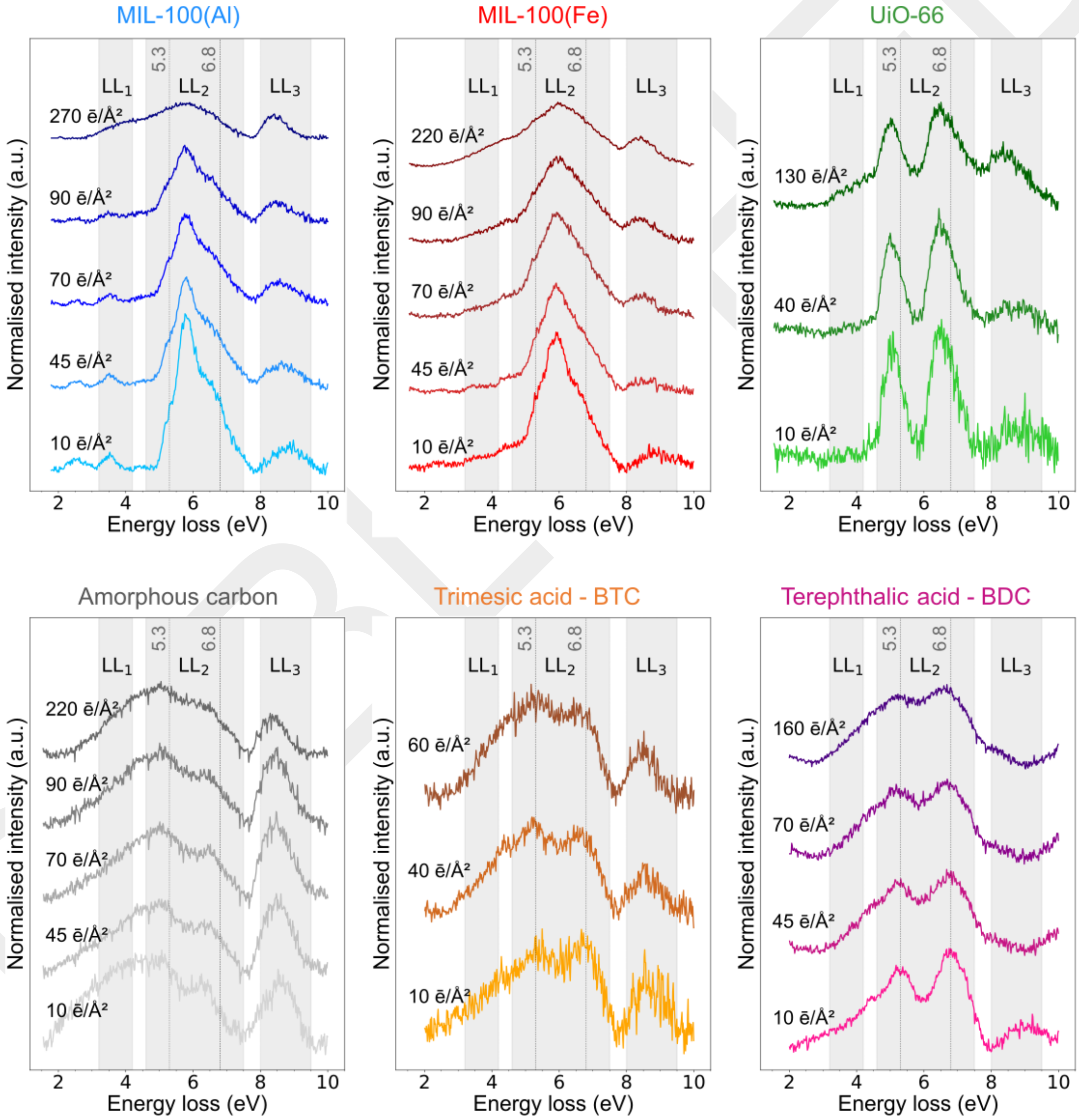

Figure S5. *Evolution of the low-loss signal with the electron dose for MIL-100(Al) in blue, MIL-100(Fe) in red, UiO-66 in green, amorphous carbon in grey, BTC in orange and BDC in pink. Each series is normalised over the total signal collected. The energy resolution is about δE = 40 meV. The shaded areas of nanoMOFs spectra are discussed in the manuscript. The indicated electron doses correspond the cumulated doses from successive acquisitions over the same area. Data were collected with a total acquisition time ranging from 2s (low-dose) to 80s (higher dose), at a constant beam current of 6 pA.*

Low-loss mapping of MIL-100(Fe) and UiO-66 by NLLS Multi-Gaussian fitting

Figure S6 gives more details on the processing of spectral maps shown in Figure 4e-f. The characteristic features observed for MIL-100(Fe) and UiO-66 were fitted with three Gaussian functions (red, orange and yellow in Figure S6b) after PCA processing and background subtraction.

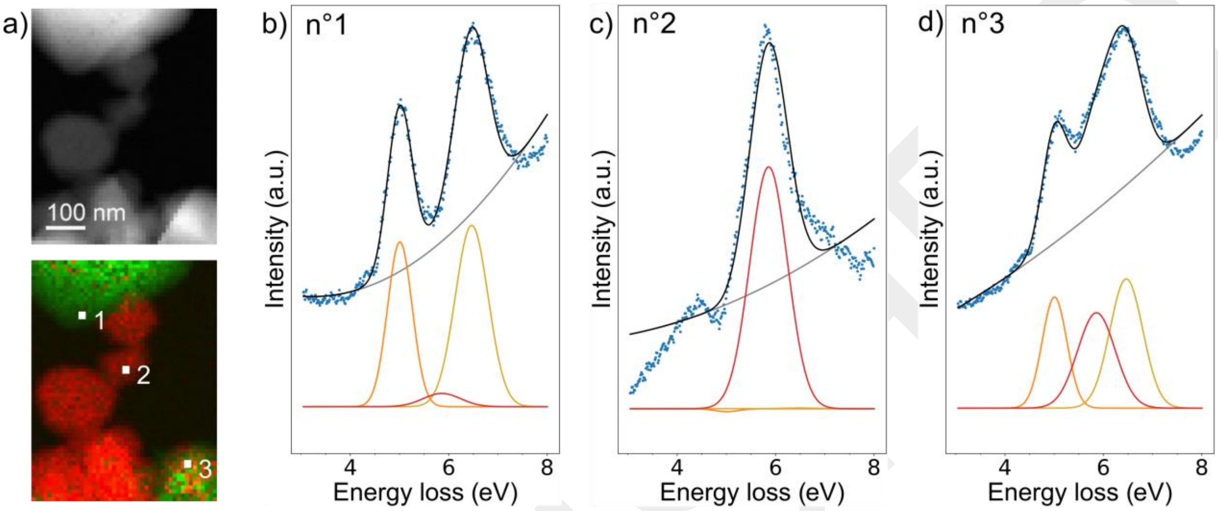

Figure S6. *(a) HAADF image of mixed MIL-100(Fe) and UiO-66 and the corresponding spectral map obtained in the LL. (b-d) Multi-Gaussian fitting of the corresponding LL signal performed in the areas labelled 1 (b), 2 (c) and 3 (d) in (a). After PCA processing, spectra (blue dots) are subtracted with a second-order polynomial function (grey). The three features are fitted with Gaussian functions (red, orange and yellow).*

Deconvolution of the ULL spectra

The Richardson-Lucy deconvolution was applied to the ULL data to improve the spectral resolution δE from 12 to 7 meV (Figure S7a-b). In the meantime, as it minimises the ZLP tail, the background subtraction of ULL data is also improved (Figure S7c).

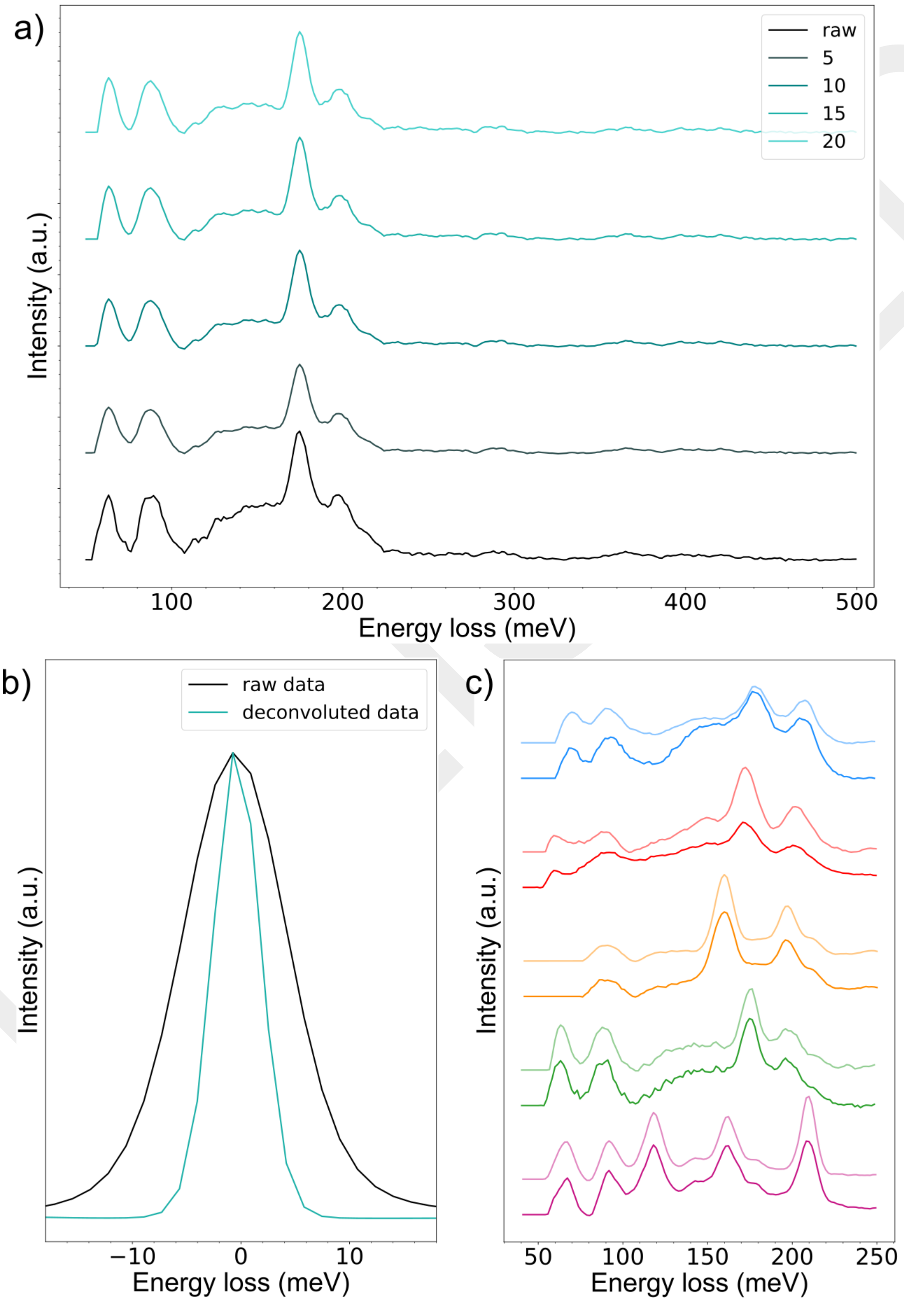

***Figure S7**: (a) ULL EELS spectra of UiO-66 obtained with different numbers of iterations (cyan gradient from 5 to 20) after background subtraction with a second-order polynomial function. (b) Comparison of the ZLP before (black) and after the Richardson-Lucy deconvolution (cyan, 10 iterations). The energy resolution achieved and measured from the FWHM is δE = 12 meV and 7 meV, respectively. (c) Comparison of the ULL spectra before (dark line) and after (light line) Richardson-Lucy deconvolution (10 iterations) obtained for MIL-100(Al) in blue, MIL-100(Fe) in red, BTC in orange, UiO-66 in green and BDC in pink. The deconvolution improves the background subtraction by reducing the ZLP tail, and leads to a better signal contrast.*

FTIR spectra of the three nanoMOFs and their organic linkers

Figure S8 shows the FTIR spectra obtained for the three nanoMOFs and their corresponding free-standing organic linkers. A complete assignment can be found in Table S1. In order to help the identification of remaining solvents, FTIR data of ethanol and water are also provided in Figure S8.

For MIL-100, adsorbed ethanol and structural water are revealed by CC and CH bending modes in the ULL_3 area, CH stretching mode (denoted ULL_5) and OH bending mode (denoted ULL_6). For UiO-66, DMF was detected through CN, CH and CO stretching modes in the ULL_3 area and adsorbed ethanol or water, whose OH bending modes were collected in the ULL_6 area.

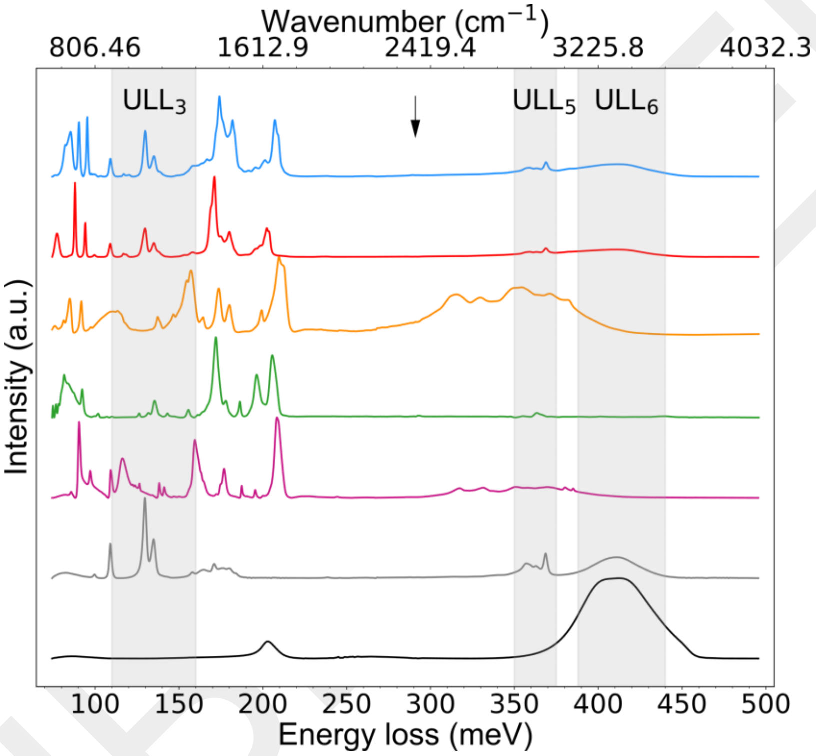

Figure S8: *FTIR spectra obtained between 4000 cm^{-1} and 600 cm^{-1} for MIL-100(Al) in blue, MIL-100(Fe) in red, BTC in yellow, UiO-66 in green, BDC in pink, absolute ethanol in grey and water in black. The spectral resolution is about 4 cm^{-1}. The arrow indicates the absence of sign of degradation detected in ULL EELS at 291 meV.*

Ultralow-loss spectra of the three nanoMOFs and their organic linkers

The ULL spectra obtained for the three nanoMOFs, their corresponding free-standing organic linkers and amorphous carbon are shown in Figure S9. A complete assignment can be found in Table S1. As described in the main text, valuable information is provided on the remaining solvents. For the three nanoMOFs, the spread signal of the ULL$_3$ area could be related to CC, CN and CO stretching modes of ethanol and DMF. Peak ULL$_5$ represents CH stretching modes. Considering the fast dehydrogenation observed by the carbon K-edge analysis, it may be associated with entrapped solvent molecules (ethanol, DMF) that could benefit from the protection of the framework against radiation damages as demonstrated by Wang *et al.*[8] For MIL-100, OH stretching mode is found in the ULL$_6$ area, indicating hydroxyl groups or structural water. This band is also present on amorphous carbon, studied as a reference specimen, which we assign to adsorbed water. Note that this excitation is not detected for UiO-66.

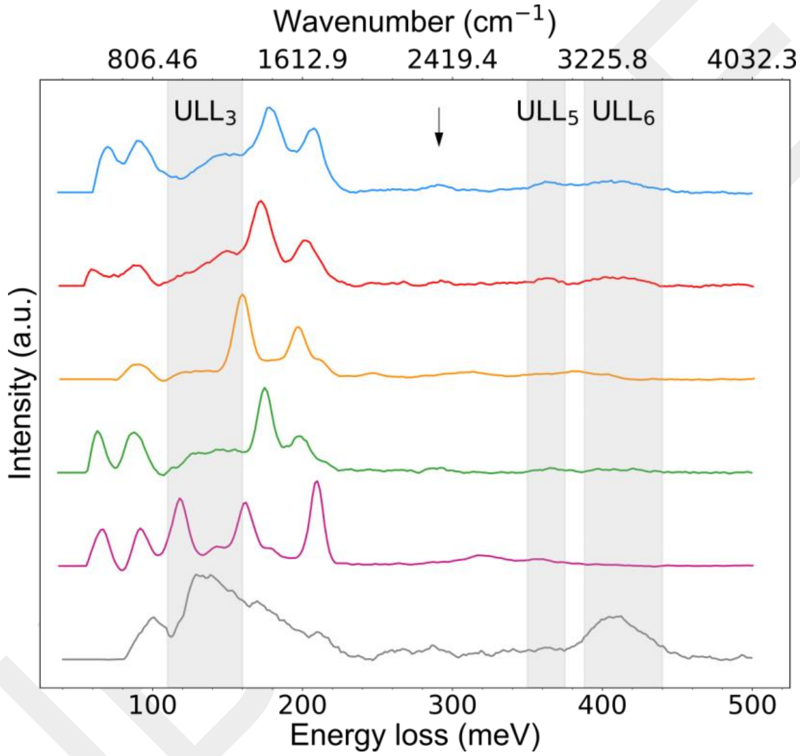

Figure S9: *Vibrational EEL spectra obtained between 30 meV and 500 meV (240 – 4030 cm^{-1}) for MIL-100(Al) in blue, MIL-100(Fe) in red, BTC in yellow, UiO-66 in green, BDC in pink and amorphous carbon in grey. Data were acquired with an energy window of 2 eV, at about 120 ē/Å^2 with a beam current of 4 pA and a total acquisition time in the order of hundreds of seconds. The energy resolution is about 7 meV after deconvolution with the Richardson-Lucy Algorithm. The arrow indicates sign of degradation at 291 meV.*

Transmission vs aloof ULL signal

As described in the main text, the ULL signal obtained in transmission and aloof configurations are similar. This attest to the detection of localised vibrational modes related to the molecular vibrations.

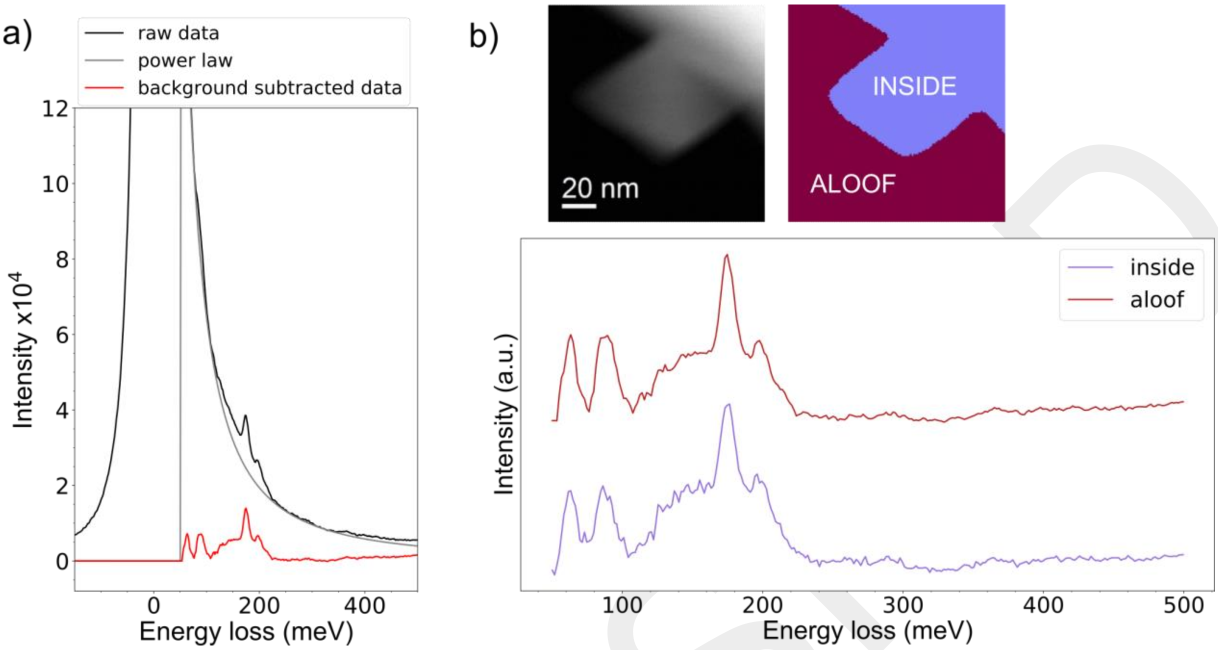

***Figure S10**: (a) Typical background subtraction performed with a power-law function. (b) Schematic representation and the corresponding spectra obtained in the aloof and transmission configurations. In the former, the EEL signal is collected in vacuum a few nanometers away from the nanoparticle. Conversely, the transmission signal results from the direct impact of the electron beam. All spectra are raw data.*

Table S1: Assignment of the FTIR and vibrational EELS peaks observed for each nanoMOFs and their corresponding organic linker.

n.o. stands for not observed and * refers to this study.

Specimen	FTIR peak position		EELS peak position (meV)	Assignment	Ref.
	cm-1	meV			
MIL-100(Al)	n.o.	n.o.	71	Al-O stretch	[9]
	663	82	91	-	-
	689	85		CH bend and benzene ring deformation	[10,11]
	728	90			
	769	95	99		
	880	109	109	CC stretch of ethanol	[12]
	944	117	116	CC bend	*
	971	120		Benzene ring deformation	*
	1047	130	120 – 160	CO stretch of ethanol	[12]
	1090	135		CH_3 bend of ethanol	
	1121	139		Benzene ring deformation	[13]
	1273	158		CO stretch of free BTC in pores and CH_2 bend of ethanol	[12,14]
	1345	167		CO stretch	*
	1405	174	180	asymmetric CO stretch of coordinated carboxylic groups	[14,15]
	1467	182		CC stretch	[14]
	1543	191			
	1578	196	209		
	1624	201			
	1672	207		symmetric CO stretch of coordinated carboxylic groups	[14,15]
	n.o.	n.o.	291	-	
	2889	358	365	CH_2 and CH_3 symmetric stretch of ethanol	[12]
	2931	363			
	2975	369		CH_3 asymmetric stretch of ethanol	

	3088	383	385 - 440	CH stretch	[13,14]
	3130 - 3550	388 - 440		OH stretch of structural water or ethanol	[12,14,15]
MIL-100(Fe)	n.o.	n.o.	60	Fe-O stretch	[10,15,16]
	624	77	75	Asymmetric Fe_3-μ_3-O stretch of iron (III)	[11,16,17]
	710	88	90	CH bend and benzene ring deformation	[10,11]
	759	94			
	803	100		CH_3 of ethanol	[12]
	880	109	105 - 160	CC stretch of ethanol	[12]
	943	117		CC bend	*
	957	119		Benzene ring deformation	*
	1047	130		CO stretch of ethanol	[12]
	1089	135		CH_3 bend of ethanol	
	1236	153		CO stretch of free BTC in pores	[14,17]
	1274	158		CH_2 bend of ethanol	[12]
	1380	171	173	symmetric CO stretch of coordinated carboxylic groups	[10,15]
	1412	175		CH_2 bend of ethanol	[12]
	1453	180		OH bend	[10,15]
	1576	195	203	CC stretch	[14]
	1599	198			*
	1632	202		asymmetric CO stretch of coordinated carboxylic groups	[10,11,15,16]
	n.o.	n.o.	291	-	-
	2888	358	365	CH_2 and CH_3 symmetric stretch of ethanol	[12]
	2928	363			
	2975	369		CH_3 asymmetric stretch of ethanol	
	3084	382	385 - 440	CH stretch	[13,14]
	3130-3550	388 - 440		OH stretch of structural water or ethanol	[10–12,14,15]
UiO-66	n.o.	n.o.	64	Zr-O stretch	[18]

	618	77	88	OH bend, CH bend and Zr_3-μ_3-O stretch	[18,19]
	631	78			
	658	82			
	680	84			
	705	87			
	744	92			
	821	102		CC bend	*
	1018	126	106 - 165	CO stretch	*
	1062	132			
	1092	135		Ring deformation	*
	1155	143			
	1255	156		CN stretch of DMF	[14]
	1347	167		CH stretch of DMF	[14]
	1387	172	176	symmetric CO stretch of coordinated carboxylic groups	[18,19]
	1436	178		OH or CC bend	*
	1503	186	200	CC stretch	[18]
	1584	196		asymmetric CO stretch of coordinated carboxylic groups	[18,19]
	1659	206	218	CO stretch of DMF	[19]
	n.o.	n.o.	291	-	-
	2935	364	365	CH stretch of benzene rings and DMF	[14,18,19]
	3544	439	n.o.	OH stretch of ethanol	[18]
BTC	613	76	89	Ring deformation	[20]
	656	81		CC bend	
	685	85		CO and CC bend	[20]
	740	92		CO, CC, CH bend	[20,21]
	786	97		CH bend	[22]
	891	110	107 - 145	OH bend	[21,22]
	955	118		CH bend	[20]

	1002	124		CC bending	22
	1108	137		CC, CH, OH bend	20,22
	1183	147	161	CH and OH bend, CC stretch	20–22
	1248	155		CO stretch	22
	1267	157		CH bend, CC stretch	20,22
	1326	164		Symmetric CO stretch	20,21
	1401	174	173 - 188	Symmetric CO stretch	20–22
	1452	180		CC stretch, CH bend	20,22
	1607	199	198	CC stretch	20,22
	1691	210	215	CO stretch	21,22
	1714	213		CO stretch	20
	1981	246	248	CC stretch	*
	2542	315	275 - 340	CH stretch	*
	2659	330			
	2840	352	340 - 420	-	-
	2992	371			
	3081	382		CH stretch	20,22
BDC	n.o.	n.o.	67	-	-
	692	86	92	OH and CH bend	23
	729	90			
	784	97			
	882	109	119	CC and CO bend	23
	938	116			
	1019	126			
	1115	138	143	CH and CO bend	23
	1139	141			
	1287	160	162	CO stretch	23
	1427	177	180	CC stretch, CH bend	23
	1512	187	193		

	1577	196			
	1682	209	210	Asymmetric CO stretch and OH bend	[23]
	~1825	~226	~228	-	-
	2559	317	298 - 342	CH stretch	*
	2670	331			
	2830	351	342 - 400		
	2983	370			
	3068	380			
	3106	385			

REFERENCES

(1) Peña, F. de la; Prestat, E.; Fauske, V. T.; Burdet, P.; Lähnemann, J.; Furnival, T.; Jokubauskas, P.; Nord, M.; Ostasevicius, T.; MacArthur, K. E.; Johnstone, D. N.; Sarahan, M.; Aarholt, T.; Taillon, J.; pquinn-dls; Migunov, V.; Eljarrat, A.; Caron, J.; Poon, T.; Mazzucco, S.; Francis, C.; Martineau, B.; actions-user; Somnath, S.; Slater, T.; Tappy, N.; Walls, M.; Cautaerts, N.; Winkler, F.; DENSmerijn. Hyperspy/Hyperspy: Release v1.6.5, 2021. https://doi.org/10.5281/zenodo.5608741.

(2) Gloter, A.; Douiri, A.; Tencé, M.; Colliex, C. Improving Energy Resolution of EELS Spectra: An Alternative to the Monochromator Solution. *Ultramicroscopy* **2003**, *96* (3), 385–400. https://doi.org/10.1016/S0304-3991(03)00103-7.

(3) Demšar, J.; Curk, T.; Erjavec, A.; Gorup, Č.; Hočevar, T.; Milutinovič, M.; Možina, M.; Polajnar, M.; Toplak, M.; Starič, A.; Štajdohar, M.; Umek, L.; Žagar, L.; Žbontar, J.; Žitnik, M.; Zupan, B. Orange: Data Mining Toolbox in Python. *Journal of Machine Learning Research* **2013**, *14* (35), 2349–2353.

(4) Cebula, I.; Lu, H.; Zharnikov, M.; Buck, M. Monolayers of Trimesic and Isophthalic Acid on Cu and Ag: The Influence of Coordination Strength on Adsorption Geometry. *Chemical Science* **2013**, *4* (12), 4455–4464. https://doi.org/10.1039/C3SC52137K.

(5) Okajima, T.; Teramoto, K.; Mitsumoto, R.; Oji, H.; Yamamoto, Y.; Mori, I.; Ishii, H.; Ouchi, Y.; Seki, K. Polarized NEXAFS Spectroscopic Studies of Poly(Butylene Terephthalate), Poly(Ethylene Terephthalate), and Their Model Compounds. *J. Phys. Chem. A* **1998**, *102* (36), 7093–7099. https://doi.org/10.1021/jp981164t.

(6) Scott, A. I. *Interpretation of the Ultraviolet Spectra of Natural Products: International Series of Monographs on Organic Chemistry*; Elsevier, 2013.

(7) Schneider, N. M.; Norton, M. M.; Mendel, B. J.; Grogan, J. M.; Ross, F. M.; Bau, H. H. Electron–Water Interactions and Implications for Liquid Cell Electron Microscopy. *J. Phys. Chem. C* **2014**, *118* (38), 22373–22382. https://doi.org/10.1021/jp507400n.

(8) Wang, C.; Qiao, Q.; Shokuhfar, T.; Klie, R. F. High-Resolution Electron Microscopy and Spectroscopy of Ferritin in Biocompatible Graphene Liquid Cells and Graphene Sandwiches. *Advanced Materials* **2014**, *26* (21), 3410–3414. https://doi.org/10.1002/adma.201306069.

(9) Lestari, W. W.; Adawiyah, R. A.; Khafidhin, M. A.; Wijiyanti, R.; Widiastuti, N.; Handayani, D. S. CO2 Gas Separation Using Mixed Matrix Membranes Based on Polyethersulfone/MIL-100(Al). *Open Chemistry* **2021**, *19* (1), 307–321. https://doi.org/10.1515/chem-2021-0033.

(10) Mahmoodi, N. M.; Abdi, J.; Oveisi, M.; Alinia Asli, M.; Vossoughi, M. Metal-Organic Framework (MIL-100 (Fe)): Synthesis, Detailed Photocatalytic Dye Degradation Ability in Colored Textile Wastewater and Recycling. *Materials Research Bulletin* **2018**, *100*, 357–366. https://doi.org/10.1016/j.materresbull.2017.12.033.

(11) Tian, H.; Araya, T.; Li, R.; Fang, Y.; Huang, Y. Removal of MC-LR Using the Stable and Efficient MIL-100/MIL-53 (Fe) Photocatalyst: The Effect of Coordinate Immobilized Layers. *Applied Catalysis B: Environmental* **2019**, *254*, 371–379. https://doi.org/10.1016/j.apcatb.2019.04.086.

(12) Burke, D. J.; Wolff, A. J.; Edridge, J. L.; Brown, W. A. The Adsorption and Desorption of Ethanol Ices from a Model Grain Surface. *J. Chem. Phys.* **2008**, *128* (10), 104702. https://doi.org/10.1063/1.2888556.

(13) Volkringer, C.; Leclerc, H.; Lavalley, J.-C.; Loiseau, T.; Férey, G.; Daturi, M.; Vimont, A. Infrared Spectroscopy Investigation of the Acid Sites in the Metal–Organic Framework Aluminum Trimesate MIL-100(Al). *J. Phys. Chem. C* **2012**, *116* (9), 5710–5719. https://doi.org/10.1021/jp210671t.

(14) Haouas, M.; Volkringer, C.; Loiseau, T.; Férey, G.; Taulelle, F. Monitoring the Activation Process of the Giant Pore MIL-100(Al) by Solid State NMR. *J. Phys. Chem. C* **2011**, *115* (36), 17934–17944. https://doi.org/10.1021/jp206513v.

(15) Nivetha, R.; Gothandapani, K.; Raghavan, V.; Jacob, G.; Sellappan, R.; Bhardwaj, P.; Pitchaimuthu, S.; Kannan, A. N. M.; Jeong, S. K.; Grace, A. N. Highly Porous MIL-100(Fe) for the Hydrogen Evolution Reaction (HER) in Acidic and Basic Media. *ACS Omega* **2020**, *5* (30), 18941–18949. https://doi.org/10.1021/acsomega.0c02171.

(16) Chaturvedi, G.; Kaur, A.; Umar, A.; Khan, M. A.; Algarni, H.; Kansal, S. K. Removal of Fluoroquinolone Drug, Levofloxacin, from Aqueous Phase over Iron Based MOFs, MIL-100(Fe). *Journal of Solid State Chemistry* **2020**, *281*, 121029. https://doi.org/10.1016/j.jssc.2019.121029.

(17) Leclerc, H.; Vimont, A.; Lavalley, J.-C.; Daturi, M.; Wiersum, A. D.; Llwellyn, P. L.; Horcajada, P.; Férey, G.; Serre, C. Infrared Study of the Influence of Reducible Iron(III) Metal Sites on the Adsorption of CO, CO2, Propane, Propene and Propyne in the Mesoporous Metal–Organic Framework MIL-100. *Phys. Chem. Chem. Phys.* **2011**, *13* (24), 11748–11756. https://doi.org/10.1039/C1CP20502A.

(18) Jin, Z.; Zhang, Y.; Ma, Q. Orthorhombic WP Co-Catalyst Coupled with Electron Transfer Bridge UiO-66 for Efficient Visible-Light-Driven H2 Evolution. *Journal of Colloid and Interface Science* **2019**, *556*, 689–703. https://doi.org/10.1016/j.jcis.2019.08.107.

(19) Valenzano, L.; Civalleri, B.; Chavan, S.; Bordiga, S.; Nilsen, M. H.; Jakobsen, S.; Lillerud, K. P.; Lamberti, C. Disclosing the Complex Structure of UiO-66 Metal Organic Framework: A Synergic Combination of Experiment and Theory. *Chem. Mater.* **2011**, *23* (7), 1700–1718. https://doi.org/10.1021/cm1022882.

(20) Mahalakshmi, G.; Balachandran, V. FT-IR and FT-Raman Spectra, Normal Coordinate Analysis and Ab Initio Computations of Trimesic Acid. *Spectrochimica Acta Part A: Molecular and Biomolecular Spectroscopy* **2014**, *124*, 535–547. https://doi.org/10.1016/j.saa.2014.01.061.

(21) Classen, T.; Lingenfelder, M.; Wang, Y.; Chopra, R.; Virojanadara, C.; Starke, U.; Costantini, G.; Fratesi, G.; Fabris, S.; de Gironcoli, S.; Baroni, S.; Haq, S.; Raval, R.; Kern, K. Hydrogen and Coordination Bonding Supramolecular Structures of Trimesic Acid on Cu(110). *J. Phys. Chem. A* **2007**, *111* (49), 12589–12603. https://doi.org/10.1021/jp076037o.

(22) Kim, Y.; Cho, K.; Lee, K.; Choo, J.; Gong, M.; Joo, S.-W. Electric Field-Induced Adsorption Change of 1,3,5-Benzenetricarboxylic Acid on Gold, Silver, and Copper Electrode Surfaces Investigated by Surface-Enhanced Raman Scattering. *Journal of Molecular Structure* **2008**, *878* (1), 155–161. https://doi.org/10.1016/j.molstruc.2007.08.002.

(23) Téllez S, C. A.; Hollauer, E.; Mondragon, M. A.; Castaño, V. M. Fourier Transform Infrared and Raman Spectra, Vibrational Assignment and Ab Initio Calculations of Terephthalic Acid and Related Compounds. *Spectrochimica Acta Part A: Molecular and Biomolecular Spectroscopy* **2001**, *57* (5), 993–1007. https://doi.org/10.1016/S1386-1425(00)00428-5.

Insight into the Nanoscale Biodegradation Mechanisms of MOFs by Electron Spectromicroscopy

Maeva Chaupard,[a,b] *Susana Trasobares,*[c] *Ruxandra Gref,*[b] *Marta de Frutos*[a]*

[a]Laboratoire de Physique des Solides, CNRS, UMR 8502, Université Paris-Saclay, F-91405 Orsay, France
[b]Institut des Sciences Moléculaires d'Orsay, CNRS, UMR 8214, Université Paris-Saclay, F-91405 Orsay, France
[c]Departamento de Ciencia de los Materiales e Ingeniería Metalúrgica y Química Inorgánica, Facultad de Ciencias, Universidad de Cádiz, 11510 Cádiz, Spain

Corresponding author: marta.de-frutos@universite-paris-saclay.fr

Supplementary Information

Supplementary materials and methods

Chemical materials

Trimethyl trimesate (98%), Aluminium nitrate nonahydrate (98%) and nitric acid (puriss. > 65%) were purchased from Alfa Aesar and Sigma-Aldrich. Dulbecco's Phosphate-Buffered Saline (PBS) 1X was provided by ThermoFisher Scientific. It contains 2.67 mM KCl, 1.47 mM KH_2PO_4, 137.93 mM NaCl and 8.06 mM $Na_2HPO_4.7H_2O$ at pH 7.0 - 7.3. Methanol (≥ 99,5%) GPR RECTAPUR® was purchased from VWR Chemicals while absolute ethanol (99%) was provided by Carlo Erba. Deionised water was purified through a Milli-Q system.

Synthesis procedure

Briefly, aluminium nitrate nonahydrate (3.82 mmol, 1.43g) and trimethyltrimesate (4.81 mmol, 1.21g) were dissolved in 20 mL of water with stirring for 5 min. Nitric acid solution (4mL, 4M) was added and stirred for 5 min. The preparation was then heated in a microwave oven (Microwave Accelerated Reaction System MARS-5, CEM, United-States) for 30 min at 210°C (1600 watts, 50%) with stirring. After cooling down in an ice bath for 15 min, the resulting yellow product was recovered by centrifugation at 10,500g for 30 min and dispersed in 50 mL of methanol. The suspension was stirred overnight. The final product was recovered by centrifugation at 12,000g for 15 min and washed four times in absolute ethanol after centrifugation at 11,000g for 12 min. To select the smallest nanoparticles, size separation was performed by two successive centrifugations of the supernatant at 6,000g for 1min40s. The suspension was stored as-is. The chemical formula of MIL-100(Al) is $Al_3O(OH)(C_9O_6H_3)_2(H_2O)_2$.

Characterisation

After synthesis, the original MIL-100(Al) nanoparticles were characterised either in suspension or in powder form, after drying at 60°C overnight. The results are presented in Figure S1.

Hydrodynamic size. Dynamic light scattering (DLS, Zetasizer Nano ZS90, Malvern, UK) was performed on the original suspensions in ethanol, diluted to reach a concentration of approximately 0.5 mg/mL. Three measurements were successively carried out on the same specimen to provide a statistical estimate.

Morphology. Transmission electron microscopy was used to image the morphology and size of the nanoparticles before and after degradation. 4µL of each suspension was deposited on a glow-discharged lacey carbon grid (300 mesh, Agar Scientific) for 10s and blotted with filter paper. Experiments were performed at 100kV on a JEOL JEM-2010 microscope equipped with a LaB_6 electron source and a Gatan Ultrascan 1K CCD camera. Images were acquired at magnifications ranging from 20 kx to 100 kx.

Porosimetry was performed using an ASAP 2020 (Micromeritics, USA) to determine the Bunauer-Emmett-Teller (BET) surface area of dried nanoparticles (approximately 70 mg) by nitrogen sorption at liquid nitrogen temperature, after degassing at 100°C under secondary vacuum overnight.

Thermogravimetric analyses (TGA 4000, PerkinElmer, USA) were performed on the dried samples. Approximately 20 mg of MIL-100(Al) was heated from 30°C to 600°C at a temperature rate of 3°C/min under an O_2 flow rate of 20 mL/min. Weight losses (wt%) were determined in Orange, an open-source software suite,[1] using a Savitzky-Golay filtered first-derivative with a second polynomial order and a window width of 23 points.

Chemical composition. Fourier-transform infrared spectroscopy (FTIR, Vertex 70, Bruker, Germany) was used in the attenuated total reflection (ATR) mode. Prior to analysis, the nanoparticles were suspended in water and centrifuged at 10,000g for 5 min. The pellet was recovered, placed on the ATR crystal and dried under ambient air flow. Data were collected between 4,000 cm^{-1} and 600 cm^{-1} with a spectral aperture of 1.5 mm, averaging 128 scans. The spectral resolution is equal to 4 cm^{-1}. To improve the comparison between the different spectra, the data were baseline corrected in Orange.[1]

Bulk characterisation of intact MIL-100(Al)

Figure S1 summarises the physicochemical properties of MIL-100(Al) measured by bulk techniques. The measurements were performed on two preparations (orange and purple in **Figure S1**). Hereafter, the presented results are mean values of the two experiments.

By using Dynamic Light Scattering (DLS, **Figure S1a**), the hydrodynamic diameter of MIL-100(Al) was estimated to 173.7 ± 1.6 nm, with a polydispersity index of 0.06 ± 0.04. This latter value, close to zero, indicates the homogeneity of the specimen size population.

Their Bunauer-Emmett-Teller (BET) surface area was measured to be approximately 2012 ± 85 $m^2.g^{-1}$ (**Figure S1b**). This result is in agreement with a previous work,[2] and reveals the high porosity of MIL-100(Al) nanoparticles. The purity of the sample was assessed by thermogravimetric analysis. As shown in **Figure S1c**, three main degradation steps are observed. They correspond to the evaporation of solvent molecules (30-150°C, 19 wt% loss), the removal of coordinated water and hydroxyl groups (230-330°C, 4 wt% loss) and the degradation of the organic fraction (360-550°C, 60 wt% loss), respectively.[3] After heating at 600°C, only inorganic residues remain (17 wt%).[3] These results are close to those of a previous study.[3] According to the theoretical formula of MIL-100(Al), the nanomaterial should contain 9 wt% of coordinated water and hydroxyl groups, 74 wt% of linkers and 17 wt% of Al_3O oxo-clusters (see **Table S1**). Hence, we suggest that the difference between the theoretical values and our experimental data probably results from the solvent and the free-standing linkers remaining inside the framework pores.

Figure S1c shows Transmission Electron Microscopy (TEM) images of the specimen. Facetted morphologies were observed, as reported elsewhere.[4,5] The crystallinity of the nanoparticles is consistent with the cubic structure first described by Volkringer et al.[2] The observed nanoparticle sizes range between 40 and 200 nm (see **Figure S4**).

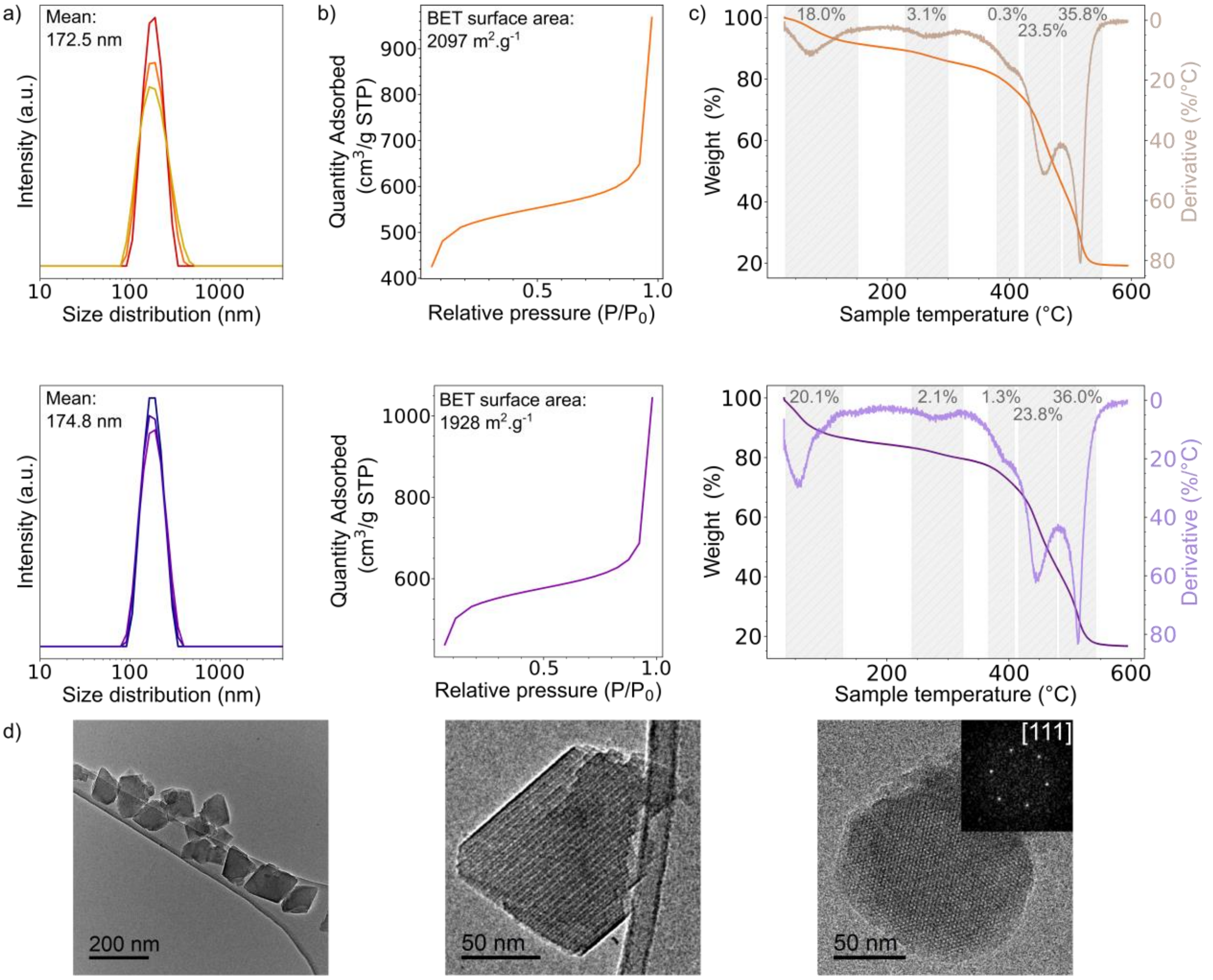

Figure S1. Characterisation of intact MIL-100(Al). *a) Intensity-based size distribution obtained by DLS. b)* N_2 *adsorption isotherm. c) TGA curve (dark) of MIL-100(Al) and the corresponding first derivative (light) obtained after a second-order Savitzky-Golay smoothing. All spectra are raw data obtained on two different synthesis indicated by the orange and purple colours. For DLS, the three lines represent the three successive measurements carried out on the same specimen for statistical estimate (see the Supplementary Materials and Methods). d) TEM images showing the well faceted shape and good crystallinity of the nanoparticles, obtained at 25kx (top row), 30kx (middle row) and 50kx (bottom row) magnifications. At the bottom, the MIL-100(Al) is observed along the [111] direction, as indicated in the inset fast-Fourier transform (FFT).*

Table S1*. Theoretical weight percent of MIL-100(Al) groups according to its chemical formula MIL-100(Al) =* $Al_3O(OH)(C_9O_6H_3)_2(H_2O)_2$.

Chemical group	Al_3O	(OH)	$(C_9O_6H_3)_2$	$(H_2O)_2$	Total
Molecular weight (g.mol^{-1})	96.94	17.00	420.28	36.00	570.23
Weight percent (wt%)	17.00	2.98	73.70	6.31	99.99

FTIR monitoring of the compositional changes during biodegradation

FTIR provides information about the chemical composition of nanomaterials. This technique was used to monitor the biodegradation of MIL-100(Al). The results are presented in **Figure S2**. First, before contact with PBS, the black spectrum displays the characteristic bands of the intact MOFs. The out-of-plane aromatic CH bending (δ_{CH}) and benzene ring deformation of the organic linkers are detected at 690-770 cm^{-1}. The CC and CO stretching modes of aromatic and coordinated carboxylic groups (ν_{CC}, ν_{CO}) are found at 1400-1670 cm^{-1}. The OH stretching modes of water molecules (ν_{OH}) are indicated around 3300 cm^{-1}. These data agrees with previous studies.[4–6]

For the degraded MIL-100(Al), a band near 1030 cm^{-1} indicates the PO stretching vibration modes (ν_{PO}).[4] It increases with the degree of biodegradation highlighting the interaction of phosphate molecules with the MOFs. Simultaneously, the δ_{CH}, ν_{CC} and ν_{CO} vibration modes progressively decrease showing a loss of the linkers. This agrees with the substitution of linkers by phosphates, as previously described in [4]. A similar biodegradation behaviour is observed at higher MOF and PBS concentrations (P/Al_3 =0.1* and P/Al_3 =0.6*).

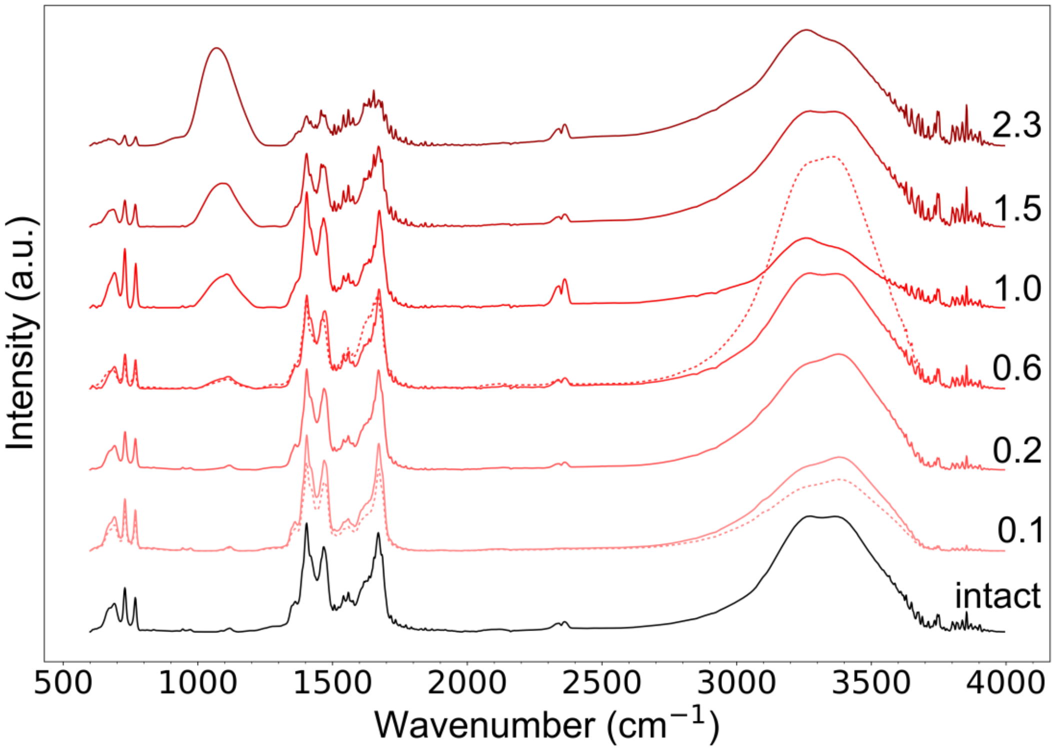

Figure S2. *FTIR spectrum of intact and degraded MIL-100(Al) in PBS at different P/Al_3 ratios, obtained between 4000 cm^{-1} and 600 cm^{-1}. Dotted line represents P/Al_3 = 0.1* and P/Al_3 = 0.6*. The spectral resolution is about 4 cm^{-1}.*

TEM images of degraded MIL-100(Al)

TEM was used to monitor the morphology changes induced by biodegradation. **Figure S3** shows images obtained for different stages of biodegradation, as a function of the MOFs concentration. MIL-100(Al) were degraded at low concentration (2.5 mg/mL) in **Figure S3a**, and at high concentration (10 mg/mL) in **Figure S3b**.

In **Figure S3a**, contact with PBS induces the formation of amorphous deposits around the nanoparticle. These amorphous structures appear to move away from the nanoparticle (fragmentation), leading to complete disassembly at high degradation stages.

Figure S3b shows the main changes in the morphology observed during the biodegradation process of MIL-100(Al) at high concentration (10 mg/mL): the erosion and the formation of amorphous deposits. Compared to the results presented in the main text (**Figure 2**, 2.5 mg/mL), here the biodegradation rate appears to be faster. The amorphous deposits are visible with sizes and in number similar to those observed for $P/Al_3 = 1.0$.

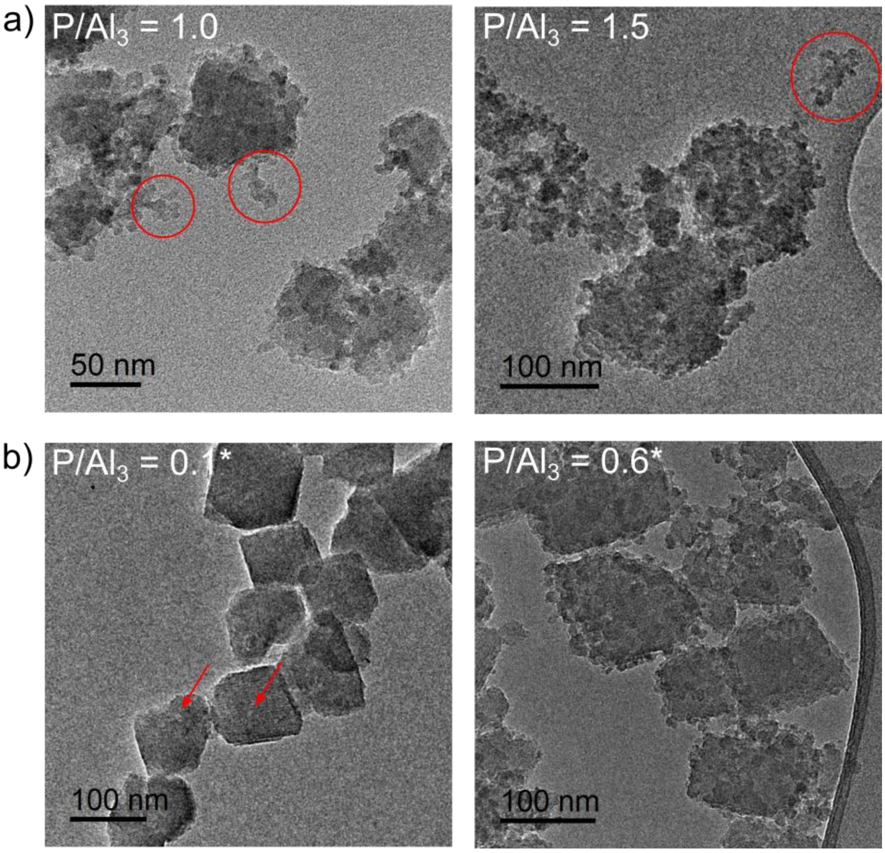

Figure S3. *TEM images of degraded MIL-100(Al). a) Fragmentation of the nanoparticles at $P/Al_3 = 1.0$ and $P/Al_3 =1.5$, indicated by red circles. b) Erosion and formation of amorphous deposits for high concentrations of MOFs (10 mg/mL). At $P/Al_3 = 0.1$*, red arrows indicate erosion that is similarly observed at $P/Al_3 = 0.1$. At $P/Al_3 = 0.6$*, the morphology change at appears more developed than for low concentration of MOFs (2.5 mg/mL): $P/Al_3 = 0.6$* displays amorphous growths with size and number corresponding to $P/Al_3 = 1.0$.*

TEM size measurement of intact and degraded MIL-100(Al)

As MIL-100(Al) suspensions are unstable in water and tend to aggregate,[4] even more so when they are degraded, the DLS is not suitable for size measurements. Therefore, TEM was used to monitor the size changes throughout the biodegradation process. To provide a statistical estimate, about one hundred of nanoparticles were analysed for each stage of biodegradation. As shown in **Figure S4**, no significant change was observed for size distributions.

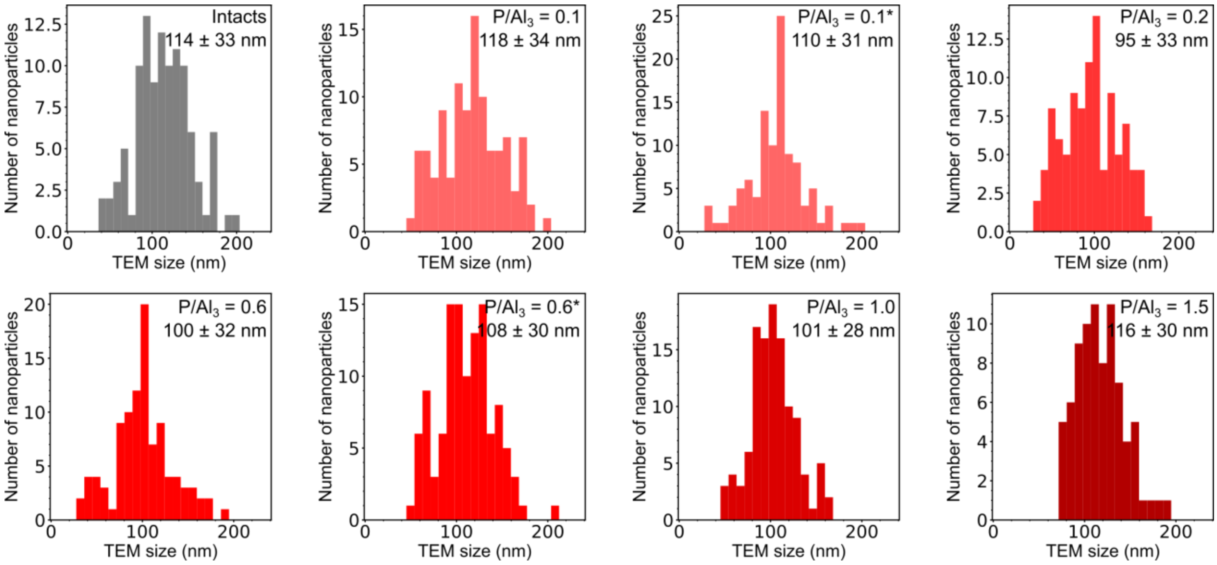

***Figure S4**. Size distributions measured by TEM for the intact and degraded MIL-100(Al) at different P/Al$_3$ ratios. For each condition, data were collected on approximately one hundred of nanoparticles. The corresponding median size value and standard deviation are indicated at the top of each plot. For high stages of degradation, the measured sizes include the amorphous deposits around the MOFs.*

HADF-STEM and iDPC-STEM imaging of intact and degraded MIL-100(Al)

The crystalline structure of MIL-100(Al) was imaged by using STEM-High Angle Annular Dark Field (HAADF) and iDPC-STEM. **Figure S5** highlights that iDPC-STEM is more appropriate that STEM-HAADF for high-resolution imaging of these beam-sensitive nanomaterials. This technique worked well for the crystalline analysis of intact and slightly degraded nanoparticles (P/Al_3 = 0.1*). After processed with an average background subtraction filter (denoising algorithm), the images reach a spatial resolution down to 2 Å. However, it was not suitable for highly degraded nanoparticles (P/Al_3 = 0.6*). This probably results from the decrease of the crystalline fraction due to the formation of the amorphous phase.

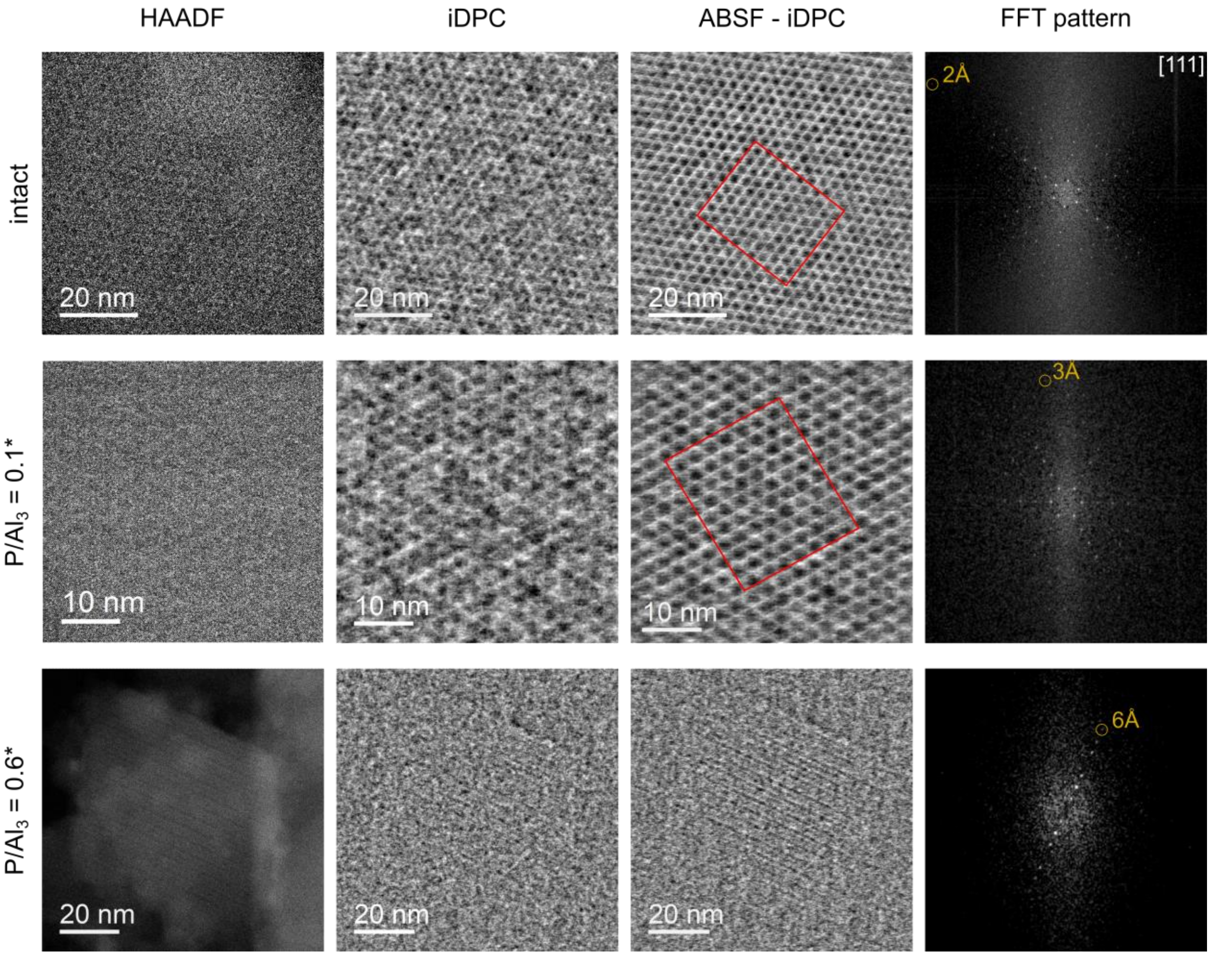

***Figure S5**. Images from STEM-HAADF and iDPC-STEM. The average background subtraction filtered (ABSF) iDPC-STEM images and their corresponding fast-Fourier transform pattern are given for intact (top row) and degraded MIL-100(Al) at P/Al_3 = 0.1* (middle row) and P/Al_3 = 0.6* (bottom row). The red rectangle indicates the sections shown in **Figure 3** of the main text.*

STEM-EDS analysis of intact and degraded MIL-100(Al)

As discussed in the main text, STEM-EDS was used to probe the changes in the elemental composition of MIL-100(Al) throughout the biodegradation process. **Figure S6** shows the elemental quantification of the intact (**Figure S6a**) and degraded MIL-100(Al) at P/Al_3 = 0.2 (**Figure S6b**) and at P/Al_3 < 1.0 (**Figure S6c**).

For the intact MIL-100(Al), EDS mainly detected carbon (55 at.%), oxygen (30 at.%) and aluminium (9 at.%). **Figure S6a** presents the measurements performed on nanoparticles from two regions to provide an estimate of the measurement variability. The oxygen content was unexpectedly low given the chemical formula of MIL-100(Al): $Al_3O(OH)(C_9O_6H_3)_2(H_2O)_2$. As MOFs are radiation-sensitive specimens, the oxygen loss is probably due to the beam-damage. Traces of fluorine and nitrogen (4 at.%) were also detected. These elements probably come from the Teflon microwave reactors and residual reagents such as aluminium nitrate and nitric acid. The presence of impurities is not surprising since nitrogen has already been detected by X-ray photoelectron spectroscopy.[4]

For the biodegraded MIL-100(Al) at P/Al_3 = 0.6* (**Figure S6b**), EDS detected carbon (58 at.%), oxygen (33 at.%) aluminium (10 at.%) and phosphorus (< 1 at.%). This is consistent with a slight stage of biodegradation as phosphorus is detected in traces and the oxygen content barely varies due to the substitution of the linkers ($C_9O_6H_3$) by phosphate molecules (PO_4^{3-}).

Then, at P/Al_3 = 1.0, the specimen displayed a more heterogeneous composition (**Figure S6c**). On MOFs (pink colour), EDS detected carbon (53 at.%), oxygen (36 at.%), aluminium (10 at.%) and phosphorus (1 at.%). This elemental composition is roughly similar to the one observed at P/Al_3 = 0.6*. Conversely, the amorphous deposits exhibited high concentrations of oxygen (71 at.%), aluminium (16 at.%) and phosphorus (10 at.%). They contain no carbon and are therefore completely inorganic. This indicates the formation of aluminium phosphate, which was further confirmed by STEM-EELS analysis.

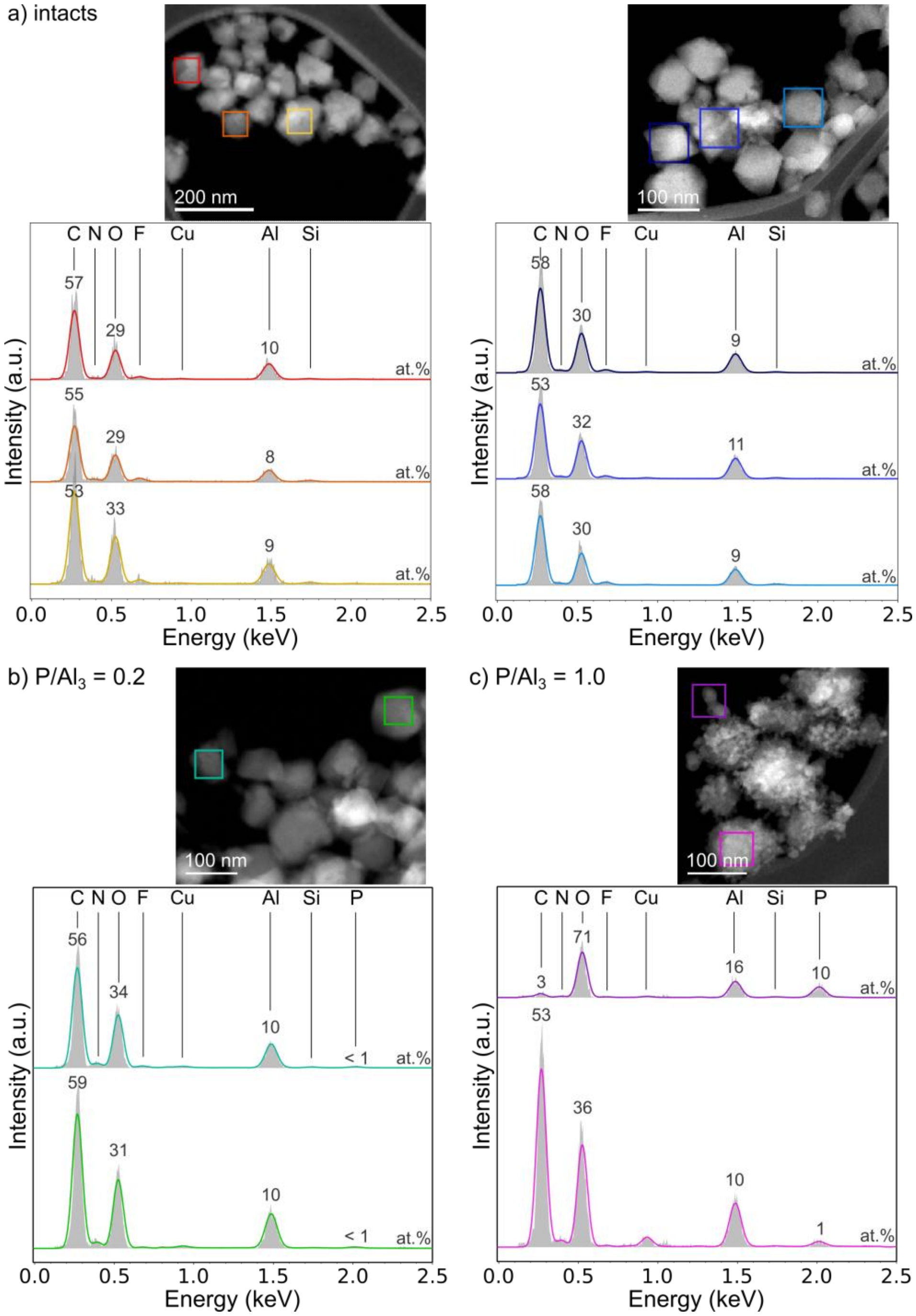

Figure S6. *STEM-HAADF images and the corresponding EDS spectra from (a-b) intact and (c-d) biodegraded MIL-100(Al) at (c) P/Al*$_3$ *= 0.2 and (d) P/Al*$_3$ *= 1.0, obtained in different areas. Two measurements are shown in (a) to provide an estimate of the measurement variability. The lines and shaded areas represent the fit and the experimental data, respectively. The numbers indicate the quantification in atomic percentage for the corresponding elements. Nitrogen and fluorine impurities come from residual reagents (aluminium nitrate, nitric acid) and Teflon microwave reactors. Chlorine, potassium and calcium are ions from water. Silicon and copper elements come from the microscope detectors and the TEM grids, respectively.*

STEM-EELS analysis of intact and degraded MIL-100(Al)

A previous study has shown that STEM-EELS analysis of MOFs is a trade-off between beam damage and signal-to-noise ratio (SNR).[6] At low electron dose (10 ē/Å^2), damage-free signatures are collected with a low SNR, while at higher electron doses, damaged signatures are collected with a good SNR. In order to investigate the chemical structure of MIL-100(Al), low electron doses were first used in this study. As shown in **Figure S9**, both the low and core-losses were analysed.

Figure S9a shows the low-loss spectral evolution of MIL-100(Al) with an increasing degree of biodegradation. The intact and degraded MOFs display a similar spectral signature. It consists of a prominent peak at 5.8 eV (indicated by the dotted line), previously attributed to the metal-linker coordination bond.[6] The absence of spectral differences between the specimens suggests that the low-loss region is not sensitive to the interactions with PBS.

Figure S9b shows the core-loss spectral evolution of MIL-100(Al) with an increasing degree of biodegradation. At low-dose (10 ē/Å^2, light colours), the carbon and oxygen K-edges of the intact and degraded MIL-100(Al) display similar signatures. On the carbon K-edge, three peaks are observed at 285.0 eV, 288.6 eV and 290.9 eV that correspond to the 1s-$\pi^*_{C=C}$, 1s-$\pi^*_{C=O}$ and 1s-$\sigma^*_{C\text{-}O}$ transitions of the linkers, respectively. On the oxygen K-edge, two contributions are observed at 534.0 eV and near 543 eV associated to the 1s-$\pi^*_{C=O}$ and 1s-$\sigma^*_{C\text{-}O}$ transitions of the linkers.[6] The absence of spectral differences between the specimens suggest that the carbon K-edge is not sensitive to the chemical changes induced by phosphate molecules. However, this is not surprising: no spectral change was expected since carbon comes from linkers that are only substituted and not chemically modified. Since some of the linkers remain in the MOFs during the process, the carbon is still detected here, unchanged, even at high stages of biodegradation (presence of carbon and oxygen from the linker at P/Al$_3$ = 1.0 and 1.5, Figure 6 and 7).

However, it should be noted that due to the low SNR of low-dose conditions, the spectra presented in **Figure S9** are cumulated over hundreds of nanometres. This results in a poor spatial resolution of the analysis (of hundreds of nanometers) which hampers, for example, to distinguish the signature of MOFs and amorphous deposits in biodegraded MIL-100(Al) at P/Al$_3$ = 1.5. This poor spatial resolution makes the low-dose condition not suitable for studying the changes of chemical composition occurring during biodegradation, as amorphous deposits measure ~ 20 nm. Therefore, higher electron doses were used in the manuscript. Note that only the core-loss was analysed at higher doses as the low-loss features disappeared due to the beam damage.[6]

The main text presents core-loss results obtained at electron doses > 300 ē/Å^2. These conditions were used to increase the SNR of low cross-section edges (such as phosphorus and aluminium L-edges) and the spatial resolution to values < 3 nm. Due to the beam damage, the collected signature could not be easily identified. A complementary beam-effect study was required to relate the damaged signature (obtained at > 300 ē/Å^2) to the original chemical structure of the MOFs (obtained at 10 ē/Å^2). Therefore, the carbon and oxygen K-edges of the intact MIL-100(Al) were collected at different electron doses (from 10 ē/Å^2 to > 300 ē/Å^2, **Figure S9b**, light to dark colours). The beam damage is observed as the electron dose increases, with the appearance of two new peaks at 287.5 eV and 536.5 eV (indicated by dotted lines). Both are attributed to the formation of carbon monoxide and carbon dioxide.[7,8] As these gases originate from the damage to the organic fraction, they represent chemical fingerprints of the linkers. Thus, in **Figure 7** (main text), the detection of the peak at 287.5 eV in the MOFs-like morphology region attests to the presence of organic moieties. Conversely, its absence in the amorphous region indicates a completely mineral phase.

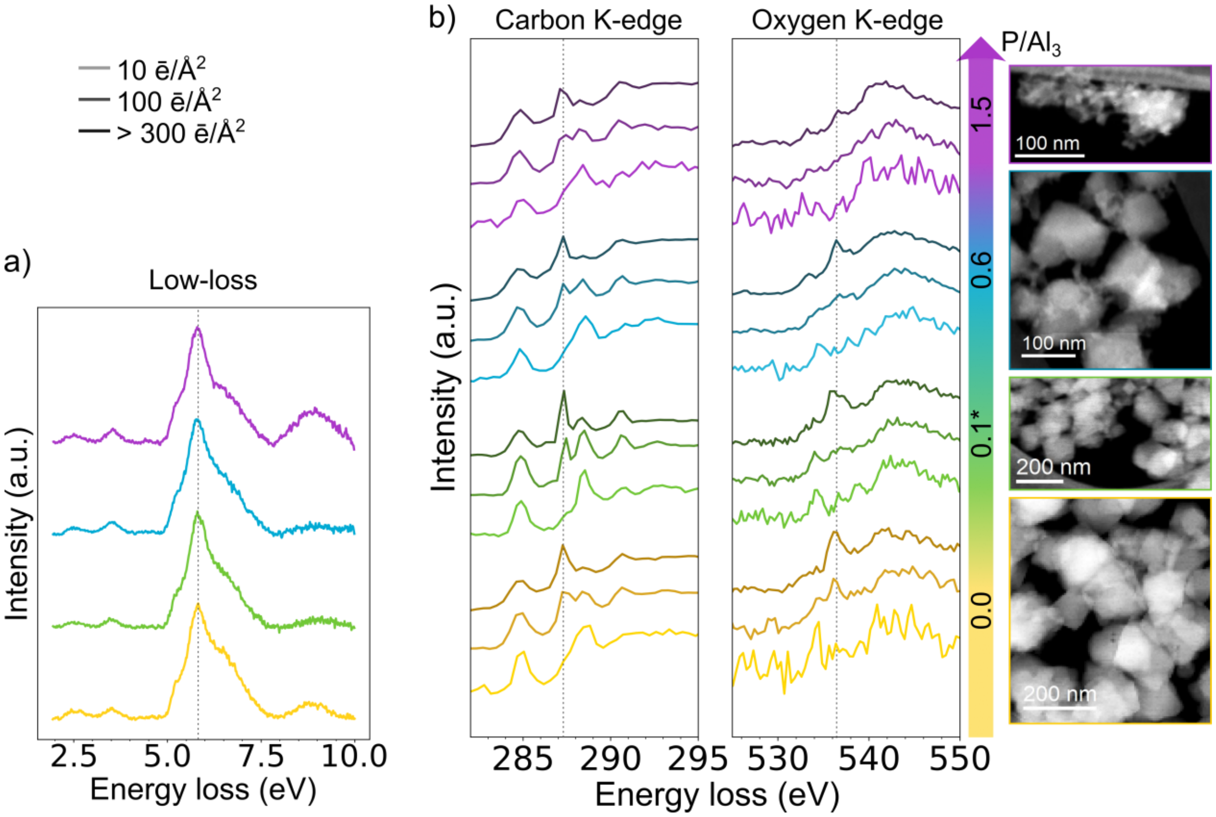

Figure S9. *EELS signatures of intact and degraded nanoparticles in the (a) low-loss and (b) core-loss regions. The low-loss spectra were obtained at 10 ē/Å^2. For the core-loss, a colour gradient indicates the increase of the electron dose from 10 ē/Å^2 to 700 ē/Å^2. Yellow, green, blue and purple represent the intact and degraded nanoparticles at P/Al$_3$ = 0.1*, 0.6 and 1.5, respectively. The spectral resolution is 0.06 eV for the low-loss and 0.8 eV for the core-loss region.*

As EDS, EELS is able to map the elemental distributions of MOFs. **Figure S10** shows the superimposition of phosphorus and carbon maps acquired on degraded MIL-100(Al) at P/Al3 = 0.6*. These maps were obtained separately, by integrating the respective edges after background subtraction. The results agree well with EDS as they show the same anti-correlated distributions of phosphorus and carbon (**Figure 6**, main text). Note that, due to the high electron dose (3.10^4 ē/Å^2), the carbon signature corresponds to degraded linkers.

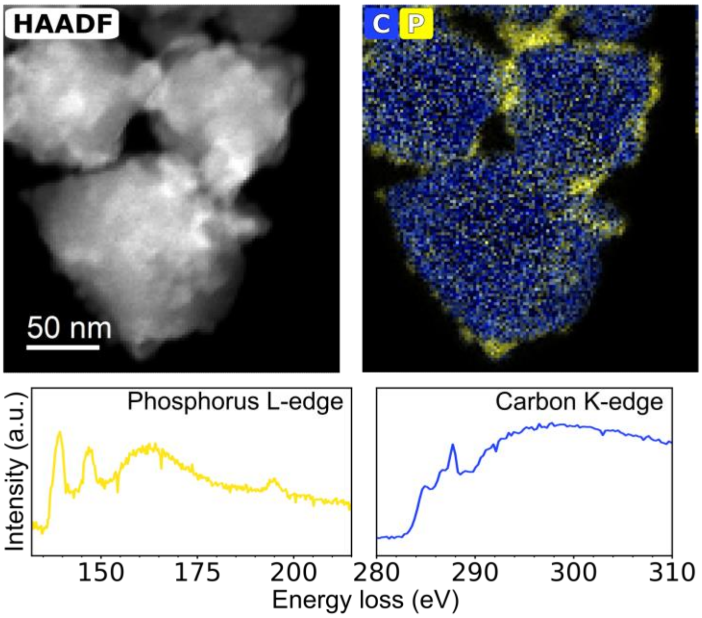

Figure S10. *STEM-HAADF image of degraded MIL-100(Al) at P/Al$_3$ = 0.6*, and the corresponding superimposed EELS elemental map of phosphorus (yellow) and carbon (blue) . The corresponding ionisation edges are shown at the bottom. These data were collected at 3.10^4 $\bar{e}$/Å^2. The spatial resolution is 2 nm. The spectral resolution is 0.5 eV*

REFERENCES

(1) Demšar, J.; Curk, T.; Erjavec, A.; Gorup, Č.; Hočevar, T.; Milutinovič, M.; Možina, M.; Polajnar, M.; Toplak, M.; Starič, A.; Štajdohar, M.; Umek, L.; Žagar, L.; Žbontar, J.; Žitnik, M.; Zupan, B. Orange: Data Mining Toolbox in Python. *J. Mach. Learn. Res.* **2013**, *14* (35), 2349–2353.

(2) Volkringer, C.; Popov, D.; Loiseau, T.; Férey, G.; Burghammer, M.; Riekel, C.; Haouas, M.; Taulelle, F. Synthesis, Single-Crystal X-Ray Microdiffraction, and NMR Characterizations of the Giant Pore Metal-Organic Framework Aluminum Trimesate MIL-100. *Chem. Mater.* **2009**, *21* (24), 5695–5697. https://doi.org/10.1021/cm901983a.

(3) Le Vuong, M. D.; Christodoulou, I.; Porcino, M.; Dong, S.-T.; Lassalle-Kaiser, B.; Haouas, M.; Gref, R.; Martineau-Corcos, C. Degradation Mechanism of Metal–Organic Framework Drug Nanocarriers Studied by Solid-State Nuclear Magnetic Resonance and X-Ray Absorption Near-Edge Structure Spectroscopy. *Chem. Mater.* **2022**, *34* (18), 8178–8189. https://doi.org/10.1021/acs.chemmater.2c01190.

(4) Vuong, D. L. M. Degradation mechanism of nanoparticle-based drug delivery systems: the case of polymer conjugate and metal-organic framework. PhD thesis, Université Paris-Saclay, France, 2022.

(5) Li, X.; Porcino, M.; Qiu, J.; Constantin, D.; Martineau-Corcos, C.; Gref, R. Doxorubicin-Loaded Metal-Organic Frameworks Nanoparticles with Engineered Cyclodextrin Coatings: Insights on Drug Location by Solid State NMR Spectroscopy. *Nanomaterials* **2021**, *11* (4), 945. https://doi.org/10.3390/nano11040945.

(6) Chaupard, M.; Degrouard, J.; Li, X.; Stéphan, O.; Kociak, M.; Gref, R.; de Frutos, M. Nanoscale Multimodal Analysis of Sensitive Nanomaterials by Monochromated STEM-EELS in Low-Dose and Cryogenic Conditions. *ACS Nano* **2023**, *17* (4), 3452–3464. https://doi.org/10.1021/acsnano.2c09571.

(7) Sham, T. K.; Yang, B. X.; Kirz, J.; Tse, J. S. K-Edge near-Edge x-Ray-Absorption Fine Structure of Oxygen- and Carbon-Containing Molecules in the Gas Phase. *Phys. Rev. A* **1989**, *40* (2), 652–669. https://doi.org/10.1103/PhysRevA.40.652.

(8) Colby, R.; Williams, R. E. A.; Carpenter, D. L.; Bagués, N.; Ford, B. R.; McComb, D. W. Identifying and Imaging Polymer Functionality at High Spatial Resolution with Core-Loss EELS. *Ultramicroscopy* **2023**, *246*, 113688. https://doi.org/10.1016/j.ultramic.2023.113688.

Bibliography

[1] The International Agency for Research on Cancer (IARC). Global Cancer Observatory.

[2] Longfa Kou, Yangzom D. Bhutia, Qing Yao, Zhonggui He, Jin Sun, and Vadivel Ganapathy. Transporter-Guided Delivery of Nanoparticles to Improve Drug Permeation across Cellular Barriers and Drug Exposure to Selective Cell Types. *Frontiers in Pharmacology*, 9, 2018.

[3] Elvin Blanco, Haifa Shen, and Mauro Ferrari. Principles of nanoparticle design for overcoming biological barriers to drug delivery. *Nat Biotechnol*, 33(9):941–951, 2015.

[4] Haesun Park, Andrew Otte, and Kinam Park. Evolution of drug delivery systems: From 1950 to 2020 and beyond. *Journal of Controlled Release*, 342:53–65, 2022.

[5] Edgar Pérez-Herrero and Alberto Fernández-Medarde. Advanced targeted therapies in cancer: Drug nanocarriers, the future of chemotherapy. *Eur J Pharm Biopharm*, 93:52–79, 2015.

[6] Romy Ettlinger, Ulrich Lächelt, Ruxandra Gref, Patricia Horcajada, Twan Lammers, Christian Serre, Patrick Couvreur, Russell E. Morris, and Stefan Wuttke. Toxicity of metal–organic framework nanoparticles: from essential analyses to potential applications. *Chem. Soc. Rev.*, 51(2):464–484, 2022.

[7] Shamsul Huda, Md Aftab Alam, and Pramod Kumar Sharma. Smart nanocarriers-based drug delivery for cancer therapy: An innovative and developing strategy. *Journal of Drug Delivery Science and Technology*, 60:102018, 2020.

[8] Yasuhiro Matsumura and Hiroshi Maeda. A New Concept for Macromolecular Therapeutics in Cancer Chemotherapy: Mechanism of Tumoritropic Accumulation of Proteins and the Antitumor Agent Smancs1. *Cancer Research*, 46(12_Part_1):6387–6392, 1986.

[9] Waliul Islam, Takuro Niidome, and Tomohiro Sawa. Enhanced Permeability and Retention Effect as a Ubiquitous and Epoch-Making Phenomenon for the Selective Drug Targeting of Solid Tumors. *Journal of Personalized Medicine*, 12(12):1964, 2022.

[10] Stefania Biffi, Rebecca Voltan, Barbara Bortot, Giorgio Zauli, and Paola Secchiero. Actively targeted nanocarriers for drug delivery to cancer cells. *Expert Opinion on Drug Delivery*, 16(5):481–496, 2019.

[11] Zhengzou Fang, Yanfei Shen, and Daqing Gao. Stimulus-responsive nanocarriers for targeted drug delivery. *New J. Chem.*, 45(10):4534–4544, 2021.

[12] Patricia Horcajada, Christian Serre, María Vallet-Regí, Muriel Sebban, Francis Taulelle, and Gérard Férey. Metal–Organic Frameworks as Efficient Materials for Drug Delivery. *Angewandte Chemie*, 118(36):6120–6124, 2006.

[13] Siyu He, Li Wu, Xue Li, Hongyu Sun, Ting Xiong, Jie Liu, Chengxi Huang, Huipeng Xu, Huimin Sun, Weidong Chen, Ruxandra Gref, and Jiwen Zhang. Metal-organic frameworks for advanced drug delivery. *Acta Pharmaceutica Sinica B*, 11(8):2362–2395, 2021.

[14] Ralph Freund, Orysia Zaremba, Giel Arnauts, Rob Ameloot, Grigorii Skorupskii, Mircea Dincă, Anastasiya Bavykina, Jorge Gascon, Aleksander Ejsmont, Joanna Goscianska, Markus Kalmutzki, Ulrich Lächelt, Evelyn Ploetz, Christian S. Diercks, and Stefan Wuttke. The Current Status of MOF and COF Applications. *Angewandte Chemie Intl Edit*, 60(45):23975–24001, 2021.

[15] Namita Singh, Somayah Qutub, and Niveen M. Khashab. Biocompatibility and biodegradability of metal organic frameworks for biomedical applications. *Journal of Materials Chemistry B*, 9(30):5925–5934, 2021.

[16] Mohamed Eddaoudi, Jaheon Kim, Nathaniel Rosi, David Vodak, Joseph Wachter, Michael O’Keeffe, and Omar M. Yaghi. Systematic Design of Pore Size and Functionality in Isoreticular MOFs and Their Application in Methane Storage. *Science*, 295(5554):469–472, 2002.

[17] Hexiang Deng, Sergio Grunder, Kyle E. Cordova, Cory Valente, Hiroyasu Furukawa, Mohamad Hmadeh, Felipe Gándara, Adam C. Whalley, Zheng Liu, Shunsuke Asahina, Hiroyoshi Kazumori, Michael O’Keeffe, Osamu Terasaki, J. Fraser Stoddart, and Omar M. Yaghi. Large-Pore Apertures in a Series of Metal-Organic Frameworks. *Science*, 336(6084):1018–1023, 2012.

[18] Patricia Horcajada, Ruxandra Gref, Tarek Baati, Phoebe K. Allan, Guillaume Maurin, Patrick Couvreur, Gérard Férey, Russell E. Morris, and Christian Serre. Metal–Organic Frameworks in Biomedicine. *Chem. Rev.*, 112(2):1232–1268, 2012.

[19] Johannes W. M. Osterrieth and David Fairen-Jimenez. Metal–Organic Framework Composites for Theragnostics and Drug Delivery Applications. *Biotechnology Journal*, 16(2):2000005, 2021.

[20] Romain Grall, Tania Hidalgo, Jozo Delic, Alfonso Garcia-Marquez, Sylvie Chevillard, and Patricia Horcajada. In vitro biocompatibility of mesoporous metal (III; Fe, Al, Cr) trimesate MOF nanocarriers. *J. Mater. Chem. B*, 3(42):8279–8292, 2015.

[21] Yuge Feng, Chengliang Wang, Fei Ke, Jianye Zang, and Junfa Zhu. MIL-100(Al) Gels as an Excellent Platform Loaded with Doxorubicin Hydrochloride for pH-Triggered Drug Release and Anticancer Effect. *Nanomaterials*, 8(6):446, 2018.

[22] Valentina Agostoni, Patricia Horcajada, Violeta Rodriguez-Ruiz, Hervé Willaime, Patrick Couvreur, Christian Serre, and Ruxandra Gref. 'Green' fluorine-free mesoporous iron(III) trimesate nanoparticles for drug delivery. *Green Materials*, 1(4):209–217, 2013.

[23] Patricia Horcajada, Tamim Chalati, Christian Serre, Brigitte Gillet, Catherine Sebrie, Tarek Baati, Jarrod F. Eubank, Daniela Heurtaux, Pascal Clayette, Christine Kreuz, Jong-San Chang, Young Kyu Hwang, Veronique Marsaud, Phuong-Nhi Bories, Luc Cynober, Sophie Gil, Gérard Férey, Patrick Couvreur, and Ruxandra Gref. Porous metal–organic-framework nanoscale carriers as a potential platform for drug delivery and imaging. *Nature Materials*, 9(2):172–178, 2010.

[24] Xue Li, Nicolas Semiramoth, Shaun Hall, Virginie Tafani, Jérome Josse, Frederic Laurent, Giuseppina Salzano, Daniel Foulkes, Priscille Brodin, Laleh Majlessi, Nour-Eddine Ghermani, Guillaume Maurin, Patrick Couvreur, Christian Serre, Marie-Françoise Bernet-Camard, Jiwen Zhang, and Ruxandra Gref. Compartmentalized Encapsulation of Two Antibiotics in Porous Nanoparticles: an Efficient Strategy to Treat Intracellular Infections. *Particle & Particle Systems Characterization*, 36(3):1800360, 2019.

[25] Maria Rosaria di Nunzio, Valentina Agostoni, Boiko Cohen, Ruxandra Gref, and Abderrazzak Douhal. A "ship in a bottle" strategy to load a hydrophilic anticancer drug in porous metal organic framework nanoparticles: efficient encapsulation, matrix stabilization, and photodelivery. *J Med Chem*, 57(2):411–420, 2014.

[26] T Chalati, P Horcajada, P Couvreur, C Serre, M Ben Yahia, G Maurin, and R Gref. Porous metal organic framework nanoparticles to address the challenges related to busulfan encapsulation. *Nanomedicine*, 6(10):1683–1695, 2011.

[27] Mahsa Rezaei, Alireza Abbasi, Reyhaneh Varshochian, Rassoul Dinarvand, and Mahmood Jeddi-Tehrani. NanoMIL-100(Fe) containing docetaxel for breast cancer therapy. *Artificial Cells, Nanomedicine, and Biotechnology*, 46(7):1390–1401, 2018.

[28] Cristina Tamames-Tabar, Denise Cunha, Edurne Imbuluzqueta, Florence Ragon, Christian Serre, María J. Blanco-Prieto, and Patricia Horcajada. Cytotoxicity of nanoscaled metal–organic frameworks. *J. Mater. Chem. B*, 2(3):262–271, 2013.

[29] Àngels Ruyra, Amirali Yazdi, Jordi Espín, Arnau Carné-Sánchez, Nerea Roher, Julia Lorenzo, Inhar Imaz, and Daniel Maspoch. Synthesis, Culture Medium Stability, and In Vitro and In Vivo Zebrafish Embryo Toxicity of Metal–Organic Framework Nanoparticles. *Chemistry – A European Journal*, 21(6):2508–2518, 2015.

[30] Tarek Baati, Leila Njim, Fadoua Neffati, Abdelhamid Kerkeni, Muriel Bouttemi, Ruxandra Gref, Mohamed Fadhel Najjar, Abdelfateh Zakhama, Patrick Couvreur, Christian Serre, and

Patricia Horcajada. In depth analysis of the in vivo toxicity of nanoparticles of porous iron(III) metal–organic frameworks. *Chem. Sci.*, 4(4):1597–1607, 2013.

[31] T. Simon-Yarza, T. Baati, F. Neffati, L. Njim, P. Couvreur, C. Serre, R. Gref, M. Fadhel Najjar, A. Zakhama, and P. Horcajada. In vivo behavior of MIL-100 nanoparticles at early times after intravenous administration. *Int J Pharm*, 511(2):1042–1047, 2016.

[32] M. T. Simon-Yarza, T. Baati, A. Paci, L. L. Lesueur, A. Seck, M. Chiper, R. Gref, C. Serre, P. Couvreur, and P. Horcajada. Antineoplastic busulfan encapsulated in a metal organic framework nanocarrier: first in vivo results. *J. Mater. Chem. B*, 4(4):585–588, 2016.

[33] Xue Li, Erika Porcel, Mario Menendez-Miranda, Jingwen Qiu, Xiaomin Yang, Christian Serre, Alexandra Pastor, Didier Desmaële, Sandrine Lacombe, and Ruxandra Gref. Highly Porous Hybrid Metal–Organic Nanoparticles Loaded with Gemcitabine Monophosphate: a Multimodal Approach to Improve Chemo- and Radiotherapy. *ChemMedChem*, 15(3):274–283, 2020.

[34] Fritz Haber, Joseph Weiss, and William Jackson Pope. The catalytic decomposition of hydrogen peroxide by iron salts. *Proceedings of the Royal Society of London. Series A - Mathematical and Physical Sciences*, 147(861):332–351, 1997.

[35] H. J. H. Fenton. LXXIII.—Oxidation of tartaric acid in presence of iron. *J. Chem. Soc., Trans.*, 65(0):899–910, 1894.

[36] Stefan Wuttke, Andreas Zimpel, Thomas Bein, Simone Braig, Katharina Stoiber, Angelika Vollmar, Dominik Müller, Kirsten Haastert-Talini, Jörn Schaeske, Meike Stiesch, Gesa Zahn, Alexander Mohmeyer, Peter Behrens, Oliver Eickelberg, Deniz A. Bölükbas, and Silke Meiners. Validating Metal-Organic Framework Nanoparticles for Their Nanosafety in Diverse Biomedical Applications. *Advanced Healthcare Materials*, 6(2):1600818, 2017.

[37] Ting Xue, Caina Xu, Yu Wang, Yanbing Wang, Huayu Tian, and Yingchao Zhang. Doxorubicin-loaded nanoscale metal–organic framework for tumor-targeting combined chemotherapy and chemodynamic therapy. *Biomater. Sci.*, 7(11):4615–4623, 2019.

[38] Gongsen Chen, Xin Leng, Juyuan Luo, Longtai You, Changhai Qu, Xiaoxv Dong, Hongliang Huang, Xingbin Yin, and Jian Ni. In Vitro Toxicity Study of a Porous Iron(III) Metal–Organic Framework. *Molecules*, 24(7):1211, 2019.

[39] JiaRui Bi, Yu Zheng, LiQing Fang, YuCheng Guan, AiQing Ma, and Jian Wu. Nano-Sized MIL-100(Fe) as a Carrier Material for Nitidine Chloride Reduces Toxicity and Enhances Anticancer Effects In Vitro. *J Inorg Organomet Polym*, 30(9):3388–3395, 2020.

[40] Seyed Dariush Taherzade, Sara Rojas, Janet Soleimannejad, and Patricia Horcajada. Combined Cutaneous Therapy Using Biocompatible Metal-Organic Frameworks. *Nanomaterials*,

10(12):2296, 2020.

[41] M. T. Marcos-Almaraz, R. Gref, V. Agostoni, C. Kreuz, P. Clayette, C. Serre, P. Couvreur, and P. Horcajada. Towards improved HIV-microbicide activity through the co-encapsulation of NRTI drugs in biocompatible metal organic framework nanocarriers. *J. Mater. Chem. B*, 5(43):8563–8569, 2017.

[42] Violeta Rodriguez-Ruiz, Andrei Maksimenko, Resmi Anand, Sandra Monti, Valentina Agostoni, Patrick Couvreur, Maria Lampropoulou, Konstantina Yannakopoulou, and Ruxandra Gref. Efficient "green" encapsulation of a highly hydrophilic anticancer drug in metal–organic framework nanoparticles. *Journal of Drug Targeting*, 23(7-8):759–767, 2015.

[43] Teresa Simon-Yarza, Mónica Giménez-Marqués, Rhizlaine Mrimi, Angelika Mielcarek, Ruxandra Gref, Patricia Horcajada, Christian Serre, and Patrick Couvreur. A Smart Metal–Organic Framework Nanomaterial for Lung Targeting. *Angewandte Chemie*, 129(49):15771–15775, 2017.

[44] Mai Dang Le Vuong, Ioanna Christodoulou, Marianna Porcino, Si-Thanh Dong, Benedikt Lassalle-Kaiser, Mohamed Haouas, Ruxandra Gref, and Charlotte Martineau-Corcos. Degradation Mechanism of Metal–Organic Framework Drug Nanocarriers Studied by Solid-State Nuclear Magnetic Resonance and X-ray Absorption Near-Edge Structure Spectroscopy. *Chem. Mater.*, 34(18):8178–8189, 2022.

[45] Marianna Porcino, Ioanna Christodoulou, Mai Dang Le Vuong, Ruxandra Gref, and Charlotte Martineau-Corcos. New insights on the supramolecular structure of highly porous core–shell drug nanocarriers using solid-state NMR spectroscopy. *RSC Adv.*, 9(56):32472–32475, 2019.

[46] Xue Li, Marianna Porcino, Jingwen Qiu, Doru Constantin, Charlotte Martineau-Corcos, and Ruxandra Gref. Doxorubicin-Loaded Metal-Organic Frameworks Nanoparticles with Engineered Cyclodextrin Coatings: Insights on Drug Location by Solid State NMR Spectroscopy. *Nanomaterials*, 11(4):945, 2021.

[47] Alfonso García Márquez, Aude Demessence, Ana Eva Platero-Prats, Daniela Heurtaux, Patricia Horcajada, Christian Serre, Jong-San Chang, Gérard Férey, Victor Antonio de la Peña-O'Shea, Cédric Boissière, David Grosso, and Clément Sanchez. Green Microwave Synthesis of MIL-100(Al, Cr, Fe) Nanoparticles for Thin-Film Elaboration. *European Journal of Inorganic Chemistry*, 2012(32):5165–5174, 2012.

[48] Valentina Agostoni, Tamim Chalati, Patricia Horcajada, Hervé Willaime, Resmi Anand, Nicolas Semiramoth, Tarek Baati, Shaun Hall, Guillaume Maurin, Hélène Chacun, Kawthar Bouchemal, Charlotte Martineau, Francis Taulelle, Patrick Couvreur, Christine Rogez-Kreuz, Pascal Clayette, Sandra Monti, Christian Serre, and Ruxandra Gref. Towards an Improved

anti-HIV Activity of NRTI via Metal–Organic Frameworks Nanoparticles. *Advanced Healthcare Materials*, 2(12):1630–1637, 2013.

[49] Barbara Roda, Valentina Marassi, Andrea Zattoni, Francesco Borghi, Resmi Anand, Valentina Agostoni, Ruxandra Gref, Pierluigi Reschiglian, and Sandra Monti. Flow field-flow fractionation and multi-angle light scattering as a powerful tool for the characterization and stability evaluation of drug-loaded metal–organic framework nanoparticles. *Anal Bioanal Chem*, 410(21):5245–5253, 2018.

[50] Valentina Agostoni, Resmi Anand, Sandra Monti, Shaun Hall, Guillaume Maurin, Patricia Horcajada, Christian Serre, Kawthar Bouchemal, and Ruxandra Gref. Impact of phosphorylation on the encapsulation of nucleoside analogues within porous iron(III) metal–organic framework MIL-100(Fe) nanoparticles. *J. Mater. Chem. B*, 1(34):4231–4242, 2013.

[51] Jarrod F. Eubank, Paul S. Wheatley, Gaëlle Lebars, Alistair C. McKinlay, Hervé Leclerc, Patricia Horcajada, Marco Daturi, Alexandre Vimont, Russell E. Morris, and Christian Serre. Porous, rigid metal(III)-carboxylate metal-organic frameworks for the delivery of nitric oxide. *APL Materials*, 2(12):124112, 2014.

[52] Seyed Dariush Taherzade, Janet Soleimannejad, and Aliakbar Tarlani. Application of Metal-Organic Framework Nano-MIL-100(Fe) for Sustainable Release of Doxycycline and Tetracycline. *Nanomaterials*, 7(8):215, 2017.

[53] Meta A. Simon, Erlina Anggraeni, Felycia Edi Soetaredjo, Shella Permasari Santoso, Wenny Irawaty, Truong Chi Thanh, Sandy Budi Hartono, Maria Yuliana, and Suryadi Ismadji. Hydrothermal Synthesize of HF-Free MIL-100(Fe) for Isoniazid-Drug Delivery. *Sci Rep*, 9(1):16907, 2019.

[54] Resmi Anand, Francesco Borghi, Francesco Manoli, Ilse Manet, Valentina Agostoni, Pierluigi Reschiglian, Ruxandra Gref, and Sandra Monti. Host–Guest Interactions in Fe(III)-Trimesate MOF Nanoparticles Loaded with Doxorubicin. *J. Phys. Chem. B*, 118(29):8532–8539, 2014.

[55] Abhik Bhattacharjee, Mihir Kumar Purkait, and Sasidhar Gumma. Doxorubicin Loading Capacity of MIL-100(Fe): Effect of Synthesis Conditions. *J Inorg Organomet Polym*, 30(7):2366–2375, 2020.

[56] X. Li, L. Lachmanski, S. Safi, S. Sene, C. Serre, J. M. Grenèche, J. Zhang, and R. Gref. New insights into the degradation mechanism of metal-organic frameworks drug carriers. *Scientific Reports*, 7(1):13142, 2017.

[57] Sara Rojas, Francisco J. Carmona, Carmen R. Maldonado, Elisa Barea, and Jorge A. R. Navarro. RAPTA-C incorporation and controlled delivery from MIL-100(Fe) nanoparticles. *New J. Chem.*,

40(7):5690–5694, 2016.

[58] Ioanna Christodoulou, Pengbo Lyu, Carla Vieira Soares, Gilles Patriarche, Christian Serre, Guillaume Maurin, and Ruxandra Gref. Nanoscale Iron-Based Metal–Organic Frameworks: Incorporation of Functionalized Drugs and Degradation in Biological Media. *International Journal of Molecular Sciences*, 24(4):3362, 2023.

[59] Sara Rojas, Isabel Colinet, Denise Cunha, Tania Hidalgo, Fabrice Salles, Christian Serre, Nathalie Guillou, and Patricia Horcajada. Toward Understanding Drug Incorporation and Delivery from Biocompatible Metal–Organic Frameworks in View of Cutaneous Administration. *ACS Omega*, 3(3):2994–3003, 2018.

[60] Alfonso García Márquez, Tania Hidalgo, Hugo Lana, Denise Cunha, María Jose Blanco-Prieto, Carmen Álvarez Lorenzo, Cédric Boissière, Clément Sánchez, Christian Serre, and Patricia Horcajada. Biocompatible polymer–metal–organic framework composite patches for cutaneous administration of cosmetic molecules. *J. Mater. Chem. B*, 4(43):7031–7040, 2016.

[61] Brenda Singco, Li-Hao Liu, Ya-Ting Chen, Yung-Han Shih, Hsi-Ya Huang, and Chia-Her Lin. Approaches to drug delivery: Confinement of aspirin in MIL-100(Fe) and aspirin in the de novo synthesis of metal–organic frameworks. *Microporous and Mesoporous Materials*, 223:254–260, 2016.

[62] Dang Le Mai Vuong. *Degradation mechanism of nanoparticle-based drug delivery systems: the case of polymer conjugate and metal-organic framework*. PhD thesis, Université Paris-Saclay, France, 2022.

[63] Ioanna Christodoulou, Tom Bourguignon, Xue Li, Gilles Patriarche, Christian Serre, Christian Marlière, and Ruxandra Gref. Degradation Mechanism of Porous Metal-Organic Frameworks by In Situ Atomic Force Microscopy. *Nanomaterials*, 11(3):722, 2021.

[64] Elena Bellido, Tania Hidalgo, Maria Victoria Lozano, Mazheva Guillevic, Rosana Simón-Vázquez, Manuel J. Santander-Ortega, África González-Fernández, Christian Serre, Maria J. Alonso, and Patricia Horcajada. Heparin-Engineered Mesoporous Iron Metal-Organic Framework Nanoparticles: Toward Stealth Drug Nanocarriers. *Advanced Healthcare Materials*, 4(8):1246–1257, 2015.

[65] Elena Bellido, Mazheva Guillevic, Tania Hidalgo, Manuel J. Santander-Ortega, Christian Serre, and Patricia Horcajada. Understanding the Colloidal Stability of the Mesoporous MIL-100(Fe) Nanoparticles in Physiological Media. *Langmuir*, 30(20):5911–5920, 2014.

[66] David B. Williams and C. Barry Carter. *Transmission Electron Microscopy: A Textbook for Materials Science*. Springer Science & Business Media, 2009.

[67] R. F. Egerton. Organic mass loss at 100 K and 300 K. *Journal of Microscopy*, 126(1):95–100, 1982.

[68] M. K. Lamvik, A. D. Magid, S. D. Davilla, and L. Córdova. Temperature directly affects the rate of irradiation-induced mass loss from phosphatidylcholine multilayers. *Ultramicroscopy*, 35(3):351–356, 1991.

[69] R. M. Glaeser. Chapter Two - Specimen Behavior in the Electron Beam. In R. A. Crowther, editor, *Methods in Enzymology*, volume 579 of *The Resolution Revolution: Recent Advances In cryoEM*, pages 19–50. Academic Press, 2016.

[70] Dganit Danino. Cryo-TEM of soft molecular assemblies. *Current Opinion in Colloid & Interface Science*, 17(6):316–329, 2012.

[71] Andy Brown and Nicole Hondow. Chapter 4 - Electron Microscopy of Nanoparticles in Cells. In Huw Summers, editor, *Frontiers of Nanoscience*, volume 5 of *Nanomedicine*, pages 95–120. Elsevier, 2013.

[72] Vladan Lučić, Alexander Rigort, and Wolfgang Baumeister. Cryo-electron tomography: The challenge of doing structural biology in situ. *Journal of Cell Biology*, 202(3):407–419, 2013.

[73] Phoebe L. Stewart. Cryo-electron microscopy and cryo-electron tomography of nanoparticles. *WIREs Nanomedicine and Nanobiotechnology*, 9(2):e1417, 2017.

[74] Rebecca F. Thompson, Matt Walker, C. Alistair Siebert, Stephen P. Muench, and Neil A. Ranson. An introduction to sample preparation and imaging by cryo-electron microscopy for structural biology. *Methods*, 100:3–15, 2016.

[75] James L. Hart, Andrew C. Lang, Asher C. Leff, Paolo Longo, Colin Trevor, Ray D. Twesten, and Mitra L. Taheri. Direct Detection Electron Energy-Loss Spectroscopy: A Method to Push the Limits of Resolution and Sensitivity. *Sci Rep*, 7(1):8243, 2017.

[76] Anqi Zheng, Kuibo Yin, Rui Pan, Mingyun Zhu, Yuwei Xiong, and Litao Sun. Research Progress on Metal–Organic Frameworks by Advanced Transmission Electron Microscopy. *Nanomaterials*, 13(11):1742, 2023.

[77] Ivan Lazić, Maarten Wirix, Max Leo Leidl, Felix de Haas, Daniel Mann, Maximilian Beckers, Evgeniya V. Pechnikova, Knut Müller-Caspary, Ricardo Egoavil, Eric G. T. Bosch, and Carsten Sachse. Single-particle cryo-EM structures from iDPC–STEM at near-atomic resolution. *Nat Methods*, 19(9):1126–1136, 2022.

[78] Xudong Pei, Liqi Zhou, Chen Huang, Mark Boyce, Judy S. Kim, Emanuela Liberti, Yiming Hu, Takeo Sasaki, Peter D. Nellist, Peijun Zhang, David I. Stuart, Angus I. Kirkland, and Peng

Wang. Cryogenic electron ptychographic single particle analysis with wide bandwidth information transfer. *Nat Commun*, 14(1):3027, 2023.

[79] M.A. Aronova and R.D. Leapman. Development of Electron Energy Loss Spectroscopy in the Biological Sciences. *MRS Bull*, 37(1):53–62, 2012.

[80] O. L. Krivanek, N. Dellby, J. A. Hachtel, J. C. Idrobo, M. T. Hotz, B. Plotkin-Swing, N. J. Bacon, A. L. Bleloch, G. J. Corbin, M. V. Hoffman, C. E. Meyer, and T. C. Lovejoy. Progress in ultrahigh energy resolution EELS. *Ultramicroscopy*, 203:60–67, 2019.

[81] Richard D. Leapman and Songquan Sun. Cryo-electron energy loss spectroscopy: observations on vitrified hydrated specimens and radiation damage. *Ultramicroscopy*, 59(1):71–79, 1995.

[82] S. Q. Sun, S-L. Shi, J. A. Hunt, and R. D. Leapman. Quantitative water mapping of cryosectioned cells by electron energy-loss spectroscopy. *Journal of Microscopy*, 177(1):18–30, 1995.

[83] Alioscka Sousa, Jaap Schut, Joachim Kohn, and Matthew Libera. Nanoscale Morphological Changes during Hydrolytic Degradation and Erosion of a Bioresorbable Polymer. *Macromolecules*, 39(21):7306–7312, 2006.

[84] Alioscka Sousa, Abdelaziz Aitouchen, and Matthew Libera. Water mapping in hydrated soft materials. *Ultramicroscopy*, 106(2):130–145, 2006.

[85] Sergey Yakovlev and Matthew Libera. Dose-limited spectroscopic imaging of soft materials by low-loss EELS in the scanning transmission electron microscope. *Micron*, 39(6):734–740, 2008.

[86] Partha Pratim Das, Giulio Guzzinati, Catalina Coll, Alejandro Gomez Perez, Stavros Nicolopoulos, Sonia Estrade, Francesca Peiro, Johan Verbeeck, Aikaterini A. Zompra, and Athanassios S. Galanis. Reliable Characterization of Organic & Pharmaceutical Compounds with High Resolution Monochromated EEL Spectroscopy. *Polymers*, 12(7):1434, 2020.

[87] Ginam Kim, Alioscka Sousa, Deborah Meyers, and Matthew Libera. Nanoscale Composition of Biphasic Polymer Nanocolloids in Aqueous Suspension. *Microscopy and Microanalysis*, 14(5):459–468, 2008.

[88] Changhe Guo, Frances I. Allen, Youngmin Lee, Thinh P. Le, Chengyu Song, Jim Ciston, Andrew M. Minor, and Enrique D. Gomez. Probing Local Electronic Transitions in Organic Semiconductors through Energy-Loss Spectrum Imaging in the Transmission Electron Microscope. *Advanced Functional Materials*, 25(38):6071–6076, 2015.

[89] Ralm G. Ricarte, Timothy P. Lodge, and Marc A. Hillmyer. Nanoscale Concentration Quantifi-

cation of Pharmaceutical Actives in Amorphous Polymer Matrices by Electron Energy-Loss Spectroscopy. *Langmuir*, 32(29):7411–7419, 2016.

[90] Peter Rez, Toshihiro Aoki, Katia March, Dvir Gur, Ondrej L. Krivanek, Niklas Dellby, Tracy C. Lovejoy, Sharon G. Wolf, and Hagai Cohen. Damage-free vibrational spectroscopy of biological materials in the electron microscope. *Nat Commun*, 7(1):10945, 2016.

[91] Diane M. Haiber and Peter A. Crozier. Nanoscale Probing of Local Hydrogen Heterogeneity in Disordered Carbon Nitrides with Vibrational Electron Energy-Loss Spectroscopy. *ACS Nano*, 12(6):5463–5472, 2018.

[92] Jordan A. Hachtel, Jingsong Huang, Ilja Popovs, Santa Jansone-Popova, Jong K. Keum, Jacek Jakowski, Tracy C. Lovejoy, Niklas Dellby, Ondrej L. Krivanek, and Juan Carlos Idrobo. Identification of site-specific isotopic labels by vibrational spectroscopy in the electron microscope. *Science*, 363(6426):525–528, 2019.

[93] Sean M. Collins, Demie M. Kepaptsoglou, Jingwei Hou, Christopher W. Ashling, Guillaume Radtke, Thomas D. Bennett, Paul A. Midgley, and Quentin M. Ramasse. Functional Group Mapping by Electron Beam Vibrational Spectroscopy from Nanoscale Volumes. *Nano Lett.*, 20(2):1272–1279, 2020.

[94] Katia March, Kartik Venkatraman, Chloe Du Truong, Dewight Williams, Po-Lin Chiu, and Peter Rez. Protein secondary structure signatures from energy loss spectra recorded in the electron microscope. *Journal of Microscopy*, 282(3):215–223, 2021.

[95] Supriya Ghosh, Hwanhui Yun, Prashant Kumar, Sabrina Conrad, Michael Tsapatsis, and K. Andre Mkhoyan. Two Distinct Stages of Structural Modification of ZIF-L MOF under Electron-Beam Irradiation. *Chem. Mater.*, 33(14):5681–5689, 2021.

[96] Zino J. W. A. Leijten, Maarten J. M. Wirix, Sorin Lazar, Wouter Verhoeven, O. Jom Luiten, Gijsbertus de With, and Heiner Friedrich. Nanoscale chemical analysis of beam-sensitive polymeric materials by cryogenic electron microscopy. *Journal of Polymer Science*, 59(12):1221–1231, 2021.

[97] Ruchi Pal, Laure Bourgeois, Matthew Weyland, Arun K. Sikder, Kei Saito, Alison M. Funston, and Jayesh R. Bellare. Chemical Fingerprinting of Polymers Using Electron Energy-Loss Spectroscopy. *ACS Omega*, 6(37):23934–23942, 2021.

[98] Robert Colby, Robert E. A. Williams, Donald L Carpenter, Núria Bagués, Brittany R. Ford, and David W. McComb. Identifying and imaging polymer functionality at high spatial resolution with core-loss EELS. *Ultramicroscopy*, 246:113688, 2023.

[99] CSD MOF Collection | CCDC.

[100] Patricia Horcajada, Suzy Surblé, Christian Serre, Do-Young Hong, You-Kyong Seo, Jong-San Chang, Jean-Marc Grenèche, Irene Margiolaki, and Gérard Férey. Synthesis and catalytic properties of MIL-100(Fe), an iron(III) carboxylate with large pores. *Chem. Commun.*, (27):2820–2822, 2007.

[101] Christophe Volkringer, Dimitry Popov, Thierry Loiseau, Gérard Férey, Manfred Burghammer, Christian Riekel, Mohamed Haouas, and Francis Taulelle. Synthesis, Single-Crystal X-ray Microdiffraction, and NMR Characterizations of the Giant Pore Metal-Organic Framework Aluminum Trimesate MIL-100. *Chem. Mater.*, 21(24):5695–5697, 2009.

[102] William Morris, Shunzhi Wang, David Cho, Evelyn Auyeung, Peng Li, Omar K. Farha, and Chad A. Mirkin. Role of Modulators in Controlling the Colloidal Stability and Polydispersity of the UiO-66 Metal–Organic Framework. *ACS Appl. Mater. Interfaces*, 9(39):33413–33418, 2017.

[103] Mengli Ding, Wenbo Liu, and Ruxandra Gref. Nanoscale MOFs: From synthesis to drug delivery and theranostics applications. *Advanced Drug Delivery Reviews*, 190:114496, 2022.

[104] Tarek Alammar, Ihor Z. Hlova, Shalabh Gupta, Viktor Balema, Vitalij K. Pecharsky, and Anja-Verena Mudring. Luminescence properties of mechanochemically synthesized lanthanide containing MIL-78 MOFs. *Dalton Transactions*, 47(22):7594–7601, 2018.

[105] Ravi Nivetha, Kannan Gothandapani, Vimala Raghavan, George Jacob, Raja Sellappan, Preetam Bhardwaj, Sudhagar Pitchaimuthu, Arunachala Nadar Mada Kannan, Soon Kwan Jeong, and Andrews Nirmala Grace. Highly Porous MIL-100(Fe) for the Hydrogen Evolution Reaction (HER) in Acidic and Basic Media. *ACS Omega*, 5(30):18941–18949, 2020.

[106] Pedro Henrique Morais Andrade. *Synthesis of TiO2@MOF composites for the photodegradation of organic pollutants*. Master dissertation, Universidade Federal de Minas Gerais, Brasil, 2021.

[107] R. F. Egerton. *Electron Energy-Loss Spectroscopy in the Electron Microscope*. Springer Science & Business Media, 2011.

[108] Maximilian Haider, Herald Rose, Stephan Uhlemann, Bernd Kabius, and Knut Urban. Towards 0.1 nm resolution with the first spherically corrected transmission electron microscope. *Microscopy*, 47(5):395–405, 1998.

[109] R.f. Egerton. Mechanisms of radiation damage in beam-sensitive specimens, for TEM accelerating voltages between 10 and 300 kV. *Microscopy Research and Technique*, 75(11):1550–1556, 2012.

[110] R. F. Egerton. Radiation damage to organic and inorganic specimens in the TEM. *Micron*, 119:72–87, 2019.

[111] Martha Ilett, Mark S'ari, Helen Freeman, Zabeada Aslam, Natalia Koniuch, Maryam Afzali, James Cattle, Robert Hooley, Teresa Roncal-Herrero, Sean M. Collins, Nicole Hondow, Andy Brown, and Rik Brydson. Analysis of complex, beam-sensitive materials by transmission electron microscopy and associated techniques. *Philosophical Transactions of the Royal Society A: Mathematical, Physical and Engineering Sciences*, 378(2186):20190601, 2020.

[112] R. F. Egerton, S. Lazar, and M. Libera. Delocalized radiation damage in polymers. *Micron*, 43(1):2–7, 2012.

[113] J. Dubochet, J. Lepault, R. Freeman, J. A. Berriman, and J.-C. Homo. Electron microscopy of frozen water and aqueous solutions. *Journal of Microscopy*, 128(3):219–237, 1982.

[114] R. Kilaas. Optimal and near-optimal filters in high-resolution electron microscopy. *Journal of Microscopy*, 190(1-2):45–51, 1998.

[115] D. R. G. Mitchell. HRTEM Filter.

[116] C. Jeanguillaume, C. Colliex, P. Ballongue, and M. Teneé. New STEM multisignal imaging modes, made accessible through the evaluation of detection efficiencies. *Ultramicroscopy*, 45(2):205–217, 1992.

[117] Hervé Abdi and Lynne J. Williams. Principal component analysis. *WIREs Computational Statistics*, 2(4):433–459, 2010.

[118] Francisco de la Peña, Eric Prestat, Vidar Tonaas Fauske, Pierre Burdet, Jonas Lähnemann, Tom Furnival, Petras Jokubauskas, Magnus Nord, Tomas Ostasevicius, Katherine E. MacArthur, Duncan N. Johnstone, Mike Sarahan, Thomas Aarholt, Joshua Taillon, pquinn dls, Vadim Migunov, Alberto Eljarrat, Jan Caron, Timothy Poon, Stefano Mazzucco, Carter Francis, Ben Martineau, actions user, Suhas Somnath, Tom Slater, Nicolas Tappy, Michael Walls, Niels Cautaerts, Florian Winkler, and DENSmerijn. hyperspy/hyperspy: Release v1.6.5, 2021.

[119] A. Gloter, A. Douiri, M. Tencé, and C. Colliex. Improving energy resolution of EELS spectra: an alternative to the monochromator solution. *Ultramicroscopy*, 96(3):385–400, 2003.

[120] Lingmei Liu, Daliang Zhang, Yihan Zhu, and Yu Han. Bulk and local structures of metal–organic frameworks unravelled by high-resolution electron microscopy. *Commun Chem*, 3(1):1–14, 2020.

[121] Ralph G. Pearson. Hard and Soft Acids and Bases. *J. Am. Chem. Soc.*, 85(22):3533–3539, 1963.

[122] D. S. Gesto, N. M.F.S.A. Cerqueira, P. A. Fernandes, and M. J. Ramos. Gemcitabine: A Critical Nucleoside for Cancer Therapy. *Current Medicinal Chemistry*, 19(7):1076–1087, 2012.

[123] Preeti Kush, Tania Bajaj, Manjot Kaur, Jitender Madan, Upendra Kumar Jain, Parveen Kumar, Akash Deep, and Ki-Hyun Kim. Biodistribution and Pharmacokinetic Study of Gemcitabine Hydrochloride Loaded Biocompatible Iron-Based Metal Organic Framework. *J Inorg Organomet Polym*, 30(8):2827–2841, 2020.

[124] Maeva Chaupard, Jéril Degrouard, Xiaoyan Li, Odile Stéphan, Mathieu Kociak, Ruxandra Gref, and Marta de Frutos. Nanoscale Multimodal Analysis of Sensitive Nanomaterials by Monochromated STEM-EELS in Low-Dose and Cryogenic Conditions. *ACS Nano*, 17(4):3452–3464, 2023.

[125] D. Voet, W. B. Gratzer, R. A. Cox, and Paul Doty. Absorption spectra of nucleotides, polynucleotides, and nucleic acids in the far ultraviolet. *Biopolymers*, 1(3):193–208, 1963.

[126] Marin Sapunar, Wolfgang Domcke, and Nađa Došlić. UV absorption spectra of DNA bases in the 350–190 nm range: assignment and state specific analysis of solvation effects. *Phys. Chem. Chem. Phys.*, 21(41):22782–22793, 2019.

[127] Kurt Kummer, Denis V. Vyalikh, Gianina Gavrila, Alexei B. Preobrajenski, Alfred Kick, Martin Bönsch, Michael Mertig, and Serguei L. Molodtsov. Electronic Structure of Genomic DNA: A Photoemission and X-ray Absorption Study. *J. Phys. Chem. B*, 114(29):9645–9652, 2010.

[128] Yan Zubavichus, Andrey Shaporenko, Vladimir Korolkov, Michael Grunze, and Michael Zharnikov. X-ray Absorption Spectroscopy of the Nucleotide Bases at the Carbon, Nitrogen, and Oxygen K-Edges. *J. Phys. Chem. B*, 112(44):13711–13716, 2008.

[129] Zhenyu Li, Darius Abramavicius, Wei Zhuang, and Shaul Mukamel. Two-dimensional electronic correlation spectroscopy of the n$\pi^{\ast}$ and $\pi\pi^{\ast} protein backbone transitions: A simulation study. *Chemical Physics*, 341(1):29–36, 2007.

[130] Jacob Stewart-Ornstein, Adam P. Hitchcock, Daniel Hernández Cruz, Peter Henklein, Joerg Overhage, Kai Hilpert, John D. Hale, and Robert E. W. Hancock. Using Intrinsic X-ray Absorption Spectral Differences To Identify and Map Peptides and Proteins. *J. Phys. Chem. B*, 111(26):7691–7699, 2007.

[131] A. P. Hitchcock, S. G. Urquhart, and E. G. Rightor. Inner-shell spectroscopy of benzaldehyde, terephthalaldehyde, ethylbenzoate, terephthaloyl chloride and phosgene: models for core excitation of poly(ethylene terephthalate). *J. Phys. Chem.*, 96(22):8736–8750, 1992.

[132] K Varlot, J. M Martin, and C Quet. EELS analysis of PMMA at high spatial resolution. *Micron*, 32(4):371–378, 2001.

[133] Brian J. Ciliax, Kenneth L. Kirk, and Richard D. Leapman. Radiation damage of fluorinated organic compounds measured by parallel electron energy loss spectroscopy. *Ultramicroscopy*,

48(1):13–25, 1993.

[134] Fumihiko Matsui, Han Woong Yeom, Iwao Matsuda, and Toshiaki Ohta. Adsorption and reaction of acetylene and ethylene on the $\mathrm{Si}(001)2\ifmmode\times\else\texttimes\fi{}1$ surface. *Phys. Rev. B*, 62(8):5036–5044, 2000.

[135] S. C. B. Myneni. Soft X-ray Spectroscopy and Spectromicroscopy Studies of Organic Molecules in the Environment. *Reviews in Mineralogy and Geochemistry*, 49(1):485–579, 2002. Number: 1.

[136] T. K. Sham, B. X. Yang, J. Kirz, and J. S. Tse. K-edge near-edge x-ray-absorption fine structure of oxygen- and carbon-containing molecules in the gas phase. *Phys. Rev. A*, 40(2):652–669, 1989.

[137] M. A. Aronova, A. A. Sousa, and R. D. Leapman. EELS characterization of radiolytic products in frozen samples. *Micron*, 42(3):252–256, 2011.

[138] Yves Auad, Michael Walls, Jean-Denis Blazit, Odile Stéphan, Luiz H. G. Tizei, Mathieu Kociak, Francisco De la Peña, and Marcel Tencé. Event-based hyperspectral EELS: towards nanosecond temporal resolution. *Ultramicroscopy*, 239:113539, 2022.

[139] Elisah J. VandenBussche and David J. Flannigan. Reducing Radiation Damage in Soft Matter with Femtosecond-Timed Single-Electron Packets. *Nano Lett.*, 19(9):6687–6694, 2019.

[140] Alberto Zobelli, Steffi Y. Woo, Anna Tararan, Luiz H. G. Tizei, Nathalie Brun, Xiaoyan Li, Odile Stéphan, Mathieu Kociak, and Marcel Tencé. Spatial and spectral dynamics in STEM hyperspectral imaging using random scan patterns. *Ultramicroscopy*, 212:112912, 2020.

[141] R. F. Egerton. Control of radiation damage in the TEM. *Ultramicroscopy*, 127:100–108, 2013.

[142] Ilse Hurbain and Martin Sachse. The future is cold: cryo-preparation methods for transmission electron microscopy of cells. *Biology of the Cell*, 103(9):405–420, 2011.

[143] You-Kyong Seo, Ji Woong Yoon, Ji Sun Lee, U-Hwang Lee, Young Kyu Hwang, Chul-Ho Jun, Patricia Horcajada, Christian Serre, and Jong-San Chang. Large scale fluorine-free synthesis of hierarchically porous iron(III) trimesate MIL-100(Fe) with a zeolite MTN topology. *Microporous and Mesoporous Materials*, 157:137–145, 2012.

[144] V. Agostoni, P. Horcajada, M. Noiray, M. Malanga, A. Aykaç, L. Jicsinszky, A. Vargas-Berenguel, N. Semiramoth, S. Daoud-Mahammed, V. Nicolas, C. Martineau, F. Taulelle, J. Vigneron, A. Etcheberry, C. Serre, and R. Gref. A “green” strategy to construct non-covalent, stable and bioactive coatings on porous MOF nanoparticles. *Sci Rep*, 5(1):7925, 2015.

[145] Xue Li. *"Cage" Nano and Micro-particles for Biomedical Applications*. PhD thesis, Université Paris-Saclay, France, 2017.

[146] Janez Demšar, Tomaž Curk, Aleš Erjavec, Črt Gorup, Tomaž Hočevar, Mitar Milutinovič, Martin Možina, Matija Polajnar, Marko Toplak, Anže Starič, Miha Štajdohar, Lan Umek, Lan Žagar, Jure Žbontar, Marinka Žitnik, and Blaž Zupan. Orange: Data Mining Toolbox in Python. *Journal of Machine Learning Research*, 14(35):2349–2353, 2013.

[147] Ereen Rezkallah, Abeer Ibrahim, AbdelRahman Dahy, Ahmed Abdel Hakiem, and Refaat Mahfouz. DFT and Thermal Decomposition Studies on Gemcitabine. *Zeitschrift für Physikalische Chemie*, 233(10):1503–1527, 2019.

[148] J. Sulé-Suso, D. Skingsley, G. D. Sockalingum, A. Kohler, G. Kegelaer, M. Manfait, and A. J. El Haj. FT-IR microspectroscopy as a tool to assess lung cancer cells response to chemotherapy. *Vibrational Spectroscopy*, 38(1):179–184, 2005.

[149] Maryam Parsian. Synthesis and characterization of polymeric magnetic nanoparticles loaded by gemcitabine /. Master's thesis, Middle East Technical University, Turkey, 2014.